University of Windsor
Scholarship at UWindsor

Electronic Theses and Dissertations   Theses, Dissertations, and Major Papers

1-1-1987

Reactively sputter-deposited titanium oxide and barium silicon titanate thin films.

Toru Yamashita
University of Windsor

Follow this and additional works at: https://scholar.uwindsor.ca/etd

Recommended Citation

Yamashita, Toru, "Reactively sputter-deposited titanium oxide and barium silicon titanate thin films." (1987). *Electronic Theses and Dissertations*. 6149.
https://scholar.uwindsor.ca/etd/6149

This online database contains the full-text of PhD dissertations and Masters' theses of University of Windsor students from 1954 forward. These documents are made available for personal study and research purposes only, in accordance with the Canadian Copyright Act and the Creative Commons license—CC BY-NC-ND (Attribution, Non-Commercial, No Derivative Works). Under this license, works must always be attributed to the copyright holder (original author), cannot be used for any commercial purposes, and may not be altered. Any other use would require the permission of the copyright holder. Students may inquire about withdrawing their dissertation and/or thesis from this database. For additional inquiries, please contact the repository administrator via email (scholarship@uwindsor.ca) or by telephone at 519-253-3000ext. 3208.

NOTE TO USERS

This reproduction is the best copy available.

UMI®

REACTIVELY SPUTTER-DEPOSITED TiO_x AND $Ba_2Si_2TiO_8$ THIN FILMS

by

Toru Yamashita

A Dissertation
Submitted to the Faculty of Graduate Studies
Through the Department of Engineering Materials
in Partial Fulfillment of the Requirements for
the Degree of Doctor of Philosophy
at the University of Windsor
Windsor, Ontario

Windsor, Ontario

March, 1987

UMI Number: DC53246

INFORMATION TO USERS

The quality of this reproduction is dependent upon the quality of the copy submitted. Broken or indistinct print, colored or poor quality illustrations and photographs, print bleed-through, substandard margins, and improper alignment can adversely affect reproduction.
In the unlikely event that the author did not send a complete manuscript and there are missing pages, these will be noted. Also, if unauthorized copyright material had to be removed, a note will indicate the deletion.

UMI®

UMI Microform DC53246
Copyright 2009 by ProQuest LLC
All rights reserved. This microform edition is protected against unauthorized copying under Title 17, United States Code.

ProQuest LLC
789 East Eisenhower Parkway
P.O. Box 1346
Ann Arbor, MI 48106-1346

C Toru Yamashita

To My Parents

ABSTRACT

Thin films of titanium oxide and barium-silicon-titanium oxide have been fabricated by reactive sputter depositon using metallic targets. The focus of the present study has been the relationships between deposition conditions and the resulting properties of the films.

The deposition unit was equipped with a triode sputtering source and an auxillary rf power supply. The flow rates of the sputtering gas (Ar) and the reactive gas (O_2) were controlled by mass flowmeters. Substrate heating was initially achieved with a ceramic heater. During the course of the work, a tantalum wire heater was designed and developed for use at higher substrate temperatures. The sputter-deposition parameters monitored in this experiment included the oxygen flow rate, the argon flow rate (which was converted to an equivalent partial pressure), the rf power density applied to the target, and the substrate temperature. Additional important parameters for the fabrication of the barium-silicon-titanium oxide thin films were the structure and the composition of the metallic target source. The deposited films were analyzed with a variety of techniques, including x-ray diffractometry, x-ray photoelectron spectroscopy, Rutherford backscattering

spectroscopy, and Raman spectroscopy. For the titanium oxide films the electrical resistivity was measured as a function of temperature to determine the conduction mechanism for each film.

Phase relations in the titanium oxide films were summarized by plotting the substrate temperature versus the oxygen flow rate to give a "metastable phase diagram". This diagram was in reasonable agreement with similar diagrams published in the literature and was also in agreement with the electrical conduction mechanism diagram constructed in the present work. The data for the average structure and composition of the films obtained by x-ray diffraction, Raman spectroscopy, and Rutherford backscattering spectroscopy were in good mutual agreement. X-ray photoelectron spectroscopy revealed the presence of a fully oxidized surface layer on all the analyzed samples, regardless of the film deposition conditions.

A metallic target containing barium, silicon, and titanium with the respective atomic ratios of 2:2:1 was prepared by combining the techniques of induction melting and powder sintering. The relative compositions of barium-silicon-titanium oxide films reactively sputter deposited from the metallic target were determined by x-ray photoelectron spectroscopy. For samples deposited at a

substrate temperature of 70° C, the relative titanium content increased and the relative silicon content decreased as the argon partial pressure was reduced and/or the applied rf power density was raised. The conditions for obtaining stoichiometric $Ba_2Si_2TiO_8$ thin films were projected from these data.

ACKNOWLEDGEMENTS

The author wishes to express his gratitude to Dr. Hisao Yamauchi for his supervision, guidance and friendship throughout the course of this study and during his entire tenure at the University of Windsor.

Acknowledgements are extended to Dr. W.V. Youdelis for his invaluable discussions and help in using induction furnace. The author is grateful to Mr. J.W. Robinson of the University of Windsor for his assistance in the maintenance of the sputter deposition system and electron microscopy analysis. The author is also grateful to Dr. R. Aroka of the University of Windsor for his great help on the Raman Spectroscopy analysis and to Dr. M. Sayer of Queen's University for his helpful discussion and assistance. The author is indebted to Mr. G. DeMaggio, Dr. B. Chao, Mr. J. Tyler and Dr. T. Takagi of the Energy Conversion Device Inc., Troy, Michigan. The author is also grateful to Dr. Y. Miyasaka and Dr. M. Kimura, Nippon Electric Company, Tokyo, Japan for their offering the useful information of fresnoite. The author wishes to express his gratitude to Dr. Whitten of Queen's University for his help of the use of Rutherford backscattering spectroscopy. Acknowledgements are also extended to Mr.R. White and Mr.P. Kawa for their

help. Assistance of computer programming by Mr. D.Curry of the University of Windsor was appreciated.

Finally, the author would like to thank Miss Kerene Boong and his friends and members of his family for their support and encouragement throughout this study.

TABLE OF CONTENTS

ABSTRACT.. i

ACKNOWLEDGEMENTS................................ iv

TABLE OF CONTENTS............................... vi

LIST OF TABLES.................................. ix

LIST OF FIGURES................................. x

CHAPTER 1 INTRODUCTION.......................... 1

CHAPTER 2 LITERATURE REVIEW..................... 5

2.1 OPTICAL PROPERTIES OF CERAMICS.............. 5

2.2 ELECTRICAL PROPERTIES OF NON-CRYSTALLINE SEMICONDUCTORS.............. 6

2.3 PIEZOELECTRIC THIN FILMS.................... 11

2.4 SPUTTERING.................................. 12

2.41 DIODE SPUTTERING........................... 12

2.42 MAGNETRON SPUTTERING....................... 13

2.43 TRIODE SPUTTERING.......................... 13

2.44 REACTIVE SPUTTERING........................ 14

2.5 THIN FILM ANALYSIS METHODS.................. 15

2.51 XPS (X-RAY PHOTOELECTRON SPECTROSCOPY)..... 15

2.52 RUTHERFORD BACKSCATTERING SPECTROSCOPY..... 16

2.53 RAMAN SPECTROSCOPY......................... 17

2.6 FILM THICKNESS MEASUREMENTS................. 18

2.7 TITANIUM OXIDES............................. 20

2.71 EQUILIBRIUM PHASE DIAGRAM.................. 20

2.72 STRUCTURES................................. 21

	2.73	OPTICAL PROPERTIES........................	22
	2.74	ELECTRICAL PROPERTIES.....................	24
	2.8	FRESNOITE.................................	26
CHAPTER 3		TiO_x THIN FILMS........................	29
	3.1	EXPERIMENTAL PROCEDURE....................	29
	3.11	TARGET PREPARATION........................	29
	3.12	THIN FILM PREPARATION.....................	29
	3.13	THICKNESS MEASUREMENTS....................	32
	3.14	PHASE AND COMPOSITION ANALYSES............	33
	3.15	RESISTIVITY MEASUREMENTS..................	34
	3.2	RESULTS AND DISCUSSION....................	36
	3.21	DEPOSITION RATE...........................	36
	3.22	PHASE RELATIONS...........................	38
	3.221	X-RAY DIFFRACTOMETRY......................	38
	3.222	X-RAY PHOTOELECTRON SPECTROSCOPY..........	42
	3.223	RUTHERFORD BACKSCATTERING SPECTROSCOPY....	46
	3.224	RAMAN SPECTROSCOPY........................	50
	3.225	COMPARISON OF METASTABLE PHASE DIAGRAMS...	53
	3.23	RESISTIVITY...............................	56
CHAPTER 4		$Ba_2Si_2TiO_8$ THIN FILMS................	62
	4.1	EXPERIMENTAL PROCEDURE....................	62
	4.11	TARGET PREPARATION........................	62
	4.12	THIN FILM PREPARATION.....................	64
	4.13	THICKNESS MEASUREMENTS....................	66
	4.14	PHASE AND COMPOSITION ANALYSES............	66

4.2	RESULTS AND DISCUSSION	67
4.21	METALLIC TARGETS	67
4.22	DEPOSITION RATE	70
4.23	COMPOSITION AND PHASES	71
CHAPTER 5	SUMMARY	75
5.1	TITANIUM OXIDE THIN FILMS	75
5.2	Ba-Si-Ti METALLIC TARGETS FOR REACTIVE SPUTTER DEPOSITION OF THIN FILMS	77
5.3	$Ba_2Si_2TiO_8$ THIN FILMS	78
CHAPTER 6	CONCLUSION	80
CHAPTER 7	RECOMENDATION FOR FUTURE RESERCH	82
CHAPTER 8	REFERENCES	84
APPENDIX A	THICKNESS MEASUREMENTS	93
APPENDIX B	DEPOSITION RATE OF TITANIUM THIN FILMS	95
APPENDIX C	RESISTIVITY MEASUREMENTS OF TiO_x THIN FILMS AT HIGH TEMPERATURES	97
APPENDIX D	CALCULATION OF $Ba_2Si_2TiO_8$ X-RAY DIFFRACTION PATTERN	99
APPENDIX E	ERROR ANALYSIS AND LEAST SQUARE METHOD FOR RESISTIVITY DATA	103
VITA AUCTORIS		106

LIST OF TABLES

Table		Page
2.1	Resistivity of single crystal titanium oxides at room temperature.	107
3.1	Deposition conditions and thicknesses of TiO_x thin film Samples (1)-(12).	108
3.2	Compositional analysis of Rutherford back-scattering spectroscopy data (figure 3.12).	109
A.1	Comparison between the thicknesses measured by Transky method and those measured by Stylus method.	110

LIST OF FIGURES

Figure		Page
2.1	Change in refractive index with wavelength for several crystals and glasses (17).	111
2.2	Frequency variation of the index of absorption for metals, semiconductors, and dielectrics (17)	112
2.3	Various forms proposed for the density of states in amorphous semiconductors. Localized states are shown shaded. (a) Overlapping conduction and valence band tails (19); (b) a real gap in the density of states suggested here as being appropriate for a continuous random network without defects; (c) the same as (b) but with a partially compensated band of defect levels; (d) the same as (b) but with overlapping bands of donor, E_Y, and acceptor, E_X, levels arising from the same defect. (ref (18))	113
2.4	Illustration of temperature dependence of electrical conductivity of an amorphous semiconductor (18).	114
2.5	Schematic diagram of diode sputtering system (16).	115
2.6	Schematic diagram of magnetron sputtering system with a ring magnet (15).	116
2.7	Schematic diagram of triode sputtering system (24).	117
2.8	Energy level diagrams of photoelectron (top) and Auger electron (bottom) excitation (27).	118
2.9	Schematic diagram of multi-technique AES/XPS analytical system (27).	119
2.10	Typical broad-range XPS spectrum from TiO_2.	120
2.11	Schematic diagram of Rutherford backscattering spectroscopy (RBS) apparatus (30).	121
2.12	Appearance of scattered light with frequencies ν_o, $(\nu_o+\nu_1)$, and $(\nu_o-\nu_1)$ (150).	122

2.13	Stokes and anti-Stokes Raman shifts and fluorescence process (34).	123
2.14	Schematic diagram of commercially used Raman spectrometer (34).	124
2.15	Schematic view of apparatus for producing multiple-beam Fizeau fringes (Tolansky technique) (131).	125
2.16	Fringe pattern produced from thin film (16).	126
2.17	Titanium-oxygen phase diagram (35).	127
2.18	Titanium-oxygen phase diagram (36).	128
2.19	Titanium-oxygen phase diagram (37).	129
2.20	Structure of rutile TiO_2 (138).	130
2.21	Structure of anatase TiO_2 (138).	131
2.22	Structure of brookite TiO_2 (138).	132
2.23	Structure of Ti_2O_3 (139).	133
2.24	Structure of Ti_2O (49).	134
2.25	Energy band structure of TiO (68).	135
2.26	Energy band structure of Ti_2O_3(71).	136
2.27	Energy band structure of Ti_4O_7 (64).	137
2.28	Energy band structure of crystalline non-stoichiometric rutile TiO_2 (76).	138
2.29	Crystallographic structure of $Ba_2Si_2TiO_8$ (projection on X-Y plane) (80).	139
2.30	Crystallographic structure of $Ba_2Si_2TiO_8$ (projection on X-Z plane) (79).	140
2.31	Electromechanical coupling factor, $2\Delta v/v$, vs temperature coefficient of delay, TCD, for sets of SAW propagation plane and direction in piezoelectric single crystals (140).	141
3.1	Set-up in sputtering deposition unit (used in the present experiment) with triode source: (1) Cu ring, (2) glass cylinder, (3)Al foil.	142
3.2	Electrical circuit diagram for resistivity measurement. a, b, c and d are electrodes. Electrodes a and c were used to avoid edge effect on the current flow from d to b.	143

3.3 Schematic diagram of resistivity measurement set-up. 144

3.4 Deposition rate, R_D, in terms of O_2 gas flow rate, F_{O_2}, when Ar gas flow rate, F_{Ar}, and partial pressure, P_{Ar}, are fixed. 145

3.5 "Metastable phase diagram" for TiO_x thin films fabricated at different substrate temperature (T_s) and oxygen gas flow rate (F_{O_2}): ○-amorphous ◐-fine polycrystalline and ⬢-fully crystalline; R-rutile, A-anatase and a-amorphous. Samples (1)-(13) were fabricated with 70 m Torr Ar partial pressure and Sample (14) was deposited with 130 m Torr Ar partial pressure. 146

3.6 Free energy of formation per mole of oxygen as a function of temperature (Ellingham diagram)(95). 147

3.7 Ti concentration with respect to oxygen gas flow rate, F_{O_2}, determined bt XPS for five TiO_x thin films at their original surface (solid symbols) and 3-min. Ar^+-bombarded fresh surface (open symbols). 148

3.8 Schematic diagram of composition distribution in the cross section of TiO_x thin film samples. 149

3.9 Narrow-range XPS spectra from TiO_2 after 0, 1, 2 and 3 minutes Ar^+ ion sputtering. 150

3.10 Typical narrow-range XPS spectra of (A) as-deposited TiO_x and (B) TiO_x after surface layer of ~100Å removed. 151

3.11 Oxygen concentration profile of TiO_2 thin film as Ar^+ sputtering continues. 152

3.12 Rutherford backscattering spectra of (A) Samples (1), (B) Sample (3) and (C) Sample (4) using 2.0 MeV He ions incident. 153

3.13 Raman spectrum of rutile granules purchased from Cerac. 154

3.14 Raman spectrum of anatase granules purchased from Cerac. 155

3.15 Raman spectrum of TiO granules purchased from Cerac. 156

3.16	Raman spectrum of glass substrate.	157
3.17	Raman spectrum of Sample (1).	158
3.18	Raman spectrum of Sample (3).	159
3.19	Raman spectrum of Sample (4).	160
3.20	Raman spectrum of Sample (5).	161
3.21	Raman spectrum of Sample (6).	162
3.22	Raman spectrum of Sample (7).	163
3.23	Raman spectrum of Sample (8).	164
3.24	Raman spectrum of Sample (9).	165
3.25	Raman spectrum of Sample (10).	166
3.26	Raman spectrum of Sample (11).	167
3.27	Raman spectrum of Sample (12).	168
3.28	"Metastable phase diagrams" for samples fabricated by means of (A) an rf diode sputterring technique (6) and (B) a dc plasmatron sputtering technique (9).	169
3.29	Resistivity of Sample (3) in terms of temperature. Curves are for three different electrical conduction mechanisms.	170
3.30	Resistivity of Sample (6) in terms of temperature. Curves are for three different electrical conduction mechanisms.	171
3.31	Resistivity of Sample (9) in terms of temperature. Curves are for three different electrical conduction mechanisms.	172
3.32	Electrical conduction mechanism diagram superimposed on the "metastable phase diagram".	173
3.33	Parameter T_0 used in eq (3.15) for the Mott mechanism in terms of substrate temperature (T_s) and oxygen gas flow rate (F_{O2}).	174
3.34	Resistivities of Samples (1) to (12) versus temperature.	175

4.1	(A) Ti metal and $BaSiO_3$ discs. (B) Composite sputtering target of $BaSiO_3$ disc embedded at the centre of Ti disc.	176
4.2	Temperature -vs- power relation of "new" heater. Tantalum wire was used as the heating element.	177
4.3	Heating program for sintering Target III.	178
4.4	Titanium-silicon phase diagram (129).	179
4.5	Silicon-barium phase diagram (129).	180
4.6	Deposition rate of Ba-Si-Ti oxide thin film Samples (a), (b) and (c) (defined in section 4.22) in terms of Ar partial pressure, P_{Ar}, and power density, W, applied to the target.	181
4.7	Target I (defined in section 4.21) after sputtering.	182
4.8	Scanning electron micrograph of thin film sputter deposited from Target I.	183
4.9	Energy dispersion spectra (using Kevex) for (A) grain and (B) background of the thin film shown in figure 4.8.	184
4.10	Spectrum of energy dispersion x-ray analysis (Kevex) of $Ba_2Si_2TiO_8$ ceramics (15).	185
4.11	Scanning electron micrographs of thin films sputter deposited from metallic Target III (defined in sectioh 4.21) at (a) P_{Ar}=150 m Torr and power density applied to the target, W= 10 W/cm^2, (b) P_{Ar}=115 m Torr and W=10 W/cm^2 and (c) P_{Ar}=85 mTorr and W=20 W/cm^2. In all the cases, the oxygen gas flow rate is kept constant at 0.2 scc/min(see next page for (b) and (c)).	186
4.12	Compositions of Samples (a), (b) and (c) (defined in figure 4.11) versus argon gas partial pressure, P_{Ar}, and power density applied to the target, W.	188
A1	Titanium thin film thickness measured by a stylus method.	189
B1	Deposition rate, R_D, of titanium thin films versus Ar partial pressure, P_{Ar}.	190

B2	Deposition rate, R_D, of titanium thin films versus power density applied to the target, W.	191
B3	Sputtering yield of Cu as a function of Kr^+ ion bombardment energy (142-147).	192
C1	Resistivity of Sample (4) with Al electrodes in terms of temperature.	193
C2	Resistivity of Sample (8) with Au electrodes in terms of temperature.	194
C3	Resistivity of Sample (8) at 115°C as a function of time.	195
D1	X-ray diffraction patterns of (a) $Ba_2Si_2TiO_8$ (BST)(in JCPD card) and (b) $BaSiTiO_5$ (in JCPD card). (c) Calculated BST pattern. Experimentally obtained x-ray diffraction pattern from the sample which had the Ba:Si:Ti ratios equal to (d) 2:2:1 and (e) 1:1:1.	196

CHAPTER 1

INTRODUCTION

A variety of dielectric thin films have been developed for optical, electrical, and mechanical applications (1). In these applications, both the crystallinity and the composition of the thin film are important parameters. For thin film insulators, amorphous films are desirable (2) since polycrystalline films are generally less insulating and single-crystal insulating films are difficult to prepare. On the other hand, for piezoelectric and ferroelectric uses, highly oriented crystalline films are required (3, 4).

To satisfy specific requirements for each application, the reactive sputter deposition technique is one of the most useful thin film preparation methods. Using this technique composition may be controlled by adjusting either the composition of the target or the amount of reactive gas (or both), and the crystallinity of the film may be controlled by varying the substrate temperature.

In the present work titanium oxide thin films and barium-silicon-titanium oxide films are fabricated by means of reactive sputtering in an rf triode sputter deposition unit. The relationships between the preparation conditions

and the crystallinity and composition of the thin films are studied.

Titanium oxide thin film coatings are promising for future applications in optical devices as well as for electronic and catalytic uses. The TiO_2 coating employed in the SHIVA laser for nuclear fusion experiments (5) may also be used for the NOVA 300 TW neodymium glass laser system (5, 6). The optical properties of TiO_2 films have been studied for crystalline and amorphous films fabricated by means of reactive diode sputtering (5, 6, 7, 8, 9, 10). It has been confirmed that TiO_2 thin films generally have high refractive indices and high laser damage thresholds (5, 6), although these properties are dependent on the deposition conditions. In contrast titanium suboxides, TiO_x ($x<2$), have been found to have high absorption indices (6, 11) and may be employed as antireflection coatings in such uses as solar absorber systems (11).

In the present study, titanium oxide thin films are fabricated by means of a reactive triode sputtering technique. Such deposition conditions as oxygen flow rate, substrate temperature, etc. are controlled to obtain samples which have a variety of degrees of crystallinity and oxidation state. The films are analyzed by various techniques, including x-ray diffractometry, x-ray photoelectron spectroscopy, Rutherford backscattering spectroscopy, Raman spectroscopy, and electrical

resistivity measurement. A "metastable phase diagram" is then constructed by plotting the substrate temperature versus the oxygen flow rate. The electrical resistivity of each film is measured as a function of temperature to determine the most probable conduction mechanism. An electrical conduction mechanism diagram is obtained and is compared to the "metastable phase diagram".

Various types of surface acoustic wave (SAW) devices have been developed using piezoelectric materials (12). Single crystal Fresnoite ($Ba_2Si_2TiO_8$) has been considered as a material for SAW devices (13). In the calculation of Yamauchi et al (14), $Ba_2Si_2TiO_8$ thin films deposited on fused quartz substrates were predicted to have competitive SAW characteristics. Previously $Ba_2Si_2TiO_8$ thin films were fabricated by means of sputter deposition techniques using ceramic targets (15, 16). However, the piezoelectric properties of the films have not yet been confirmed. One of the major problems has been the low deposition rates resulting from the low sputtering rates of ceramic targets (15, 16). Reactive sputter deposition techniques may provide higher film deposition rates since the sputtering rates of metallic targets are usually much higher than those of ceramic targets.

In the present study, various types of metallic targets are tested for reactive sputter deposition of barium-silicon-titanium oxide thin films on (100) Si

substrates. From the analysis of the structures and compositions of the resulting films an attempt is made to project the sputter deposition conditions for the fabrication of stoichiometric $Ba_2Si_2TiO_8$ thin films.

CHAPTER 2

LITERATURE REVIEW

2.1 OPTICAL PROPERTIES OF CERAMICS

A dielectric material reacts to electromagnetic radiation differently from free space because it contains electrical charges that can be displaced. For a sinusoidal electromagnetic wave, there is a change in wave velocity and intensity described by the complex coefficient of refraction:

$$n^* = n - ik$$

where n is the refractive index and k is the absorption index. The index n is determined as follows:

$$n = \frac{v_o}{v}$$

where v_o is the velocity of light in a vacuum and v is the velocity of light in the medium. The refractive index is a function of the frequency of the light, normally decreasing as the wavelength increases (figure 2.1) (17).

The optical properties of dielectric materials are generally of interest because of their good transmission in the optical part of the spectrum as compared with other

classes of materials (figure 2.2) (17). At short wavelengths this good transmission is terminated at the ultraviolet absorption edge, which corresponds to radiation energies and frequencies where absorption of energy arises from electronic transitions between levels in the valence band to unfilled states in the conduction band. At long wavelengths the relatively good transmission of dielectrics is terminated by elastic vibration of the ions in resonance with the imposed radiation.

For the application to antireflection coatings, multilayer coatings are commonly used. Antireflective coatings against a wide range of wave lengths can be obtained by controlling the thickness of each layer and/or changing the materials (143).

2.2 ELECTRICAL PROPERTIES OF NON-CRYSTALLINE SEMICONDUCTORS

The concept of "density of states" for electrons may still remain valid even for non-crystalline solids (18). Actually the densities of states of many non-crystalline materials have been determined using various experimental methods. Such states lie in bands separated by energy gaps, just as in crystals. Localized states in the gap are a consequence of defects. As long as the short-range order which is present in the crystalline phase is essentially

unchanged (i.e. similar bond lengths, bond angles, and local coordination with those in the crystal), the gross features of the crystalline density of states are preserved, though there are some differences.

Cohen, Fritzsche, and Ovshinsky (19) supposed that an amorphous structure would lead to overlapping band tails of localised states (CFO model) as shown in figure 2.3(a). One of the principal features of this model was the existence of "mobility edges" (19) at energies in the band tails. These separate the localized states from the extended states. The difference between the energies of the mobility edges in the valence and conduction bands is called the "mobility gap". The proposal of overlapping tails, i.e. the CFO model, is now considered unlikely to apply to amorphous semiconductors and insulators that are transparent in the visible or infrared region (17). However, this idea may still be valid in some liquids. Semiconductors, in which all bonds are saturated and there are no long-range fluctuations, should have a density of states as shown in figure 2.3(b) with a true band gap. Deep tails should arise only from gross density or bond-angle fluctuations.

Alternative suggestions to the CFO model for states in the gap are shown in figures 2.3(c) and (d). In figure 2.3(c) a band of deep acceptors is partially occupied by electrons originating from a shallower band of donors. The role of donors and acceptors can be reversed. This simple

model, proposed by Davis and Mott (18, 20), was based on several experimental results which implied a finite density of states at the Fermi level, E_F. As long as the total density of states in the gap is not large, this model allowed optical transparency. Mott (142) suggested that, if the states arose from a defect centre, e.g. a dangling bond, then they could act both as deep donors (E_Y) and acceptors (E_X), with single and double occupancy conditions leading to two bands separated by an appropriate correlation energy. This is shown in figure 2.3(d). If the narrow bands near the Fermi level overlap strongly, then this model is essentially the same as the model shown in figure 2.3(c).

Three kinds of mechanism of conduction may be expected for electrons in amorphous semiconductors according to the concept of the density of states and mobility edge. These mechanisms are:

i) Transport by carriers excited beyond the mobility edges into non-localized states at E_c (energy level at the bottom of the conduction band) or E_V (energy level at the top of the valence band). The conductivity (for electrons) is:

$$\sigma = \sigma_1 \exp \left(- \frac{E_C - E_F}{kT} \right)$$

where E_F is the Fermi level and σ_1 is a constant.

ii) Transport by carriers excited into localized states at the band edges and hopping at energies close to E_A (energy

level at the bottom of the conduction band in the mobility gap) or E_B (energy level at the top of the valence band in the mobility gap). The conductivity for electrons is:

$$\sigma = \sigma_2 \exp \left(- \frac{E_A - E_F + W_1}{kT} \right)$$

where W_1 is the activation energy for hopping and σ_2 is a constant. W_1 is a function of T.

iii) If the density of states at E_F is finite, then there will be a contribution from carriers with energies near E_F which can hop between localized states by a process analogous to impurity conduction in heavily doped crystalline semiconductors. In this case

$$\sigma = \sigma_3 \exp \; (- W_2 / kT)$$

where σ_3 is a constant ($\sigma_3 \leq \sigma_2$) and W_2 is the hopping energy, which is of an order of half the width of the density of states is as shown in figure 2.3(c). At temperatures such that kT is less than the bandwidth, or if the density of states is as shown in figure 2.3(a) or (d), hopping will not be between nearest neighbours. Instead variable-range hopping, described below, will occur:

$$\sigma = \sigma_3' \exp \left(- T_o / T \right)^{1/4}$$

where

$$T_o = C \left(\alpha^3 / kN(E_F) \right)^{1/4}$$

and

$$\alpha = \left(2m^* W_o \right)^{1/2} / h \qquad \text{and } C \cong 2$$

in which m^* is the effective mass of electron and W_o is the energy level for an electron in a single potential well.

The above conduction mechanisms are illustrated in terms of $\log \sigma$ versus $1/T$ as shown in figure 2.4.

More recently, Triberis et al (21) introduced a novel mechanism of conduction in a high temperature regime where the hops are characterised by the absorption and emission of many phonons using a percolation theory. This temperature regime is also called the small-polaron hopping regime. A carrier trapped by a defect in a crystal or in an Anderson localized state in a non-crystalline material will always distort its surroundings to some extent to reduce its energy. If the interaction energy between the carrier and the phonons is strong in comparison with the bandwidth, a "small-polaron" may form. For such a case Triberis et al (21) derived the following equation for the conductivity at high temperatures (i.e. $\hbar\omega \ll kT$):

$$\sigma = \sigma_0 \exp (T_p/T)^{2/5}$$

where σ_0 is a constant and

$$T_p = 8.5 N_s^{1/2} \alpha^{3/2} / kN_o$$

in which N_s is the concentration of sites where electron can move, α^{-1} is the spatial extent of the electronic wavefunction localised at a single site and N_o is the density of states which is assumed to be constant in the energy range where polaron hopping conduction occurs.

2.3 PIEZOELECTRIC THIN FILMS

Some piezoelectric materials contain electric dipoles, each of which consists of a positive and a negative charge some distance apart. In such materials, to obtain piezoelectric activity, the dipoles must be oriented to a certain degree.

If a stress is applied to such materials they develop an electric moment whose magnitude is proportional to the applied stress. This is known as the direct piezoelectric effect. If a uniaxial tensile stress σ is applied along one of the diad axes of a piezoelectric material, the magnitude of the electric moment per unit volume, or the polarization charge per unit area (P), is given by

$$P = d \cdot \sigma$$

where d is a constant, called a piezoelectric modulus. As is implied by this equation, a change from a tensile stress to an equal compressive stress reverses the direction of the polarization.

An important characteristic of the piezoelectric material is the electromechanical coupling factor, k^2. It is usually defined as follows (22):

$$k^2 = \frac{\text{(resultant electrical energy)}}{\text{(imput mechanical energy)}}$$

Piezoelectric thin films can be used for transducers, oscillators, convolvers, optical image scanners and surface-acoustic-wave (SAW) devices (12). For the case of SAW devices, the SAW propagation velocity on the piezoelectric material surface is as important as the k^2 value. In order to use SAW devices in a certain (usually wide) range of temperature, the temperature coefficient of delay (TCD), i.e. the temperature dependence of the SAW velocity, is required to be small, i.e. of the order of 0~50 ppm/K (13).

2.4 SPUTTERING

2.41 DIODE SPUTTERING

A simple source of ions for sputtering is provided by the well-known phenomenon of the glow discharge due to an applied electric field between two electrodes in a low pressure gas. Figure 2.5 shows the structure of a diode. The gas breaks down to conduct electricity when a certain minimum voltage is reached between the target and chamber. The substrate onto which the film material is sputter deposited from the target is usually placed at the same electric potential level as the chamber, as shown in figure 2.5. The gas (usually Ar) introduced into the chamber is now ionized. The ionized gas atoms (e.g. Ar^+) are

accelerated by the applied field toward the target and sputter out the atoms on the target surface.

2.42 MAGNETRON SPUTTERING

The set up of magnetron sputtering is the same as that of diode sputtering except for the existence of magnets installed behind the target as shown in figure 2.6. The magnetic field induced by these magnets causes the electrons to move helically around the lines of magnetic force. These electrons collide with neutral sputtering gas and then ionize them. In this way, the plasma is able to be maintained at low pressures. The sputtering operation at a low pressure "results in" a high deposition rate (23) and fewer contaminated products (i.e. thin films) (24).

2.43 TRIODE SPUTTERING

Auxiliary electrons are supplied thermionically from a filament and drawn to the anode as shown in figure 2.7. With the discharge gas adjusted to the desired operating pressure, the cathode (filament) is electrically heated to a temperature at which it emits electrons to support a discharge. When the power is applied to the anode, electrons are accelerated toward it. Argon atoms are excited or ionized by electron collisions, and a plasma is

initiated. The target may have negative voltage of any value applied to it without affecting the plasma, other than within the ion sheath (the dark-field region) that forms around the target. Every ion reaching the edge of the sheath is accelerated to the target and has a probability of causing ejection of atoms from the target surface.

Advantages of triode sputtering are; plasma can be obtained at low pressure and independently from the power applied to the target.

2.44 REACTIVE SPUTTERING

When reactive gas is deliberately added to the sputtering system, the desired compound may be produced in a film form using a metallic target. To the author's knowledge, reactive sputtering by means of a triode sputtering technique has not been reported. Reactive sputtering can be done using diode or magnetron sputtering apparatus. The non-reactive (discharge) gas and reactive gas mixture or reactive gas only is introduced into the sputtering chamber. The reaction to form the compound mainly takes place on the substrate surface (24). Reactions may also occur on the target surface. Reactions in the gas phase have been considered to be unlikely because of problems of conserving momentum and dissipating the heat of reaction (24, 26).

Advantages of reactive sputtering are as follows:

i) In general, metals are ductile and have lower melting

temperatures than compounds, e.g. metal oxides, metal nitrides, etc. The manufacture of desired target shapes from metals is thus easier and less expensive than forming non-metallic materials into the target shapes.

ii) By changing the ratio of reactive gas and non-reactive gas in the sputtering chamber, films having a composition gradient along the direction perpendicular to the substrate surface may be obtained. Also a precise composition control may be achieved.

iii) In most cases, the deposition rates of metals are higher than those of their compounds. Thus reactive sputtering gives higher deposition rates.

Since no information about reactive triode sputtering techniques was available, an "original" sputtering set up was designed and employed in the present work.

2.5 THIN FILM ANALYSIS METHODS

2.51 XPS (X-RAY PHOTOELECTRON SPECTROSCOPY)

Although the first photoelectron emission studies began in the early part of this century(27), XPS study did not begin until the 1950's (28). Finally, in the late 1960's, a commercial XPS system became available to measure the surface chemical properties of solids (29).

Figure 2.8 is an electron energy level diagram of a solid illustrating the mechanisms necessary for emission of

photoelectrons. In this diagram a photon is absorbed such that:

$$h\nu = E_{KE} + E_{BE} + \phi$$

where $h\nu$ is the photon energy, E_{KE} is the electron kinetic energy. E_{BE} is the electron binding energy and ϕ is the work function of the spectrometer. E_{BE} is defined as the energy difference between the Fermi level and the energy level of the electron that has been removed.

Figure 2.9 is a schematic illustration of an XPS system. The sample is positioned in front of the energy analyzer, and photoelectrons are produced from the sample when exposed to x-rays. The electron current from the electron multiplier can be monitored with pulse counting electronics to produce an N(E) spectrum, i.e. a spectrum of the number of electrons versus energy. A typical spectrum obtained from TiO_2 in a broad scanning mode is shown in figure 2.10.

2.52 RUTHERFORD BACKSCATTERING SPECTROSCOPY

The strength of Rutherford Backscattering Spectroscopy (RBS) resides in the speed of the technique, its ability to perceive depth distributions of atomic species below the surface, and the quantitative nature of the results. The four basic physical concepts upon which RBS is based are: (1) energy transfer from a projectile to a

target nucleus in an elastic two body collision, (2) the likelihood of the occurrence of such a two-body collision, (3) the average energy loss of an atom moving through a dense medium and (4) the statistical fluctuations in the energy loss of an atom moving through a dense medium. The simplified set-up for RBS is schematically shown in figure 2.11(30). The light ions (usually H^+ or He^+) are projected into the sample and the detector measures the energy and number of the backscattered ions.

2.53 RAMAN SPECTROSCOPY

Raman spectroscopy depends on the frequency of the light scattered by molecules as they undergo rotations and vibrations. When a monochromatic light of frequency ν_o is directed at a cell containing a dust-free transparent substance, most of the light passes through it unaffected. However, some of the light($\sim$0.1 percent) is scattered by the sample molecules in all directions, as shown in figure 2.12. The scattered radiation contains photons which have the same frequency, ν_o , as the incident light (elastic scattering which is often called the Rayleigh line), but, in addition, the emergent radiation contains other frequencies (due to inelastic scattering) such as ($\nu_o - \nu_1$) and ($\nu_o + \nu_1$). This was observed by Raman (31, 32) in 1928 (the Raman shifts). Since, in thermal equilibrium, the

population of higher energy modes is less than that of lower energy modes and falls off exponentially with the energy, Raman shifts with a positive $\Delta \nu$ (anti-Stokes lines) are less intense than those with a negative $\Delta \nu$ (Stokes lines), and the intensity of the anti-Stokes lines falls off rapidly as $|\Delta \nu|$ increase.

The phenomena of fluorescence and Raman scattering must be distinguished. In fluorescence, the incident photon is completely absorbed and the molecule concerned is thereby raised to an excited electronic level. After a certain lifetime in this upper state, the molecule undergoes a downward transition and thereby re-radiates light of a frequency lower than that which it had absorbed (33). This mechanism is radically different from that of the Raman effect, in which the photon as a whole is never absorbed, but rather perturbs the molecule and induces it to undergo a vibrational or rotational transiton (see figure 2.13)(34). Each scattering species gives its own characteristic vibrational Raman spectrum, which can be used for its qualitative identification. The experimental set up is schematically shown in figure 2.14(34).

2.6 FILM THICKNESS MEASUREMENTS

The use of Fizeau fringes for thickness measurements is commonly called the Tolansky method. A schematic diagram

of Fizeau fringes produced by multiple-beam interference is shown in figure 2.15. The Fizeau plate is partially transparent and should be optically flat to have highly reflectivity. Surfaces of samples must be coated by high reflective materials if the sample surfaces do not have enough reflectivity. When the Fizeau plate is brought in contact with the film surface, and the interferometer is illuminated with a parallel monochromatic beam at normal incidence and viewed with a low-power microscope, dark fringes can be observed which trace out the points of equal air-gap thickness. The two adjacent fringes are separated by $\lambda/2$ (where λ is the wavelength of the monochromatic beam). If the surfaces of the samples are highly reflecting and very close to the Fizeau plate, the reflected fringe system consists of very fine dark lines against a white background. By adjusting the relative positions of the flats to form a wedge-shaped air gap, the fringes can be made to run in straight lines perpendicular to the steps on the opaque film. The fringes show a displacement as they pass over the film step edge. This displacement expressed as a fraction of the $\lambda/2$ fringe spacing gives the film thickness. The film thickness can be calculated by the following equation:

$$\frac{\text{Fringe Offset (filar units)}}{\text{Fringe Spacing (filar units)}} \times \frac{\lambda}{2} = \text{Film Thickness}$$

The fringe offset and spacing were measured with the filar eyepiece as shown in figure 2.16.

2.7 TITANIUM OXIDES

2.71 EQUILIBRIUM PHASE DIAGRAM

The equilibrium phase diagram of the titanium-oxygen system has been studied by many investigators (35-39). The first construction of such a phase diagram was carried out by DeVries et al in 1954 (35), using the data previously reported in the literature (figure 2.17). At that time, only titanium solid solutions (-Ti), with TiO, Ti_2O_3, Ti_3O_5 and Ti $_2$ phases were identified. Wahlbeck et al (36) modified this diagram using the results of their x-ray studies (figure 2.18). In this modified phase diagram, some "new" phases were added: Ti_2O and Magneli phases Ti_nO_{2n-1} $(4 \leq n \leq 10)$. In 1982, Gruber et al (37) offered a further modification of the diagram, using additional experimental data such as those obtained by means of magneto-resistance and electrical conductivity measurements. The revised phase diagram is given in figure 2.19. Two additional new phases, i.e. Ti_3O and Ti_6O, are seen in this phase diagram. The phase relations were later elaborated using techniques of thermopower, Hall coefficient, electrical conductivity and magneto-resistance measurements (38, 39).

2.72 STRUCTURES

According to reported phase diagrams (37) (section 2.71), the titanium oxides exist in a variety of forms: Ti_6O, Ti_3O, Ti_2O, TiO, Ti_2O_3, Ti_3O_5, Magneli phases [Ti_nO_{2n-1} ($n \geq 4$)] and TiO_2. Four different structures have been known for TiO_2, that is, rutile, anatase, brookite (40) and the high pressure phase which has an "α-PbO_3" structure (41). The structure of rutile as shown in figure 2.20 was first analyzed by Vegard in 1916 (42). Every titanium atom is surrounded by six oxygen atoms which form a slightly distorted octahedron. Each of the oxygen atoms is in contact with three titanium atoms which form an equilateral triangle. The anatase structure, which was analyzed also by Vegard (42), is demonstrated in figure 2.21. In this structure, as was the case of the rutile structure, every titanium atom is located at the centre of an octahedron formed by six oxygen atoms and every oxygen atom is surrounded by three titanium atoms. Figure 2.22 shows the structure of brookite. All the Ti_nO_{2n-1} ($n \geq 4$) phases are so-called Magneli phases (43). After Magneli studied these phases in molybdenum and tungsten oxides, Anderson et al (44, 45) investigated the Magneli phases in the titanium-oxygen system. It is described (43) as consisting of parallel-sided slabs which contain a certain

amount of rutile [TiO_6] octahedra. Identical slabs are united by octahedra sharing faces which are called "crystallographic shear" (CS) planes. Across CS planes, adjacent slabs are relatively displaced towards one another. Since the displacement necessitates the elimination of an oxygen plane, the metal atom density is higher at the CS plane than in rutile (the regions between the CS planes).

Ti_3O_5 was found to be isomorphous with "pseudo brookite" (46). Zachariasen (47) found that Ti_2O_3 had a corundum structure as shown in figure 2.23. Ehrlich (48) revealed that the structure of TiO was of the NaCl type. The structure of Ti_2O is shown in figure 2.24 (49). It was found (49) that Ti_3O had the same structure as Ti_2O but contained a certain fraction of vacancies in the oxygen sites. The phase with the least amount of oxygen was identified as Ti_6O (50) which had a hexagonal superlattice structure.

2.73 OPTICAL PROPERTIES

It is well known that TiO_2 (rutile) has a high refractive index of $\sim$2.7, (17, 51) which is higher than that for anatase i.e. $\sim$2.5 (9, 51). For the case of TiO_2 thin films, the refractive index varies with the grain size and the rutile-anatase ratio (6, 9). The thin films having larger grain size and/or higher rutile concentration have

higher refractive index.

Since TiO_2 has a high laser damage thresholds, the TiO_2 coating is one of the candidate materials for the NOVA 300TW neodymium glass laser system at Lawrence Livermore Laboratory (5, 6). The laser damage resistance of the TiO_2 thin films deposited by means of rf diode sputtering techniques was measured as a function of the grain size and the ratio of rutile to anatase (5, 6). The results indicated that the thin films which consisted of smaller grains possessed higher damage thresholds without any significant differences due to the rutile-anatase ratio.

While TiO_2 has a high refractive index, TiO_x $(x<2)$ films are characterized by high absorption indices (52). Thus TiO_x $(x<2)$ materials are expected to be used as selective absorbers for solar thermal conversion (11). Such absorbers are required to have low reflectances in the visible light region and high reflectances in the infra-red region (11). Schiller et al (52) studied the absorption coefficient of the TiO_x thin films fabricated using a reactive plasmatron sputtering technique in terms of the pressure ratio of the O_2 and Ar gases. According to their results, the absorption coefficient increased and the refractive index decreased monotonically with decreasing pressure ratio of the O_2 and Ar gases.

2.74 ELECTRICAL PROPERTIES

There have been a number of reports on the electrical conductivities of various titanium-oxide phases as a function of temperature (53-65). The band structures of phases, TiO (66-70), Ti_2O_3 (59, 66, 71-75), Ti_4O_7 (64) and rutile (TiO_2)(66, 76), have also been reported. The conductivities of titanium oxide single crystals at room temperature are summarized in Table 2.1. Phases Ti_2O_3 and Ti_3O_5 exhibit transitions from semiconductor to metallic conduction (s-m transition) when heated. The transition temperatures were determined at ∿400K and ∿200K, respectively (55, 59, 61, 65). The conductivity of TiO decreases with increasing temperature (i.e. metallic) (65) while the conductivities of Ti_5O_9, Ti_7O_{13}, Ti_8O_{15} and TiO_2 increase with increasing temperature (semiconductive) (61, 62, 77). However, some discrepancies are found in the data of Ti_4O_7 and Ti_6O_{11}. Bartholomew et al (65) reported that Ti_4O_7 had an s-m transition at ∿140K but Ti_6O_{11} did not have such a transition. On the other hand, Lakkis et al (64) and Marezio et al (61) did not observe s-m transitions in Ti_4O_7, and Marezio et al (61) observed an s-m transition in Ti_6O_{11}. These discrepancies may be due to the difficulties in the fabrication of single crystals of a single Magneli phase (61, 64).

The band structures of TiO (66), Ti_2O_3 (71, 73, 75), Ti_4O_7 (64) and rutile (TiO_2)(66, 76) are illustrated in figure 2.25-28. The main features of these band structures are as follows:

i) TiO: Since the titanium 3d band is partially filled with electrons, metallic conductivity results (see figure 2.25).

ii) Ti_2O_3: The titanium 3d band is split into 4 sub-bands. At temperatures below 400K the lowest sub-band is filled with electrons and the higher sub-bands are empty. Thus, Ti_2O_3 is semiconductive. At high temperatures (>400K), some of the electrons in the lowest sub-band are transfered into the next higher band. This is caused by an anomalous increase in the c/a ratio of the lattice parameters above 400K. In this case, the electrical conduction becomes metallic (see figure 2.26).

iii) Ti_4O_7: As mentioned in section 2.72, Ti_4O_7 is one of the Magneli phases. Thus, the CS planes exist periodically in the rutile phase. The band structures were calculated separately for the Ti^{3+} chains in the CS planes and the Ti^{4+} chains in the rutile phase (64) (see figure 2.27).

iv) TiO_2: The oxygen 2s band is filled with electrons and the titanium 3d level, which is $\sim$3 eV higher than the top of the oxygen 2s band, is empty. The impurity levels due to the Ti interstitials, Ti^{3+} ions and Ti^{2+} ions are known to be located in the band gap (76) (see figure 2.28).

2.8 FRESNOITE

Fresnoite was discovered by Alfors et al (78) during the course of a geological study of the sanbornite deposits in Eastern Fresno County, California in 1965. Alfors et al revealed that Fresnoite had the chemical formula of $Ba_2Si_2TiO_8$ (BST) and measured the crystallographic and optical data: fresnoite has a tetragonal lattice of a=8.52±0.01Å and c=5.210±0.05Å, and a refractive index of 1.775±0.003. They successfully synthesized BST from $BaCO_3$, SiO_2 and TiO_2 by sintering for 5.5 hours at 1350 °C (78). This synthetic fresnoite was confirmed to have the same x-ray diffraction pattern as the mineral fresnoite. The structure of fresnoite was analyzed in detail by Moore (79), Moore et al (80) and Masse et al (81): the crystal structure, interatomic distances and bond angles were determined as shown in figure 2.29 and 2.30. In figure 2.29, the BST unit cell is projected onto the x-y (or a-b) plane, indicating that fresnoite is centrosymmetric in this plane. In the y-z (a-c) plane, however, fresnoite is not symmetric. In 1970, Robbins (82) measured the piezoelectricity of fresnoite, and pointed out that the compound $BaSiTiO_5$ previously found by Rase et al in 1955 (83) did not exist but was a mixture of fresnoite and $BaTi_4O_9$ .A detailed discussion of the $BaSiTiO_5$ phase is given

in appendix D.

Using synthetically grown single crystals, Kimura et al (84), Haussuhl et al (85) and Kimura (86) measured the elastic, dielectric, piezoelectric, optical and thermal properties of fresnoite. Halliyal et al (87, 88) and Markgraf et al (89) analysed the dielectric, piezoelectric properties of glass ceramics of fresnoite. The characteristics of surface acoustic waves (SAW) were calculated for bulk fresnoite by Melngailis et al (90) and Yamauchi (13), and for fresnoite thin films by Yamauchi et al (14). Yamauchi et al concluded that a fresnoite thin film whose z-axis was aligned perpendicular to a fused quartz substrate might have not only zero temperature coefficient of delay (TCD) but also other useful SAW characteristics. Therefore, fresnoite is expected to be one of the potential materials for SAW devices. For an SAW device material, a high electromechanical coupling factor (k^2) and a low TCD are required. However it is not straightforward to find such materials. For example, $LiNbO_3$ has a high k^2 but its TCD is also high. On the other hand, quartz has a near zero TCD but k^2 is very small. Fresnoite ($Ba_2Si_2TiO_8$) crystals have intermediate values for both k^2 and TCD (in comparison with those of $LiNbO_3$ and quartz). Figure 2.31 shows the relations between k^2 and TCD for selected piezoelectric materials. For bulk piezoelectric materials, a trade-off relationship is observed between k^2

and TCD. It is, however, possible to design materials which are free from this trade-off relationship. One of the possibilities is to control the composition of piezoelectric ceramics (6). Another way is to use thin films with proper substrate materials, i.e. composite materials (14).

Ayukawa (15) and White (16) investigated the fabrication techniques of fresnoite (BST) thin films having the z(or c)-axis perpendicular to the substrate material. Both employed a triode rf sputtering technique. They utilized a variety of substrate materials such as soda-lime glass, fused quartz, (100) NaCl, (0001) mica, (111) Si and (100) Si, and a wide range of the substrate temperature from room temperature to 650°C. However, all deposited films revealed amorphous phases. Those thin films deposited on fused quartz substrates crystallized after annealing at 780 °C 10 hrs in a vacuum, while the crystallization temperature of those deposited on (100) Si single crystal substrates was ~700 °C. Thus, it has been projected that higher substrate temperatures than 650 °C are required to obtain c-axis oriented thin films. White (16) also revealed that the thin film composition was different from the target composition.

CHAPTER 3

TiO_x THIN FILMS

3.1 EXPERIMENTAL PROCEDURE

3.11 TARGET PREPARATION

Disc-shaped targets of 2.5 cm diameter were cut from titanium metal sheets of 2 mm thickness (99.7% pure :Johnson-Matthey). Each target was polished by emery papers (from #320 to #800 grit). Epoxy silver solder (Dynaloy 336) was used to mount the target on a copper target holder. The solder was dried at room temperature for 24 hours.

3.12 THIN FILM PREPARATION

The titanium oxide thin films were fabricated by means of a reactive sputtering technique using a titanium metal target in an rf-triode sputtering-deposition unit, as shown in figure 3.1. The filament and anode were connected with a plasma discharge module. The electrons emitted from the cathode (filament) were accerelated towards the anode. The electron acceleration voltage was controlled by the plasma

discharge module, while the power applied to heat the cathode was controlled by the filament module. Once the current between the anode and cathode was set at a certain level, both the plasma discharge module and filament module were automatically adjusted to maintain the current level. To ionize the Ar gas (i.e. to form the "plasma"), the Ar gas molecules were struck by electrons emitted from the cathode (see figure 3.1). The reactive gas (O_2) was not introduced in the sputtering source together with the sputtering gas (Ar). This was because the filament which was made of tantalum wire would be oxidized and eventually burned out. Actually, the reactive gas was introduced through a copper pipe ring with gas outlet holes installed in the vicinity of the substrate; the flow of O_2 being concentrated on the substrate surface. To separate O_2 gas from Ar gas in the sputtering chamber a glass cylinder ((2) in figure 3.1) was placed above the target and an aluminum foil with a hole ((3) in figure 3.1) was put on the glass cylinder. The diameters of the glass cylinder and the hole in the aluminum foil were 9.5cm and 4cm, respectively. The substrate-target distance was set at 6cm. Although a higher deposition rate could have been achieved if the substrate-target distance were set shorter (24), such a geometrical situation led to an instability of the plasma. The O_2 gas inlet ring was located 4.5cm above the target while the aluminum foil was 3.5cm above the target. Both Ar

and O_2 gas flows were individually controlled by the flow controllers (Vacuum General: Model 80-4). The Ar gas flow rate (F_{Ar}) was chosen in the range of 12.0 scc/min to 45.0 scc/min, while the O_2 gas flow rate (F_{O_2}) was varied from 0.1 scc/min to 0.8 scc/min. A diffusion pump and a mechanical pump were used to evacuate the sputtering chamber. The background pressure (before sputtering) was $\sim 1.0 \times 10^{-6}$ Torr. A variable orifice was installed between the chamber and diffusion pump. This enabled the pressure inside the chamber to be controlled by changing the angle of opening of the orifice. In the present experiment, the variable orifice was usually fully-open. The pressures inside the chamber were chosen from the range between 70 m Torr and 130 m Torr. Glass microscope slides (28at% Si, 8at% Na, 3at% K and 61at% O) were used as the thin film substrates. The 2.5 cm square shaped glass slide was cut into four pieces and then cleaned in an ultrasonic cleaner being immersed in ethanol. The four pieces were put back together on a stainless steel substrate holder. A ceramic heater (N.T.K.: AS 220C; 5cm x 5cm) and a thermocouple (chromel-alumel, 0.5mm diam.) were attached to the substrates. The substrate temperature (T_s) was varied from room temperature to 380 ^{o}C. Temperatures of 450 ^{o}C and 650 ^{o}C were reached using a heater of a different type. Details of this "high temperature heater" are given in section 4.12.

3.13 THICKNESS MEASUREMENTS

To measure the thickness of a thin film using an interferometer, a high reflectivity at the sample surface is required. Neither TiO_x films nor the glass substrate do not have a sufficiently high reflectivity. Thus aluminum was thermally evaporated and deposited in a vacuum on each thin film sample to obtain a reasonably high reflectivity. The thickness from the substrate to the top of the film edge was measured by an interferometer (Varian: Model 980-4000). The measurement was made at four different spots on each sample. In appendix A, the values obtained by interferometry are compared with those measured by a stylus method (Dektak surface profilometer available at Surface Science Western, University of Western Ontario, London, Ontario).

The deposition rate increased as the power applied to the Ti metal target was increased (in the range of 20 to 60 W/cm^2). The excess heat from the target can cause the silver solder between the target and copper target holder to melt even though the target holder is water cooled. If it occurs, it leads to the detachment of the target from the target holder. Taking into account the heat generated by the target due to the Ar^+ ion bombardment, a power density of 40 W/cm^2 was applied between the target and the

substrate throughout the present work.

3.14 PHASE AND COMPOSITION ANALYSES

All the titanium oxide thin films deposited on glass substrates were analized by x-ray diffractometry. Since the deposited films were about 4000Å thick, the diffraction peaks from the films were superimposed on a broad peak, i.e. amorphous peak, from the glass substrate.

Thin films deposited at room temperature with an Ar partial pressure (P_{Ar}) equal to 70 m Torr were analyzed by x-ray photoelectron spectroscopy (XPS) on an SSX-100 Spectrometer (available at Surface Science Western, University of Western Ontario, London, Ontario) and on a PHI 550 ESCA/SAM system (available at Energy Conversion Devices(E.C.D.), Troy, Michigan). A fully crystallized sample was also examined at Surface Science Western. In both cases, the compositions were analysed before and after the surface of the sample was cleaned by Ar^+ ion bombardment. The eroded depths in these samples were estimated at about 50Å in the Surface Science Western experiment and 100Å in the E.C.D. experiment. The XPS data were analyzed to determine the bond type and the composition using both narrow-range scanning and broad-range scanning techniques.

The compositions of fully and weakly crystallized samples were determined by Rutherford backscattering

spectroscopy (RBS) (at Physics Department, Queen's University, Kingston, Ontario). H^+ projectile ions were projected upon the TiO_x films with an energy of 2 MeV and the energy and number of backscattered H^+ ions were measured by a detector. In this RBS apparatus, the scattering angle was set at 160.0^o and the resolution was 14.00 KeV at the Gaussian full width half maximum. The compositions of the thin films were analyzed from the relative peak heights.

Some of the thin film samples were also analysed by a surface Raman scattering technique using the 4880Å excitation lines of an argon-neon laser (available at the Department of Chemistry and Biochemistry, University of Windsor). Although a compositional analysis is not possible in Raman spectroscopy, the aim of this particular study was to extract short-range bonding information.

3.15 RESISTIVITY MEASUREMENTS

In order to study the electrical properties of the titanium oxide thin films, surface resistivities were measured at various temperatures. Gold or aluminum electrodes were deposited on the surface of the TiO_x thin films by a thermal evaporation technique in vacuum. The geometry of electrodes and the electrical circuit are schematically shown in figure 3.2. An electrometer

(Kiethley: Model 610) was used. The electrodes (a) and (c) in figure 3.2 were fabricated so that the edge effect on the current flow from (b) to (d) would be circumvented. A schematic cross section of the resistivity measurement apparatus is shown in figure 3.3. A Cu wire was mechanically attached to the gold or aluminum electrode at the thin film surface. The thin film was placed on a ceramic heater and was heated up to 60 °C. A maximum temperature of 60 °C was chosen to maintain the crystallographic structural stability of the deposited thin films as well as the chemical stability of the thin film-electrode interface. The resistivity behaviour above 60 °C are shown in appendix C. The thin film and ceramic heater were sealed in a copper chamber to prevent any electrostatic effects. The copper chamber was then immersed in a liquid nitrogen filled styrofoam cryo-box. This enabled the resistivity of the thin films to be measured at temperatures as low as -191 °C. The measured resistances varied from 3×10^{2} to $3 \times 10^{11}\,\Omega$ depending on the samples and temperature. The resistivities were calculated under the following assumptions: (i) the current flows homogeneously in the titanium oxide film but not in the substrate material, and (ii) the current flow was limited in the width of electrode (b) shown in figure 3.2. Resistivity values obtained using the above assumptions ranged from as low as $3 \times 10^{-4}\,\Omega$m to as high as $1 \times 10^{6}\,\Omega$m depending on the particular sample and

temperature (91). (Note that the resistivity of soda glass is ~$1 \times 10^{11} \Omega m$ (91)).

3.2 RESULTS AND DISCUSSION

3.21 DEPOSITION RATE

The deposition rate (R_D) was measured as a function of oxygen gas flow rate (F_{O_2}) and oxygen gas partial pressure (P_{O_2}) for various fixed values of Ar gas flow rate (F_{Ar}) and Ar gas partial pressure (P_{Ar}). The results are shown in figure 3.4. A change in the angle of opening of the variable orifice resulted in different partial pressures of O_2 and Ar, even though the flow rates of O_2 and Ar remained constant. This is due to the pumping speed in the chamber being dependent on the angle of opening of the variable orifice. All the samples used in figure 3.4 were deposited at room temperature and at a fixed power density of 40 W/cm^2.

The curves shown in figure 3.4 look similar. All show that R_D increases with increasing F_{O_2} or P_{O_2} initially, reaches a maximum, then decreases with any further increase in F_{O_2} or P_{O_2}. This initial increase in R_D, due to increasing F_{O_2} or P_{O_2}, did not show in some of previous experimental data by Abe et al (121), Tanaka et al (7) or Wu et al (92): their results showed a plateau instead of a

hump. On the other hand, the results of Schiller et al (8) and Geraghty et al (77) showed the hump in terms of R_D with respect to P_{O_2} . All of these film samples were fabricated using an rf diode sputtering unit with the exception of those of Schiller et al's which were prepared using an rf plasmatron unit.

Schiller et al's study of the R_D-P_{O_2} relationship was more comprehensive. The deposition rate, R_D, was measured as a function of P_{O_2} and the target-substrate distance. According to their results, the height of the hump decreased with decreasing target-substrate distance. Therefore, it may be concluded that the appearance of a plateau or hump depends on the experimental set-up. This phenomenon has yet to be fully explained.

The initial rise of R_D, with increasing F_{O_2} or P_{O_2}, may be explained by the oxidation of titanium at or in the vicinity of the substrate surface. Note that the ratio of the specific volumes of bulk TiO_2 to Ti metal is 1.77. Moreover, since thin-film samples, especially when they are non-crystalline, have a lot of defects such as vacancies and voids, their specific volumes are usually larger than those of crystalline bulk samples. It should be remarked that a pure Ti thin film fabricated at T_s=80°C (and P_{O_2}=0 Torr) was highly crystallized and showed a c-axis textured structure.

The decrease in R_D with any further increase in F_{O_2} or

P_{O_2} after showing a maximum can be explained in two ways. The first is the occurance of back diffusion (23). Because P_{Ar} is constant, the F_{O_2} or P_{O_2} effect should be focused upon. Since the O_2 gas is concentrated within the vicinity of the substrate (therefore F_{O_2} is more significant than P_{O_2} in this set-up), the Ti atoms sputtered from the Ti target undergo many collisions with O_2 particles. If these collisions are significant, the Ti atoms do not deposit on the substrate but rather are deflected back to the target. The second possibility is target poisoning due to O_2 gas introduced for reactive sputtering. Once the target gets oxidized, target poisoning occurs and R_D reduces to 1/10 of the maximum R_D value (7, 8, 77, 92, 93). The main reasons for this are the lower sputtering yield and the higher secondary electron emission of the compounds, and the resulting energy consumption to accerelate these electrons instead of to sputter out the surface atoms.

3.22 PHASE RELATIONS

3.221 X-RAY DIFFRACTOMETRY

The degree of crytallinity of and the phases present in fourteen titanium oxide thin films which were fabricated under various substrate temperatures (T_S) and oxygen gas flow rates (F_{O_2}) were analyzed by means of x-ray diffractometry. The results were summarized in figure 3.5

as a "metastable phase diagram". The Ar partial pressure (P_{Ar}) was kept constant at 70 m Torr, except for Sample (14) in figure 3.5. The deposition condition and measured thickness of each sample are listed in table 3.1.

The titanium oxide thin films deposited at $T_s \lesssim 180\,^{o}C$ were all amorphous, while crystallized suboxides were obtained for Samples (1), (4), (5) and (6). Sample (2) in figure 3.5 deposited at T_s=320°C and F_{O_2}=0.2 scc/min was determined to be a mixture of anatase and rutile phases. Sample (3) fabricated at T_s=380°C and F_{O_2}=0.3 scc/min and Sample (13) deposited at T_s=650°C and F_{O_2}=0.6 scc/min showed only a pure rutile phase. While a pure rutile phase was anticipated for Sample (14) (since it was located in the vicinity of Sample (13)), the actual result for Sample (14) was a mixture of rutile and anatase phases. This was caused by the increase of P_{Ar} from 70 m Torr to 130 m Torr when Sample (14) was fabricated. Thus, it should be noted that the "metastable phase diagram" given in figure 3.5 is strictly valid only for films deposited at P_{Ar}=70 m Torr.

From figure 3.5, it can be said that the degree of crystallinity increased with increasing T_s at a constant F_{O_2}, or increasing F_{O_2} at a constant T_s (if $T_s \gtrsim 180\,^{o}C$). Also, as both F_{O_2} and T_s increased, the oxygen content of all non-amorphous films increased. No information of the oxygen content was obtained for the amorphous films (deposited at $T_s \lesssim 180^{o}C$).

The crystallization temperatures were measured for two amorphous samples deposited under the conditions of F_{O_2}=0.1 and 0.3 scc/min holding P_{Ar} constant at 70 m Torr, i.e. Samples (10) and (12). The samples were heated in air in the temperature range of 200°C to 560°C. The increment of annealing temperature was approximately 40°C. The period for each annealing procedure was four hours. After each annealing, samples were analysed by x-ray diffractometry. The first sharp diffraction peak was observed in both samples after annealing at 320°C. This peak was the 101 diffraction peak of anatase phase. According to Hse et al (94), the ion-sputtered film crystallized into a mixed anatase-rutile structure on slow annealing and into pure anatase with fast annealing. On the other hand, electron-beam evaporated films crystallized, at around 300 °C, always into anatase. The crystallization temperature of 320°C found in this study is close to this temperature of 300°C.

In order to determine the compositions of the amorphous thin films by x-ray diffraction techniques, three amorphous TiO_x films, for which the values of x were expected to be less than 2, were annealed in a high vacuum in which $P_{O_2} \cong 1 \times 10^{-8}$ m Torr. The P_{O_2} was measured by a residual gas analyzer (Dataquad SMS). These three films were those numbered (9), (10) and (11) in figure 3.5. To prevent further oxidation but to enhance the crystallinity,

a short annealing time and a high annealing temperature were used: the three amorphous TiO_x thin films were annealed at 570°C for 1 hour in a high vacuum (of 1×10^{-6} Torr). X-ray diffractometry revealed that all the three amorphous films turned into TiO_2 crystalline films.

This may be explained thermodynamically by using the Ellingham diagram (95) as shown in figure 3.6. From this figure, the reactions at 570°C occur as follows:

$$Ti + O_2 \rightarrow TiO_2 \quad \Delta G_1^{o}{}' = -190 \text{ kcal/mol Ti} \quad (3.1)$$

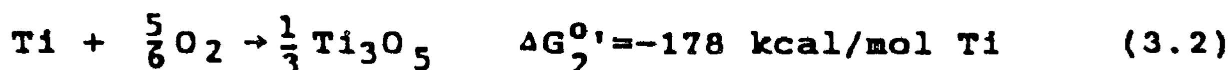

$$Ti + \frac{5}{6}O_2 \rightarrow \frac{1}{3}Ti_3O_5 \quad \Delta G_2^{o}{}' = -178 \text{ kcal/mol Ti} \quad (3.2)$$

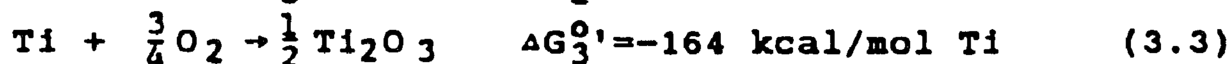

$$Ti + \frac{3}{4}O_2 \rightarrow \frac{1}{2}Ti_2O_3 \quad \Delta G_3^{o}{}' = -164 \text{ kcal/mol Ti} \quad (3.3)$$

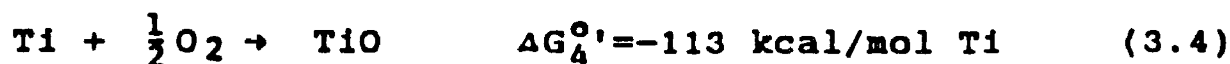

$$Ti + \frac{1}{2}O_2 \rightarrow TiO \quad \Delta G_4^{o}{}' = -113 \text{ kcal/mol Ti} \quad (3.4)$$

where ($\Delta G^{o}{}'$)'s are free energies of formation in the standard states. Therefore, from eqs. (3.1) and (3.2):

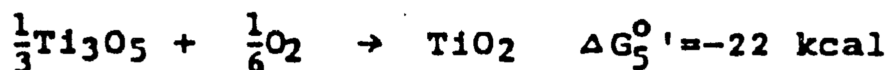

$$\frac{1}{3}Ti_3O_5 + \frac{1}{6}O_2 \rightarrow TiO_2 \quad \Delta G_5^{o}{}' = -22 \text{ kcal}$$

or

$$2Ti_3O_5 + O_2 \rightarrow 6TiO \quad \Delta G_5^{o} = -132 \text{ kcal/mol } O_2 \quad (3.5)$$

From eqs. (3.1) and (3.3):

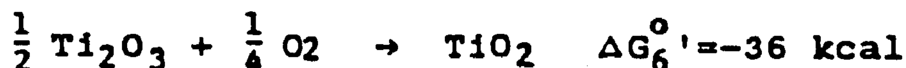

$$\frac{1}{2}Ti_2O_3 + \frac{1}{4}O_2 \rightarrow TiO_2 \quad \Delta G_6^{o}{}' = -36 \text{ kcal}$$

or

$$2Ti_2O_3 + O_2 \rightarrow 4TiO_2 \quad \Delta G_6^{o} = -144 \text{ kcal/mol } O_2 \quad (3.6)$$

Equations (3.1) and (3.4) give:

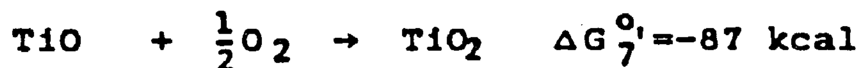

$$TiO + \frac{1}{2}O_2 \rightarrow TiO_2 \quad \Delta G_7^{o\prime} = -87 \text{ kcal}$$

or

$$2TiO + O_2 \rightarrow 2TiO_2 \quad \Delta G_7^{o} = -174 \text{ kcal/mol } O_2 \quad (3.7)$$

In order to judge the directions of the above reactions, a straight line was drawn from the origin to a point of 1.3×10^{-6} Pa ($=10^{-8}$ Torr) on the P_{O_2} scale in figure 3.6 . It is observed in figure 3.6 that the cross point of this line with a vertical line at 570°C (or 843 k) is located (at $\Delta G \cong -40$ kcal/mol O_2) above all the three free energies of formation (per mol O_2) given in Eqs. (3.5), (3.6) and (3.7).This leads to the conclusion that all the reactions given by eqs. (3.5)-(3.7) proceed towards the right to form TiO_2. Therefore, the amorphous TiO_x's were not able to be crystallized without further oxidation when heated even in a high vacuum chamber where the partial pressure of oxygen was very low (i.e. 1×10^{-8} Torr).

3.222 X-RAY PHOTOELECTRON SPECTROSCOPY (XPS).

X-ray photoelectron spectroscopy (XPS) techniques were used to try to determine the compositions of TiO_x thin films and the types of atomic bonds present in them. This process was performed at Surface Science Western and at

E.C.D.

A broad scanning XPS technique was employed to determine the compositions of the TiO_x thin films. Five thin films were analyzed on their natural surfaces (as deposited and exposed to air afterwards), and on fresh surfaces obtained after approximately 50Å of surface material were sputtered off by "in situ" Ar^+ bombardment (for 3 minutes at 4 keV). The films examined had the following deposition characteristics: amorphous TiO_x 's deposited at (a) T_s=80°C; F_{O_2}=0 scc/min, (b) T_s=80°C; F_{O_2} =0.1 scc/min, (c) T_s=100°C; F_{O_2}=0.2 scc/min, (d) T_s=120°C; F_{O_2}=0.3 scc/min, and (e) a fully crystallized rutile thin film. All the films were deposited at P_{Ar}=70 m Torr and films (b), (c) and (d) were expected to have values of x smaller than 2 for the TiO_x formula.

In figure 3.7, the resultant titanium concentration was plotted in terms of F_{O_2}. Open symbols signify the data from the original surfaces while solid symbols represent the data from fresh surfaces created by 4 keV Ar^+ etching. Figure 3.7 shows that the titanium concentrations in films (b), (c), (d), and (e) were almost identical regardless whether the surface was etched by Ar^+ or not. Before etching, all the films, except for film (a), had titanium concentrations of 33±1 at%, which was the same as the TiO_2 composition. This may imply that the surface layers formed on films (b), (c) and (d) may have been thicker than the

removed surface layers (~50Å) and not completely removed by the Ar^+ bombardment. This situation is schematically demonstrated in figure 3.8. Film (a) which was deposited without reactive O_2 gas, had a titanium concentration of ~45 at% instead of 100 at%. Figure 3.7 also shows that the titanium concentrations increased in all the samples after Ar^+ etching.

The fully crystallized specimen (e) was analyzed by using a narrow scanning XPS techcique: the XPS spectrum at fresh surface was obtained with respect to the Ar^+ sputtering time, as shown in figure 3.9. XPS was performed on the original film surfaces as well as on fresh surface after one, two and three minutes of Ar^+ etching. After three minutes of etching, about 50Å of the surface material was removed. (This is a rough estimation based on the Ar^+ etching rate of SiO_2 (96)). The original surface gave characteristic peaks at 458.5 eV and 464.3 eV, labelled by A and B, respectively, in figure 3.9 which corresponded to $Ti\text{-}2p_{3/2}$ and $Ti\text{-}2p_{1/2}$ electrons in TiO_2 (97). After the specimen surface was bombarded by 4 keV Ar^+, two additional weak peaks, (A' and B' in figure 3.9), appeared. The intensity of these peaks, which were located at 457.3 eV and 462.2 eV, increased with sputtering time. Measuring these energies relative to the oxygen 1s level at 530.5 eV, as shown in figure 2.10, $\Delta E_{A'}$=73.2 eV and $\Delta E_{B'}$=68.3 eV were obtained. The value of $\Delta E_{A'}$ is in good agreemeht with that

for Ti-2 $p_{3/2}$ of Ti_2O_3 (i.e. 73.4 ± 0.3 eV) reported by Sayers et al (98). The value of $\Delta E_{B'}$ probably corresponds to the Ti-2 $p_{1/2}$ electron of Ti_2O_3.

The narrow range XPS spectra of amorphous samples (b), (c) and (d) were taken (at E.C.D. company) before and after the "in situ" Ar^+ etching of the surface layer as deep as 100Å (figure 3.10 for Sample (6)). The XPS peaks from the original surfaces were identical with those for TiO_2, as was concluded from the XPS data measured previously at Surface Science Western. The Ti_2O_3 peaks which appeared in the etched samples in figure 3.9 did not clearly appear in figure 3.10. However, it is obvious that the shapes of these XPS spectra were changed by Ar^+ bombadment.

The oxygen concentration of sample (c) was measured in terms of sputtering time as shown in figure 3.11. The original surface had an oxygen concentration of 67.2±1 at%. The 0.5 at% excess oxygen content, compared to the oxygen concentration of stoichiometric TiO_2 (66.7 at% O_2), is due to an experimental error. As the Ar^+ bombardment proceeded, the oxygen concentration decreased at the fresh surface. The new surface composition appeared to approach that of Ti_2O_3. Such reduction in oxygen content had been reported previously using XPS techniques (99, 100) and Auger Electron Spectroscopy (101, 102, 103). Also, a crystallized Ti_2O_3 layer was discovered on the surface of a TiO_2 granule by x-ray diffraction after the surface was etched by 30 keV

Xe ions (104, 105). It should be noted that 4 keV Ar ions were used throughout the present surface cleaning. The mechanism for the reduction in oxygen concentration may be a preferential sputtering effect which removes more oxygen atoms than titanium atoms from the TiO_2 crystal to yield bonds of Ti_2O_3 type. The existence of bonds of Ti_2O_3 type or Ti^{3+} ions has been reported by a number of investigators using various experimental techniques - XPS (98, 106-110); Raman spectroscopy (73, 74, 111, 112); energy loss spectroscopy (113, 114), low energy electron diffraction (LEED) (113, 114); ultraviolet photoelectron spectroscopy (113, 114); and infrared spectroscopy (75). On the other hand, Auger electron spectroscopy (AES) has provided no evidence of the existence of bonds of Ti_2O_3 type (103, 109, 113, 115, 116). This is probably due to the lower sensitivity of AES in the investigation of the bond type, as compared to XPS.

3.223 RUTHERFORD BACKSCATTERING SPECTROSCOPY

The compositions of selected thin film samples were analysed by Rutherford backscattering spectroecopy (RBS).. RBS has the following advandages:

i) The compositions can be determined without any standards.

ii) The compositions can be measured regardless of

crystallinity.

iii) The results obtained from an RBS analysis are more representative of the bulk composition of the thin film: an RBS analysis provides information from a depth up to 10 μm, while such a technique as XPS only provides information from the surface layer of the thickness of few tens of angstroms.

The compositions are determined from the heights or intensities of the energy spectra. The intensity from an atom of element I is given by the following relation (30):

$$h_o^i = \sigma_i(E_o)\Omega\, Q\, \delta/[\epsilon_o]_i \cos\theta_1 \qquad (3.8)$$

where subscript "o" indicates corresponding quantities evaluated for an atom located on the surface.

$\sigma_i(E_o)$: The average differential scattering cross section between the projectile and the sample evaluated at the incident energy E_o.

Ω : The solid angle spanned by the detector aperture.

Q : The total number of incident projectiles bombarding the sample.

δ : The energy width of a channel of the detecting system.

$[\epsilon_o]_i\cos\theta_1$: The stopping cross section factor evaluated at the surface for a given scattering

geometry multiplied by the cosine of the angle of incidence of the beam against the sample normal.

All parameters in eq.(3.8) are apparatus constants except $\sigma_i(E_o)$ and $[\epsilon_o]_i$, both of which depend on elements. Therefore, for the case of TiO_x samples, the relative intensities of the energy spectra for Ti and O can be calculated by applying eq. (3.8):

$$\frac{h_o^{Ti} = \sigma_{Ti}(E_o)\,\Omega\,Q\,\delta \,/\, [\epsilon_o]_{Ti} \cos\theta_1}{h_o^{0} = \sigma_0(E_o)\,\Omega\,Q\,\delta \,/\, [\epsilon_o]_0 \cos\theta_1} \qquad \begin{matrix}(3.9)\\(3.10)\end{matrix}$$

The total intensity of the energy spectrum for an element is known to be linearly proportional to the total number of atoms (30). Thus the ratio of the total intensities H_o^{Ti} and H_o^0 for Ti and O is given by:

$$\frac{H_o^{Ti}}{H_o^0} = \frac{\sigma_{Ti}(E_o)}{\sigma_o(E_o)} \cdot \frac{[\epsilon_o]_{Ti}}{[\epsilon_o]_0} = \frac{1}{x} \qquad (3.11)$$

where x is the subscript for oxygen in TiO_x. The ratio of $[\epsilon_o]$'s is normally within 10% of unity (31), and thus eq. (3.11) may be approximated as:

$$\frac{H_o^{Ti}}{H_o^0} \cong \frac{\sigma_{Ti}(E_o)}{\sigma_0(E_o)} \frac{1}{x} \qquad (3.12)$$

The compositions of three thin film samples were obtained using the relation given by eq. (3.12). These samples were prepared under different conditions: (1): T_s =350°C, F_{O_2} =0.1 scc/min, (3): T_s =380°C, F_{O_2}=0.3 scc/min, (4): T_s =250 °C, F_{O_2} =0.1 scc/min (see figure 3.5). The results of RBS analyses are summarized in figure 3.12 which is a plot of the total intensity versus the energy of backscattered particles. The symbols, (A), (B) and (C) in figure 3.12 correspond to the sample numbers (1), (3) and (4), respectively. The values of H_o^{Ti} and H_o^{O} are taken as indicated in these figure because the peaks from oxygen and titanium are superimposed . The scattering cross section of each element for a H^+ particle has been determined (31): 2.632 for Ti, and 0.3122 cm^2 for O. The total intensities, H_o^{Ti} and H_o^{O} , were obtained by measuring the edge heights of the spectra in figure 3.12. Substituting these values into eq. (3.12), the compositions of the thin film samples were calculated and the results are listed in table 3.2. The analysed compositions of samples (3) and (4) are in good agreement with those determined by x-ray diffraction method. However, the result obtained from Sample (1) is not ; the oxygen concentration of this sample is higher than that estimated by an x-ray diffraction method. This may be due to the presence of more than two phases including Ti_2O_3 which may be the phase of the minimum oxygen concentration as compared to other phases within the

same sample. If phases other than the Ti_2O_3 phase are amorphous or present by an insignificant amount, they would not be detected in an x-ray diffraction experiment.

3.224 RAMAN SPECTROSCOPY

The atomic bonding states of all the samples except Samples (2), (13) and (14), (as numbered in figure 3.5), were studied by Raman spectroscopy. Since Raman spectroscopy is a powerful tool for the analysis of the bonding states including the short-range-order states, many studies have been done on titanium oxides (73, 74, 111, 117-120). These works include studies of the bond structure of Ti_2O_3 which has a metal-semiconductor transition of around 400°C (73, 74) and the thin film structure of titanium oxides (111, 117-120).

Analyses were made for standard bulk materials of TiO_2 (rutile), TiO_2 (anatase) and TiO as well as for the substrate glass material at the Department of Chemistry, University of Windsor. In all instances, a laser beam of 4880 Å wavelength was used as an incident beam. The standard bulk samples of anatase and TiO were purchased from Cerac (Milwaukee, USA) while the rutile sample was prepared by heating the anatase sample at 1000°C for 36 hrs (c.f. rutile-anatase transition temperature = 900°C (77)). All the standard samples were analysed by x-ray diffraction to

reconfirm the structures. In figure 3.13-16, the Raman spectroscopy results are shown plotting the scattering intensity with respect to the wave number (N_W). Every specimen possessed specific peaks. The rutile sample showed major peaks at N_W=231, 444 and 608 cm^{-1}. These peak positions were in good agreement with those reported in Exarhos' work (117) (N_W=231, 444, 608 cm^{-1}). (The peak at N_W = 140 cm^{-1} in figure 3.13 is due to the remained anatase phase.) Major peads at N_W=140, 393, 513, 637 cm^{-1} for anatase sample were also in good agreement with those reported in Exarhos' work (117) (N_W=143, 390, 510 and 633 cm^{-1}). (Note that the peak at 194 cm^{-1} is due to Ar^+ ions in the laser source.) The Ti_2O_3 phase is known to have peaks at N_W=228, 269, 302, 347, 452, 530 and 564 cm^{-1} acccording to Nemanich et al (111), Mooradian et al (73), and Shin et al (74). To the author's knowledge no Raman spectroscopy results of TiO have been reported. In the present study, only a single peak at N =463 cm^{-1} was obtained for the TiO sample(figure 3.15). This peak, however, may be due to the bonds of Ti_2O_3 type in the surface layer of the TiO granule sample. The substrate glass material possessed a single broad peak at N_W = 570 cm^{-1}(figure 3.16).

The results of Raman spectroscopy for the titanium oxide thin film samples are shown in figures 3.17-27. The numbers (1), (3) -(12) in the figures correspond to the sample numbers as assigned in figure 3.5. Specific peaks were observed only in three of the samples, i.e. Samples (1), (3) and (6). An x-ray diffraction analysis revealed

that Sample (1) had the Ti_2O_3 phase while RBS results indicated that it might contain different phases. The Raman peaks from Sample (1) are located at N =354, 462, 546 cm^{-1} . Note that peaks at 354 and 462 cm^{-1} are known to be from the Ti_2O_3 phase (73, 74, 111). The 546 cm^{-1} peak may be due to some other phase. Three peaks were obtained for Sample (3) at N_w=220, 442 and 609 cm^{-1} , all of which were in good agreement with those reported for rutile (117). The present conclusion that Sample (3) is of rutile phase is consistent with other experimental results by x-ray diffraction, XPS and RBS. Sample (6) possesses a peak at N_w=464 cm^{-1} , which is where the TiO standard material has one specific peak. Therefore, the Ti_6O_{11} structure in Sample (6) (as revealed by an x-ray diffraction measurement) may have a bond common to the bonds of Ti_2O_3 type which are known to exist along the CS planes in Magneli phases (43).

The samples other than the above three and the substrate glass sample showed no Raman peaks. The possible reasons why peaks were absent include:

i) that these specimens are not Raman active,

ii) that the atomic positions in the thin films are totally disordered, e.g. the angles between Ti-O-Ti and/or the lengths of Ti-O bondings are random, and

iii) that the TiO_x thin films absorb the incident laser beam.

Even in the amorphous materials, some short-range order must remain. Therefore, situation (ii) may not be the case.

If situation (i) is correct, it is worthwhile to analyse these samples by means of infrared (IR) spectroscopy, because IR and Raman spectroscopies are usually interdependent. Situation (iii) is quite probable since the optical properties of TiO_x's depend on the oxygen content as mentioned in section 2.73.

3.225 COMPARISON OF METASTABLE PHASE DIAGRAMS

In this study, a metastable phase diagram of the titanium-oxygen binary system was obtained as a plot of the substrate temperature (T_s) versus the oxygen gas flow rate (F_{O_2}), as shown in figure 3.5. Similar phase diagrams were reported by W. T. Pawlewicz et al (5, 6) using thin film samples fabricated by an rf reactive diode sputtering technique [figure 3.28(A)] and also by S. Schiller et al (9) for samples prepared by dc reactive plasmatron (planer magnetron) sputtering [figure 3.28(B)]. The main features of the phase diagram shown in figure 3.28(A) are summarized as follows:

i) Crystalline TiO_2 phases are found when the oxygen gas partial pressure (P_{O_2}) is higher than 10 m Torr.

ii) The anatase phase is found in a region of T_s from 200°C to 400°C and of P_{O_2} from 10 to 50 m Torr.

iii) The suboxide regions are not identified. (In the suboxide region, the value of x for TiO_x is less than 2.)

On the other hand, the phase diagram given in figure

3.28(B) shows the following features:

i) Amorphous phases are obtained when T_s is lower than ~$50^\circ C$.

ii) At low oxygen gas partial pressures (P_{O_2}<0.2 m Torr), a suboxide region has appeared.

iii) A high anatase content (80%) is obtained in a region of T_s from 150 to 250°C and of P_{O_2} from 0.2 to 0.25 m Torr.

The major differences between phase diagrams (A) and (B) are:

i) At low T_s's, diagram (A) shows a rutile phase, while diagram (B) represents fine-polycrystalline and amorphous phases.

ii) A suboxide region has appeared only in diagram (B) (for P_{O_2}'s less than 0.15 m Torr).

iii) A 100% rutile region appears in both diagrams (A) and (B) but in different T_s ranges; T_s>500°C in diagram (A) and T_s>300°C in diagram (B).

Another important difference is that the oxygen partial pressure range used for phase diagram (A) (0-150 m Torr) was much wider than that used for diagram (B) (0-0.45 m Torr). However, this difference itself would not have a significant influence on the geometry of the phase diagram unless the ratio of the oxygen gas partial pressure to the argon gas partial pressure (P_{O_2}/P_{Ar}) is significantly different.

The phase diagram determined in the present study is given in figure 3.5. As mentioned earlier, it is somewhat similar to phase diagram (B): a rutile phase has appeared at high T_s's (>350° C) and high P_{O_2}'s (>0.3 scc/min), and a mixture of anatase and rutile phases has been found at medium T_s (350°C) and P_{O_2} (0.2 scc/min). The suboxide and amorphous phase fields have appeared in this phase diagram. However, the positions of these phase fields are different from those in phase diagram (B). In diagram (B), the boundary between the suboxide and TiO_2 phases were nearly vertical, that is, it occured at an almost constant oxygen partial pressure. In the present case this boundary was drawn from a region of low oxygen flow rates and high substrate temperatures towards a region of high oxygen flow rates and low substrate temperatures. Nonetheless, general features of the phase diagram obtained in the present study are in reasonable agreement with those of diagram (B) obtained for samples fabricated by means of a reactive dc plasmatron sputtering technique.

Phase diagram (A) looks quite different from both of these diagrams. This difference may be attributed to the difference in the thin film preparation techniques. For the case of the present triode-sputtering source, the Ar plasma is initiated and maintained even at lower Ar gas partial pressures than those required for the case of a diode-sputtering source. This is due to bombardment of the

Ar gas by the electrons emitted from an independent filament and accelerated by the additional anode(see figure 3.1). Moreover, the plasma is confined and concentrated in the vicinity of the target due to geometrical design and magnet walls of the present triode sputtering source. The Ar plasma is also concentrated in a plasmatron (or planar magnetron) because a magnetic field confines the electron movement just above the target (see section 2.42). Thus in these two sputtering methods, the total Ar gas pressure can be kept at a lower level for initiating and maintaining the plasma than in a diode sputtering method. It is plausible that both the phase diagrams obtained in the present study and diagram (B) are those for low Ar partial pressures, while phase diagram (A) is one for a high Ar partial pressure .

3.23 RESISTIVITY

The surface resistivities were measured to study the relationship between the electrical conduction mechanisms and phases. The surface resistances of all the samples shown in figure 3.5, except for two specimens (13) and (14), were measured in the temperature range from $-191^{\circ}C$ to $60^{\circ}C$. The minimum temperature $-191^{\circ}C$ was obtained by liquid nitrogen. As mentioned in section 3.15, the highest temperature of $60^{\circ}C$ was determined to assure the stability

of the resistance during the measurement (see appendix C). The resistance was measured on the way both heating up and cooling down. The data obtained either ways agreed reasonably well. Resistances were converted to resistivities with the assumption that the electrical current passed uniformly through the entire films without any leakage (No electrical conduction was assumed through the substrate material, i.e. a soda-lime glass). Note that the resistivity of a typical soda-lime glass is $\sim 1 \times 10^{11}$ Ωm (91), while the resistivities of the thin film samples of TiO_2 were anticipated in the range between 3×10^{-4} Ωm and 1×10^{6} Ωm. As discussed in section 2.2, the following electrical conduction mechanisms are considered to be most probable in the presenmt TiO_x film samples because they showed semiconductive behaviors:

1)the Boltzmann mechanism (18):

$$\rho = \rho_{01} \exp (T_a / T) \tag{3.13}$$

2)the Polaron mechanism (21)

$$\rho = \rho_{02} \exp (T_p / T)^{2/5} \tag{3.14}$$

3)the Mott mechanism (18)

$$\rho = \rho_{03} \exp (T_o / T)^{1/4} \tag{3.15}$$

In these equations ρ_o's and Ta's are constants. As mentioned in section 2.2, even if the Boltzmann mechanism

is dominant, the three kinds of activation energies are possible to fit in eq. (3.1) depending on the temperature range. In the temperature range, i.e. from −191°C to 60°C, employed in the present experiment, only one activation energy may be assumed for the Boltzmann mechanism. This assumption was also employed by Meaudre et al (122) and Mott (123, 124).

The constants for eqs (3.1)−(3.3), e.g. ρ_{o1}, Ta, etc, were determined with the experimental data of ρ versus T by means of the least square method. The mechanism which yielded the minimum "standard deviation" was chosen as the most probable one for each sample. The definition of the "standard deviation" and error analysis are given in appendix E. The resultant curves of ρ versus T for the three mechanisms are given in figures 3.29, 31 and 30 for Samples (3), (6) and (9), respectively. The regions for the three conduction mechanisms are identified in the T_S versus P_{O_2} plane as shown in figure 3.32. Only Sample (3) was found to obey a Boltzmann mechanism. Since it was fully crystallized, it is reasonable for Sample (3) to have a conduction mechanism of the Boltzmann type. Samples (2) and (6) were found to fit the polaron mechanism. All the other samples were determined to have conduction mechanisms of the Mott type. The band structure of a rutile (TiO_2) single crystal is well established (66). The band gap energy between valence and conduction bands is ~3.0 eV (66, 125). On the other hand, Sample(3) in this study indicated an activation

energy of only 0.11 eV. This result, however, agrees well with Tanaka et al's work (7). In their investigation, TiO_2 thin film samples were fabricated by a reactive rf sputtering technique and an activation energy of 0.1 eV was obtained from resistivity measurements. The activation energy calculated from the optical absorption coefficient data was 3.15 eV which was in good agreement with the known value for the band gap i.e. ~3.0 eV. The resistivity is controlled by the impurity levels located in the band gap caused by various types of crystallographic defects. An activation energy of 0.11 eV may be due to interstitial Ti ions (76). The values of T_o determined for all the samples using eq. (3.3) are plotted as a function of T_s and F_{O_2} in figure 3.33.Parameter, T_o is defined as follows (18):

$$T_o = C \, [\, \alpha^3 / N(E_F)\, k \,]^{1/4} \tag{3.4}$$

where $N(E_F)$ is the one-electron density of states at the Fermi level, E_F, α is the inverse of the localization length of the one electron wavefunctions, k is the Boltzmann constant, and C is a constant approximately equal to 2. Thus, the increasing of T_o means either the shortening of localized length or increasing the $N(E_F)$ or both dominant. In figure 3.33, the open circles represent the data for Samples (2) and (6) for which the polaron mechanism seems to be governing and therefore the two data points deviate from the general tendency for other data points. In

general, the values of T_o are larger for the thin films deposited at lower values of T_s and/or F_{O_2}. For the case of amorphous Si, both the resistivity and T_o increase with increasing the amount of doped Au (124). Yamaguchi (126) however, concluded that this was mainly attributed to decreasing of $N(E_F)$ because the energy levels near the Fermi level due to dangling bonds are reduced by doped Au atoms. The results given in the present study may indicate that the thin films deposited at lower T_s and/or F_{O_2} have smaller $N(E_F)$ and/or localized length, or both.

The results of the resistivity measurements are summarized in figure 3.34 as a plot of $\log\rho$ versus $(1/T)^{1/4}$. Numbers (1)-(12) in the figure correspond to the specimen numbers assigned in figure 3.5. For Samples (4)-(12), T_s is a more significant variable than F_{O_2}, i.e. the resistivity data for those deposited at the same T_s but at different F_{O_2}'s behave similarly. On the other hand, the resistivities of thin films (1)-(3) deposited at a high T_s ($\sim$350°C) were found to range widely in figure 3.34. This may be ascribed to the fact that Samples (1)-(3) have different degrees of crystallinity and different conduction mechanisms, i.e. the Mott, the polaron and the Boltzmann mechanism, respectively. All the samples (1)-(12) show semiconductive behaviour, i.e. the resistivity decreases with increasing temperature. As mentioned in section 2.74, single crystals of TiO possess the metallic temperature

dependence of resistivity. However, Sample (4) exhibits semiconductive behaviour. This discrepancy may be attributed to the fact that the thin film was weakly crystallized or partially amorphous. Therefore, its band structure may not be exactly the same as that of single crystal TiO. The thin films deposited at low T_s show higher resistivities (see figure 3.34). This may be explained by the hopping conduction mechanism. Since the electrons need phonon assistance to jump from one site to another in the hopping mechanism, they cannot move right across the specimen. This mechanism may be more significant for the more atomically disordered samples which correspond to those deposited at low temperatures.

Although the values of T_o strongly depended on the deposition conditions, the compositions of Samples (7)-(12) were not able to be identified by x-ray diffractometry, XPS or Raman spectroscopy.

CHAPTER 4

$Ba_2Si_2TiO_8$ THIN FILMS

4.1 EXPERIMENTAL PROCEDURE

4.11 TARGET PREPARATION

Ba-Si-Ti oxide thin films have been fabricated from $Ba_2Si_2TiO_8$ (BST) ceramic targets by means of a triode reactive sputtering technique in the rf mode (15, 16, 127). The following difficulties have been encountered in the fabrication process of near stoichiometric BST thin films:

i) During the process of sputtering at a high power level, ceramic targets were heated and then cracked into small pieces by thermal stresses.

ii) When the power level was lowered, the sputtering rate declined to a low level, which required a long sputtering time for the sample preparation.

iii) The relationships between the compositions of the targets and the deposited thin films were investigated (16) and a particular composition for the target ceramic was predicted so that the composition of the thin films fabricated from the ceramic target might be close to stoichiometry. However, the ceramic of the predicted

composition was not successfully sintered (16).

If metallic (instead of ceramic) targets are utilized these difficulties may be removed because metals are good heat conductors and ductile materials. Therefore, an attempt was made to fabricate metallic targets. Three different types of metallic targets were prepared: (I) a composite of $BaSiO_3$ (ceramic) and Ti (metal) designed as shown in figures 4.1 (A) and (B), (II) a pressed powder disc consisting of a mixture of BaO (ceramic) and $TiSi_2$ (metallic) powders, and (III) a pressed disc of a Ba-Si-Ti alloy powder. In the fabrication of a target of type (I), $BaSiO_3$ was fabricated by mixing $BaCO_3$ and SiO_2 powders to stoichiometry and calcining the mixture at 1200°C. (The calcining temperature of 1200 °C was determined by monitoring the phases in the mixture by x-ray diffraction). Then, the $BaSiO_3$ powders was pressed and sintered in air into a disc of the diameter of 20 mm and a thickness of 1.2 mm at 1350°C for two hours. At the center of a titanium metal disc of the diameter of 25.4 mm and the thickness of 2 mm, a hole of the size of the sintered $BaSiO_3$ disc was made as shown in figure 4.1 (A). The $BaSiO_3$ ceramic disc was pushed into the hole on the titanium disc as shown in figure 4.1 (B). In order to prepare a target of type (II), $TiSi_2$ and $BaCO_3$ powders were first mixed to the ratios of Ba:Si:Ti equal to 2:2:1. The powder mixture was the calcined in air at 900°C for four hours. The powder was pressed into discs of 25.4 mm

diameter which were then sintered in an Ar atmosphere at 930 °C for four hours. A Ba-Si-Ti alloy target (of type (III)) was prepared as follows:

1) Barium metal granules and $TiSi_2$ powder were weighed to shoichiometic compositions, i.e. Ba:Si:Ti=2:2:1.

2) They were melted together in an alumina crucible by means of a vacuum induction furnace (available in the Department of Engineering Materials).

3) The alloy ingot was ground into powder which was then pressed into a disc of 25.4 mm diameter.

4) The disc was sintered in an Ar atmosphere at 950°C, (The diameter of the sintered disc was reduced to 24.0 mm).

The target discs of all the three types were mounted on copper target holders as mentioned in section 3.11.

4.12 THIN FILM PREPARATION

An attempt was made to reactively deposit BST thin films on (100) silicon substates by means of an rf triode sputtering source. It should be stressed again that (001) oriented BST thin films are required to obtain piezoelectricity. The same sputter-deposition arrangement as mentioned in section 3.12 was employed. (100) silicon single crystal wafers were used as substrates because of the following reasons:

1) (100) Si has a good lattice matching with (001) BST if

direction [010] or [001] on (100) Si is parallel to [100] or [010] on (001) BST. That is, since the lattice parameters of Si and BST in the (001) plane are respectively 5.45 Å and 8.52 Å, three units of the Si lattice parameter make up 96% of the BST lattice parameter.

ii) If surface acoustic wave (SAW) devices can be fabricated using BST thin films deposited on Si substrates, there is a possibility for use in integrated circuits (IC's), since the base material of commercial IC's is Si.

iii) Since it has been expected that a high substrate temperature ($\sim 700\,^{\circ}C$) is required to obtain a c-axis oriented BST thin film (15, 16, 127) the substrate material should have a high melting point.

Prior to being set in the sputtering chamber, the Si wafer was placed in a 5% HF solution for 10 minutes in order to remove the oxide layer on the surface. The wafers were then washed with distilled water and ethanol, and dried.

A substrate heater which can reach temperatures as high as 800 °C was designed for reason (iii) stated above. This heater was modified from one originally designed for the substrate heater in a molecular beam epitaxy (MBE) unit (136). Tantalum wire was used for the heating element, and a frame cover was made of 0.5 mm thick stainless steel sheet. Figure 4.2 shows the relationship between the applied power and achieved temperature.

4.13 THICKNESS MEASUREMENTS

The thin film thickness was measured by means of an interferometer. The same process as described in section 3.13 was used. The deposition rate, R_D, was in the range of 200 to 1000 Å/hr, depending on the power level (of 10 W/cm^2 to 20 W/cm^2) applied to the target and the partial pressure of Ar gas (of 85 m Torr to 150 m Torr).

4.14 PHASE AND COMPOSITION ANALYSES

The composition of target material was analysed by an energy-dispersive x-ray analyzer (KEVEX) attached to a scanning electron microscope (SEMCO Nanolab 7) available at the Department of Engineering Materials, University of Windsor.

For the composition analysis of BST thin films, KEVEX was not used because both the thin film material and the substrate material contained a common element, Si, and the depth of x-ray signals for analysis was estimated to be larger than the thin film thickness. Instead, an XPS technique was employed since only a few surface layers were responsible in this analytical technique (135) (XPS techniques were previously discussed in section 3.222).

4.2 RESULTS AND DISCUSSION

4.21 METALLIC TARGET PREPARARTION

Three types of "metallic" targets (termed Targets I, II and III) were fabricated for reactive sputtering of barium-silicon-titanium oxide thin films.

Target I

A composite target was prepared by embedding a $BaSiO_3$ ceramic disc at the centre of Ti metal disc. The $BaSiO_3$ ceramic was sintered from a mixture of $BaCO_3$ and SiO_2 powders.

The stoichiometrically weighed powders were mixed thoroughly by mortar and pestle and heat treated for 4 hrs at three different temperatures, 1000, 1100 and 1200°C. The mixture was analyzed by x-ray diffractometry after each heat treatment. The following phases were identified: $BaCO_3$ and $BaSiO_3$ after heating at both 1000°C and 1100°C, and BaO and $BaSiO_3$ after heating at 1200°C. Thus, at 1200°C, calcination was completed. It appeared less Si was found in the calcined powder than stoichiometic $BaSiO_3$ according to the x-ray diffraction results. This implies that a certain amount of Si, possibly in an amorphous SiO_2 form, was undetected by x-ray

diffraction. The powder was then pressed into 20 mm diameter discs with a 1000 MPa pressure and sintered at 1350 °C for 2 hrs. An x-ray diffraction analysis revealed that the target was made up of the $BaSiO_3$ phase only.

Target II

BaO and $TiSi_2$ powders were mixed and pressed into a disc shape. This disc was sintered at 930°C for 4 hrs in an Ar atmosphere. It was expected that grains of BaO powder [the melting point of which is 1923°C (128)] were cemented by sintered $TiSi_2$ [the melting point of which is 1540°C (45)]. However, the discs were still friable powder after this sintering and they swelled up during the x-ray diffraction measurement. This may be caused by the following reaction of BaO with moisture:

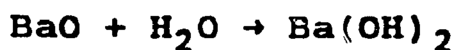

$$BaO + H_2O \rightarrow Ba(OH)_2$$

Thus, Target II was too unstable to be used for sputtering.

Target III

An alloy containing Ba, Si and Ti with an atomic ratio of 2:2:1 respectively was successfully prepared by melting in a vacuum induction furnace (available at the Department of Engineering Materials, University of Windsor). $TiSi_2$ powder was placed at the bottom of an Al_2O_3 crucible (of 4 cm diameter and 9 cm hight). Granules of barium metal,

stored in mineral oil, were placed on the powder to help the oil evaporate more easily. The melting conditions in terms of time and temperature are given in figure 4.3. Note that the total length of the period when the temperature was kept higher than 1000°C was 10 mins in order to homogenize the melt.

The ingot obtained was analyzed by x-ray diffractometry and was found to contain phases of BaSi and Ti_5Si_3 along with small amounts of some unidentifiable phases. The ingot was quite brittle and easily broken with a hammer. The pieces of the ingot were ground into a powder with a mortar and pestle. The ground powder was pressed into a disc with an axial stress of 1000 MPa.

The phase diagrams of binary systems, Ti-Si and Si-Ba, are shown in figures 4.4 and 4.5 respectively. The phase diagram of the Ba-Ti system has not been reported, as of yet. Since this bulk material, i.e. the ingot, mainly contained two intermetallic compounds, BaSi and Ti_5Si_3, the sintering temperature of 950 °C was chosen taking into account the melting temperatures of the two phases. After sintering, the discs had a good solid disc shape. X-ray diffraction revealed that the major phases in the sintered targets were $BaSi_2$ and Ti_5Si_3. However, both $BaSi_2$ and BaSi are very reactive with water:

$$BaSi_2 + 2H_2O \rightarrow Ba(OH)_2 + 2Si + H_2\uparrow$$

$$BaSi + 2H_2O \rightarrow Ba(OH)_2 + Si + H_2\uparrow$$

The resultant phases were confirmed by x-ray diffractometry. Thus, both the ingot and the sintered discs must be stored in dry air or vacuum.

4.22 DEPOSITION RATE

The thicknesses of BST thin films deposited from a target of type III (as defined in section 4.11) were measured as a function of the power density applied to the target (W), and the Ar gas partial pressure (P_{Ar}). The oxygen gas flow rate (F_{O_2}) and the substrate temperature (T_s) were kept constant at 0.2 scc/min and 70 °C respectively, during the thin film deposition. The results are illustrated in figure 4.6 where letters (a), (b) and (c) correspond to the sample names: Sample (a) was deposited at W=10 W/cm^2 and P_{Ar}=150 m Torr; Sample (b) at W=10 W/cm^2 and P_{Ar}=115 m Torr, and Sample (c) at W=20 W/cm^2 and P_{Ar}=85 m Torr. The deposition rate (R_D) increased either with decreasing P_{Ar} or with increasing W, as expected from a pure titanium metal target. (Detailed discussion of pure Ti thin film fabrication is given in appendix B.) T is behaviour of R_D may be explained in a parallel manner as in Appendix B, taking into account the kinetic energies of the sputtering gas molecules and the "back-diffusion" effect (23).

4.23 COMPOSITION AND PHASES

The phases, surface topography and composition of the thin films deposited from Target I (as described in section 4.11) were analyzed using x-ray diffractometry, SEM and EDXA (Kevex).

As previously described, Target I was a ceramic-metal composite target. Thin films were sputter deposited from this target for 8 hours under the following conditions: W=9 w/cm^2, F_{Ar}=44 scc/min and T_s=220 °C. Oxygen gas was not introduced into the chamber. The applied power density was the maximum allowed to maintain a steady plasma. The post-sputter target is shown in figure 4.7. Many thermal cracks can be seen in the ceramic portion.

The thin films were analyzed by x-ray diffractometry and were found to be amorphous. An SEM photograph of the film surface topography is shown in figure 4.8. Small grains ($\sim 10 \mu m \phi$) are scattered on a smooth background. The composition of these grains and the smooth surface were analyzed by EDXA. The results for grains and the smooth surface are shown in figure 4.9(A) and (B), respectively. The positioning of the peaks in figure 4.9(A) is very similar to that of BST (15) shown in figure 4.10. The

Si substrate as well, the composition of the smooth surface was not able to be determined.

The phases, surface topography, and compositions of three thin film samples, (a), (b) and (c), deposited under different conditions, using Target III (which was described in section 4.11) were analyzed by means of x-ray diffractometry, SEM and XPS. The sputter-deposition conditions of Samples (a), (b), and (c) were given previously in section 4.22. X-ray diffractometry showed thses thin films to be amorphous. (Note that the substrate temperature was kept constant at 70°C during the preparationof all the three samples.) Two additional thin films were prepared for the structural analyses under the same deposition conditions as those for Sample (b) other than the substrate temperatures. Both samples deposited at T_s = 450°C and 500°C were also found to be amorphous. Thus no crystallized as-deposited thin films were obtained with the substrate temperature less than 500°C. SEM micrographs of the thin film surfaces can be seen in figures 4.11 (a), (b) and (c). The surface of Sample (b) had portions which flaked off, while the surfaces of the other two films were very smooth. This flake-off was due to the improperly cleaned substrate surface (for Film (b)). In figure 4.12, the compositions of Samples (a), (b) and (c) determined by means of XPS were plotted as a function of the applied power density, W, and

the Ar partial pressure, P_{Ar}. The XPS data was corrected using the factors determined by White et al (127) for the individual elements in the Ba-Si-Ti oxide thin films. Correct ratios of Ba:Si:Ti were obtained in such a way that the correction factors (1.15 for Ba, 0.562 for Si, 1.18 for Ti) were multiplied by the atomic ratio obtained from the XPS analyses. The relative concentration of Ti increased while the relative concentration of Si decreased, with decreasing P_{Ar} or increasing W. These figures clearly show that the chemical composition of the thin film can be altered by varying P_{Ar} and/or W. This may be ascribed to the characteristic dependences of the sputtering yields for individual elements on the incident particle energy and/or the "back-diffusion" effect (23). When P_{Ar} is reduced, the plasma density decreases and the accelerating energy of Ar^+ ions increases because of the constant power (not voltage) supplied to the target. Since the sputtering yield of each element depends not only on the energy of the incident particle (130) but also on the size, mass and bonding energy of an atom of the element, the composition of the thin film can be altered by changing the applied power level. For the case of "back-diffusion", the atoms knocked out of the target undergo collisions with the particles in the plasma and then are scattered with a wide range of the scattering angle, and some of them may go back to the target (23). The efficiency of back-diffusion is also

dependent upon the particle size, mass, and kinetic energy of the ejected atoms as well as the plasma density. This means that, even within the "back-diffusion" mechanism, the composition shift in the deposited film (when P_{Ar} and/or W are changed) can be explained.

Using the data of the sample (c) shown in figure 4.12, it is projected that the stoichiometric $Ba_2Si_2TiO_8$ may be sputter deposited from the Ba-Si-Ti metallic target whose compositions of Ba:Si:Ti are equal to 2:1.9:0.7. Other sputtering conditions should be W=20 W/cm^2, P_{Ar}=85 m Torr, F_{O_2}=0.2 scc/min and T_s=70°C. These conditions, however, are not those for obtaining c-axis oriented $Ba_2Si_2TiO_8$ thin films. Much higher substrate temperatures (>700° C) are required for obtaining such oriented thin films as discussed elsewhere (15, 16, 127).

CHAPTER 5

SUMMARY

5.1 TITANIUM OXIDE THIN FILMS

TiO_x thin films were reactively sputter-deposited from titanium metal targets onto glass substrates, using substrate temperatures of 80 °C to 650 °C and oxygen flow rates of 0.1 scc/min to 0.8 scc/min. The sputtering was accomplished with a triode source operated in the rf mode. The fabricated thin films were characterized by x-ray diffractometry, x-ray photoelectron spectroscopy, Rutherford backscattering spectoscopy, Raman spectroscopy and resistivity measurements.

From x-ray diffraction of the films, the following crystalline phases were identified: TiO, Ti_2O_3, Ti_4O_7, Ti_6O_{11}, anatase (TiO_2), and rutile (TiO_2). Some films were believed to consist of a single phase and others to contain two or more phases. The phase relationships in the individual samples were summarized in the "metastable phase diagram" constructed by plotting the substrate temperature versus the oxygen flow rate. This diagram clearly showed that: (a) for a fixed oxygen flow rate, both the degree of crystallinity and the degree of oxidation increased as the

substrate temperature increased and (b) for fixed substrate temperatures above 200 °C, the crystallinity and oxidation increased as the oxygen flow rate increased. For substrate temperatures below 200 °C, the deposited films were found to be amorphous. It should be noted that the crystallization temperatures of amorphous films fabricated under different conditions of substrate temperature and oxygen flow rate were all about 320 °C.

X-ray photoelectron spectroscopy of the as-deposited films appeared to indicate that the films were all of the rutile composition, regardless of the deposition conditions. Such a situation would suggest the presence of a fully oxidized surface layer of about 5 nm thickness in which the Ti:O ratio equaled 1:2. For a rutile sample, in-situ argon ion etching seemed to cause the formation of Ti_2O_3 bonds.

The compositions of selected samples analyzed by Rutherford backscattering spectroscopy were in reasonable agreement with the x-ray diffraction results. Raman spectroscopy also confirmed these data for Ti_2O_3, anatase, and rutile for which Raman spectra had been published.

The resistivities of the films were measured over the temperature range of -191 °C to 60 °C. Even at one given temperature the measured resistivities ranged widely (from

3×10^{-4} to $1\times10^{6}\Omega$ m at room temperature, for example). Using simplified assumptions, electrical conduction mechanisms were determined for individual samples. The fully crystalline rutile sample was found to follow the Boltzmann mechanism, while all the amorphous samples and some of the weakly crystalline samples followed the Mott mechanism. Most of the samples containing suboxide phases seemed to obey the polaron mechanism or a mechanism intermediate between the Boltzmann and the Mott. Thus, a clear correspondence between the mapping of conduction mechanisms and metastable phases was established. It should be noted that the rutile sample gave an activation energy of 0.11 eV for the Boltzmann process which probably corresponded to a impurity level due to interstitial Ti ions.

5.2 Ba-Si-Ti METALLIC TARGETS FOR REACTIVE SPUTTER DEPOSITION OF THIN FILMS

Three types of metallic targets (one of which was a ceramic-metallic composite disc) were prepared for reactive sputter deposition of barium-silicon-titanium oxide thin films. The most useful of the targets was a metallic powder disc (sintered at 950 °C in an argon atmosphere). The two major phases in this disc were $BaSi_2$ and Ti_5Si_3. The powder for this disc was prepared by mixing weighed quantities of barium granules and Si_2Ti powder to give the following

ratios of elements: Ba:Si:Ti = 2:2:1. The resulting mixture was induction melted at 1250°C.

5.3 $Ba_2Si_2TiO_8$ THIN FILMS

Thin films were reactively sputter deposited from the sintered target (described in the previous section) onto (100) Si substrates. The sputtering parameters controlled were - (i) rf power density applied to the target (in the range of 10 W/cm^2 to 20 W/cm^2), (ii) argon gas flow rate (6 scc/min to 23 scc/min), (iii) oxygen flow rate (0.2 scc/min to 0.5 scc/min), and (iv) substrate temperature (70°C to 500°C).

All of the resulting films were amorphous. Relative amounts of titanium and silicon in the films were monitored by x-ray photoelectron spectroscopy. It was found that as the argon gas partial pressure decreased and/or the applied rf power density increased, the relative amount of titanium in the films increased and that of silicon decreased. By extrapolating the data obtained, the conditions under which stoichiometric $Ba_2Si_2TiO_8$ thin films would be deposited from a Ba-Si-Ti metallic target using the present sputtering system may be predicted as follows:

i) metallic target composition, Ba:Si:Ti = 2 : 1.9 : 0.7

ii) rf power density = 20 W/cm^2

iii) argon gas partial pressure = 85 m Torr

iv) oxygen flow rate = 0.2 scc/min

v) substrate temperature = 70 $^{\circ}$C

CHAPTER 6

CONCLUSION

1) A "metastable phase diagram" was obtained to show the phase relationship in titanium oxide thin films in terms of the substrate temperature and the reactive oxygen gas flow rate or the corresponding partial pressure of the oxygen gas. The titanium oxide thin films were reactively sputter deposited on the glass substrate at a fixed partial pressure (i.e. 70m Torr) of the sputtering argon gas.

2) A diagram of the plausible electrical conduction mechanism for titanium oxide thin films was constructed. The electrical conduction mechanism seemed to be dependent on the degree of crystallinity:

   Boltzmann mechanism - fully crystalline rutile film
   Polaron mechanism - partially crystalline films
   Mott mechanism - weakly crystalline and amorphous films

3) A metallic target containing Ba, Si and Ti with the compositional ratios of 2:2:1 was successfully prepared for reactive sputtering-deposition of barium-silicon-

titanium oxide thin films.

4) The relative concentration of silicon in the sputter-deposited barium-silicon-titanium oxide thin films decreased and that of titanium increased, with decreasing the partial pressure of the sputtering gas (Ar) and/or increasing the sputtering power density.

CHAPTER 7

RECOMMENDATION FOR FUTURE RESEARCH

1) The optical constants of the deposited titanium oxide films should be measured in terms of their compositions.

2) High resolution transmission electron microscopy studies should be carried out to directly identify the phases in the titanium oxide thin films.

3) Since phases of some thin films can be changed depending on the thickness, the "metastable phase diagram" constructed in the present study may depend on the thickness. Therefore the diagram should be reconfirmed by using the samples which have different thicknesses.

4) To obtain information about short range order states, infrared absorption analyses should be done on the titanium oxide thin films, which showed no clear Raman spectra in the present study.

5) A metallic target whose constituents are Ba, Si and Ti of the respective atomic ratios equal to 2:1.74:0.67 should be fabricated and sputter-deposited with the power density

applied to the target of 20 W/cm^2, in order to obtain stoichiometric $Ba_2Si_2TiO_8$ thin films.

6) To control the crystallinity of $Ba_2Si_2TiO_8$ thin films, high substrate temperatures ($\sim700\,^{o}C$) must be attained. This condition may be satisfied by using the tantalum wire heater which was newly designed and developed in the present work.

CHAPTER 8

REFERENCES

1. K.L. Chopra, section 1 "Thin Film Phenomena," McGraw-Hill Inc., London, 1979, pp. 1-9.

2. L.I. Maissel and R. Glang, "Handbook of Thin Film Technology," McGraw-Hill Inc., Section 16, 1970.

3. F.S. Hickernell, J. Appl. Phys., 44, 1061 (1973).

4. S.B. Krupanidhi, N. Maffei, M. Sayer and K. El-Assal, J. Appl. Phys. 54, 6601 (1983).

5. W.T. Pawlewicz and R. Bush, Thin Solid Films, 63, 251 (1979).

6. W.T. Pawlewicz, P.M. Martin, D.D. Hays and I.B. Mann. SPIE Optical Thin Films, 325, 105 (1982).

7. M. Tanaka, M. Takeuchi, F. Kaneko, H. Nagasaka and T. Shibata, Transaction of Ibaraki University, Ibaraki Daigaku Kogakubu Kenkyu Shuho(in Japanese) 32, 141 (1984).

8. S. Shiller, G. Beister and W. Sieber, Thin Solid Films, 111, 259 (1984).

9. S. Schiller, G. Beister, W. Sieber, G. Schirmer and E. Hacker, Thin Solid Films, 83, 239 (1981).

10. O. Christensen, O.H. Olsen, N.E. Holm and J. Sorensen, Thin Solid Films, 100, 181 (1983).

11. S. Yoshida, Thin Solid Films, 56, 321 (1979).

12. Denshi Zairyo Kogyo-Kai Hen, "Surface Wave and Application" (Hyomenha Debais to Sono Ohyo)(in Japanese), Nikkan Kogyo Shinbun-sha, (1978), p. 72.

13. H. Yamauchi, J. Appl. Phys., 49, 6162 (1978).

14. H. Yamauchi, K. Yamashita and H. Takeuchi, J. Appl. Phys., 50, 3160 (1979).

15. M. Ayukawa, M.A.Sc. Thesis, The University of Windsor, Windsor, Ontario, 1983.

16. R.J. White, M.A. Sc. Thesis, The University of Windsor, Windsor, Ontario, 1986.

17. S. Musikant, "Optical Materials," Marcel Dekker, (1985),pp. 1-21.

18. N.F. Mott and E.A. Davis, "Electronic Processes in Non-crystalline Materials," Second Ed., Clarendon Press, (1979).

19. M.H. Cohen, H. Fritzsche and S.R. Ovshinsky, Phys. Rev. Lett., 22, 1065 (1969).

20. E.A. Davis and N.F. Mott, Phil. Mag., 22, 903 (1970).

21. G.P. Triberis and L.R. Friedman, Solid State Phys. C, 14, 4631 (1981).

22. T. Ikeda, "Fundamentals of Piezoelectric Materials Science" (Atsuden Jairyo Gaku no Kiso), Ohmu-sha, Tokyo, (1984).

23. W.D. Westwood, Prog. Surf. Sci., 7, 71 (1975).

24. L.I. Maissel and R. Glang, Section 4 in "Handbook of Thin Film Technology," McGraw-Hill, London, 1970, pp.4.1-4.44.

25. ibid. Section 11.

26. A. Kimbara, "Sputtering," Tokyo Daigaku Shuppan-kai, Tokyo, (1984), pp.225-230.

27. L.E. Davis, "Modern Surface Analysis," The Metallurgical Society of AIME, Wairendale,Pa.,(1979), pp. 1-5.

28. K. Siegbahn, "Alpha, Beta and Gamma-Ray Spectroscopy," North Holland, Amsterdam, (1965).

29. R. Holm and S. Storp, Appl. Phys., 12, 101 (1977).

30. W.K. Chu, J.W. Mayer and M.A. Nicolet, "Backscattering Spectrometry," Academic Press, (1978).

31. C.V. Raman, Indian J. Phys., 2, 387 (1928).

32. C.V. Raman and K.S. Krishnan, ibid., p399.

33. W.J. Moore, Section 17 in " Physical Chemistry," Prentice-Hall, New Jersey, (1972).

34. T.R. Gilson and P.J. Hendra, "Laser Raman Spectroscopy," Wiley-Interscience, (1970).

35. R.C. DeVries and R. Roy, Am. Ceram. Soc. Bull., 33, 370 (1954).

36. P.G. Wahlbeck and P.W. Gilles, J. Am. Ceram. Soc., 49, 180 (1966).

37. H. Gruber and E. Krautz, Phys. Stat. Sol. (a), 69, 287 (1982).

38. H. Gruber and E. Krautz, Phys. Stat. Sol. (a), 75, 511 (1983).

39. H. Gruber and E. Krautz, Z. Metallkd., 77, 203 (1986).

40. R.W.G. Wyckoff, Section 1 in "Crystal Structures," 2nd Ed. Willey-Interscience, New York, (1963), pp.107-109.

41. P.Y. Simons, F. Dachille and R. Roy, Am. Mineral., 53, 1929 (1968).

42. L. Vegard, Phil. Mag., 32, 65 (1916).

43. L.A. Bursill and B.G. Hyde, "Prog. in Solid State Chemistry" (A Reiss and J.O. McCaldin, Eds.), Vol.7, Pergamon, Oxford (1972),p. 177.

44. S. Anderson, B. Collen, V. Kuylenstierna and A. Magneli, Acta Chemi. Scand., 11, 1641 (1957).

45. S. Anderson, B. Collen, G. Kruse, U. Kuylenstierna, A. Magneli, H. Pestmalis and Asbrink, ibid, p1653.

46. A.A. Rusakov and G.S. Zhdanov, Daklady Akad. Nauk. SSSR, 77, 411 (1951).

47. W.H. Zachariaser Skrifter Norske Videnskaps-Akad. Oslo I. Mat. Naturv. Kl., Nr 4, 165S, S21 (1928).

48. P.Z. Ehrlich, Electrochem., 45, 362 (1939).

49. B. Holmberg, Acta Chem. Scand., 16, 1245 (1962).

50. S. Yamaguchi, M. Koiwa and M. Hirabayashi, J. Phys. Soc. Japan, 21, 2096 (1966).

51. W.D. Kingery, H.K. Bowen and D.R. Uhlmann, "Introduction to Ceramics" Second Ed., John Wiley and Sons, Section 13 (1976).

52. S. Schiller, G. Beister, S. Schneider and W. Sieber Thin Solid Films, 72, 475 (1980).

53. D.C. Cronemeyer, Phys. Rev., 87, 876 (1952).

54. R.G. Breckenridge and W.R.Hosler, Phys. Rev., 91, 793 (1953).

55. F.J. Morin, Phys. Rev. Lett., 3, 34 (1959).

56. L.E. Hollander, Jr and P.L. Castro, Phys. Rev., 119, 1882 (1960).

57. E.H. Greener and D.H. Whitmore, J. Appl. Phys., 32, 1320 (1961).

58. J. Yahia and H.P.R. Frederikse, Phys. Rev., 123, 1257 (1961).

59. J.M. Honig and T.B. Reed, Phys. Rev., 174, 1020 (1968).

60. T.C. Chi and R.J. Sladek, Phys. Rev. B, 7, 5080 (1973)

61. A.D. Inglis, Y. LePage, P. Strobel and C.M. Hurd, J. Phys. C, 16, 317 (1983).

62. C. Schlenker, S. Ahmed, R. Buder and M. Gourmala, J. Phys. C, 12, 3503 (1979).

63. M. Marezio, D. Tranqui, S. Lakkis and C. Schlenker, Phys. Rev. B, 16, 2811 (1977).

64. S. Lakkis, C. Schlenker, B.K. Chakraverty, R. Buder and M. Marezio, Phys. Rev. B, 14, 1429 (1976).

65. R.F. Bartholomew and D.R. Frankel, Phys. Rev., 187, 828 (1969).

66. N.B. Hannay, "Semiconductors," Chapman and Hall, Ltd., (1959),p. 612.

67. V.A. Gubanov, A.L. Ivanovsky and G.P. Shveikin, J. Phys. Chem. Solids., 45, 719 (1984).

68. L.M. Huisman, A.E. Carlsson, C.D. Gelatt, Jr. and H. Ehrenreich, Phys. Rev. B, 22, 991 (1980).

69. J.B. Goodenough, Phys. Rev. B, 5, 2764 (1972).

70. J. M. Schoen and S.P. Denker, Phys. Rev., 184, 864 (1969).

71. L.L. Van Zandt, J.M. Honig and J.B. Goodenough, J. Appl. Phys, 39, 594 (1968).

72. N.B. Hannay, "Semiconductors," Chapman and Hall, Ltd., (1959),p. 614.

73. A. Mooradian and P.M. Raccah, Phys. Rev. B, 12, 4253 (1971).

74. S.H. Shin, R.L. Aggarwal, B. Lax and J.M. Honig, Phys. Rev. B, 9, 583 (1974).

75. G. Lucovsky, R.J. Sladek and J.W. Allen, Phys. Rev.B, 16, 5452 (1977).

76. H. Yanagida and M. Takada, "Electronics Materials of Ceramics" (Denshi Zairyo Seramikusu)(in Japanese), Gihodo, Tokyo, (1983).

77. K.G. Geraghty and L.F. Donaghey, J. Electrochemi Soc., 123, 1201 (1976).

78. J.T. Alfors, M.C. Stinson, R.A. Matthews and A. Pabst, Am. Min., 50, 314 (1965).

79. P.B. Moore, Science 156, 1361 (1967).

80. P.B. Moore and S.J. Louisnathan, Z. Kristallogr. Bd., 130, 438 (1969).

81. R. Masse, J.C.Grenier and A. Duriff, Bull. Soc. fr. Mineral Cristallogr., XC, 20 (1967).

82. C.R. Robbins, J. Res. N.B.S., 74A, 229 (1970).

83. D.E. Rase and R. Roy, J. Am. Cerami. Soc., 38, 389 (1955).

84. M. Kimura, Y. Fujino and T. Kawamura, Appl. Phys. Lett., 29, 227 (1976).

85. S. Haussuhl, J. Eckstein, K. Recker and F. Wallrafen, J. Crys. Gr., 40, 200 (1977).

86. M. Kimura, J. Appl. Phys., 48, 2850 (1977).

87. A. Halliyal, A.S. Bhalla, S.A. Markgraf, L.E. Cross and R.E. Newnham, Ferroelectrics (1985).

88. A. Halliyal, A. S. Bhalla, R.E. Newnham and L.E. Cross J. Mat. Sci., 16, 1023 (1981).

89. S.A. Markgraf, A. Halliyal, A.S. Bhalla and R.E. Newnham, Ferroelectrics (1985).

90. J. Melngailis, J.F. Vetelino, A. Jhunjhunwala, J.B. Reed, R.E. Fahey and E. Stern, Appl. Phys. Lett., 32, 203 (1978).

91. "Butsuri Jo-su-hyo," Asakura Shoten, 136 (1969).

92. L.C. Wu and J.E. Green, J. Appl. Phys., 50, 4966 (1979).

93. A.R. Nyaiesh and L. Holland, J. Vac. Sci. Technol., 20, 1389 (1982).

94. L.S. Hsu and C.Y. She, Optics Letters, 10, 638 (1985).

95. R.A. Swalin, "Thermodynamics of Solids," John Wiley and Sons Inc., p114 (1972).

96. Ms. Johnston, personal communication, Surface Science Western, University of Western Ontario, Canada (1985).

97. C.D. Wagner, "Handbook of X-ray Photoelectron Spectroscopy, Perkin-Elmer Co., 68 (1978).

98. C.N. Sayers and N.R. Armstrong, Surf. Sci., 77, 301 (1978).

99. H. Demiryont and J.R. Sites, J. Vac. Sci. Technol., A2, 1457 (1984).

100. R. Holm and S. Storp, Appl. Phys., 12, 101 (1977).

101. H.J. Mathieu, J.B. Mathieu, D.E. McClure and D. Landolt, J. Vac. Sci. Technol., 14, 1023 (1977).

102. S. Thomas, Surf. Sci., 55, 754 (1976).

103. S. Hofmann and J.M. Sanz, Mikrochim. Acta, 10, 135 (1983).

104. T.E. Parker and R. Kelly, J. Phys. Chem. Solids, 36, 377 (1975).

105. R. Kelly and N.Q. Lam, Radi. Effe., 19, 39 (1973).

106. G. Nogami, J. Electrochem. Soc., 13, 76 (1985).

107. C.H. Hwang, K. Cho and K. Kawamura, "Rapidly Quenched Metals," Elsevier Science Publishers, (1985),p.1469.

108. N. Wagner, O. Brummer and N. Sauer, Crystal Res. and Technol, 17, 1151 (1982).

109. N.R. Armstrong and R.K. Quinn, Surf. Sci., 67, 451 (1977).

110. S. Veaudevan, M.S. Hegde and C.N.R. Rao, Solid State Commun., 27, 131 (1978).

111. R.J. Nemanich, C.C. Tsai and G.A.N. Connell, 44, 273 (1980).

112. V.E. Henrich, G. Dresselhaus and H.J. Zeiger, Phys. Rev. Lett., 36, 1335 (1976).

113. W.J. Lo, Y.W. Chung and G.A. Somorjai Surface Sci., 71, 199 (1978).

114. V.E. Henrich, G. Dresselhaus and H.J. Zeiger, Phys. Rev. Lett., 36, 1335 (1976).

115. G.D. Davis, N. Natan and K.A. Anderson, Appl. Surf. Sci., 15, 321 (1983).

116. C.N.R. Rao and D.D. Sarma, Phys. Rev. B, 25, 2927 (1982).

117. G.J. Exarhos, J. Chem. Phys., 81, 5211 (1984).

118. L.S. Hsu, C.Y. She and G.J. Exarhos, Applied Optics, 23, 3049 (1984).

119. G.J. Exarhos and W.T. Pawlewicz, Applied Optics, 23, 1986 (1984).

120. R.J. Nemanich, R.T. Fulks, B.L. Stafford and H.A. Vander Plas, Appl. Phys. Lett., 46, 670 (1985).

121. T. Abe and T. Yamashina, Thin Solid Films, 30, 19 (1975).

122. M. Meaudre and R. Meaude, J. Non-Crystalline Solids, 68, 281 (1984).

123. N.F. Mott, Phil. Mag., 24, 911 (1971).

124. ibid, 19, 835 (1969).

125. C. Kittel, "Introduction to Solid State Physics," 5th. Ed., John Willey and Sons, Inc., Section 7 (1976)

126. M. Yamaguchi, J. Non-Crystalline Solids, 77, 535 (1985).

127. R.J. White, M. Ayukawa, G. Demaggio, J.W. Robinson and H. Yamauchi, To appear in Proc. World Congress of High Tech Ceramics, (1987).

128. C. Wagner and H. Binder, Z. Anorg. U. Allgem. Chem., 297, 334 (1958).

129. F.A. Shunk, "Constitution of Binary Alloys, Second Supplement," McGraw-Hill, (1958).

130. R.V. Stuart and G.K. Wehner, J. Appl. Phys., 33, 2345 (1962).

131. L.I. Maissel and R. Glang, "Handbook of Thin Film Technology" McGraw-Hill Inc., Section 11, 1970.

132. N. Laegried and G.K. Wehner, J. Appl. Phys., 32, 365 (1961).

133. P. Kawa unpublished work, University of Windsor, Windsor, Ontario, (1987).

134. B.D. Cullity, "Elements of X-ray Diffraction," 2nd Ed., Addison-Wesley Publication Co., Inc., Section 4 (1980).

135. R. Behrisch, "Sputtering by Particle Bombardment II," Springer-Verlag, Berlin, (1983).

136. A.Ishizaka, personal communication, Hitachi Central Research Lab., Tokyo, Japan, (1986).

137. H.A. Szymanski, "Raman Spectroscopy," Plenum Press, Chapter 1 (1967).

138. "Crystal Structures of Minerals," London, G. Bell and Sons Ltd. (1965).

139. Y. Arai, "Material Science of Ceramics" (seramikusu no Zairyo-Kagaku) (in Japanese), Dai-Nippon Tosho, Tokyo, p45 (1980).

140. M. Kimura, Ph.D Dissertation, Waseda University, Tokyo, Japan, (1978).

141. R.V. Stuart and G.K. Wehner, J. Appl. Phys., 33, 2345 (1962).

142. N.F. Mott, Phil. Mag., 26, 505 (1972).

143. A. Kinbara and H. Fujiwara, "Thin Films" (Hakumaku), Syokabo, Section 5 (1980).

144. P. Sigmund, Phys. Rev., 184, 383 (1969).

145. G.K. Wehner, R.V. Stuart and D. Rosenburg, General Mills Annual Report of Sputtering Yields. Number 2254, 1961.

146. M.I. Guseva, Sov. Phys. Sol. St., 1, 1410 (1960).

147. O. Almen and G. Bruce, Nucl. Instrum. Methods, 11, 257 (1961).

148. G. Dupp and A. Scharmann, Z. Physik, 192, 284 (1966).

149. F. Keywell, Phys. Rev., 97, 1611 (1955).

150. B.P. Straughan and S. Walker, "Spectroscopy" vol.2, Chapman and Hall, Section 4 (1976).

APPENDIX A

THICKNESS MEASUREMENTS

The thicknesses of thin film samples were measured by two different techniques: (i) a stylus technique (available at Surface Science Western in the University of Western Ontario, Ontario) and (ii) Tolansky's (interferometer) technique (at the Department of Engineering Materials, University of Windsor).

The stylus method utilizes a fine diamond tip of radius 0.7 to 2 μm. This needle is pressed onto the surface with a pressure of 1 kPa (which corresponds to a tip mass of only 0.1 g) and is moved uniformly across the surface. Any vertical movement of the tip, which is caused by surface irregularities is converted to an electrical signal which is then amplified and recorded. It is claimed (131) that the minimal thickness difference that can be recorded by this method is 2.5 nm with a precision of ±2%.

The Ti metal thin films deposited on glass substrates were measured by both the stylus method on a Dektak surface profilometer and Tolansky's method on an interferometer. A typical recording of the profile from a Ti metal film on a glass substrate is shown in figure A1. The thickness measurements were performed two and four times on each

sample by the stylus method and Tolansky's method, respectively. The average values were then calculated and are summarised in table A1.

APPENDIX B

DEPOSITION RATE OF TITANIUM THIN FILMS

The titanium thin films were deposited from a Ti metal target at varied conditions. The experimental parameters were: Ar gas flow rate (F_{Ar}) which was varied from 20 to 45 scc/min, and the power density (W) applied to the target which was varied from 10 to 60 W/cm^2. Figure B1 shows the deposition rate (R_D) plotted in terms of F_{Ar}. Four lines are drawn for constant values of W of 10, 20, 40 and 60 W/cm^2. Figure B1 shows that for all lines, R_D decreased monotonically with F_{Ar}. This may be attributed to the "back diffusion" (23), in which the atoms sputtered out from the target surface were diffused back to the target after a collision with the sputtering gas or plasma. Laegried et al (132) estimated that 50% of the sputtered material returned to the target at a pressure of 130 m Torr.

Figure B2 shows the relationship between R_D and W at a constant F_{Ar} of 30 scc/min. R_D linearly increased with W. Since the atoms on the target surface are sputtered out by the exchange of the kinetic energy from the incident projectile ions to the surface atoms, the number of sputtered atoms increases with increasing the incident ion energy. However, when the energy of the incident particles

exceeds a certain value, the efficiency of the sputtering process deteriorates because of channeling (95). Therefore, in general, R_D changes as a function of W as shown in figure B3 (49–53).

APPENDIX C

RESISTIVITY MEASUREMENTS OF TiO_x THIN FILMS AT HIGH TEMPERATURES

The resistivities of Samples (4) and (8) (which are identified in figure 3.5) were measured at high temperatures (>50 °C). Aluminum and gold were respectively deposited to form electrode pads on these samples using a thermal evaporation technique. Figure C1 shows the relationship between the resistivity, ρ , and temperature measured for Sample (4) in the temperature range of 25°C to 65°C. The data points are randomly scattered. This may be due to the oxidation of the Al electrodes. On the other hand, the results obtained for Sample (8), as illustrated in figure C2, show that the resistivity (log ρ) starts to deviate from the linear relationship at ~70°C on heating. Figure C3 shows that the resistivity (log ρ) varies almost linearly with time for a constant temperature of around 115 °C. Since the gold is free of oxidation in this temperature range, this increment in the resistivity may have been caused by either the crystallization or the oxidation of the thin films. However, as mentioned in section 3.221, amorphous thin film samples crystallized at ~320 °C. Therefore the possibility of crystallization of the thin

films at 70°C seems to be slim. Thus the deviation of the log ρ-vs-1/T plot from a straight line at 70 °C is likely to have been caused by the oxidation of the thin film.

APPENDIX D

CALCULATION OF $Ba_2Si_2TiO_8$ X-RAY DIFFRACTION PATTERN

As mentioned in section 2.8, the existence of the $BaSiTiO_5$ phase which had been reported in 1955 by Rase et al (83) was denied by Robbins (82). Robbins pointed out that the compound which Rase et al had identified as $BaSiTiO_5$ was a mixture of $Ba_2Si_2TiO_8$ and $BaTi_4O_9$. However, in Robbins' paper (82), no clear evidence neither theoretical nor experimental were presented. According to the author's knowledge, there have been no other reports on the "$BaSiTiO_5$" phase. The powder diffraction data of $BaSiTiO_5$ is filed among the JCPDS cards without a high-quality symbol while the data of $Ba_2Si_2TiO_8$ carries a high-quality symbol.

In this section, the x-ray diffraction pattern of $Ba_2Si_2TiO_8$ is calculated using the crystallographic structure data reported by Masse et al (81) and then compared to the experimental results (133).

The structure factor (F) was calculated using the formula (134):

$$F = \sum_{n=1}^{N} f_n \left[\cos 2\pi (hu_n + kv_n + lw_n) + i \sin 2\pi (hu_n + kv_n + lw_n) \right]$$

Thus:

$$|F|^2 = \left[\sum_{n=1}^{N} f_n \cos 2\pi (hu_n + kv_n + lw_n) \right]^2 + \left[\sum^{N} f_n \sin 2\pi (hu_n + kv_n + lw_n) \right]^2$$

where h, k, l are Miller indices, u_n, v_n, w_n are the coordinates of n-th atom in the unit cell and N is the total number of atoms in the unit cell. The atomic scattering factors, f_n's, were taken from Cullity's table (134). Note that f_n is a function of $\sin\theta/\lambda$, where θ is the Bragg angle and λ is the wavelength of the incident x-ray. Since the values for $f_{Ba^{++}}$ are not listed in the table, f_{Xe} values were used for $\sin\theta/\lambda < 0.1$ $\mathring{A}^{-1}$ and the values for f_{Ba} were employed for $f_{Ba^{++}}$ when $\sin\theta/\lambda$ 0.1 $\mathring{A}^{-1}$.

The relative intensity (I) was calculated using the following equation (134):

$$I = |F|^2 P \left(\frac{1 + \cos^2 2\theta}{\sin^2\theta \cos\theta}\right)$$

where P is a multiplicity factor and the last factor is the Lorentz-polarization factor. Then intensity I was normalized by the maximum peak intensity I_{max}.

In the actual calculation, the data for the coordinates of atoms in the $Ba_2Si_2TiO_8$ unit cell (see figure 2.29 and 2.30) were taken from Masse et al's work (81). Figure D1(c) shows the calculated $Ba_2Si_2TiO_8$ diffraction pattern. Actually this calculated pattern can be reproduced by superimposing the JCPDS patterns for $Ba_2Si_2TiO_8$ and $BaSiTiO_5$ as shown in figures D1(a) and (b), respectively. (In figures (a) and (b), copper K_α line was assumed in the conversion of the "d" values to "2θ"'s.) As

Robbins pointed out, these two patterns are very similar. Only differences between the two patterns are (i) peaks at $2\theta = 14.8^{\circ}$ and 29.7° for $Ba_2Si_2TiO_8$ do not show in the $BaSiTiO_5$ pattern and (ii) peaks at $2\theta = 47.3^{\circ}$, 47.7° and 57.2° for $BaSiTiO_5$ are not included in the $Ba_2Si_2TiO_8$ pattern. The only differences between the two patterns are (i) peaks at should be noted that, in the two JCPDS cards, only peaks whose relative intensities are higher than 10% of the maximum intensity are listed. According to the present calculation, all the five peaks which are not commonly listed in both the $Ba_2Si_2TiO_8$ and $BaSiTiO_5$ JCPDS cards have relative intensities close to 10% or less. This may be the reason why these peaks were not commonly listed in the JCPDS cards for the two phases. If this was the case, it is likely that the two phases may have identical diffraction patterns, indicating that those phases are exactly identical. In order to investigate this point, two different samples which have the Ba:Si:Ti ratios equal to (i) 2:2:1 and (ii) 1:1:1 were prepared (133). Raw powder materials, $BaCO_3$, SiO_2 and TiO_2 were weighed to these ratios. Sample (i) was sintered at 1300 °C and Sample (ii) was sintered at 1250 °C (133). Diffraction patterns for these samples are schematically demonstrated in figures D1(d) and (e). Pattern (i),i.e. figure D1(d), is the same as that of calculated (i.e. figure D1(c)), while Pattern (ii), i.e. figure D1(e), seems to have not only the

$Ba_2Si_2TiO_8$ peaks but also some other peaks which seem to be those from $BaTi_4O_9$.

It is almost certain that $BaSiTiO_5$ phase which was reported by Rase et al (83) does not exist. Sample (ii) which has the composition equivalent to $BaSiTiO_5$ most probably consisted of two phases, i.e. $Ba_2Si_2TiO_8$ and $BaTi_4O_9$. This means that the tie line which passes the $BaSiTiO_5$ composition is the $BaO-SiO_2-TiO_2$ ternary phase diagram is nearly perpendicular to the line which connects $BaTiO_3$ with the SiO_2 corner. In other words, the $BaTiO_3-SiO_2$ system is not a quasi-binary system.

APPENDIX E

ERROR ANALYSIS AND LEAST SQUARE METHOD FOR RESISTIVITY DATA

1) Experimental Error

The relative error in reading the value of resistance using an electrometer was about the same in each range of the meter. That is, the error of this type was more or less constant when the resistance, R, was plotted with a logarithmic scale:

$$\left|\Delta \log R\right| < \mathrm{Max} \left|\frac{\Delta R}{R}\right| \cong 0.05$$

Thus, the error bar is slightly longer than the diameter of the circle for each experimental datum in figures 3.29–3.31. The error in measuring temperature was $\pm 2\ ^{\circ}C$, which was within the datum circle dimension in these figures.

2) Least Square Method

The least square method was applied for the data of ln R as a function of (1) 1/T for the Boltzmann mechanism, (2) $(1/T)^{\frac{2}{5}}$ for the polaron mechanism and (3) $(1/T)^{\frac{1}{4}}$ for the Mott mechanism:

$$\ln R = a^{(i)} (1/T)^{n(i)} + b^{(i)}$$

where superscript (i) represent one of the conduction mechanisms mentioned above, i.e. i=1, 2 or 3 and n(i)= 1, 2/5 and 1/4 for i=1, 2, and 3 respectively. Constants $a^{(i)}$ and $b^{(i)}$ were determined for each set of data.

In order to measure the degree of curve fitness for each conduction mechanism, the square sum of the deviations of datum points from the fitted curve was calculated:

$$S^{(i)} = \sqrt{\frac{\sum_{p=1}^{N} \left\{ [a^{(i)} \ (1/T_p)^{n(i)} + b^{(i)}] - \ln R \ (T_p) \right\}^2}{N - 1}}$$

where N is the total number of data, T_p is the temperature of the p-th data and in $R(T_p)$ is the p-th data of in R at temperature T . For the case of Sample (9) shown in figure 3.31, $S^{(1)}$=0.14 for the Boltzmann mechanism, $S^{(2)}$=0.08 for the polaron mechanism and $S^{(3)}$=0.06 for the Mott mechanism. Therefore, the Mott mechanism is the most plausible for this set of data.

However in comparison of the three theoretical curves with experimental data taking into account the experimental error estimated previously, the difference in the degrees of curve fitness of the Mott and polaron mechanisms was almost within the experimental error. On the other hand the curve fitted for the Boltzmann mechanism was significantly deviated from the experimental data. Thus, it seemed that only when $|\Delta S|>0.05$, two fitted curves were significantly different. Nontheless, mechanism having the least value of

S was chosen among the three possible mechanisms as the plausible electrical conduction mechanism in the construction of the conduction mechanism map given in figure 3.32.

VITA AUCTORIS

The author was born in Sapporo, Hokkaido, Japan on December 10, 1958.

Education: Hich school Diploma, obtained at Minami Senior Secondary School, Sapporo, Hokkaido, Japan, 1977.

B.Eng. in Metallurgical Engineering, obtained at the Hokkaido University, Sapporo, Hokkaido, Japan, 1981.

M.Eng. in Metallurgical Engineering, obtained at the Hokkaido University, Sapporo, Hokkaido, Japan, 1983.

Societies Canadian Ceramic Society

American Society for Metals

American Institute of Mining, Metallurgical and Petroleum Engineers (AIME)

Materials Research Society

Publication derived from this thesis:

Yamashita, T., J.W.Robinson and H.Yamauchi, (1987), "TiO_x Thin Films Fabricated by Means of RF Reactive Sputtering Using a Triode Source," In Proceedings of World Congress on High Tech Ceramics (VI CIMTEC),Edited by P. Vincenzini, Elsevier Science, Amsterdam, in press.

Yamashita,T., J.W.Robinson and H.Yamauchi,(1986), "Metastable Phase Diagram of TiO_x Thin films" TMS Technical Paper: F86-5, The Metallurgical Society of AIME,Wairendale.

Yamashita,T., J.W.Robinson and H.Yamauchi,(1986),"Reactive Sputtering Deposition of Titanium Oxide Films By Means Of An RF Triode Sputtering Source" In Defect Properties and Processing of High-Technology Nonmetallic Materials, MRS Proceedings Vol. 60,Edited by Y. Chen, W.D. Kingery and R.J. Stokes, Materials Research Society, Pittsburgh, pp 373-378.

Table 2.1
Resistivity of single crystal titanium oxides at room temperature.

SINGLE CRYSTAL TITANIUM OXIDES	ELECTRICAL RESISTIVITY (Ωm) AT ROOM TEMPERATURE	REFERENCE
TiO	6×10^{-6}	55
Ti_2O_3	1×10^{-4}	59
Ti_3O_5	1×10^{-2}	65
Ti_4O_7	1×10^{-5}	65
Ti_5O_9	1×10^{-5}	65
Ti_6O_{11}	1×10^{-4}	65
Ti_8O_{15}	1×10^{-4}	65
TiO_2	1×10^{10}	54

Table 3.1
Deposition conditions and thicknesses of TiO_x thin film sample (1)-(12).

SAMPLE #	DEPOSITION CONDITION		THICKNESS (Å)
	F_{O_2} (scc/min)	Ts (°C)	
(1)	0.1 ± 0.02	350 ± 5	5200 ± 500
(2)	0.2	330	3200 ± 300
(3)	0.3	370	1500 ± 200
(4)	0.1	250	5200 ± 500
(5)	0.2	250	3900 ± 400
(6)	0.3	240	4800 ± 500
(7)	0.1	180	1600 ± 200
(8)	0.2	180	4300 ± 400
(9)	0.3	185	4000 ± 400
(10)	0.1	80	4200 ± 400
(11)	0.2	100	4700 ± 500
(12)	0.3	120	1800 ± 200

Table 3.2
Compositional analysis of Rutherford backscattering spectroscopy data (figure 3.12).

SAMPLE #	H_{Ti} (cm)	H_O (cm)	$\frac{\sigma^*_{Ti}}{\sigma_O}$	COMPOSITION
(1)	2.25 ± 0.03	0.45 ± 0.03	8.4305	$Ti_2O_{3.4}$ ($Ti_2O_{3.1}$ — $Ti_2O_{3.6}$)
(3)	2.00 ± 0.03	0.50 ± 0.03	8.4305	$TiO_{2.1}$ ($TiO_{2.0}$ — $TiO_{2.3}$)
(4)	2.00 ± 0.03	0.25 ± 0.03	8.4305	$TiO_{1.0}$ ($TiO_{0.9}$ — $TiO_{1.2}$)

* from ref. (30)

Table A.1
Comparison between the thickness measured by Transky method and those measured by Stylus method.

	THICKNESSES MEASURED BY		DIFFERENCE
	STYLUS METHOD	TRANSKY METHOD	
SAMPLE A1	2800 Å	2800 Å	0%
SAMPLE A2	800 Å	900 Å	+ 13%
SAMPLE A3	16000 Å	18000 Å	+ 13%

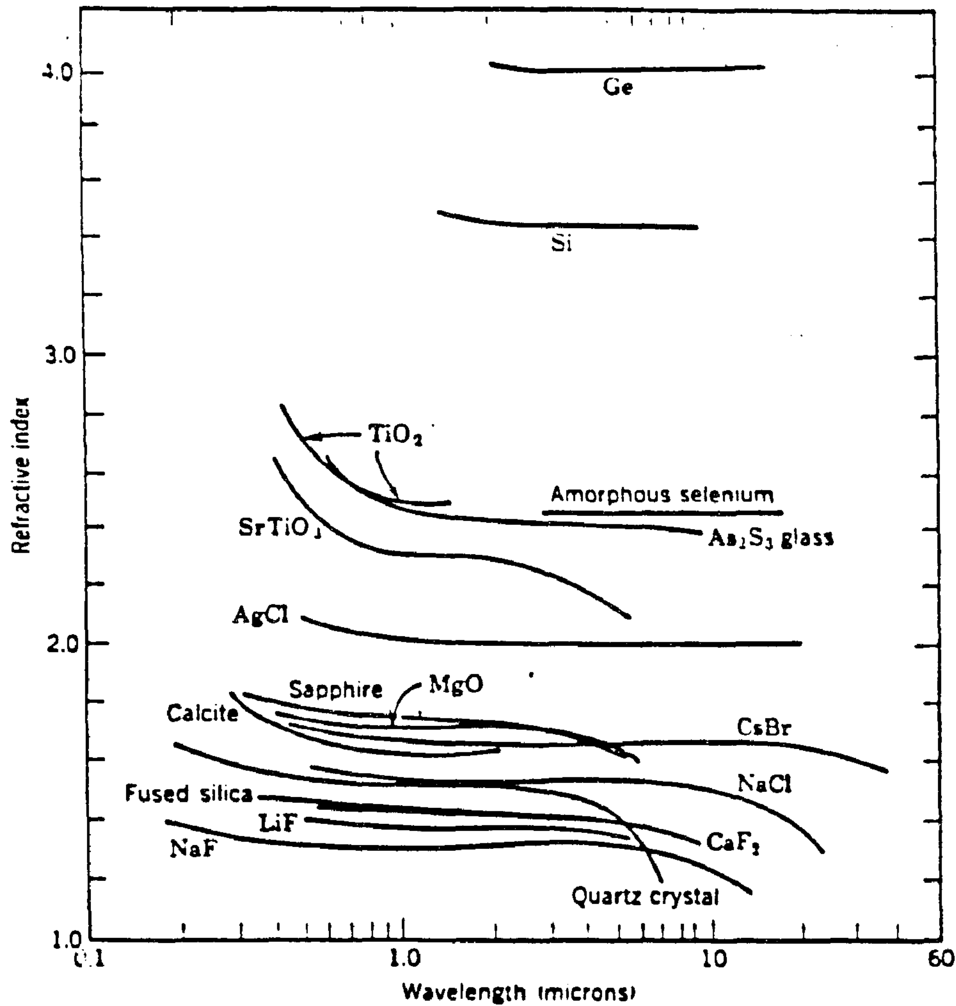

Figure 2.1 Change in refractive index with wavelength for several crystals and glasses (17).

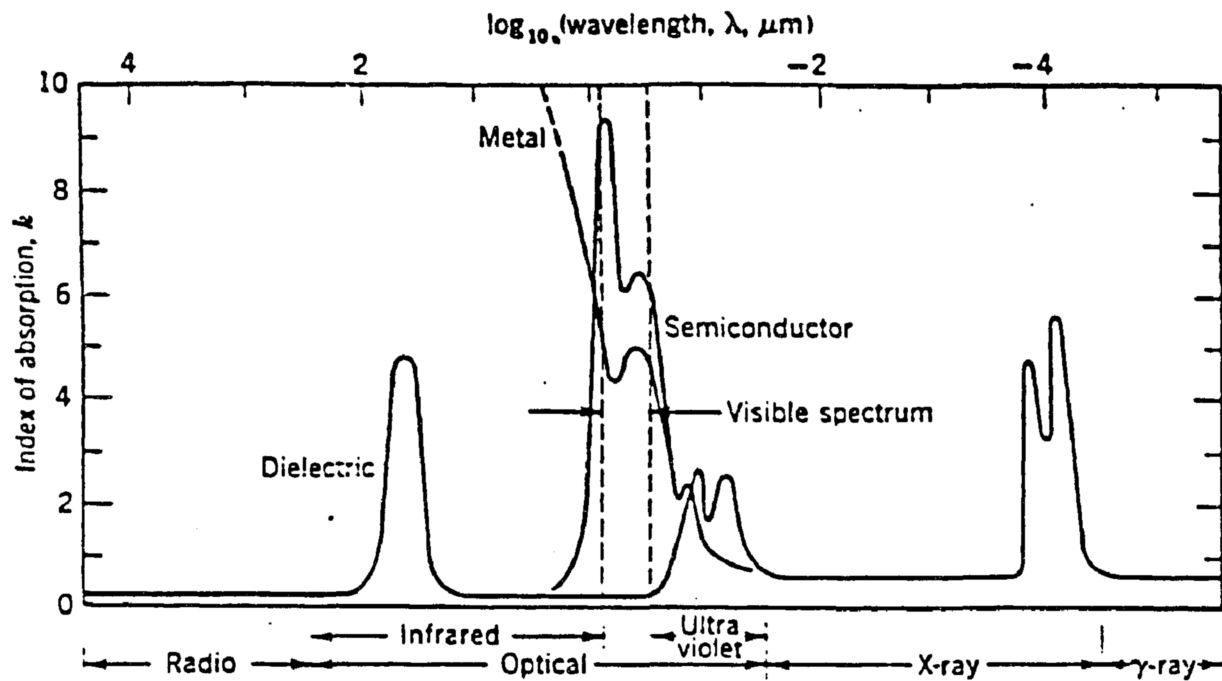

Figure 2.2 Frequency variation of the index of absorption for metals, semiconductors, and dielectrics (17)

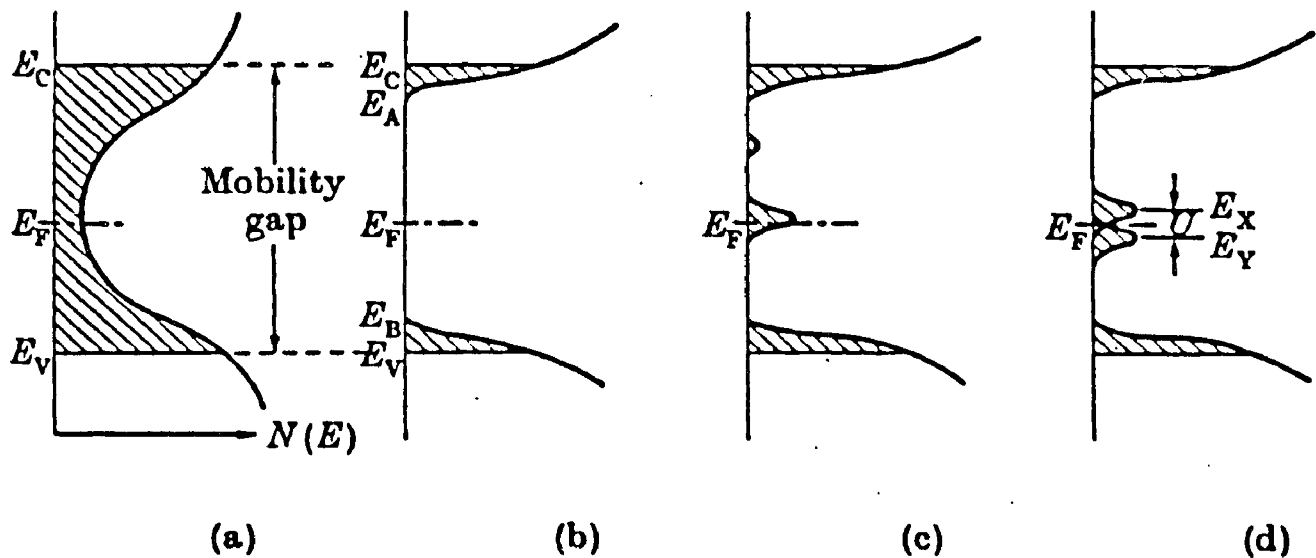

Figure 2.3 Various forms proposed for the density of states in amorphous semiconductors. Localized states are shown shaded. (a) Overlapping conduction and valence band tails (19); (b) a real gap in the density of states suggested here as being appropriate for a continuous random network without defects; (c) the same as (b) but with a partially compensated band of defect levels; (d) the same as (b) but with overlapping bands of donor, E_Y, and acceptor, E_X, levels arising from the same defect. (ref (18))

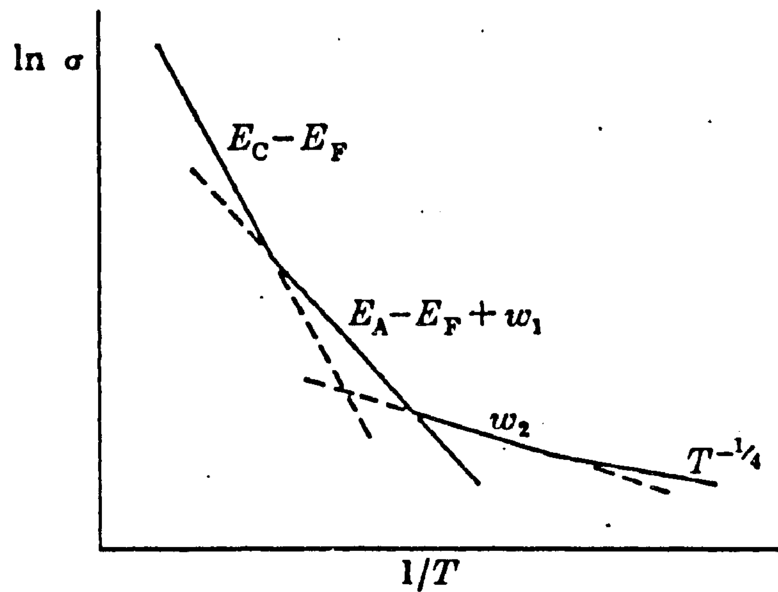

Figure 2.4 Illustration of temperature dependence of electrical conductivity of an amorphous semiconductor (18).

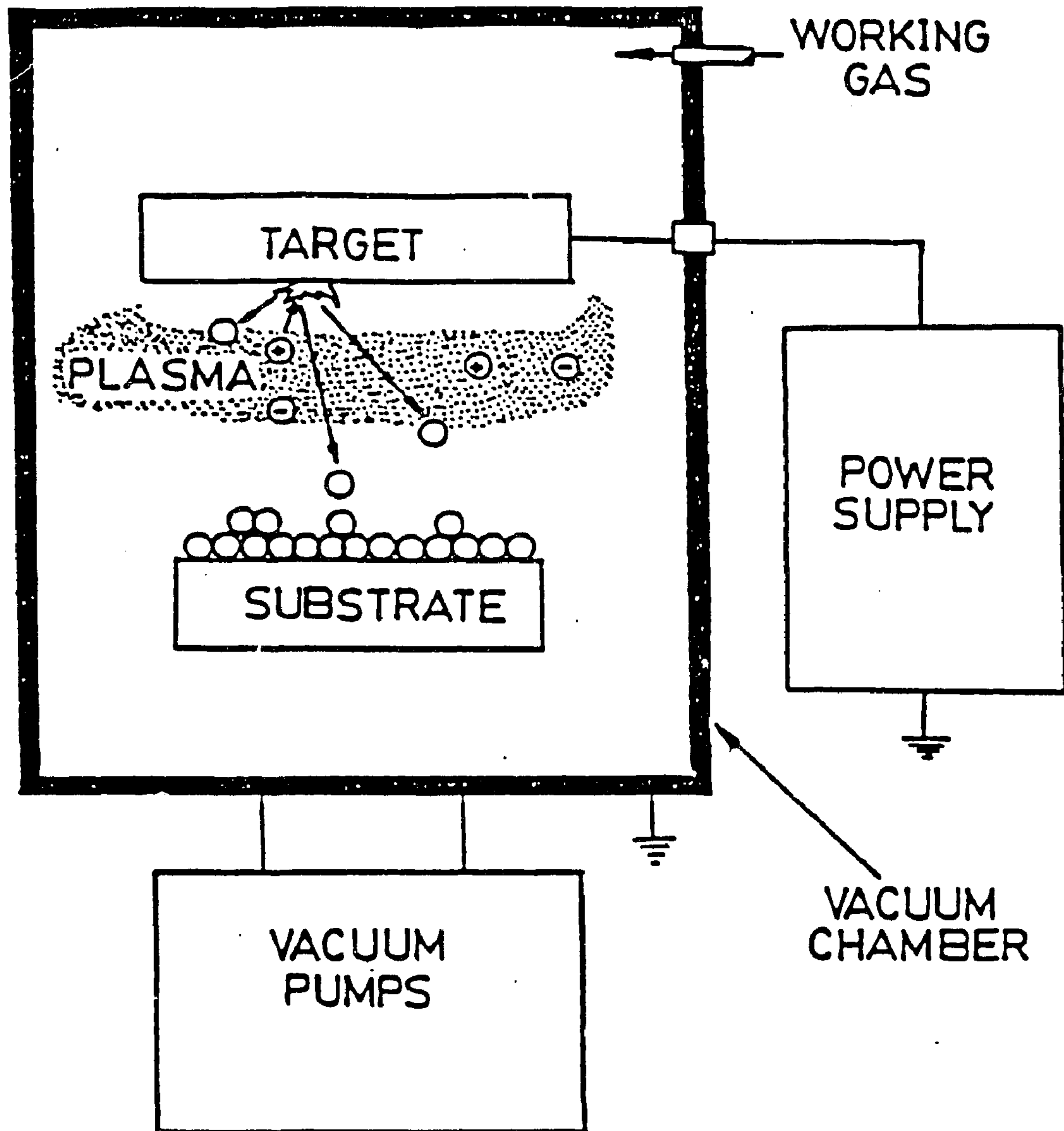

Figure 2.5 Schematic diagram of diode sputtering system (16).

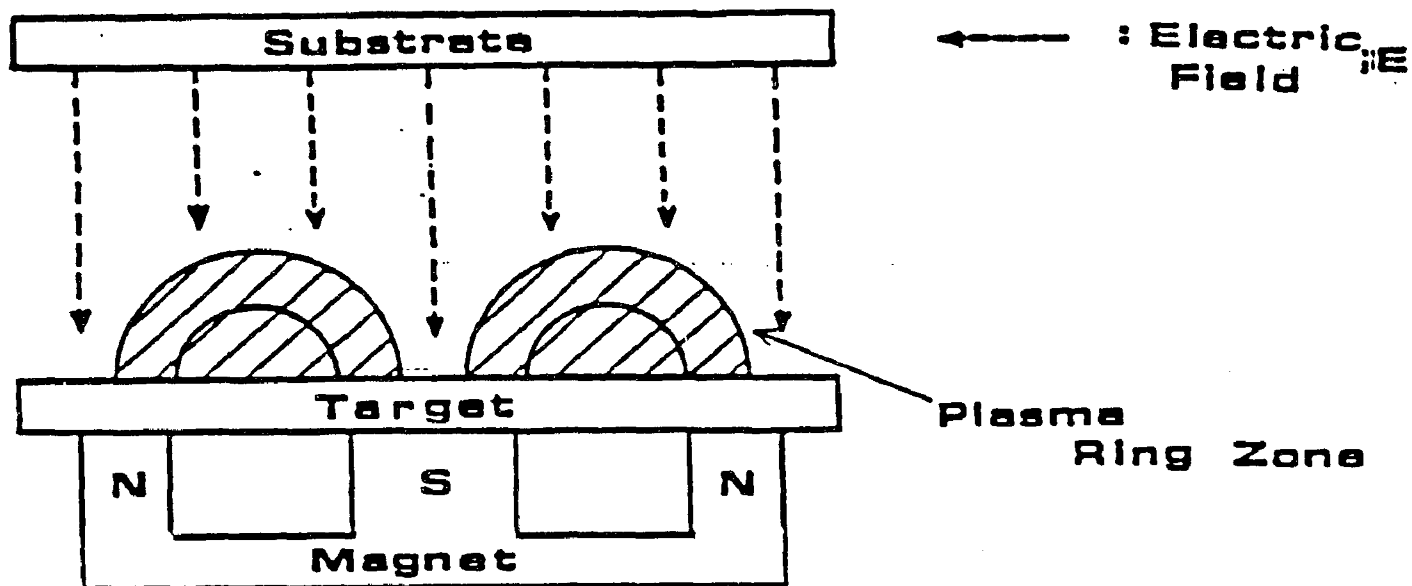

Figure 2.6 Schematic diagram of magnetron sputtering system with a ring magnet (15).

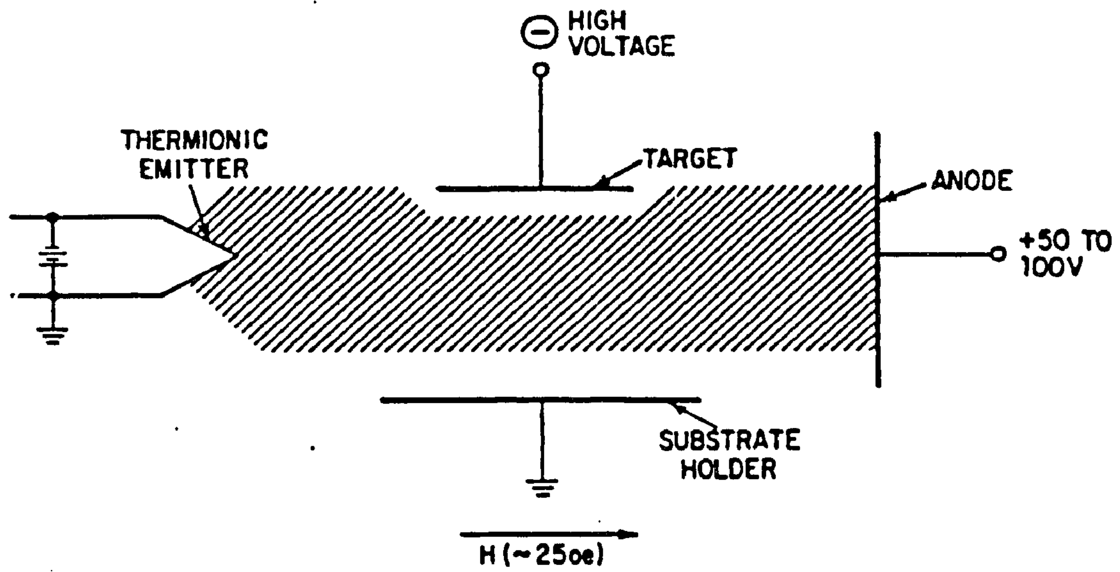

Figure 2.7 Schematic diagram of triode sputtering system (24).

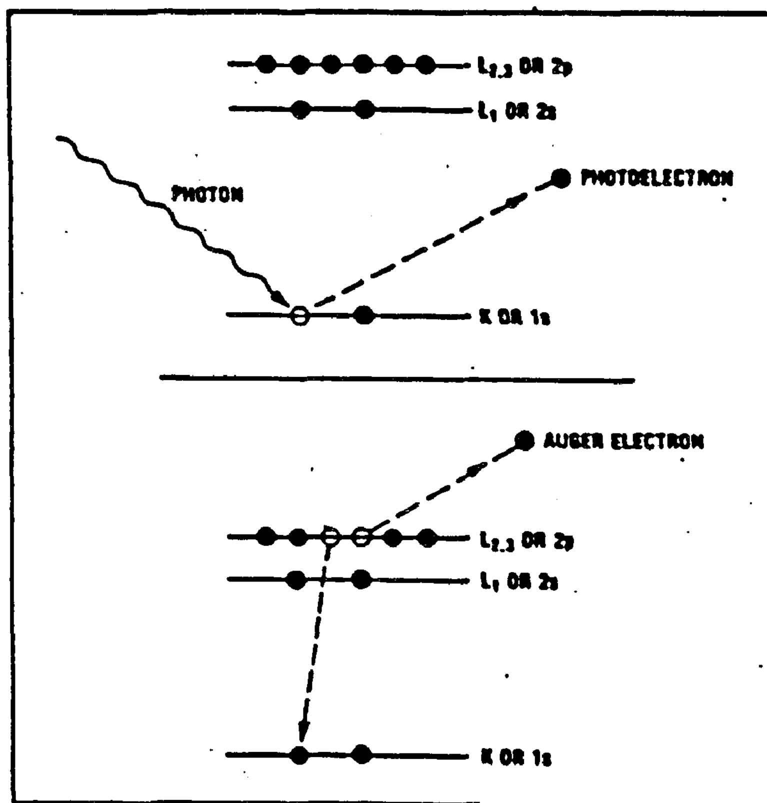

Figure 2.8 Energy level diagrams of photoelectron (top) and Auger electron (bottom) excitation (27).

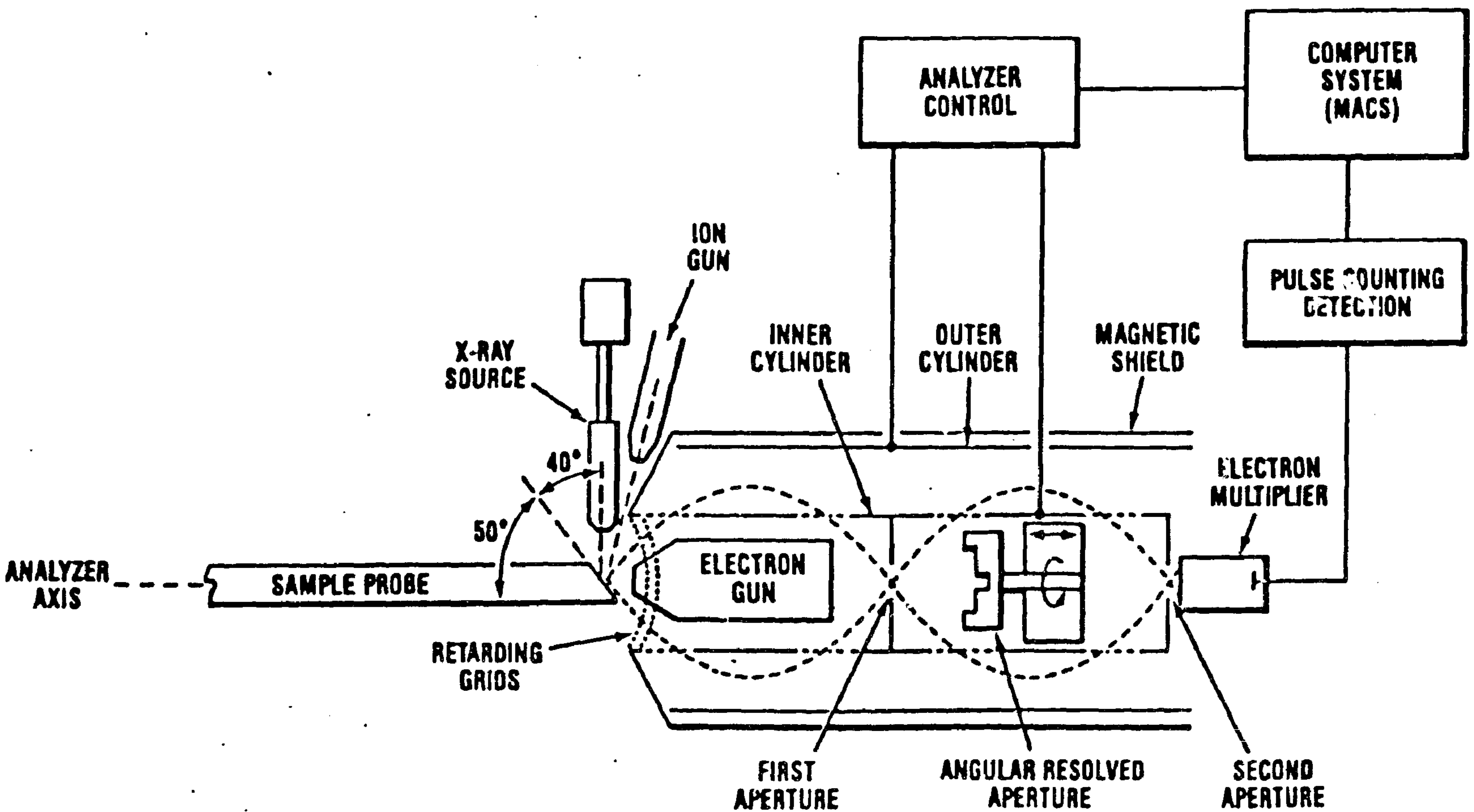

Figure 2.9 Schematic diagram of multi-technique AES/XPS analytical system (27).

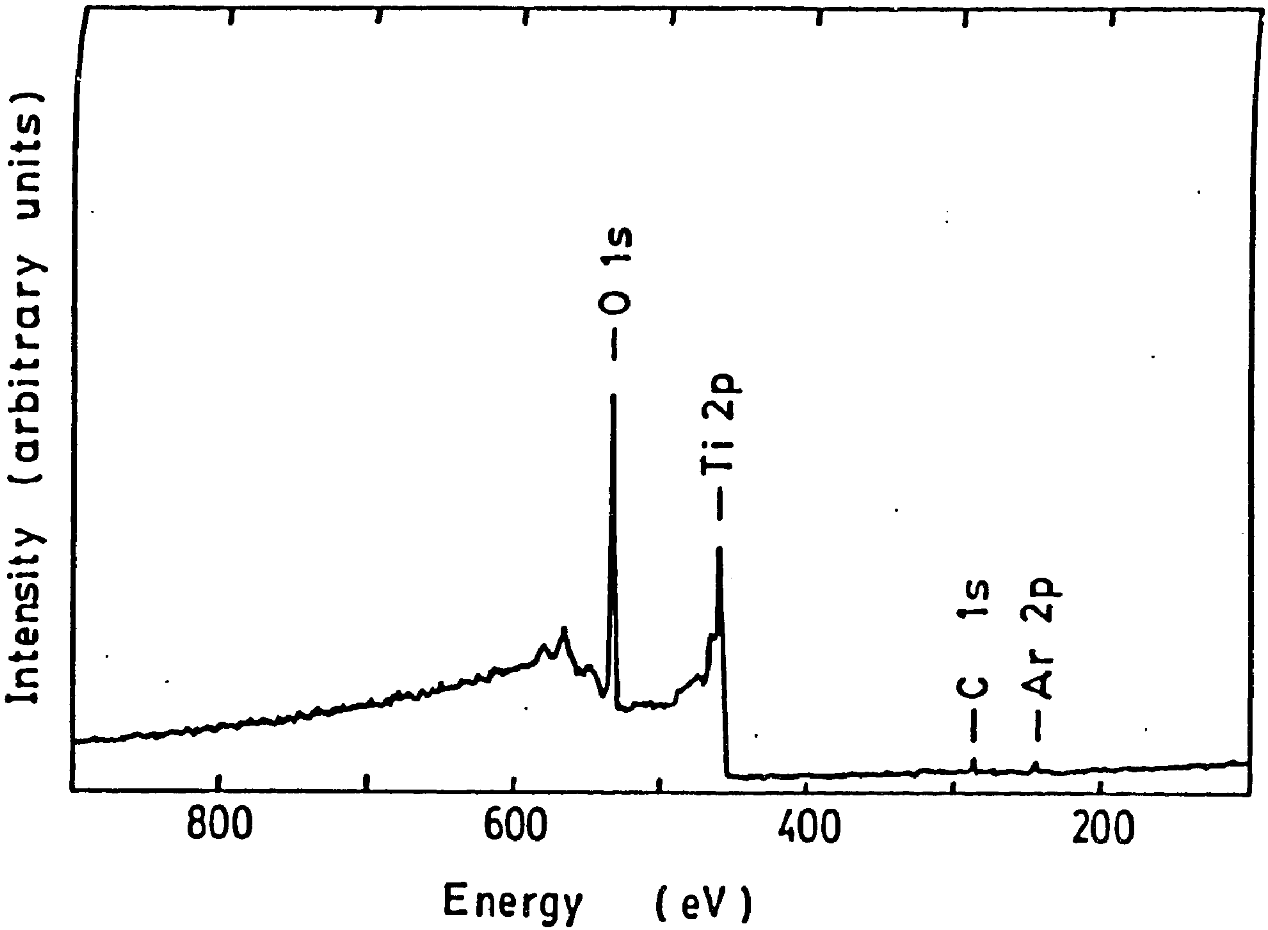

Figure 2.10 Typical broad-range XPS spectrum from TiO_2.

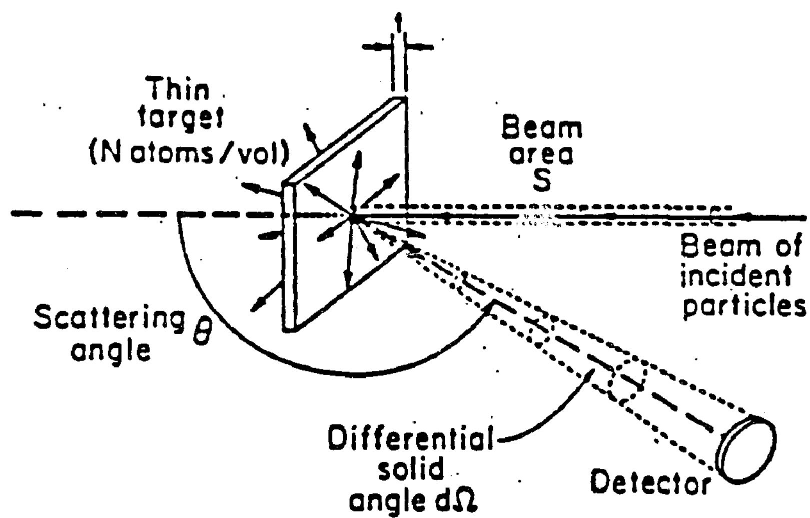

Figure 2.11 Schematic diagram of Rutherford backscattering spectroscopy (RBS) apparatus (30).

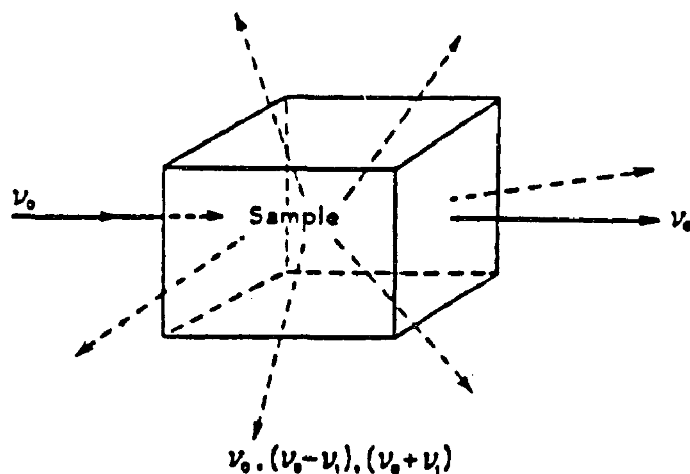

Figure 2.12 Appearance of scattered light with frequencies ν_0, $(\nu_0 + \nu_1)$, and $(\nu_0 - \nu_1)$ (150).

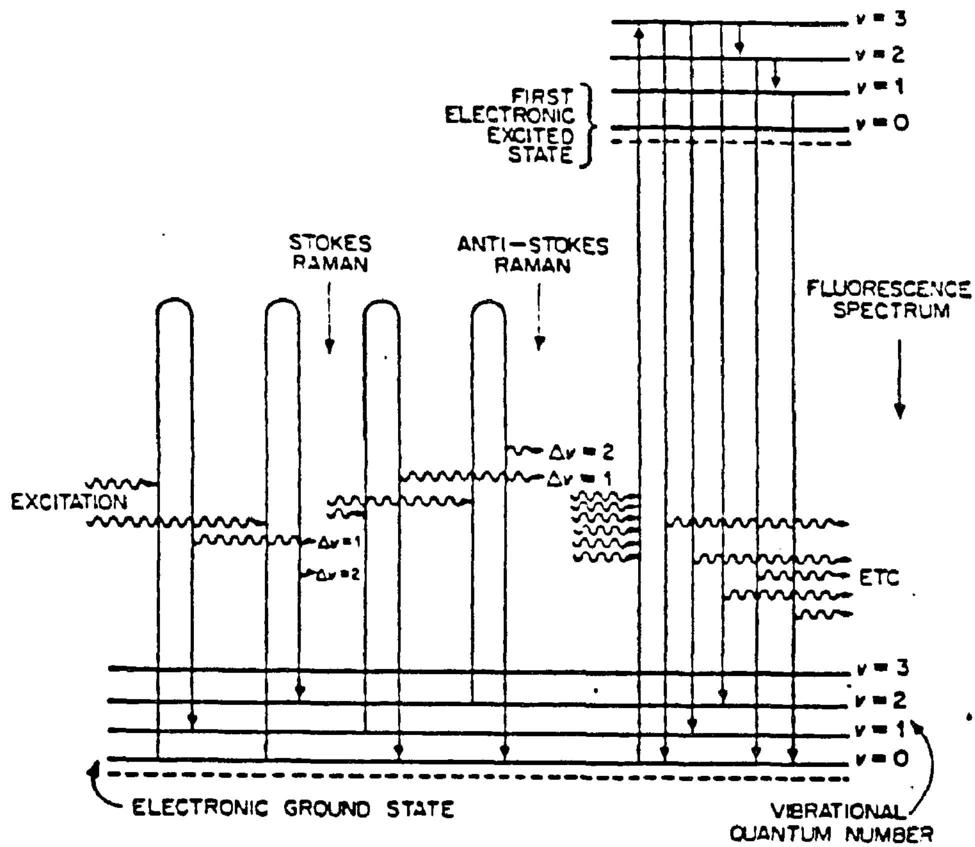

Figure 2.13 Stokes and anti-Stokes Raman shifts and fluorescence process (34).

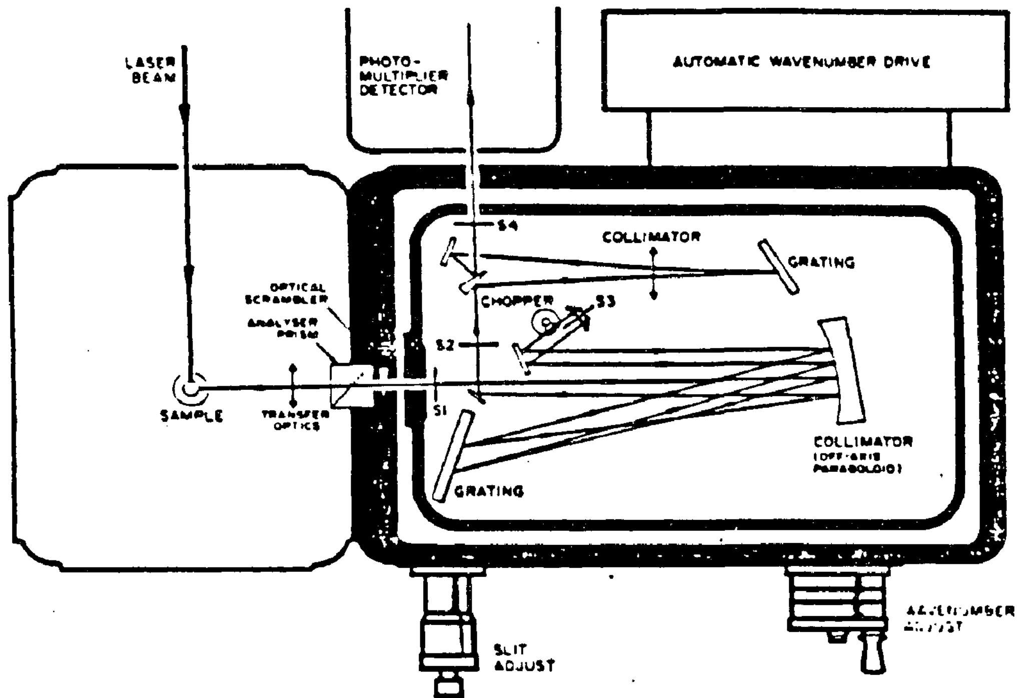

Figure 2.14 Schematic diagram of commercially used Raman spectrometer (34).

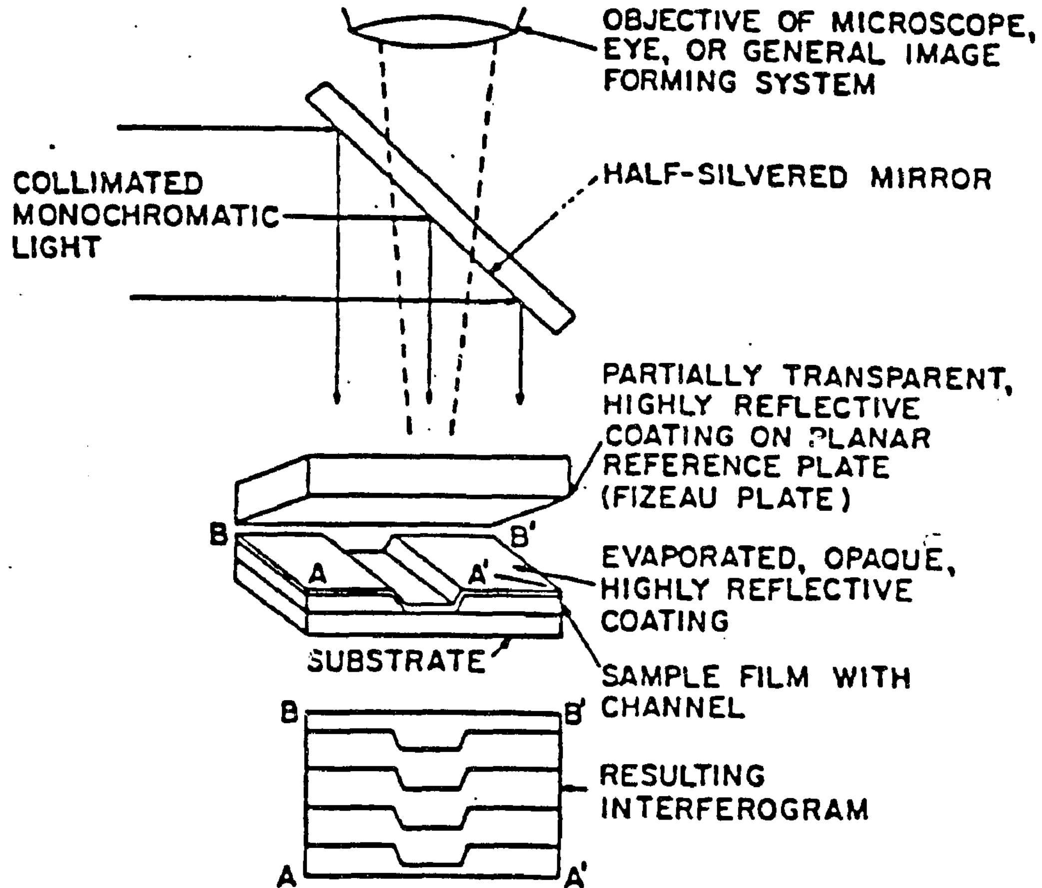

Figure 2.15 Schematic view of apparatus for producing multiple-beam Fizeau fringes (Tolansky technique) (131).

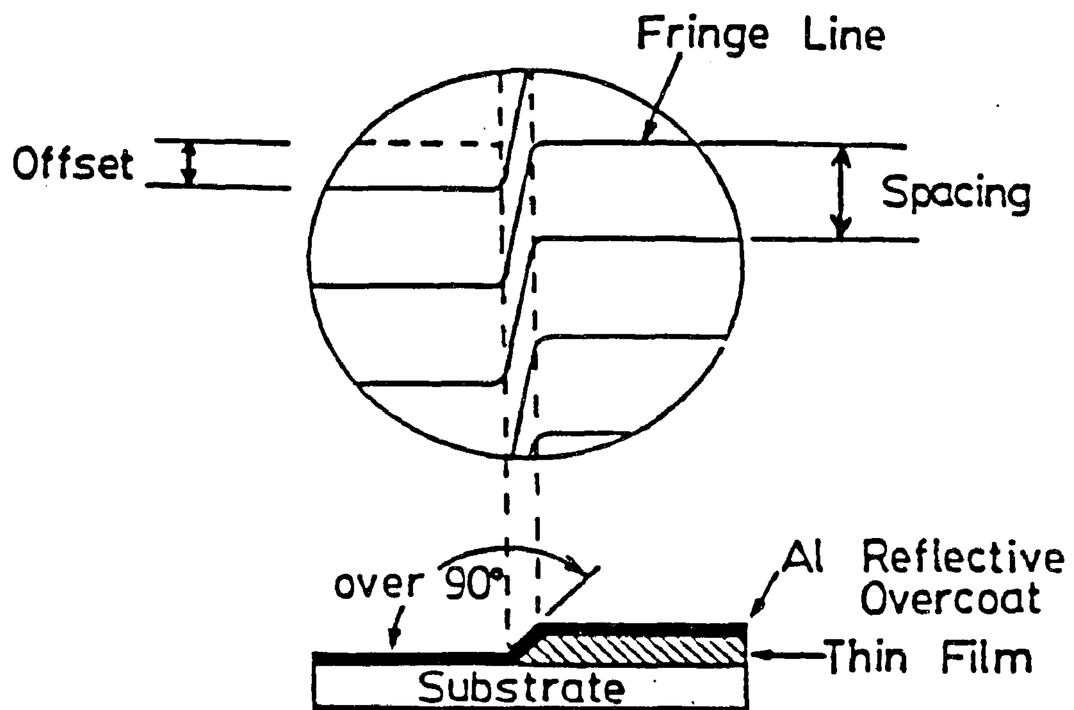

Figure 2.16 Fringe pattern produced from thin film (16).

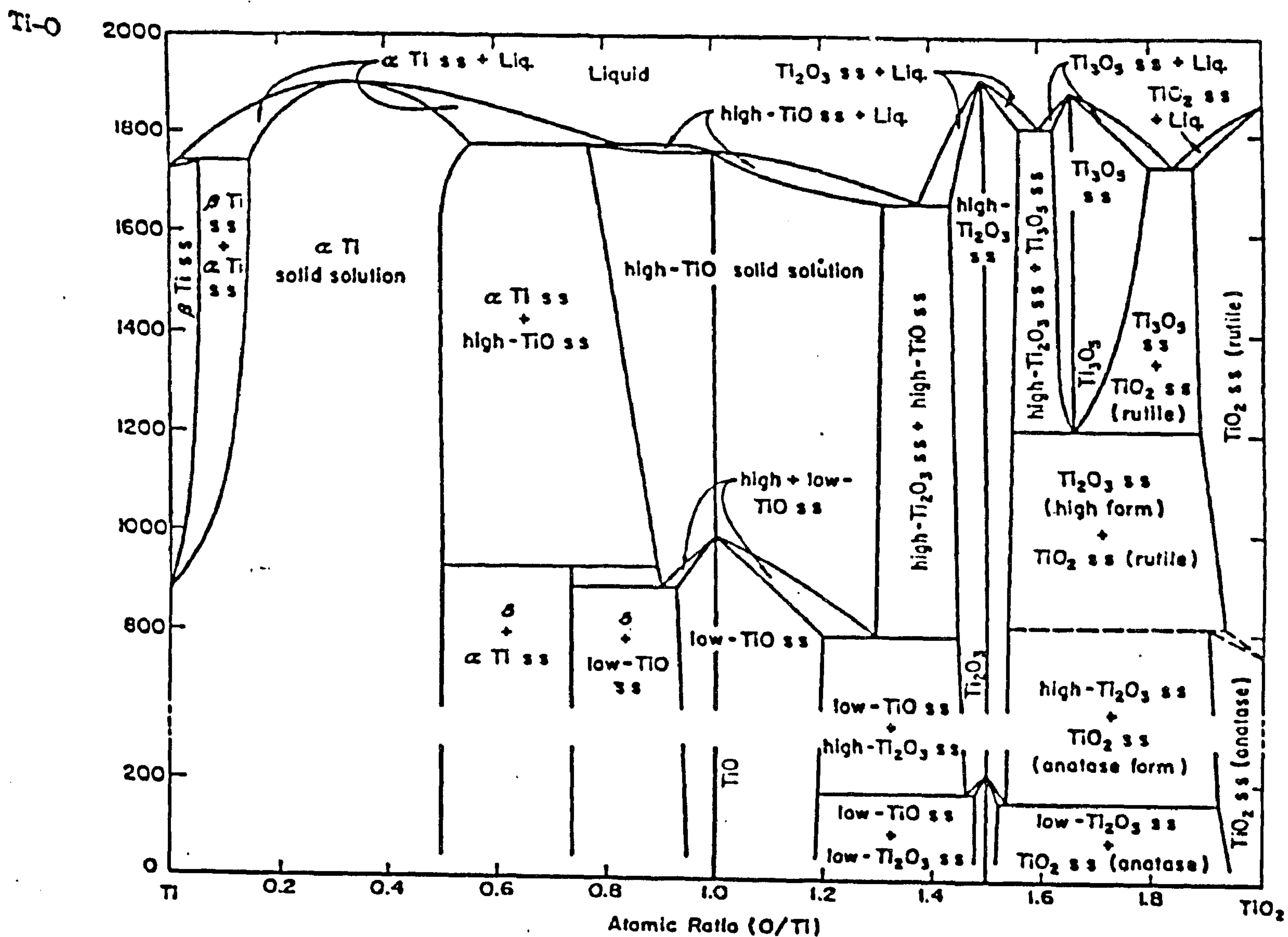

Figure 2.17 Titanium-oxygen phase diagram (35).

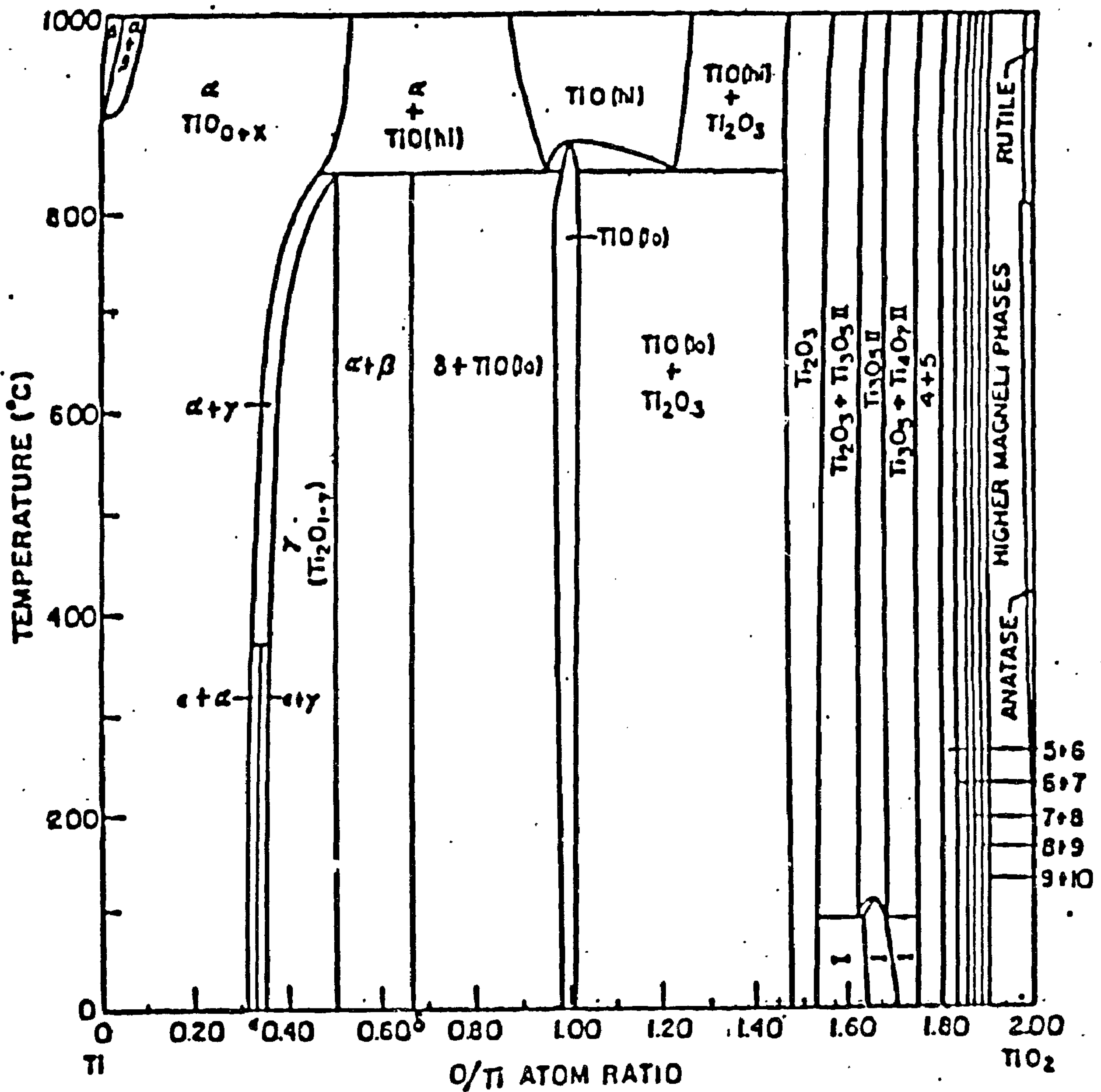

Figure 2.18 Titanium-oxygen phase diagram (36).

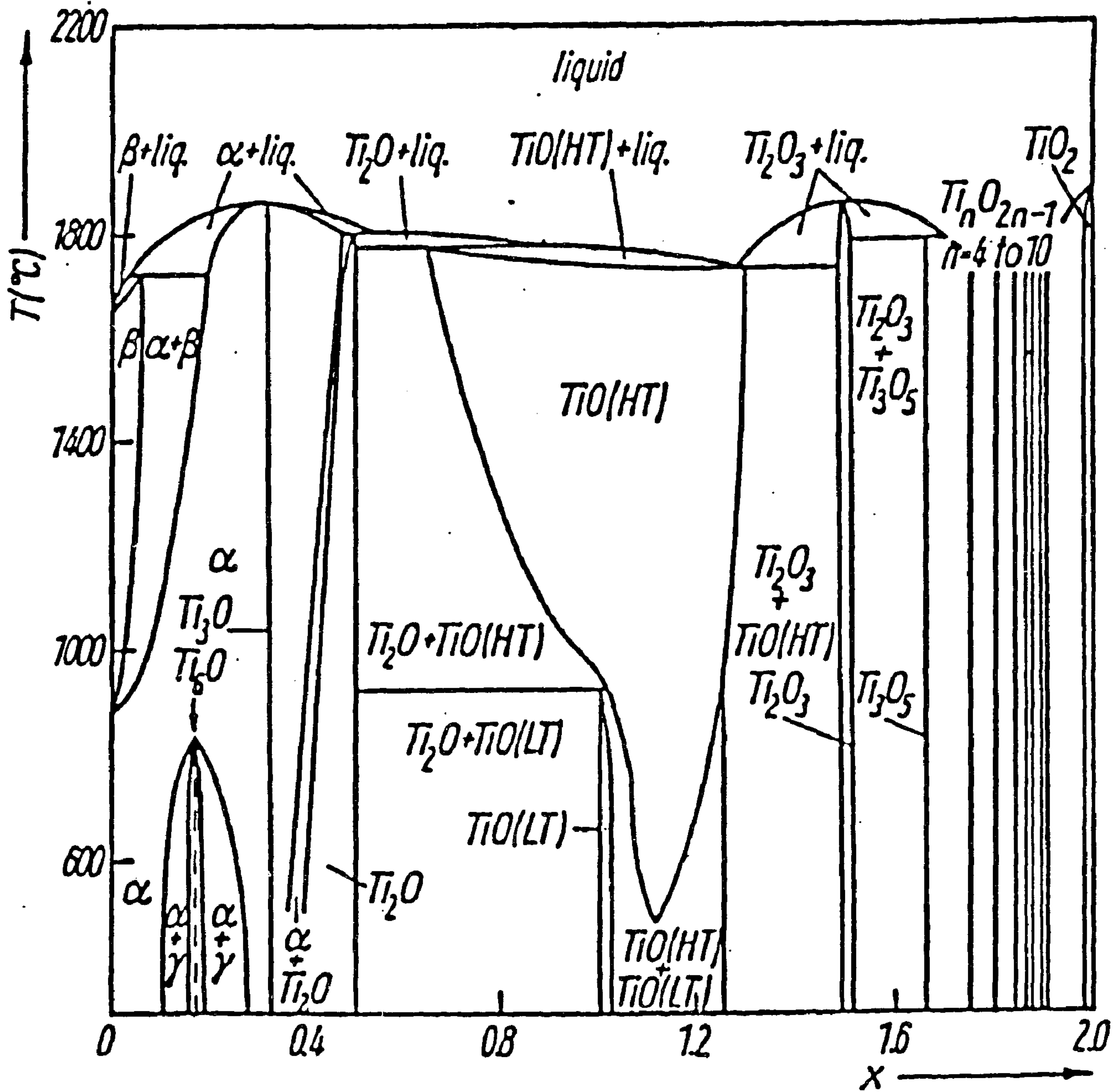

Figure 2.19 Titanium-oxygen phase diagram (37).

THE RUTILE GROUP TETRAGONAL $D_{4h}^{14} = P4/mnm$ $Z = 2$

		a (Å)	c (Å)	c/a
Pyrolusite	MnO_2	4·40	2·87	0·665
Rutile	TiO_2	4·58	2·95	0·644
Cassiterite	SnO_2	4·72	3·17	0·672
Plattnerite	PbO_2	4·94	3·37	0·682

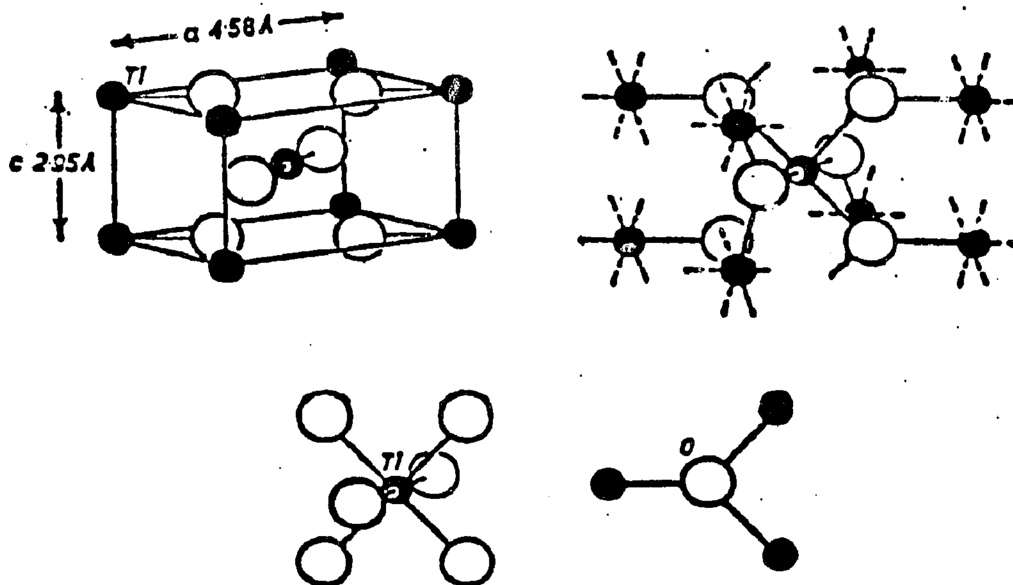

Figure 2.20 Structure of rutile TiO_2 (138).

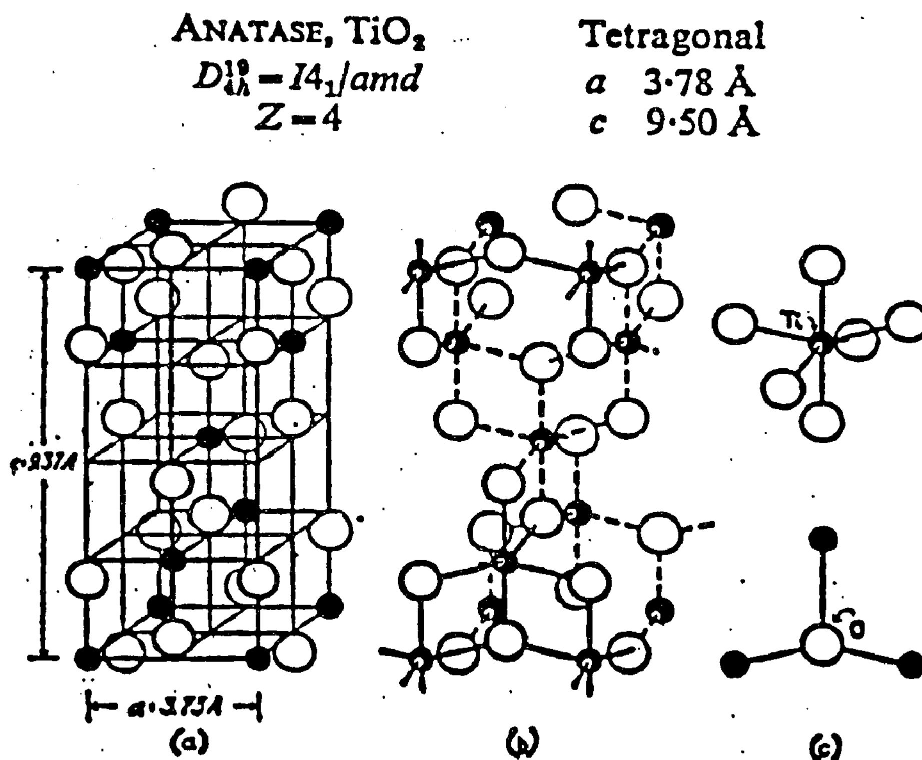

Figure 2.21 Structure of anatase TiO_2 (138).

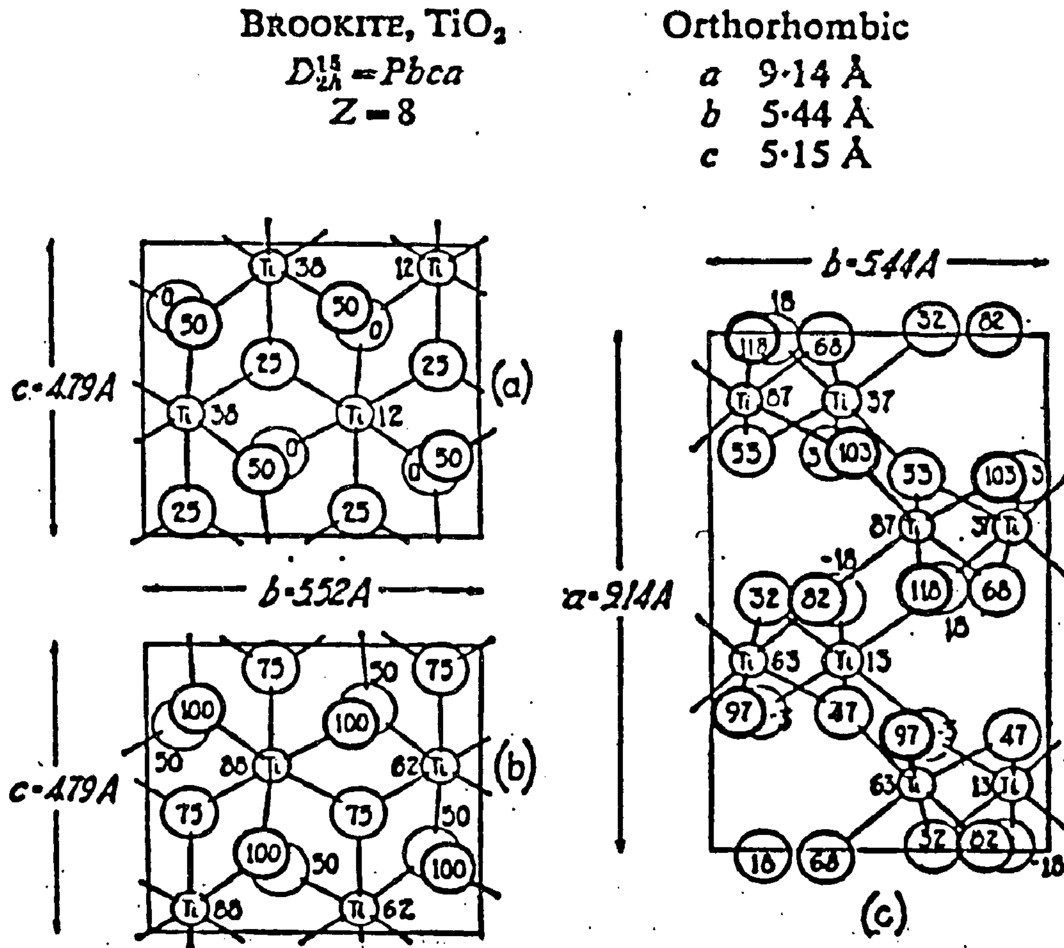

Figure 2.22 Structure of brookite TiO_2 (138).

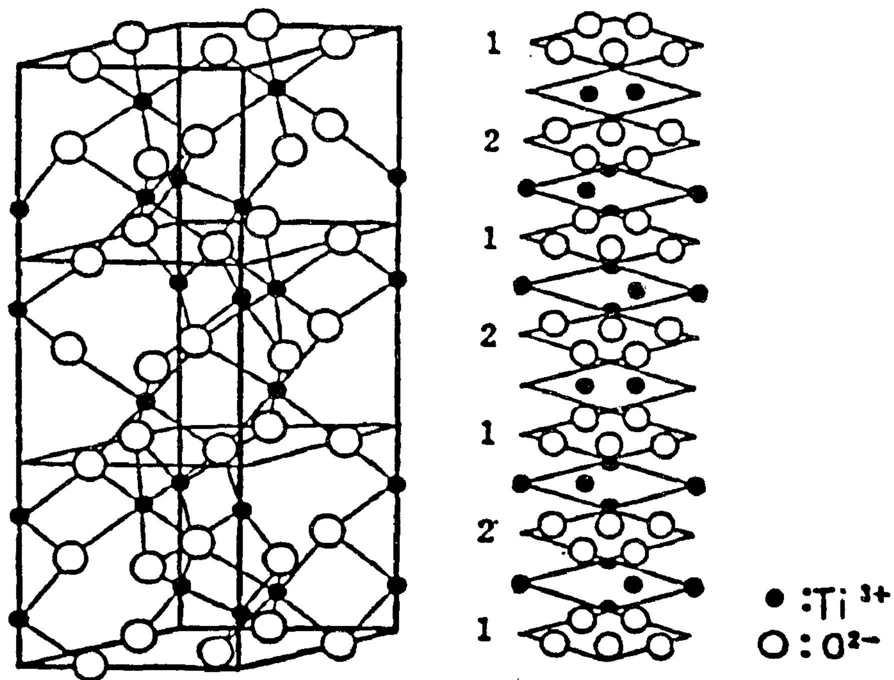

Figure 2.23 Structure of Ti_2O_3 (139).

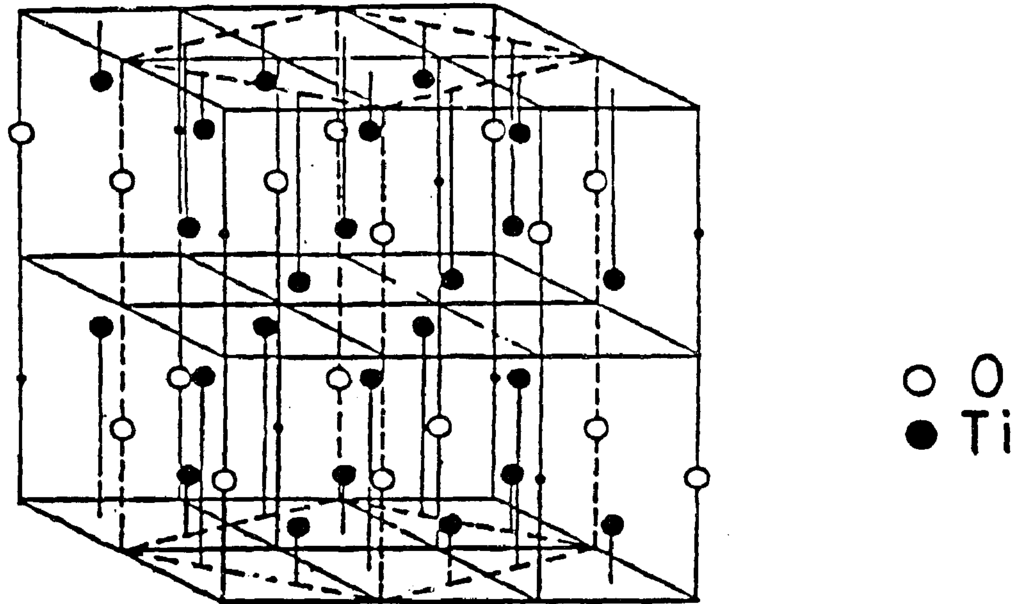

Figure 2.24 Structure of Ti_2O (49).

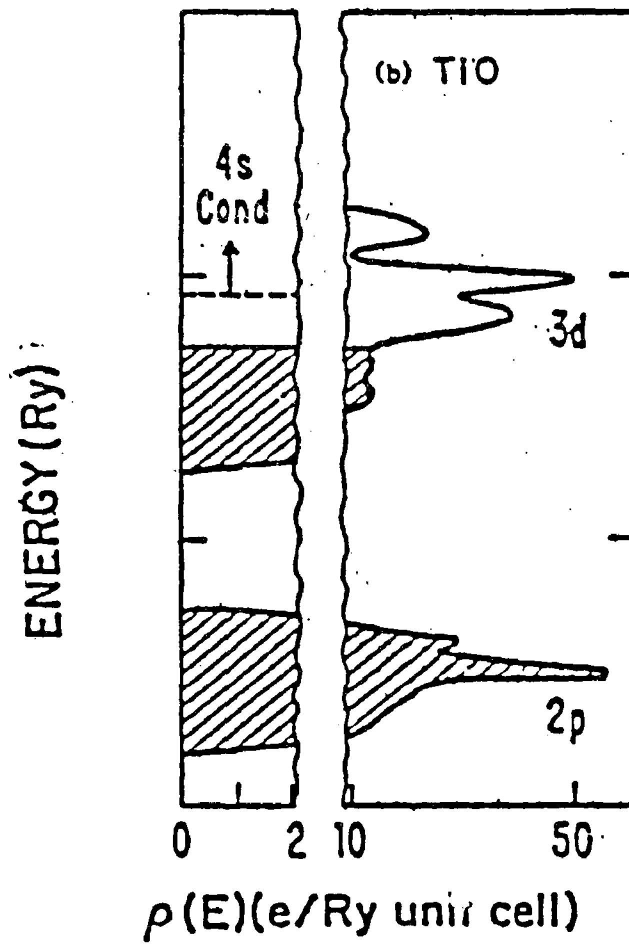

Figure 2.25 Energy band structure of TiO (68).

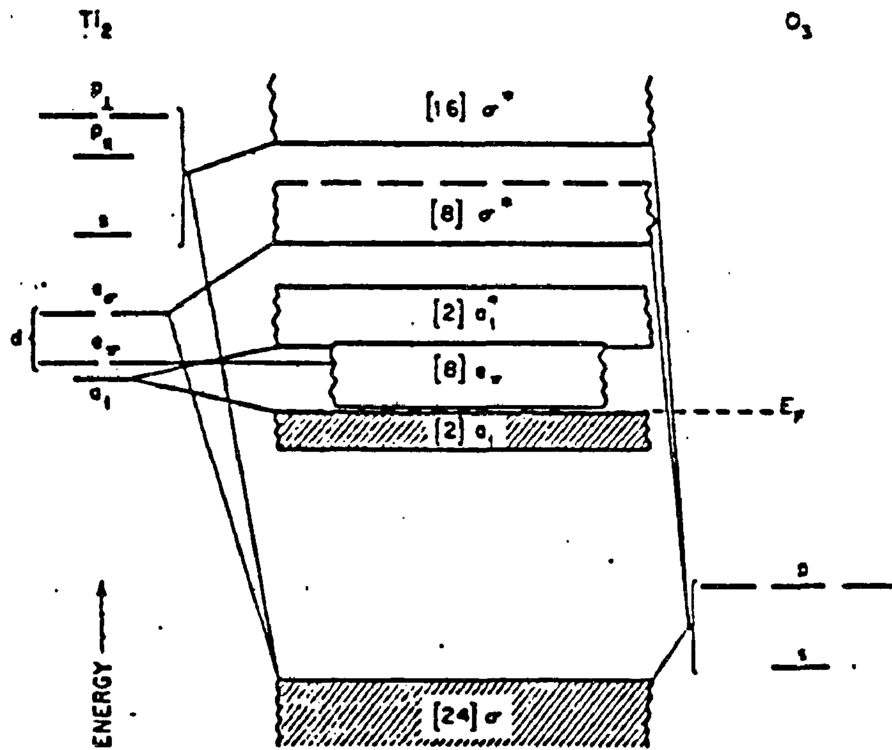

Figure 2.26 Energy band structure of Ti_2O_3 (71).

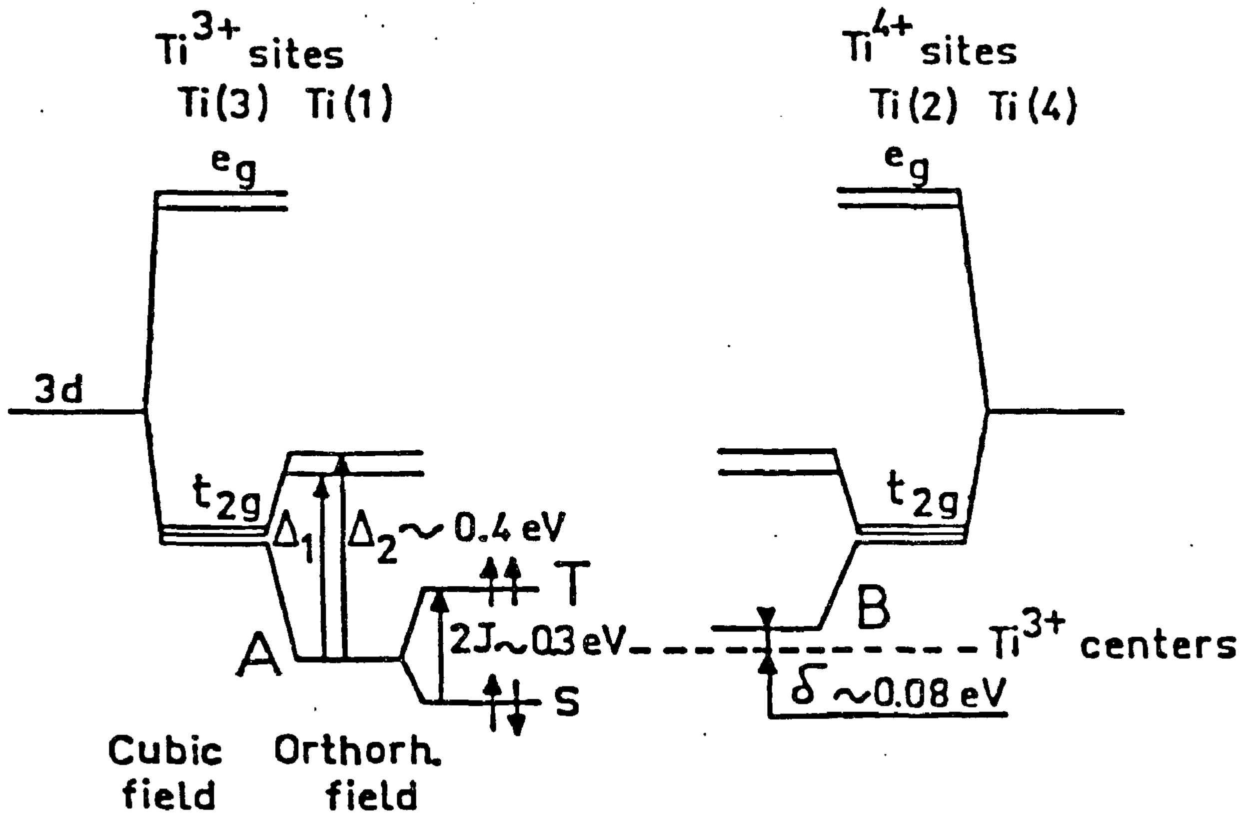

Figure 2.27 Energy band structure of Ti_4O_7 (64).

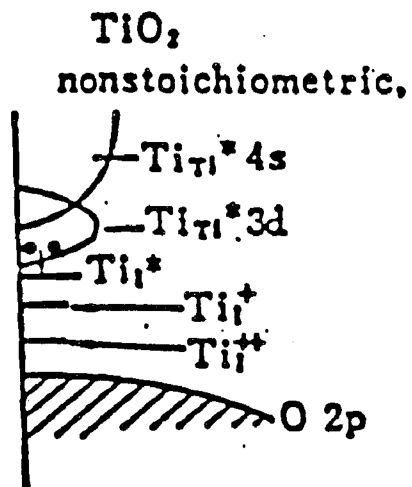

Figure 2.28 Energy band structure of crystalline non-stoichiometric rutile TiO_2 (76).

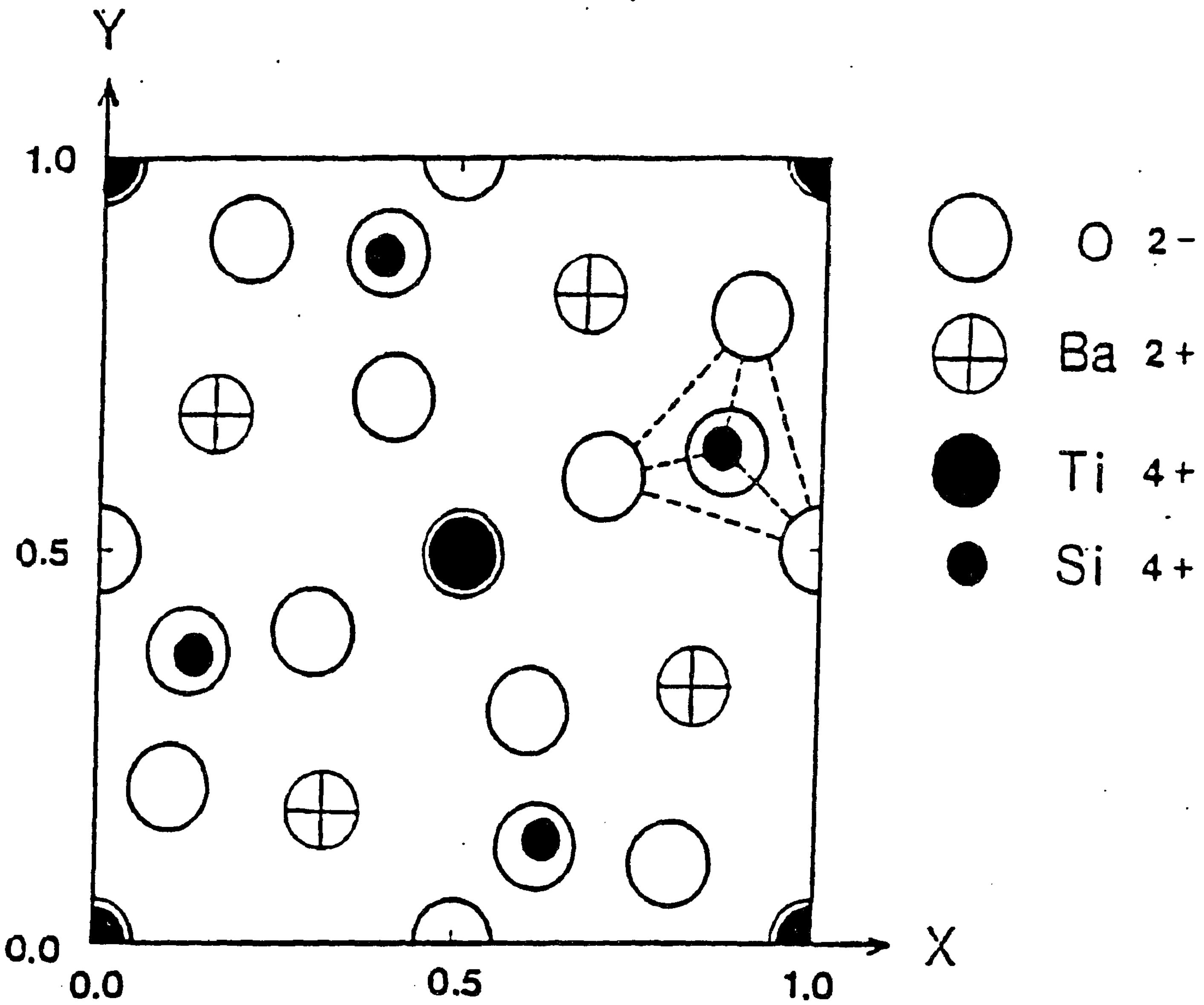

Figure 2.29 Crystallographic structure of $Ba_2Si_2TiO_8$ (projection on X-Y plane) (80).

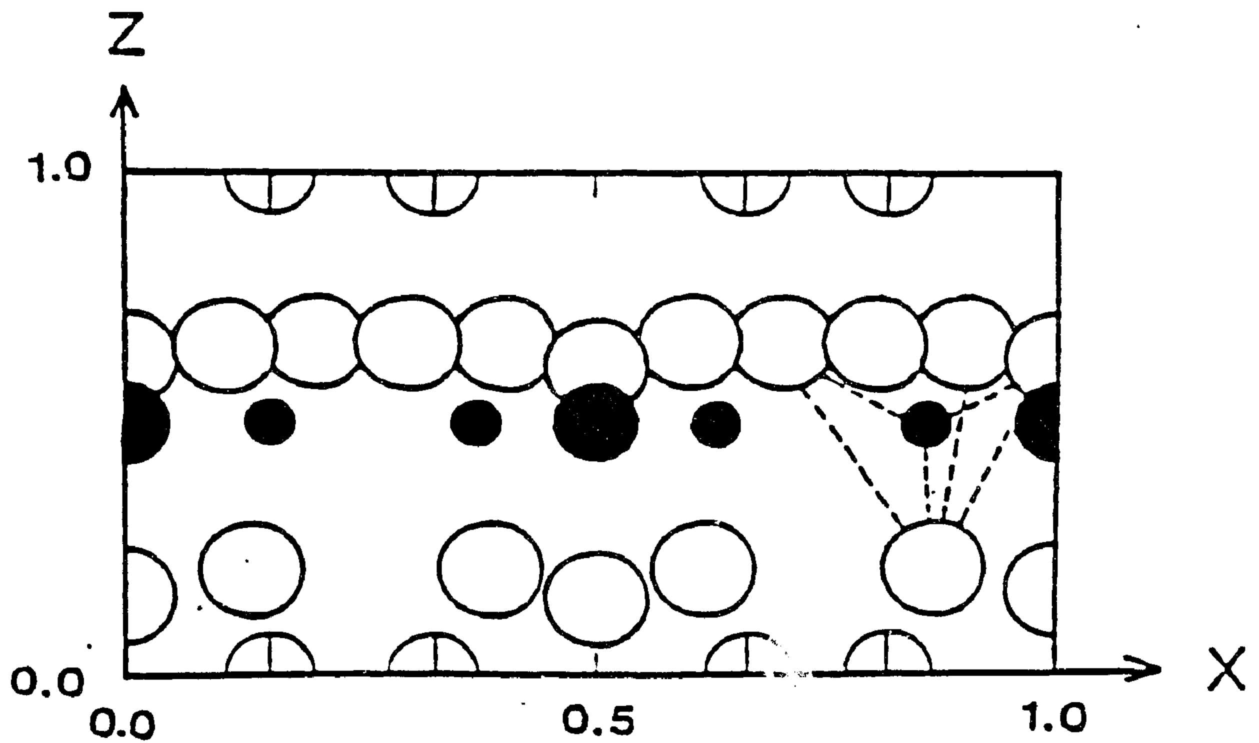

Figure 2.30 Crystallographic structure of $Ba_2Si_2TiO_8$ (projection on X-Z plane) (79).

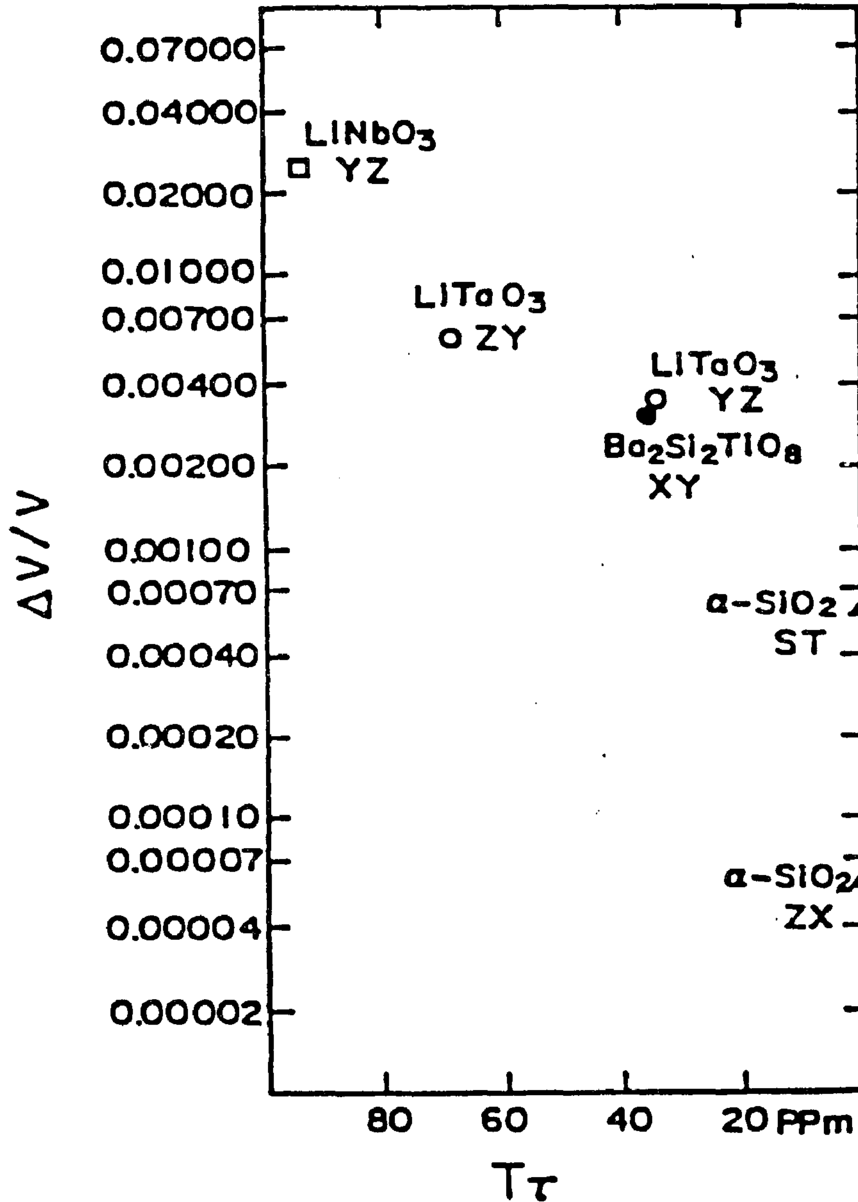

Figure 2.31 Electromechanical coupling factor, $2\Delta v/v$, vs temperature coefficient of delay, TCD, for sets of SAW propagation plane and direction in piezoelectric single crystals (140).

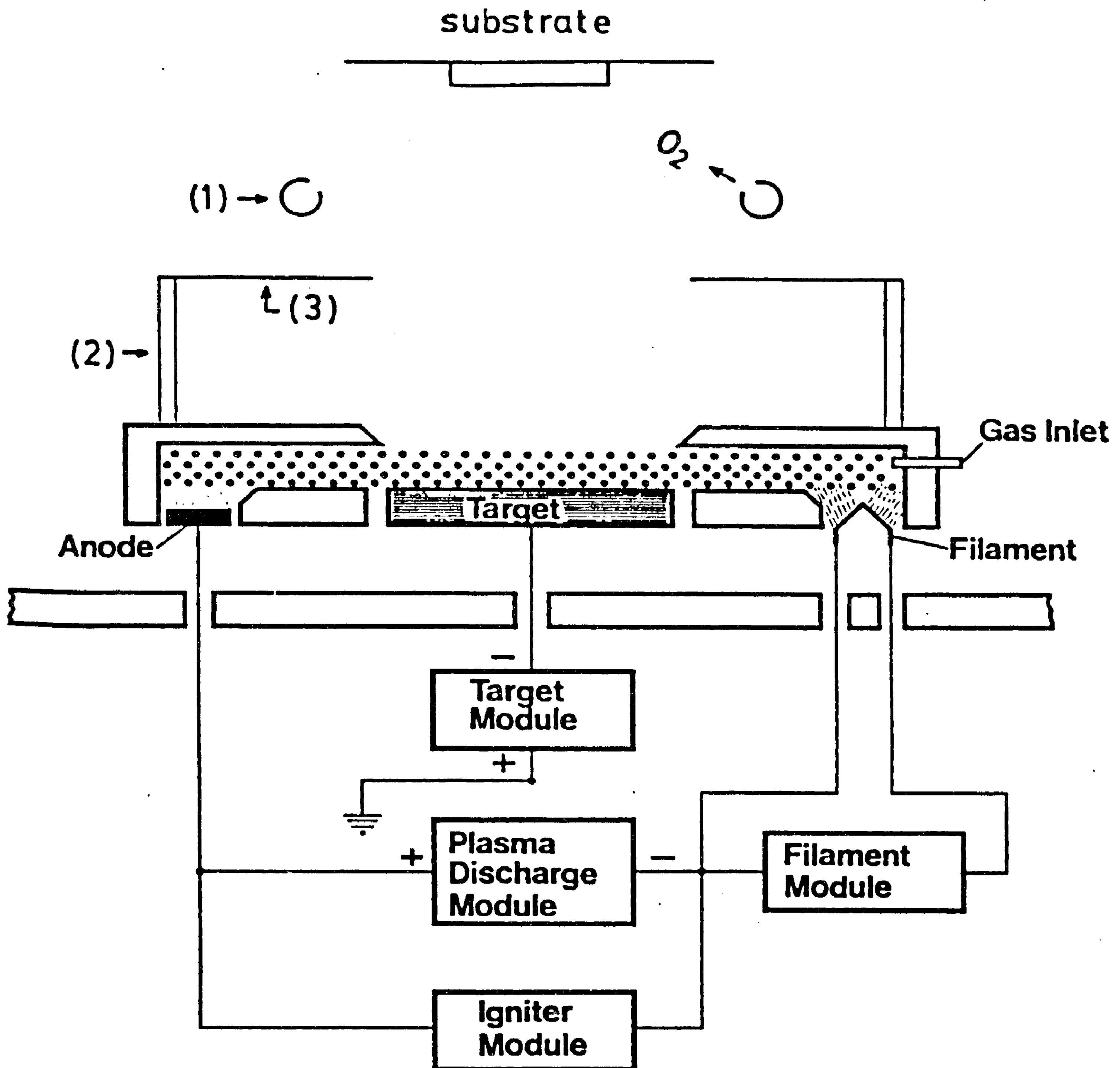

Figure 3.1 Set-up in sputtering deposition unit (used in the present experiment). with triode source: (1) Cu ring, (2) glass cylinder, (3) Al foil.

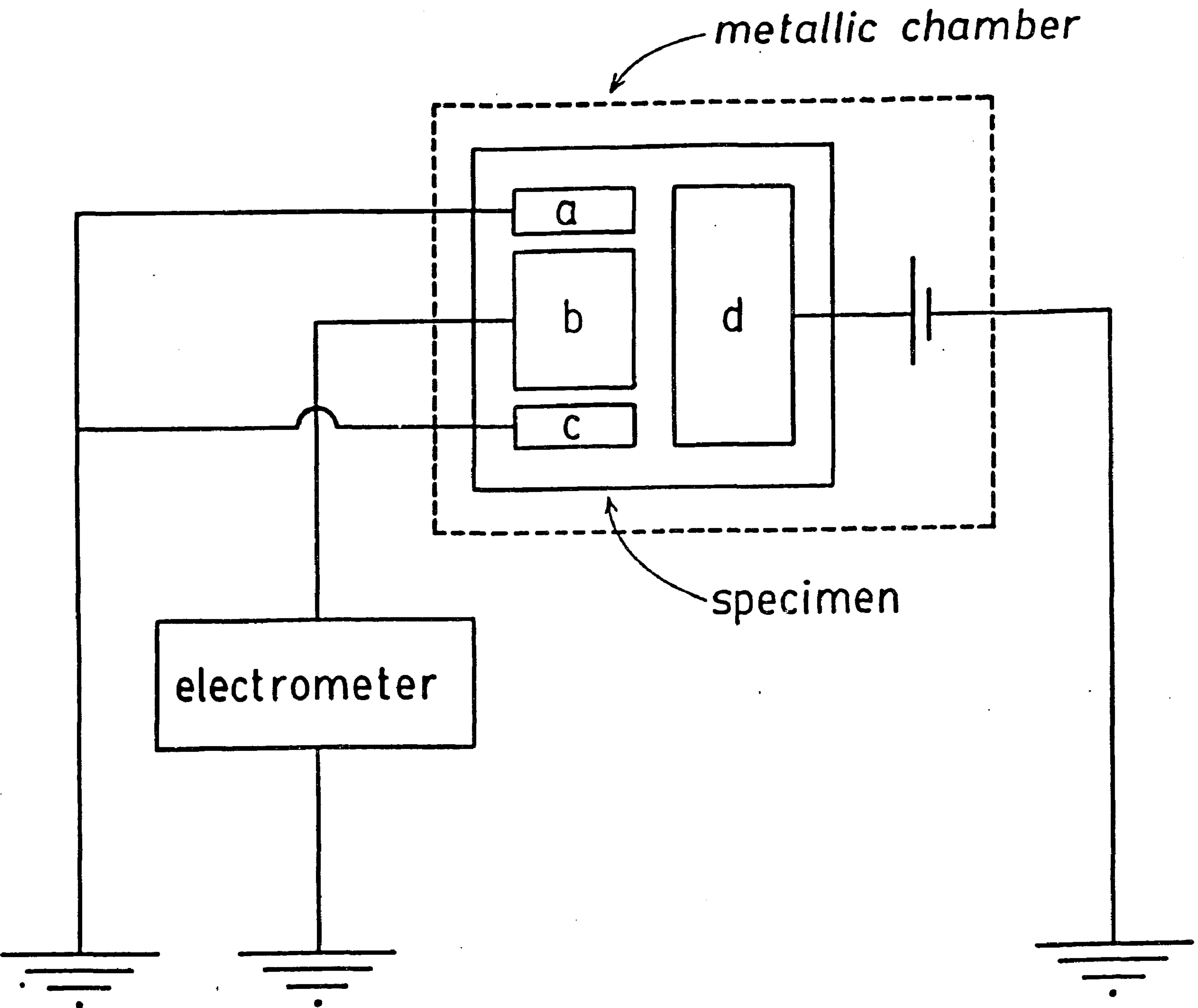

Figure 3.2 Electrical circuit diagram for resistivity measurement. a, b, c and d are electrodes. Electrodes a and c were used to avoid edge effect on the current flow from d to b.

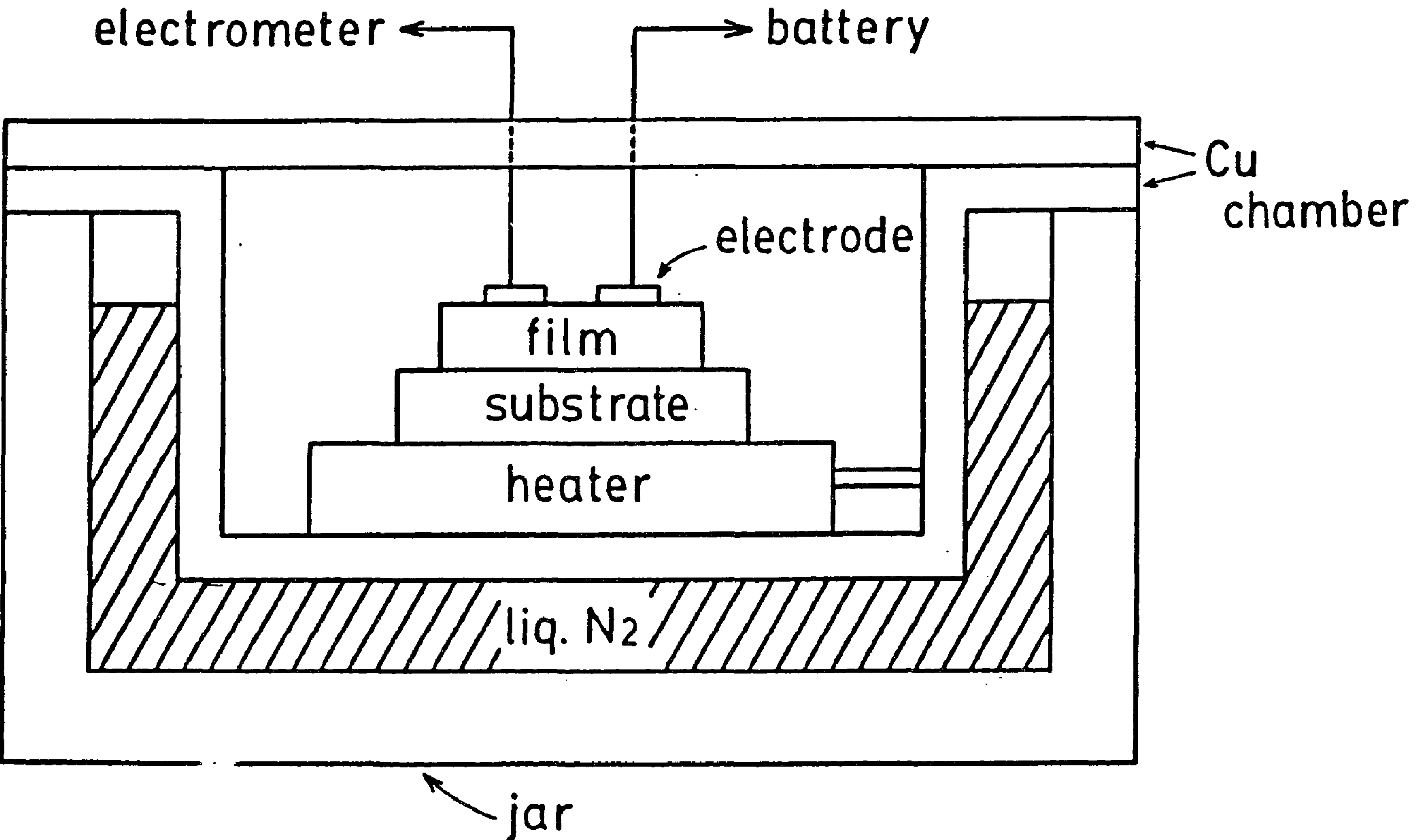

Figure 3.3 Schematic diagram of resistivity measurement set-up.

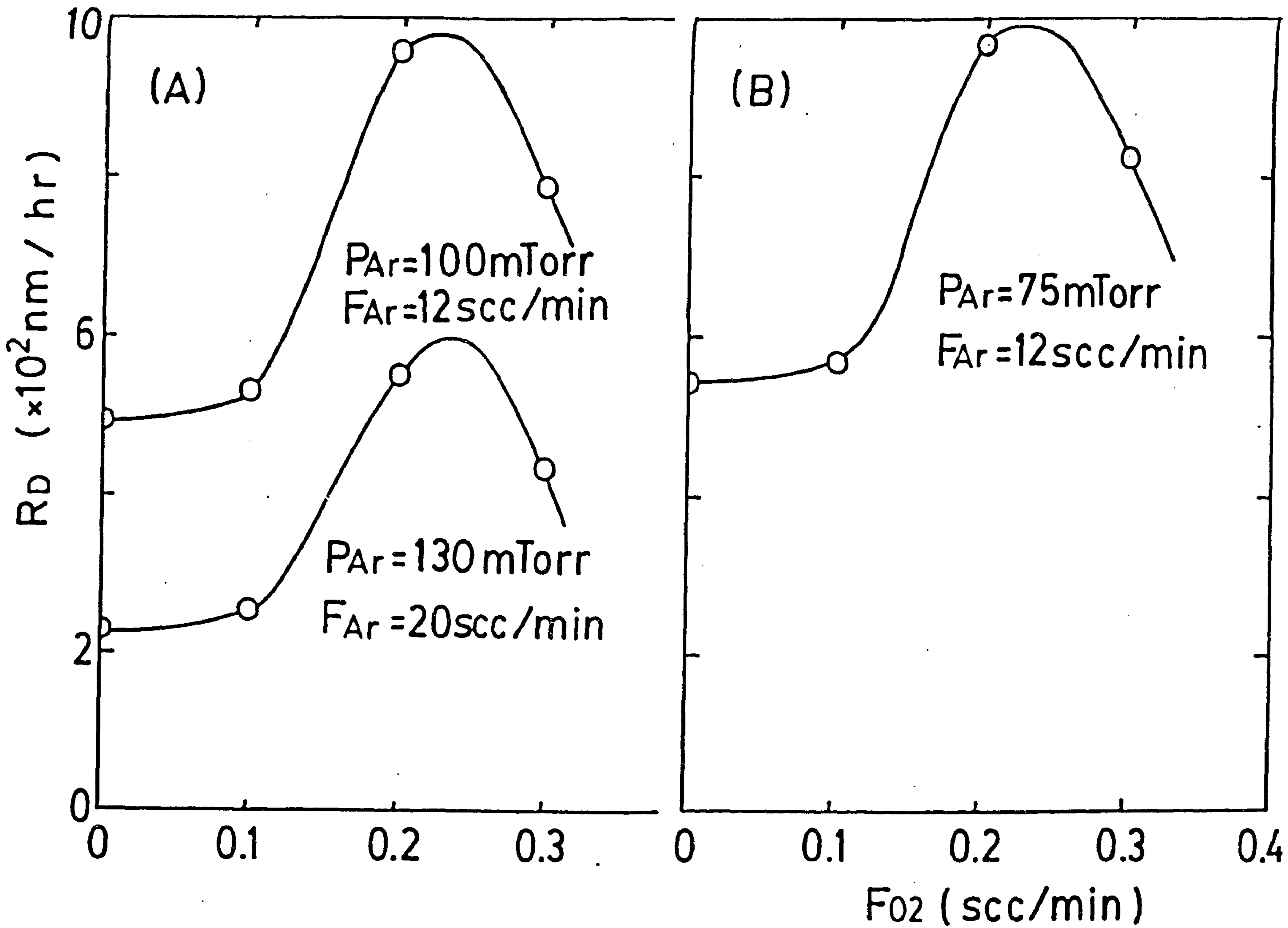

Figure 3.4 Deposition rate, R_D, in terms of O_2 gas flow rate, F_{O_2}, when Ar gas flow rate, F_{Ar}, and partial pressure, P_{Ar}, are fixed.

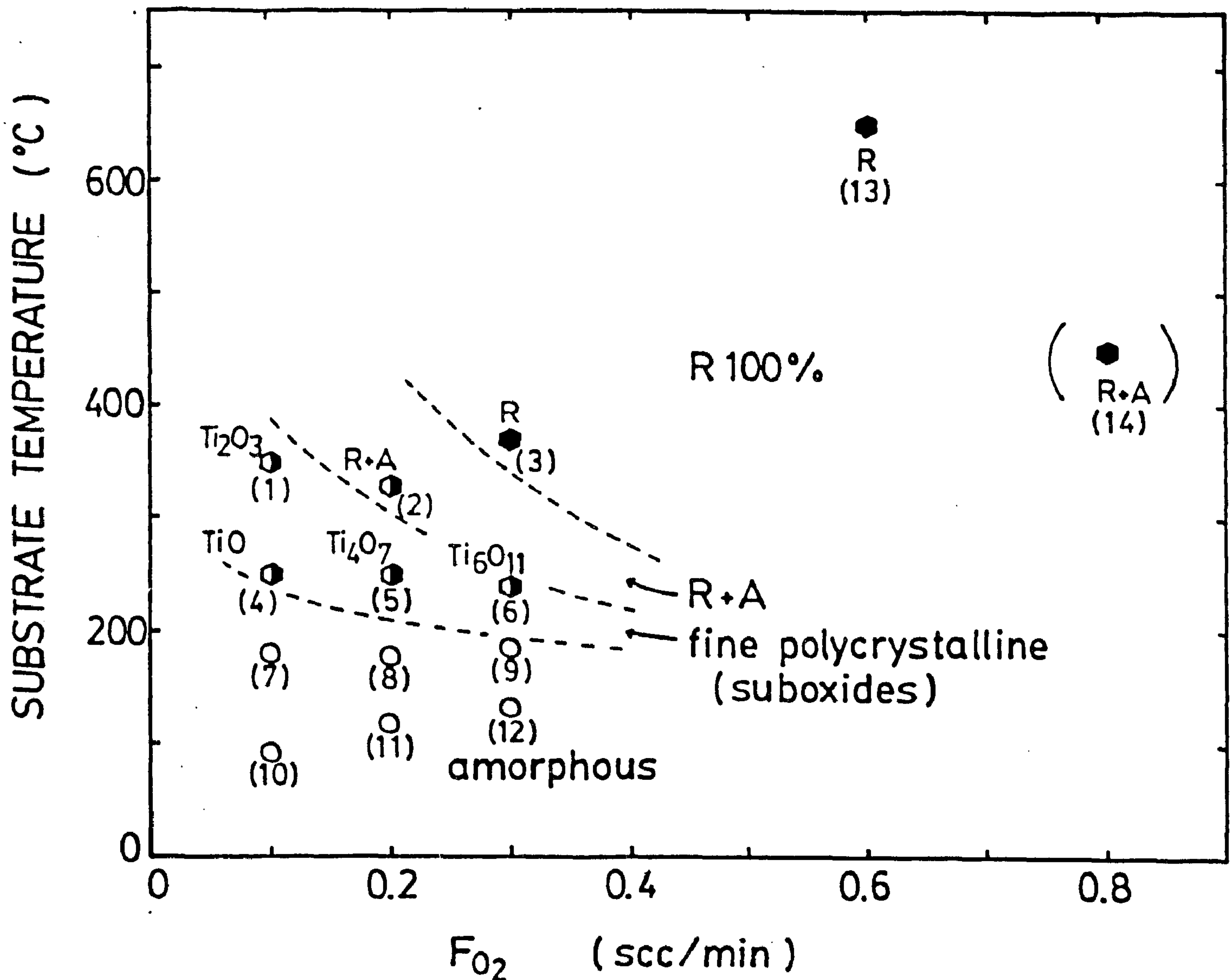

Figure 3.5 "Metastable phase diagram" for TiO_x thin films fabricated at different substrate temperature (T_s) and oxygen gas flow rate (F_{O_2}): ○-amorphous ◐-fine polycrystalline and ⬢-fully crystalline; R-rutile, A-anatase and a-amorphous. Samples (1)-(13) were fabricated with 70 m Torr Ar partial pressure and Sample (14) was deposited with 130 m Torr Ar partial pressure.

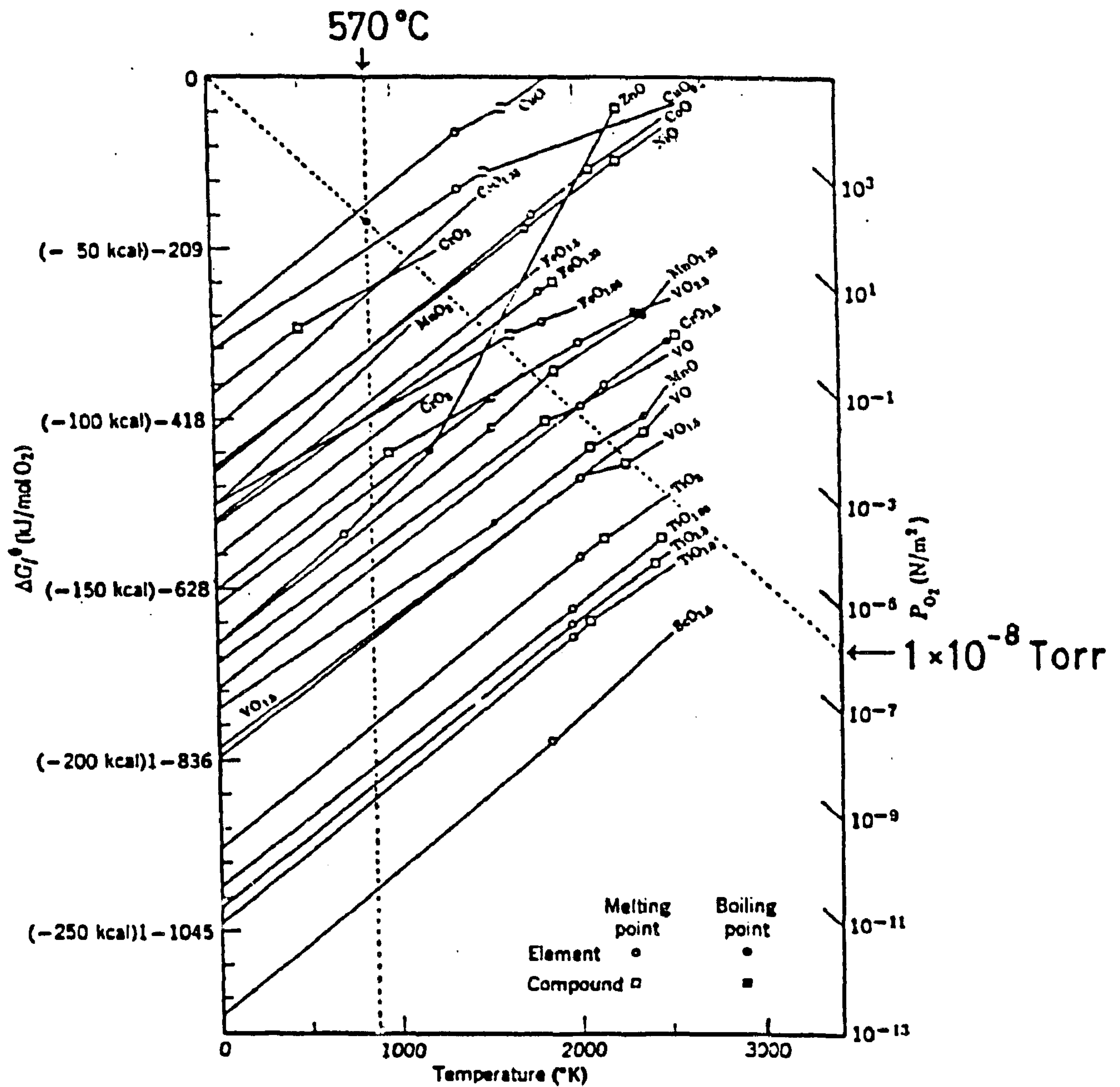

Figure 3.6 Free energy of formation per mole of oxygen as a function of temperature (95).

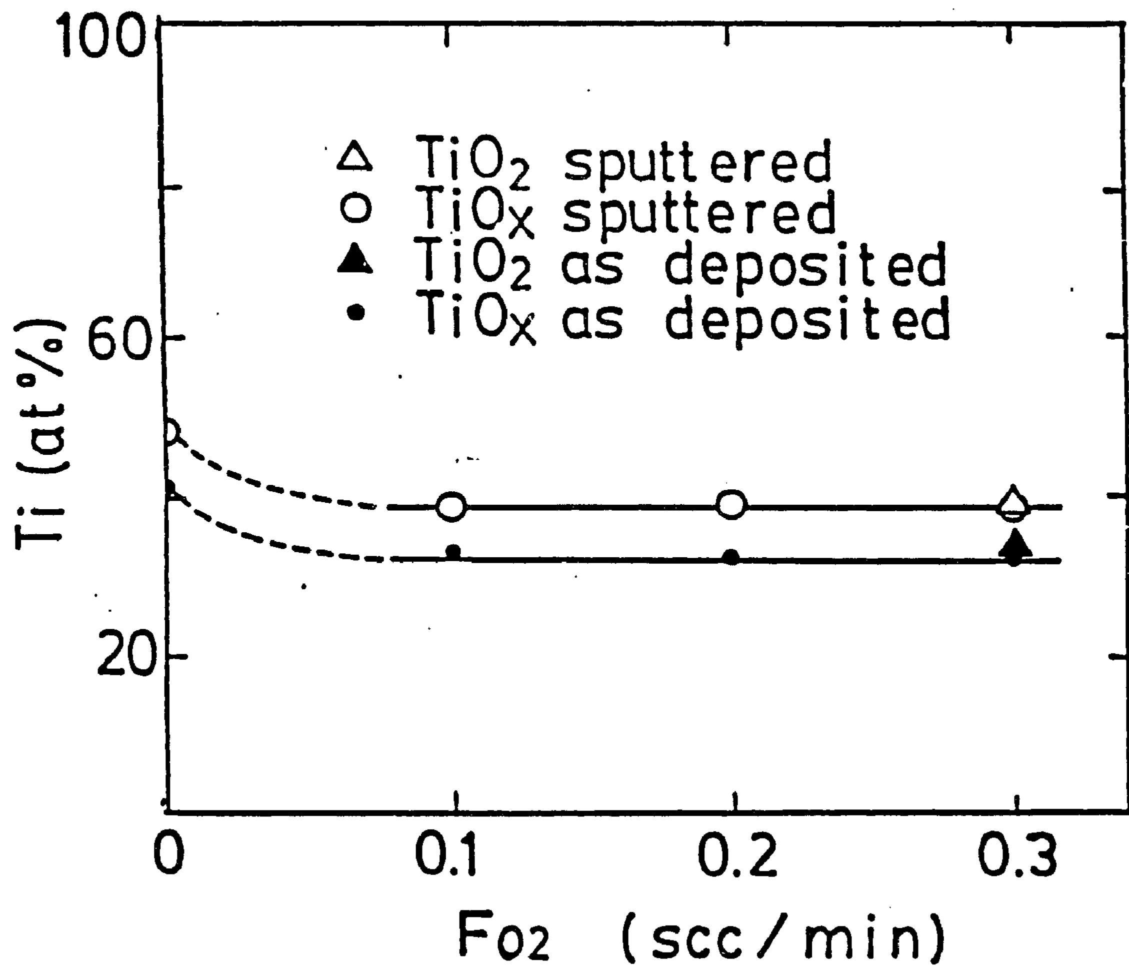

Figure 3.7 Ti concentration with respect to oxygen gas flow rate, F_{O2}, determined bt XPS for five TiO_x thin films at their original surface (solid symbols) and 3-min. Ar^+-bombarded fresh surface (open symbols).

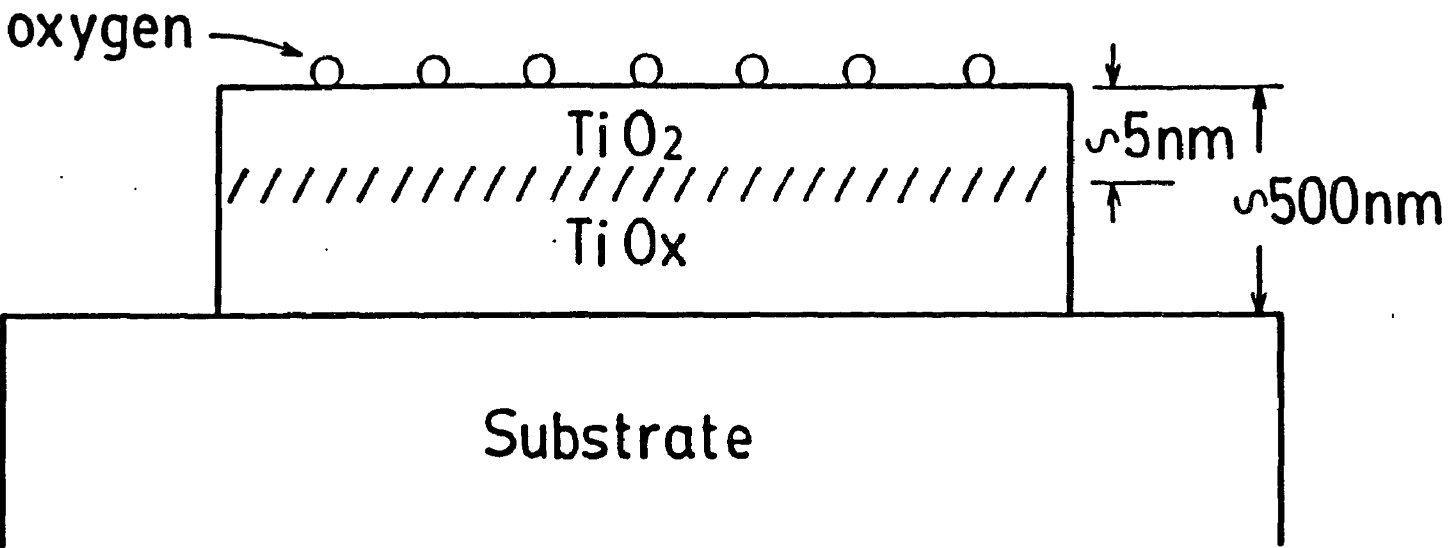

Figure 3.8 Schematic diagram of composition distribution in the cross section of TiO_2 thin film samples.

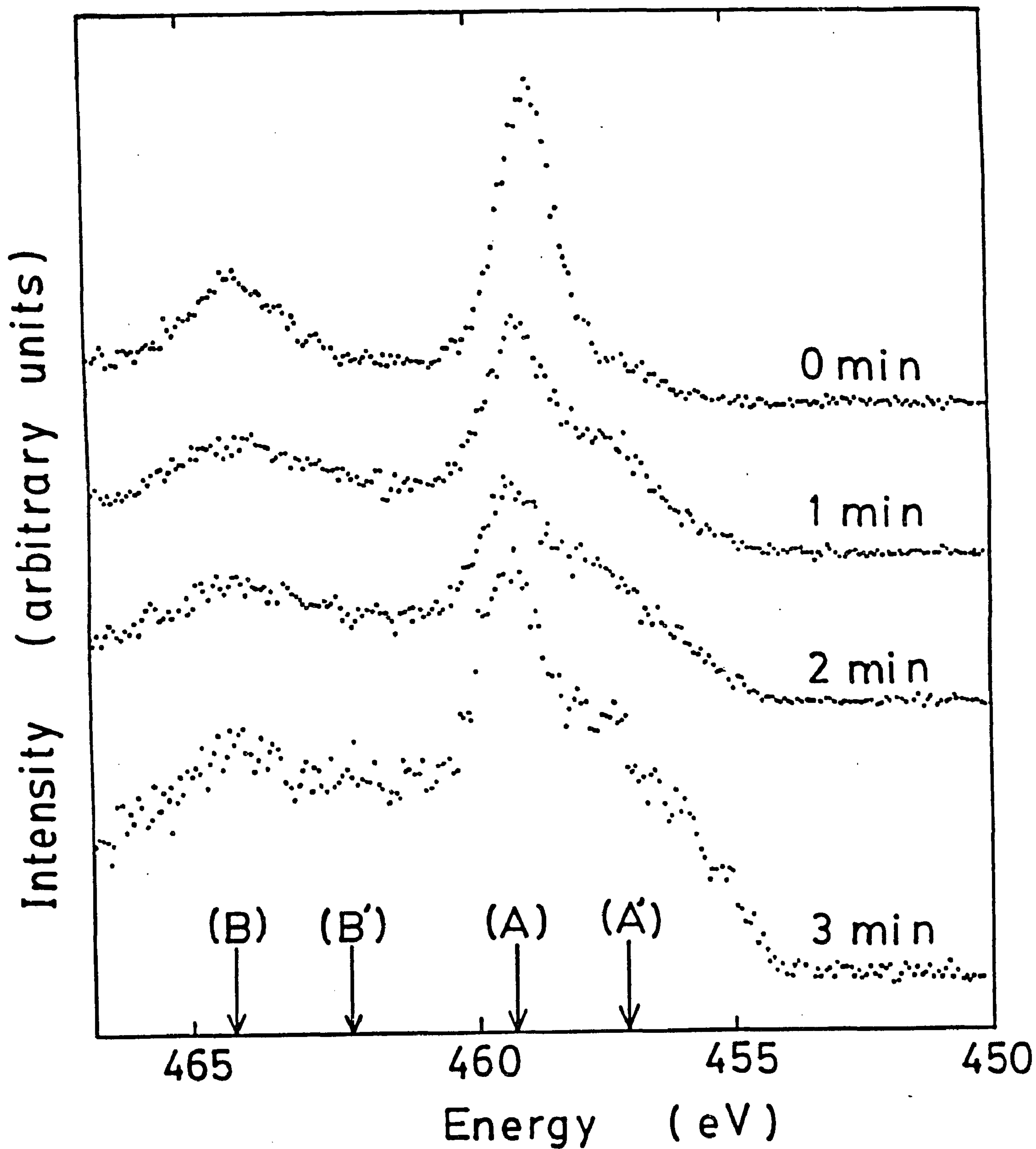

Figure 3.9 Narrow-range XPS spectra from TiO_2 after 0, 1, 2 and 3 minutes Ar^+ ion sputtering.

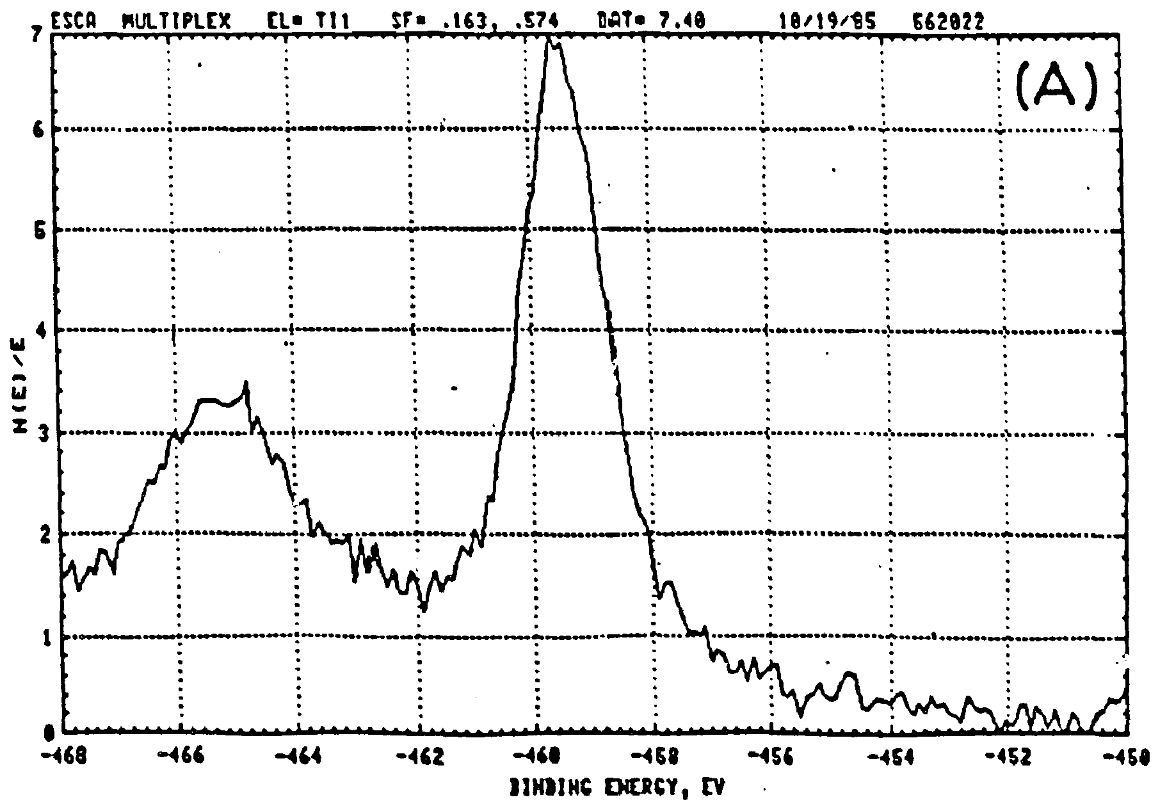

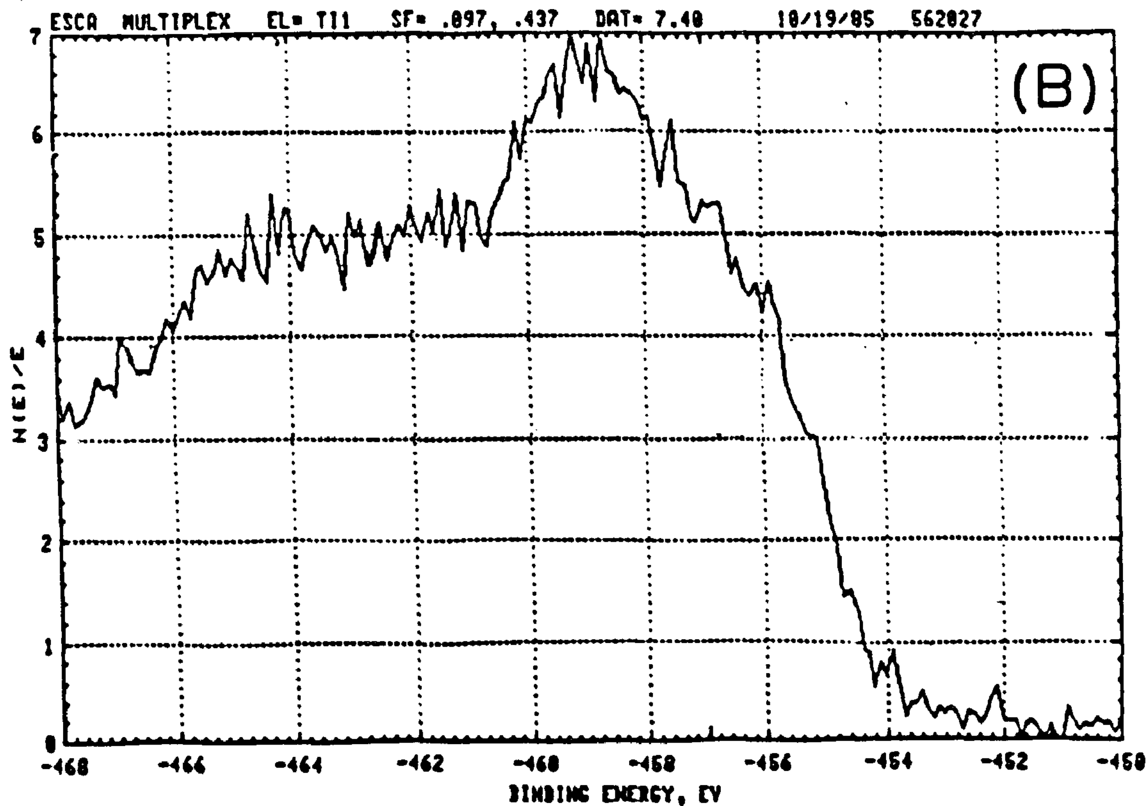

Figure 3.10 Typical narrow-range XPS spectra of (A) as-deposited TiO_x and (B) TiO_x after surface layer of ~100Å removed.

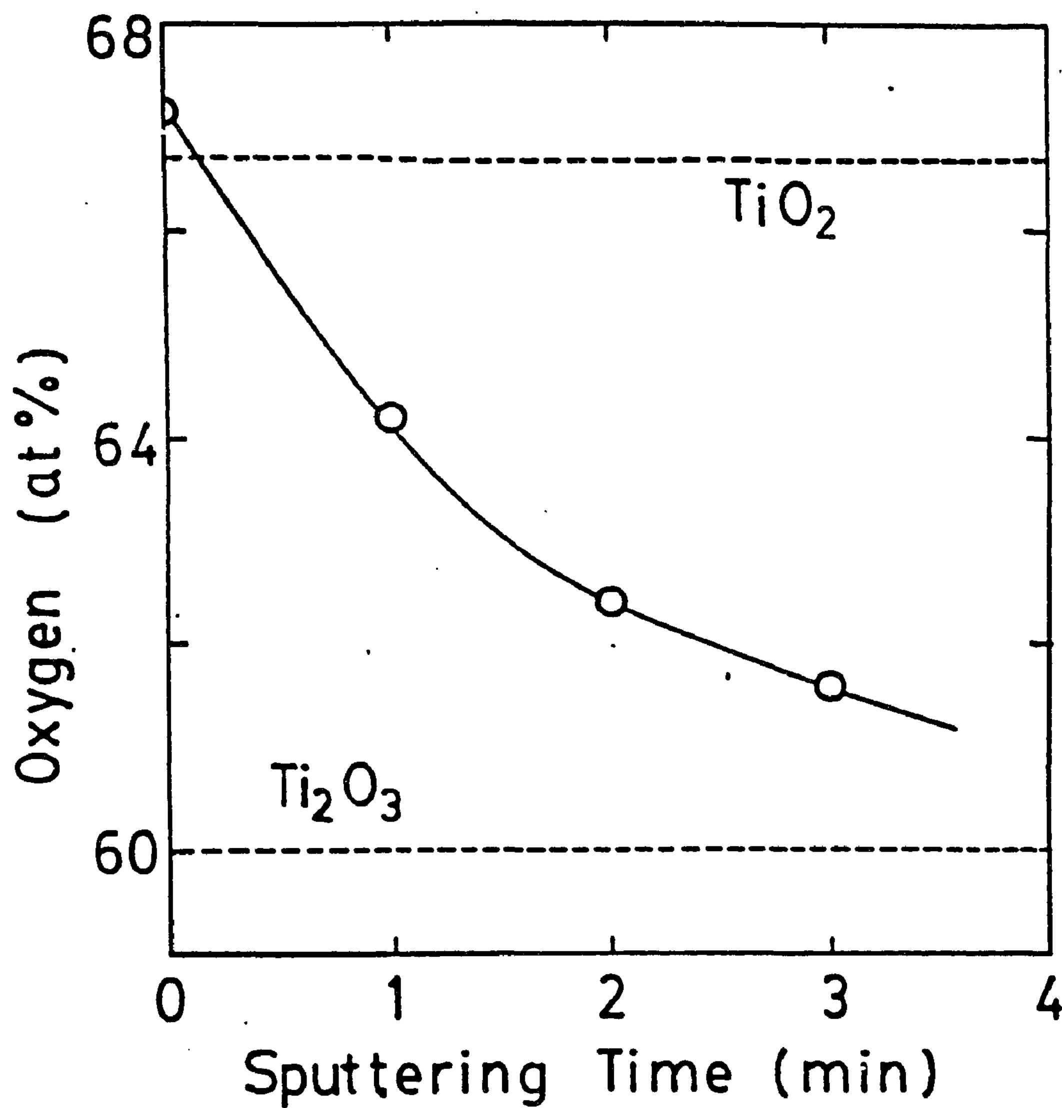

Figure 3.11 Oxygen concentration profile of TiO_2 thin film as Ar^+ sputtering continues.

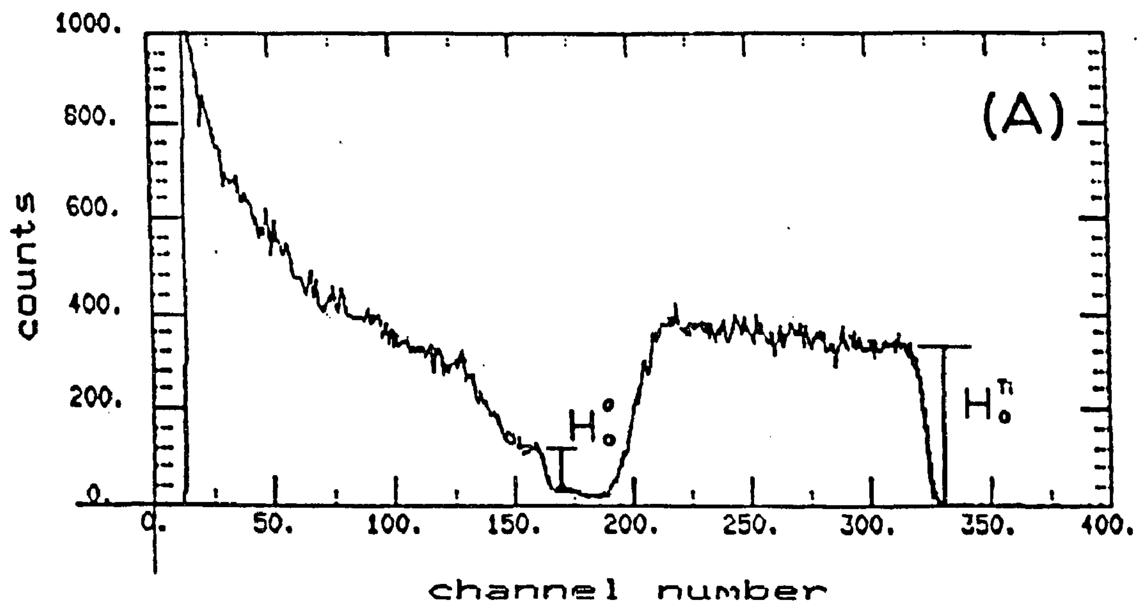

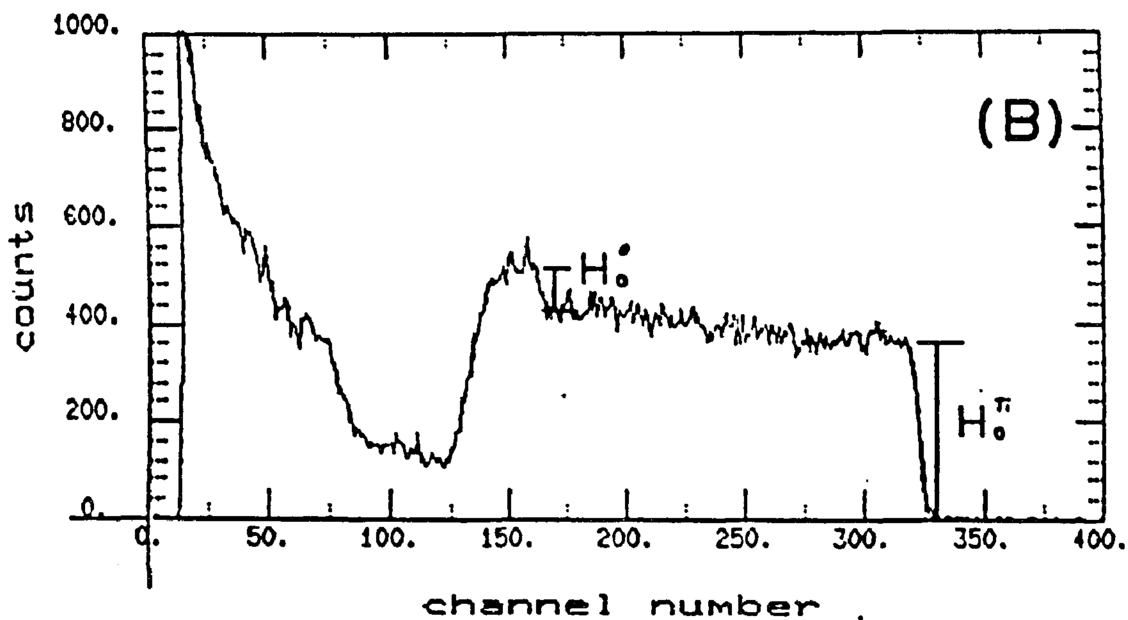

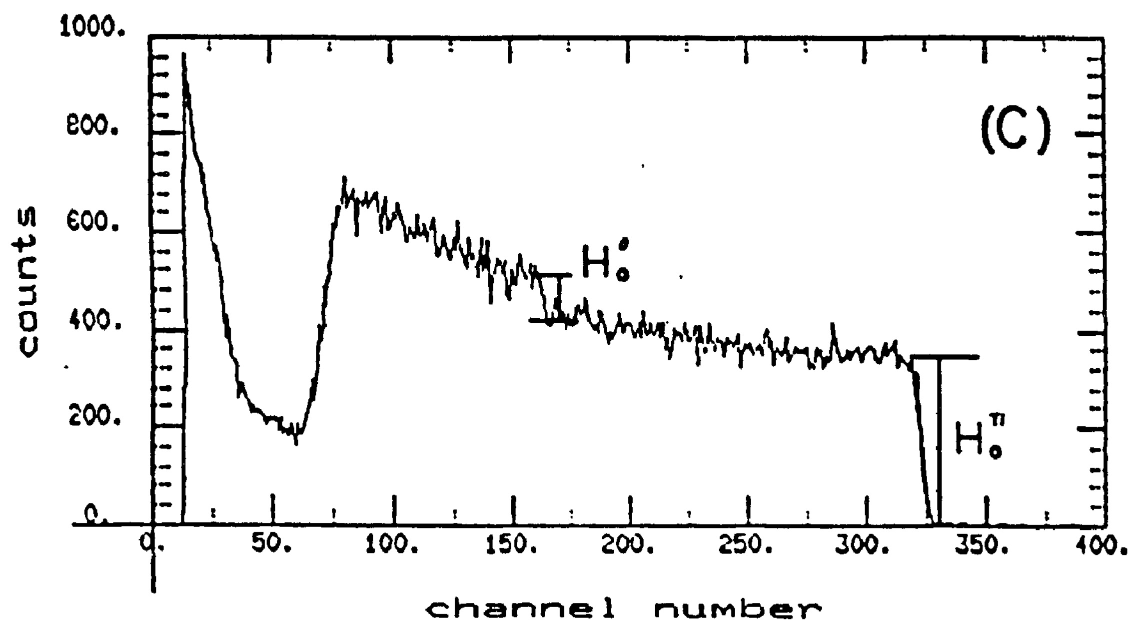

Figure 3.12 Rutherford backscattering spectra of (A) Samples (1), (B) Sample (3) and (C) Sample (4) using 2.0 MeV He ions incident.

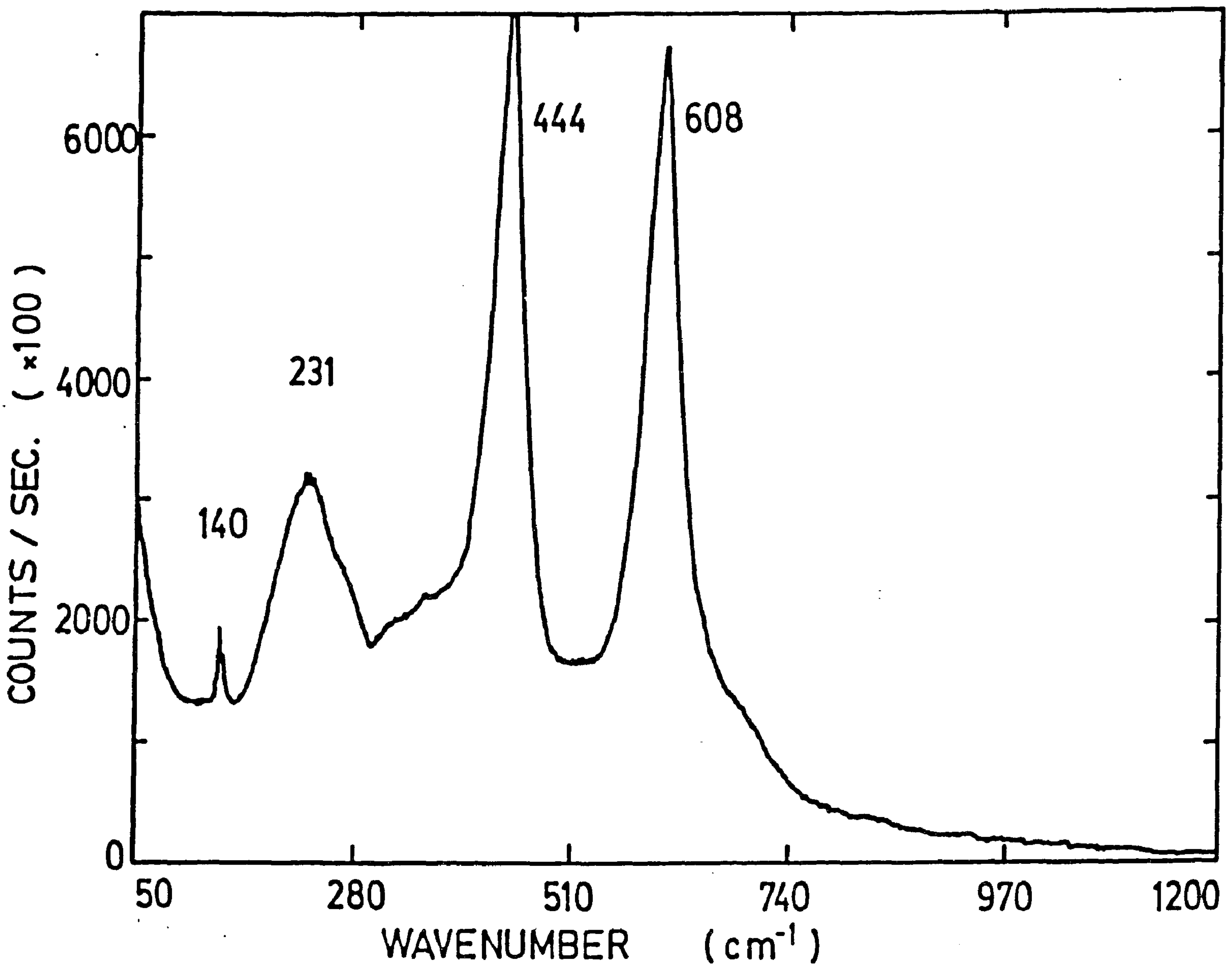

Figure 3.13 Raman spectrum of rutile granules purchased from Cerac.

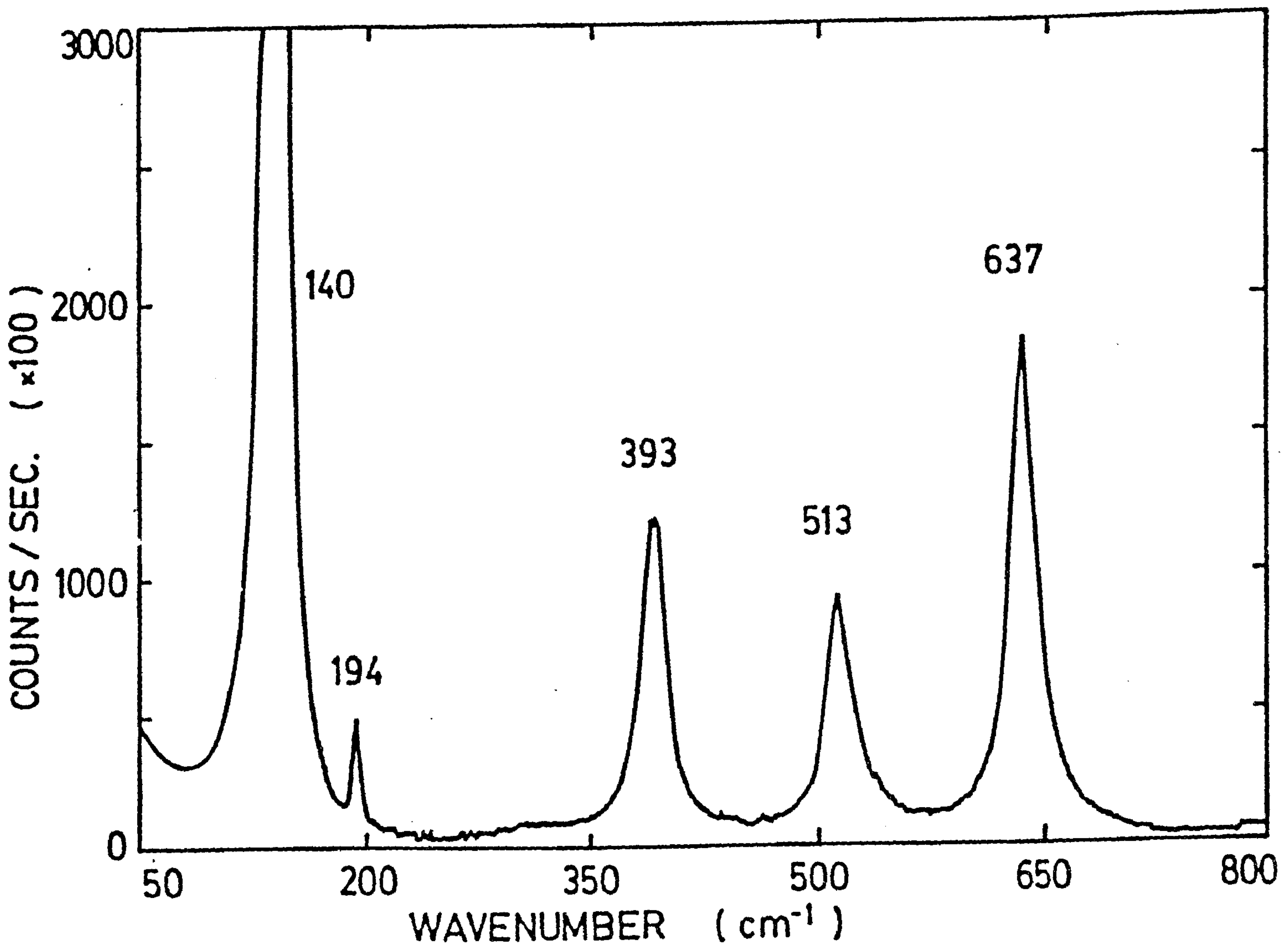

Figure 3.14 Raman spectrum of anatase granules purchased from Cerac.

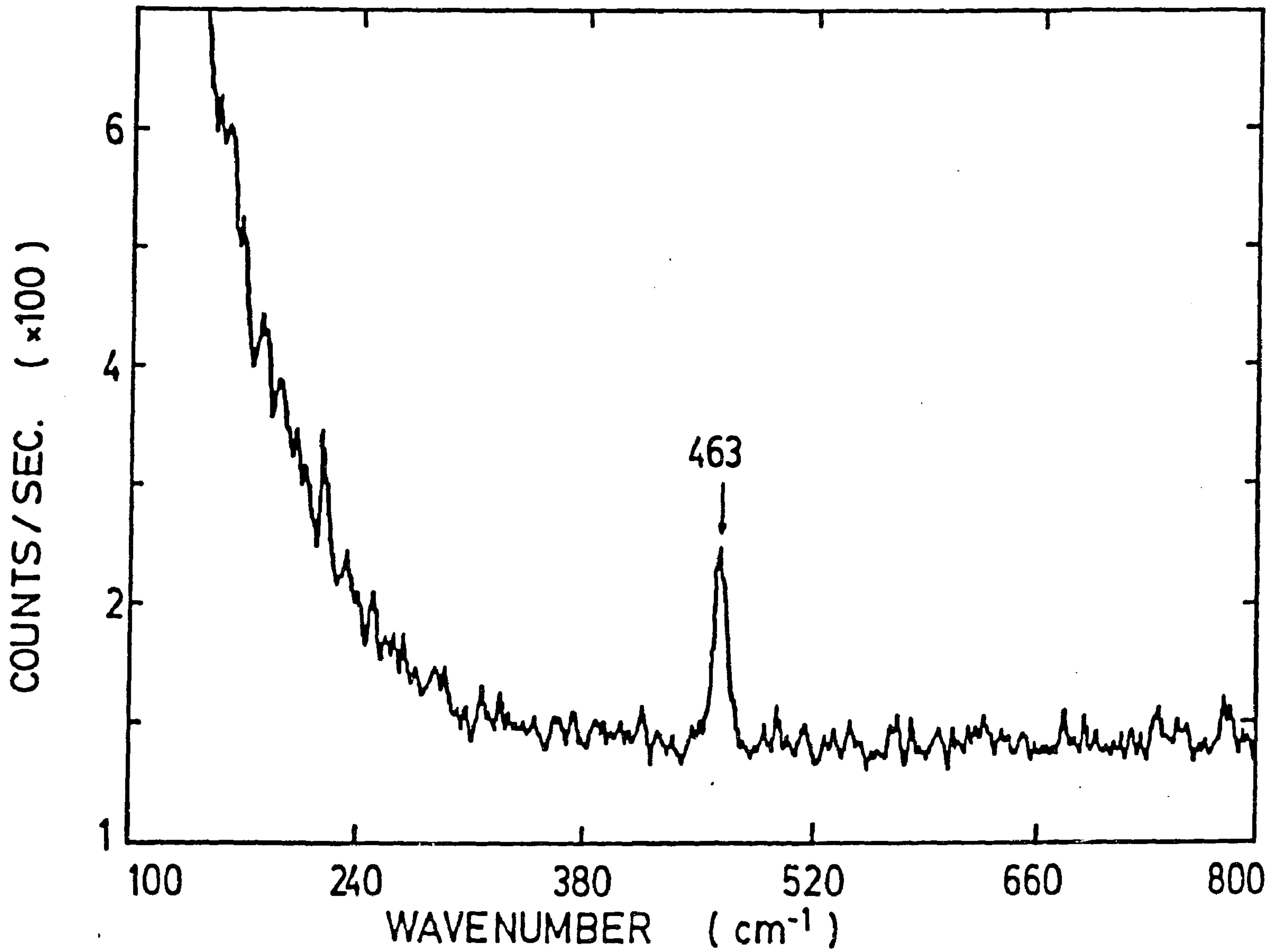

Figure 3.15 Raman spectrum of TiO granules purchased from Cerac.

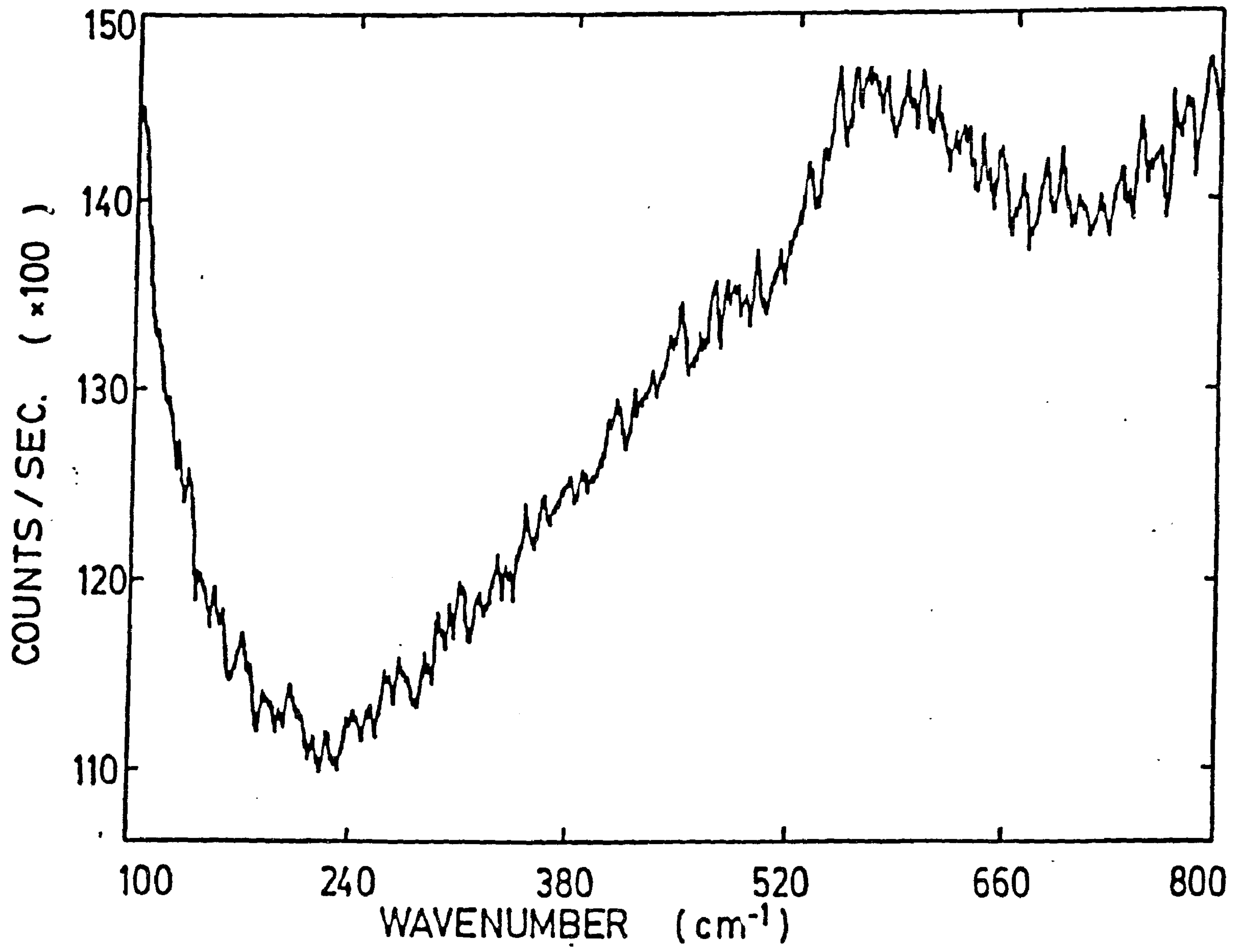

Figure 3.16 Raman spectrum of glass substrate.

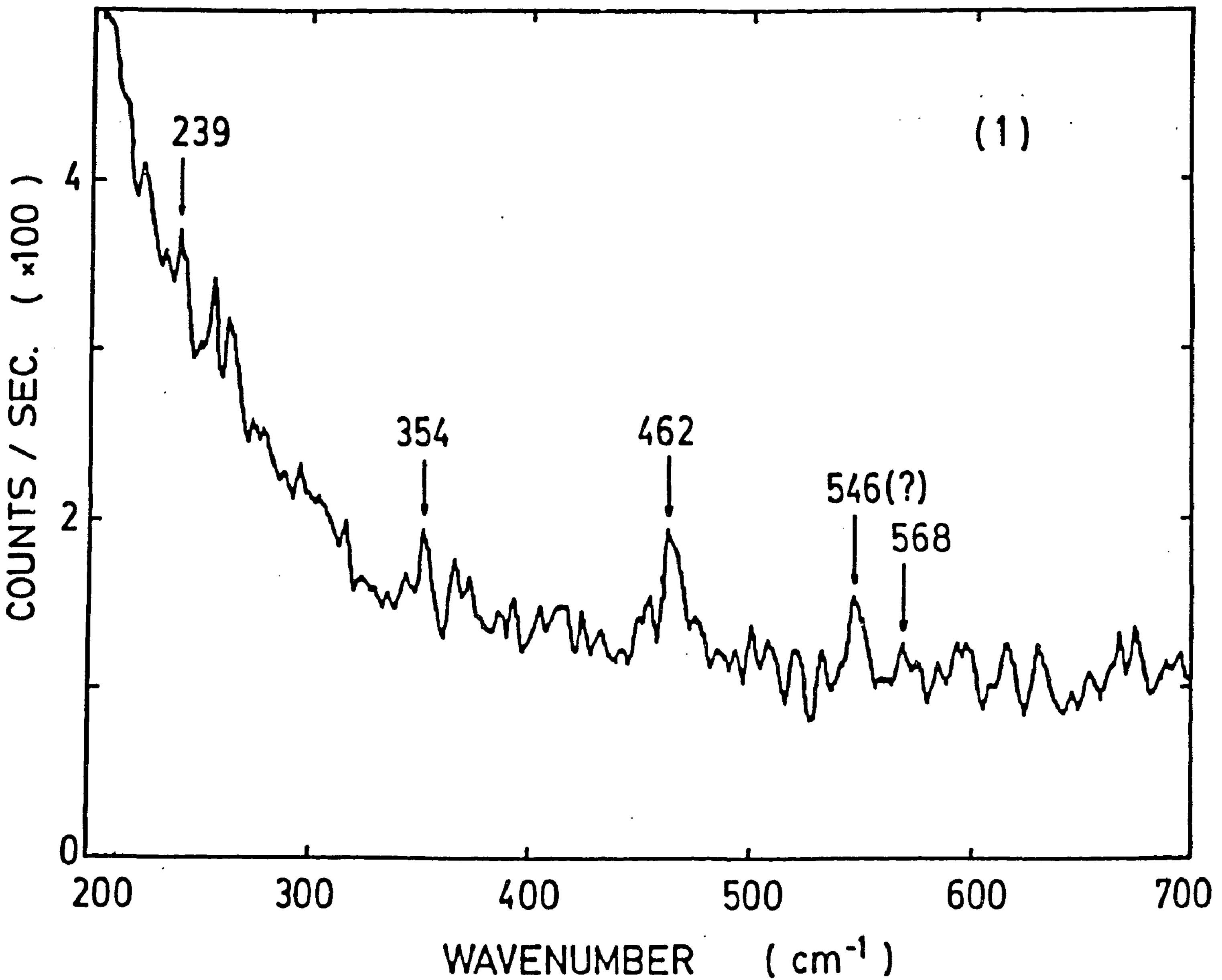

Figure 3.17 Raman spectrum of Sample (1).

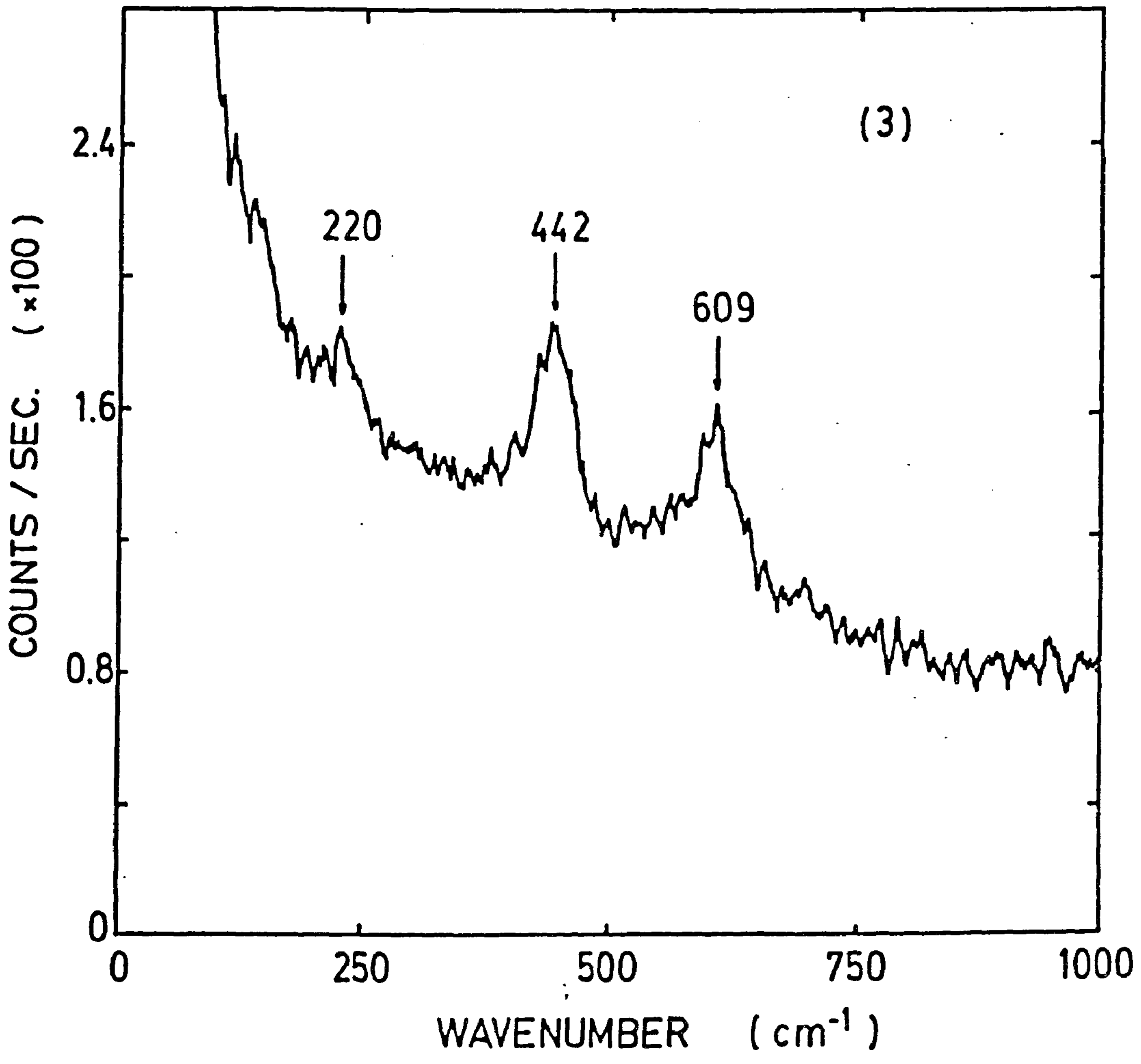

Figure 3.18 Raman spectrum of Sample (3).

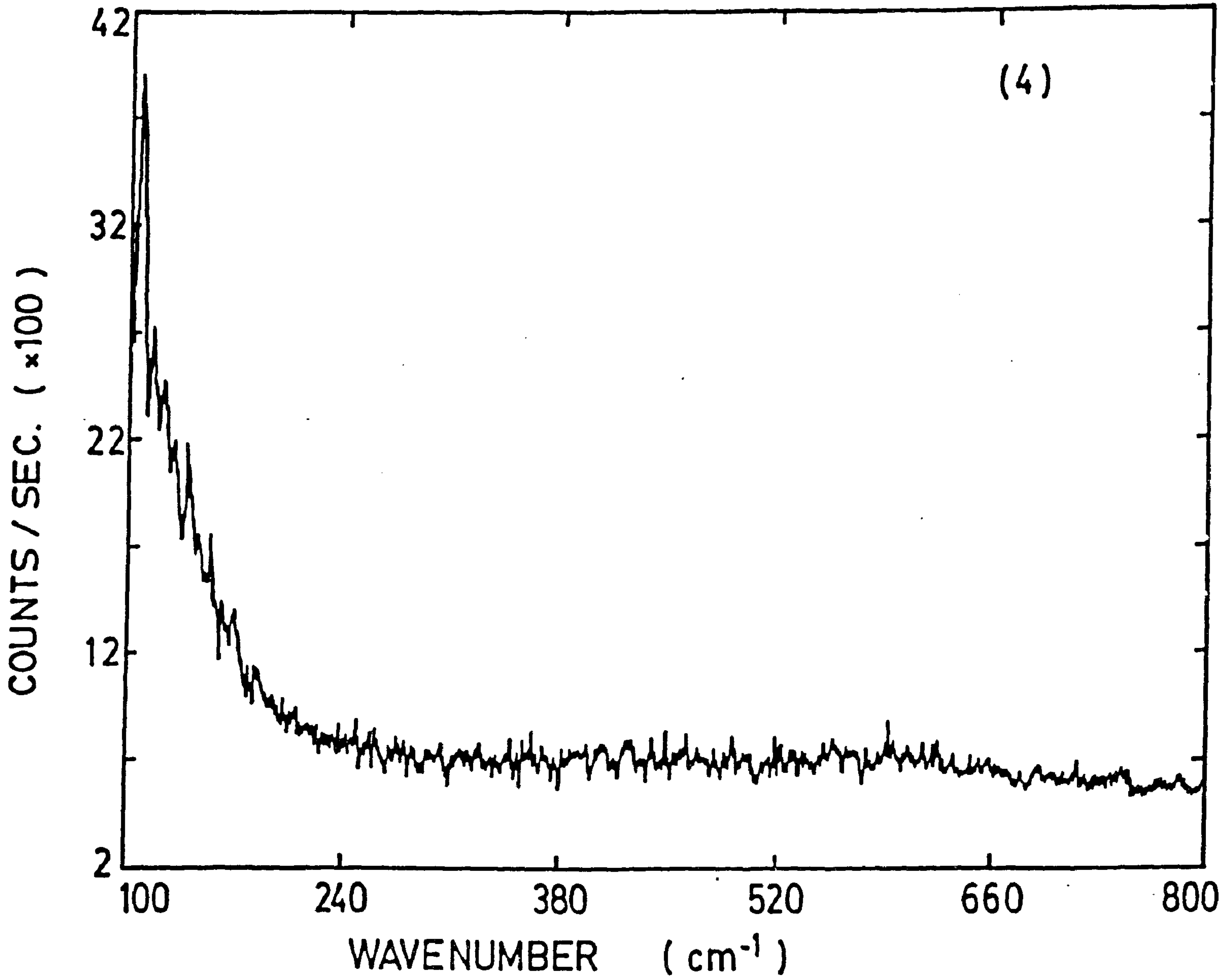

Figure 3.19 Raman spectrum of Sample (4).

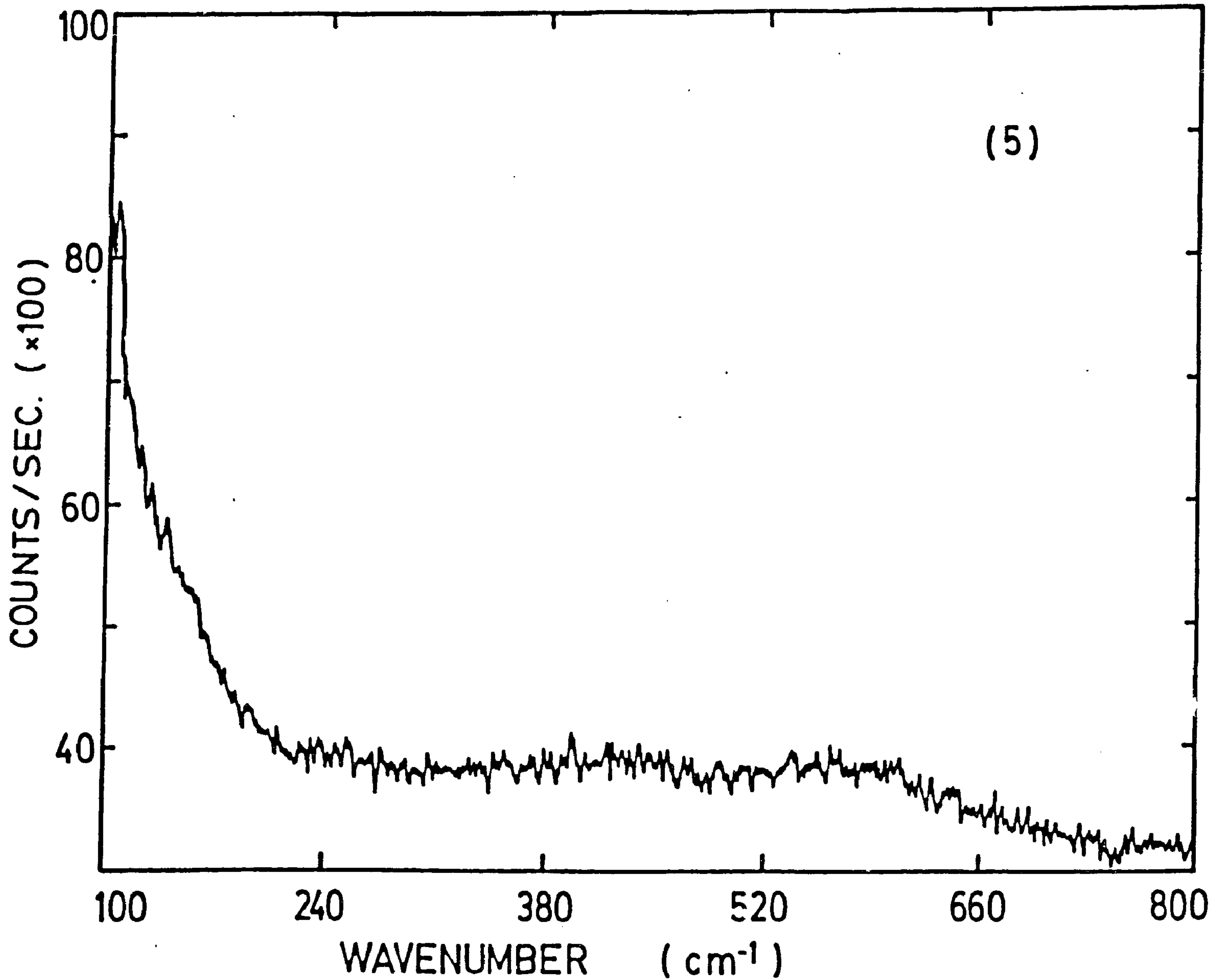

Figure 3.20 Raman spectrum of Sample (5).

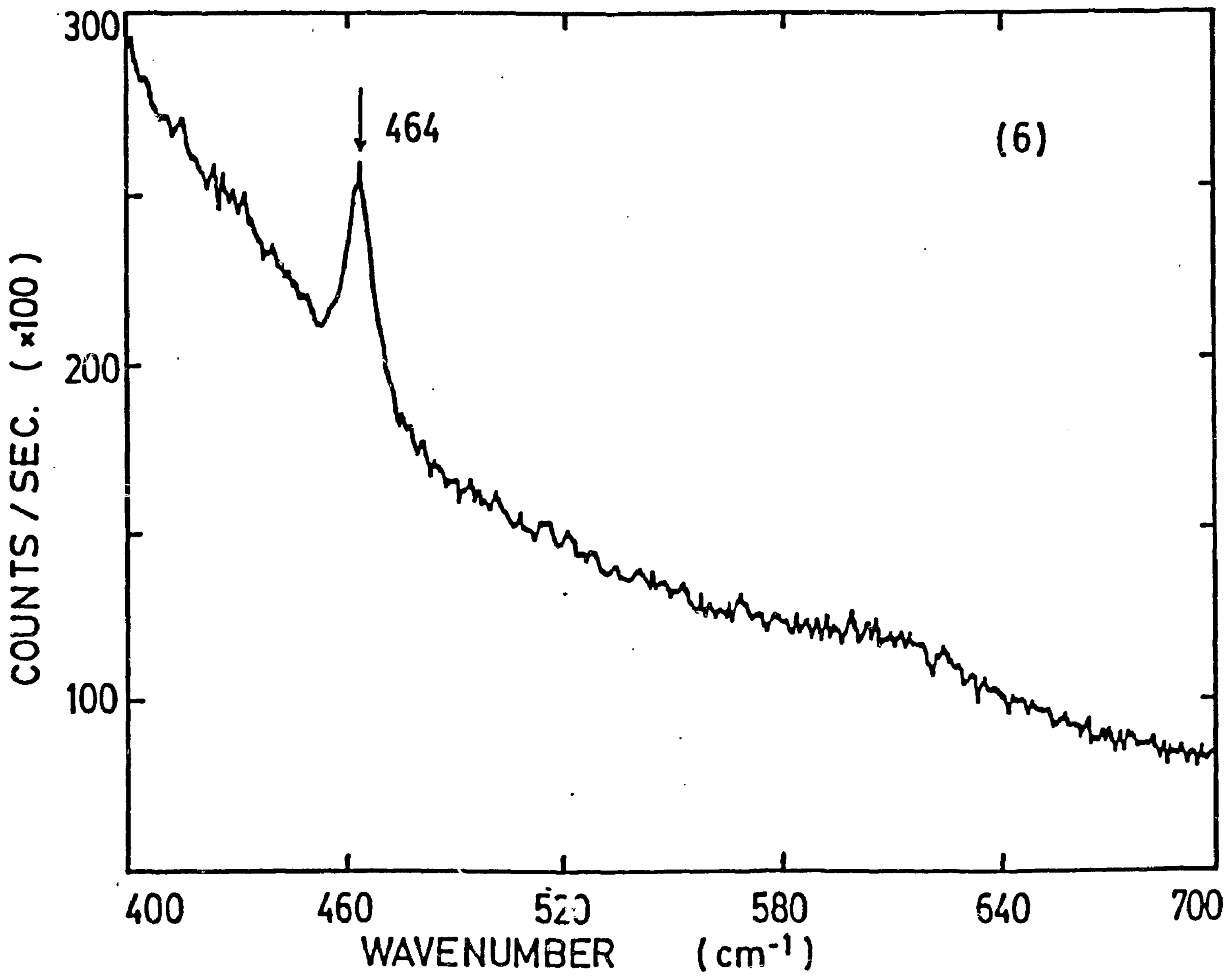

Figure 3.21 Raman spectrum of Sample (6).

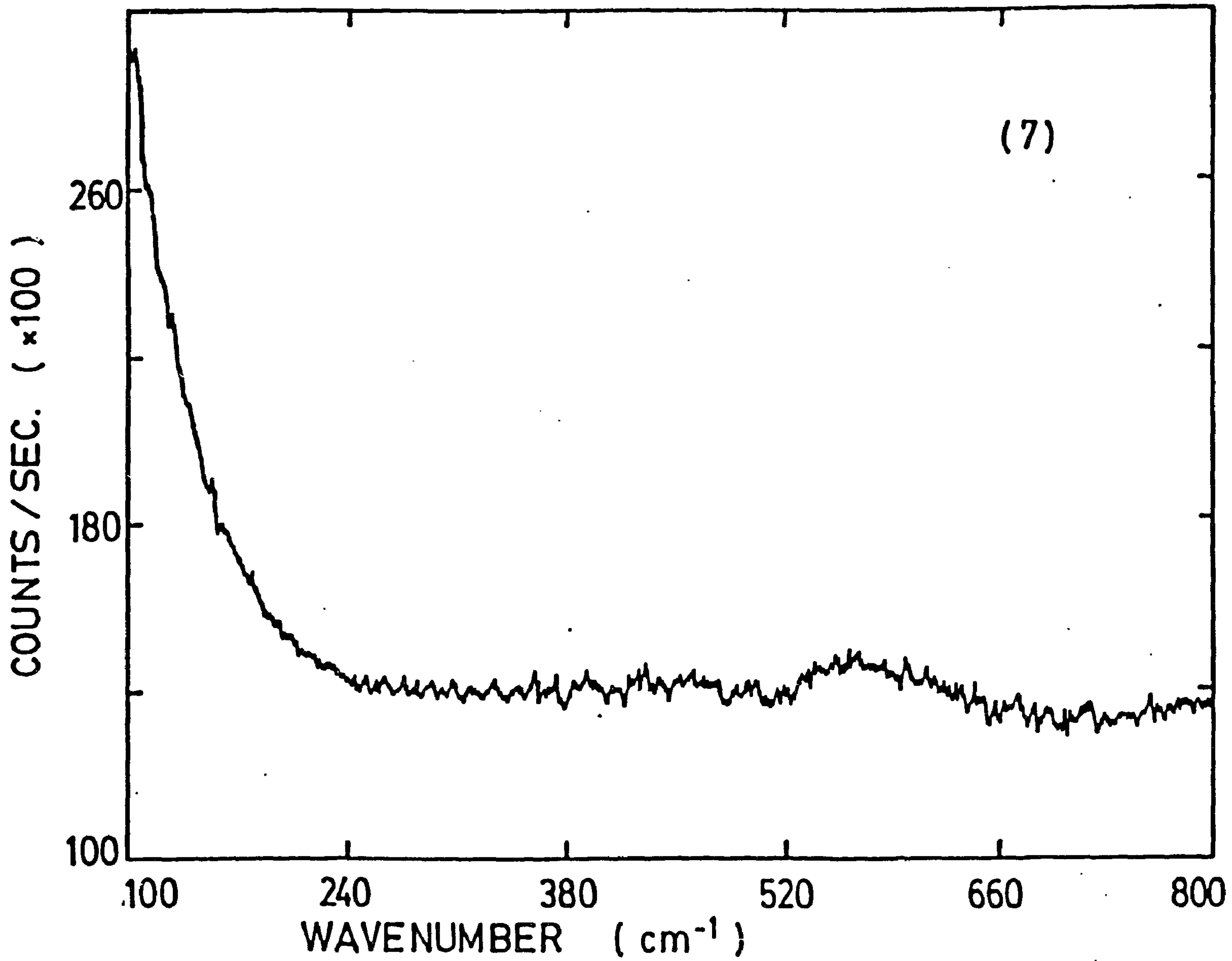

Figure 3.22 Raman spectrum of Sample (7).

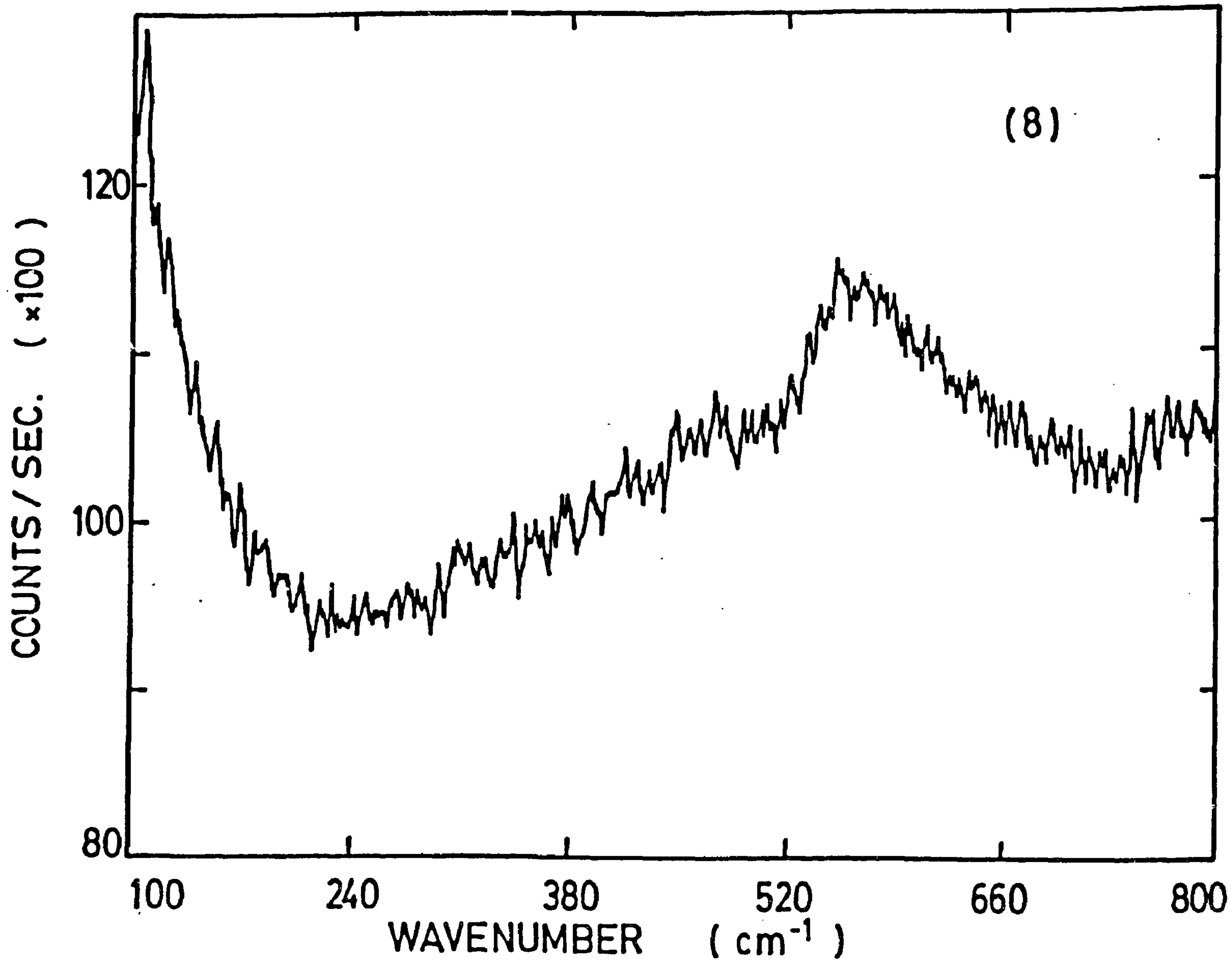

Figure 3.23 Raman spectrum of Sample (8).

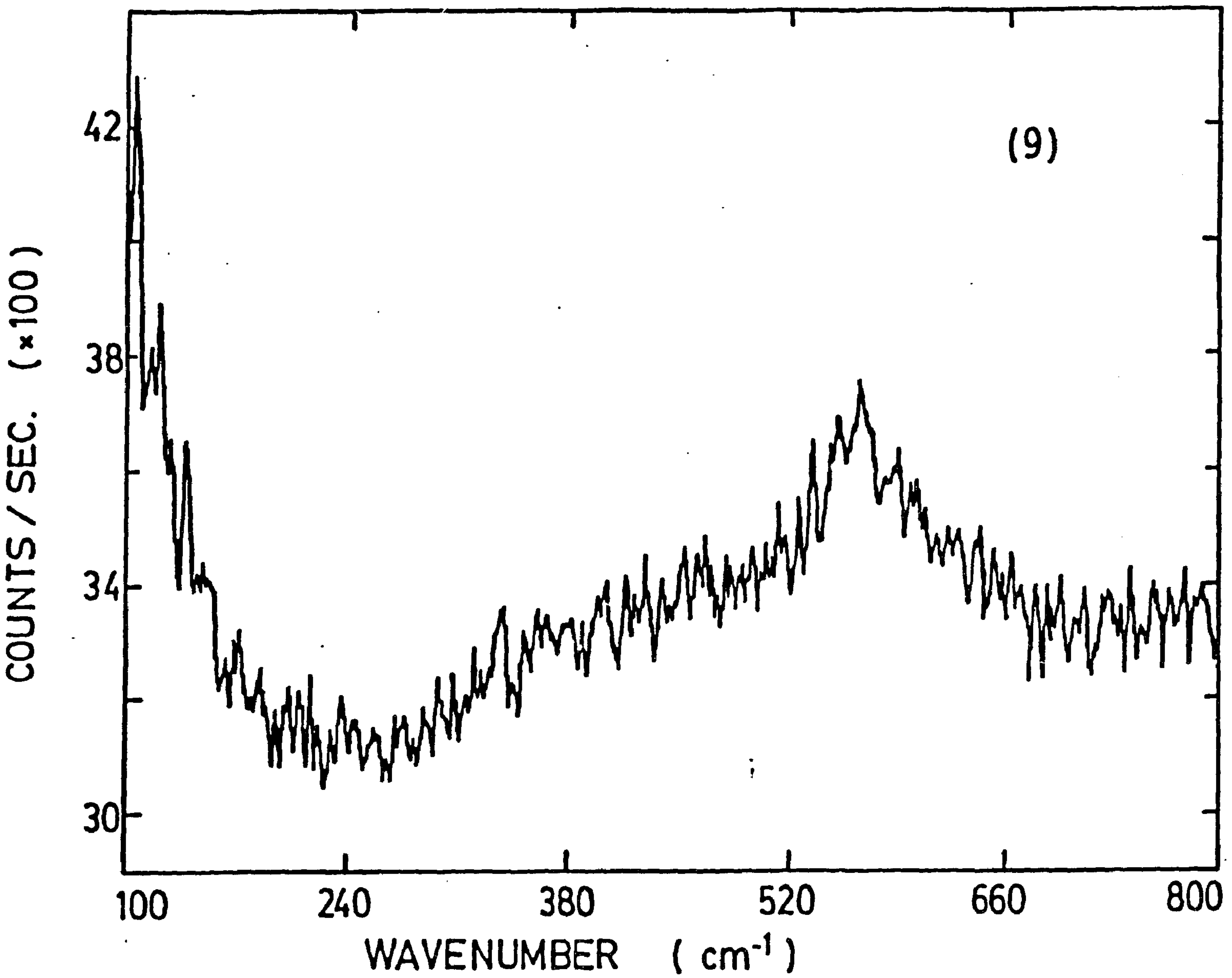

Figure 3.24 Raman spectrum of Sample (9).

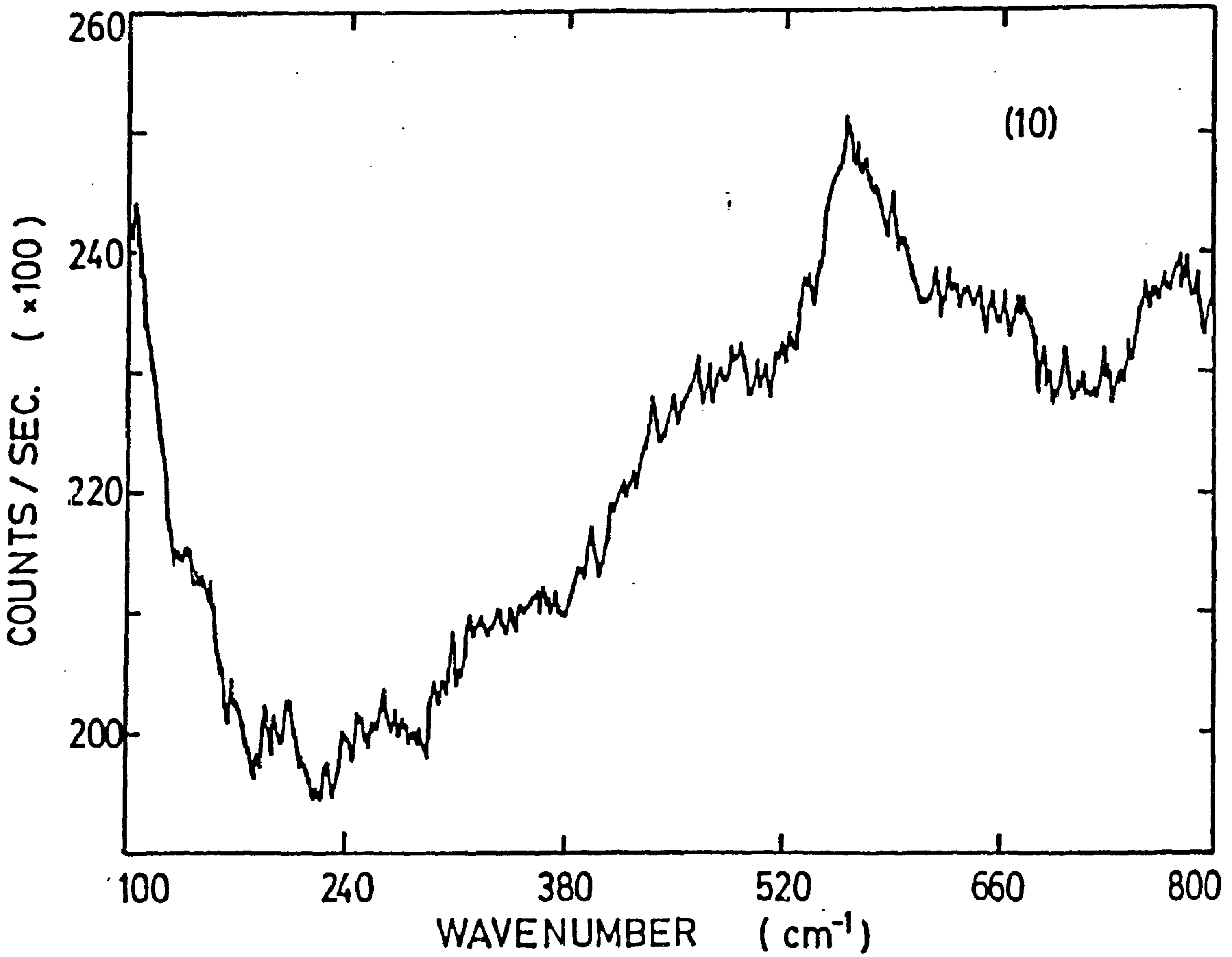

Figure 3.25 Raman spectrum of Sample (10).

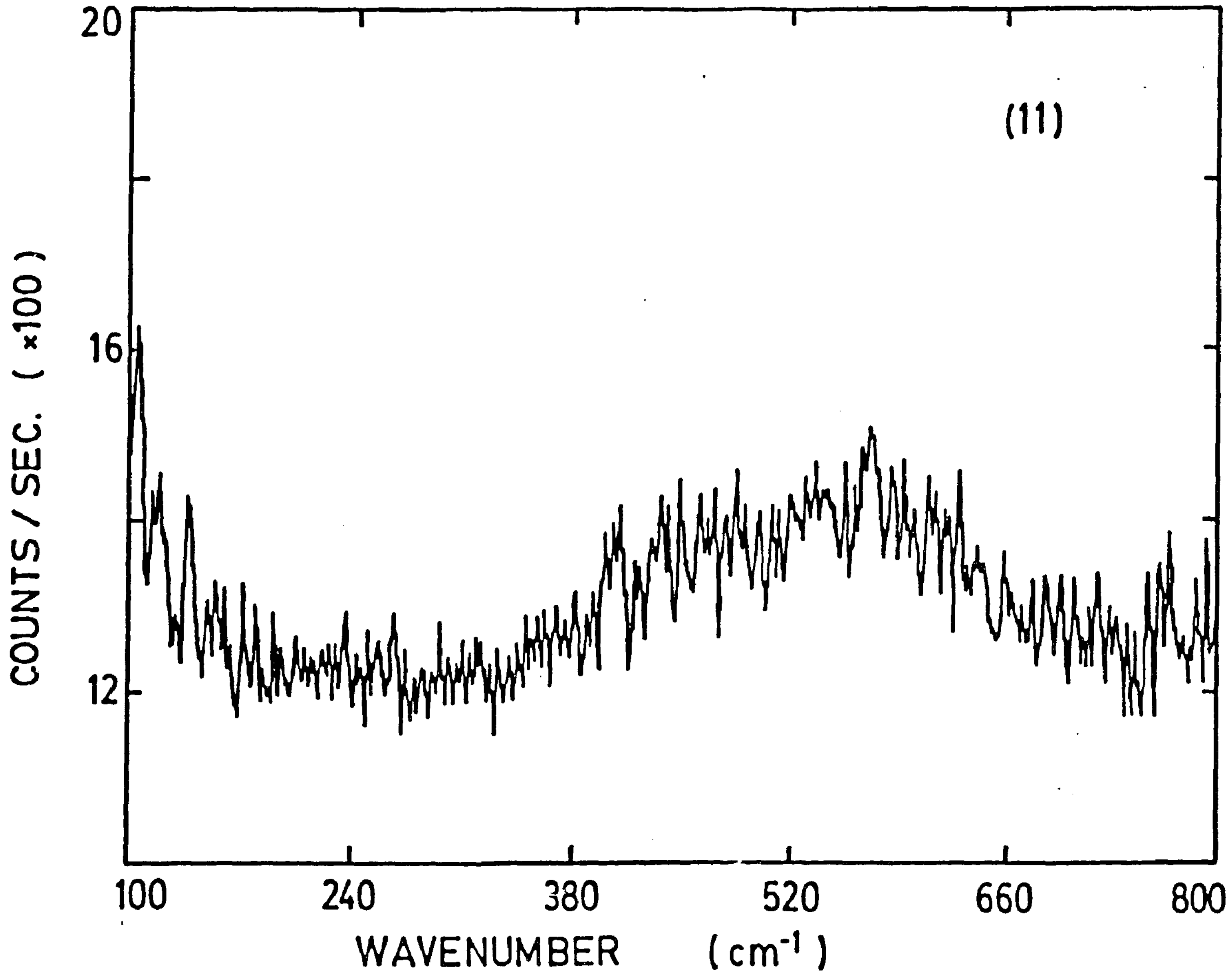

Figure 3.26 Raman spectrum of Sample (11).

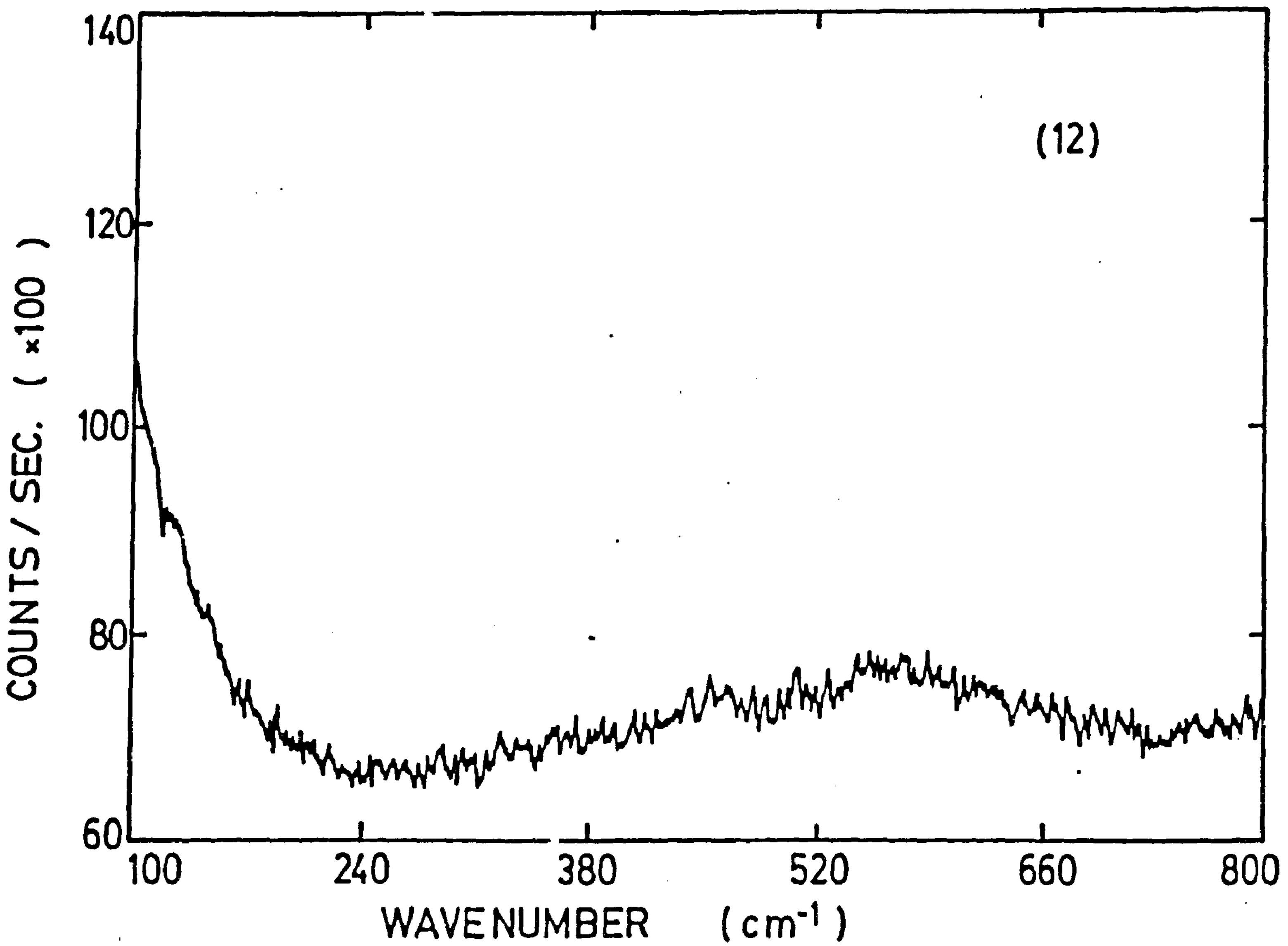

Figure 3.27 Raman spectrum of Sample (12).

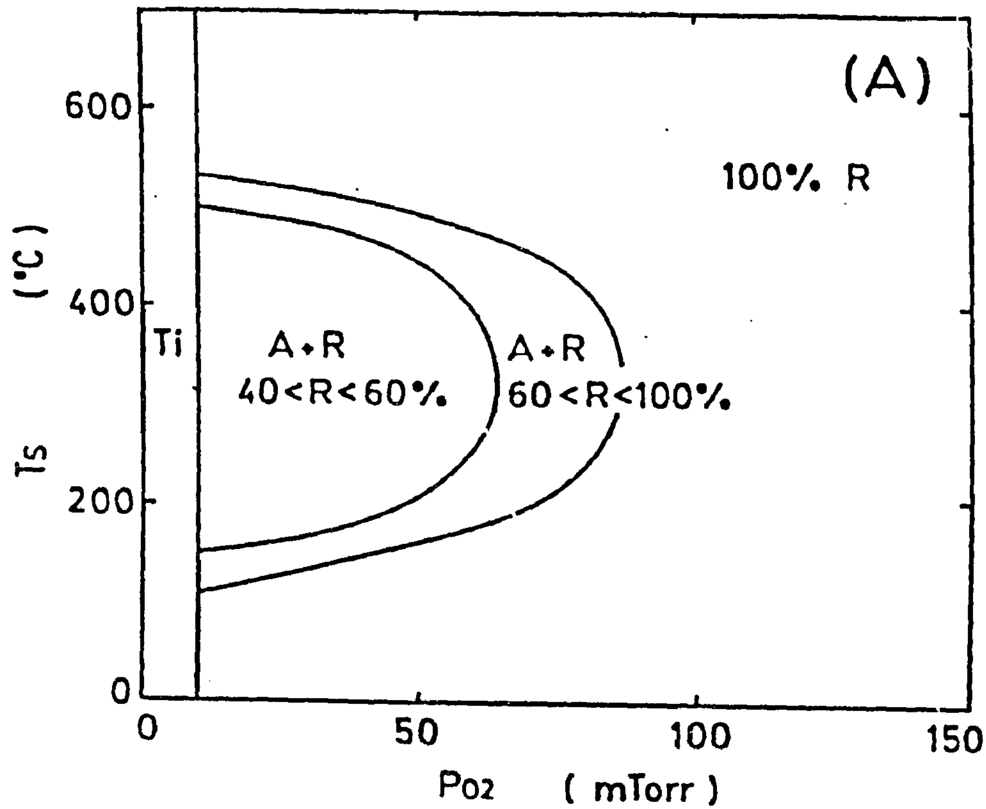

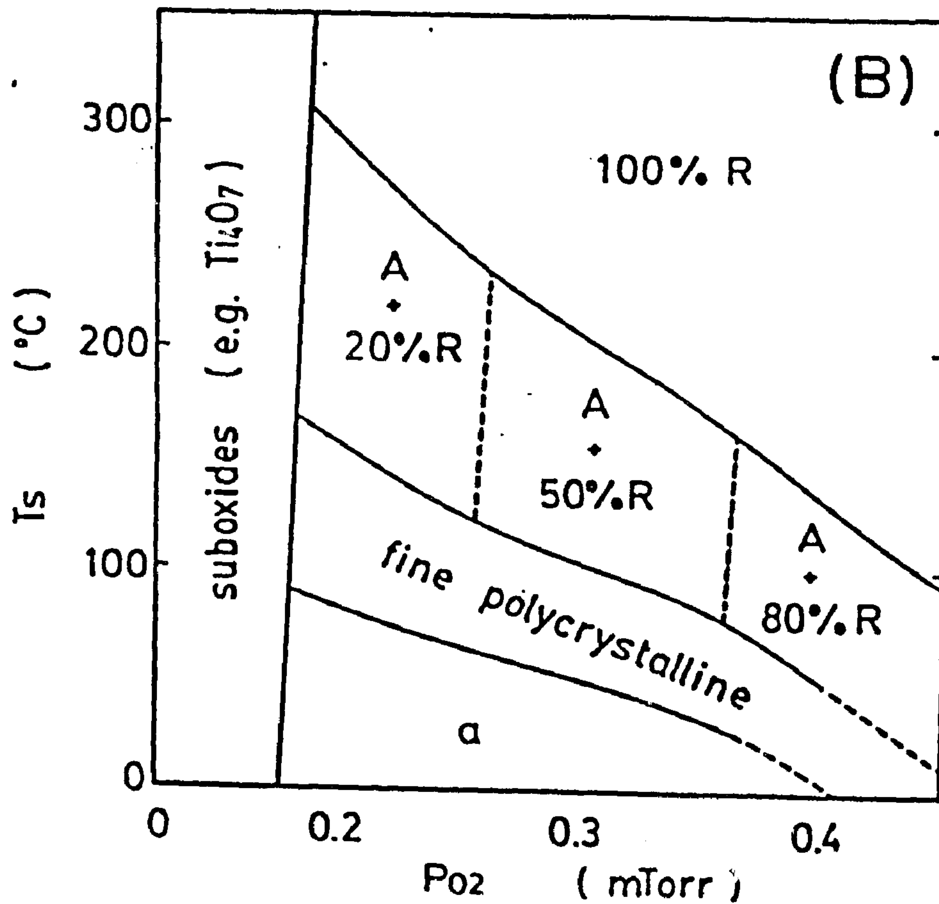

Figure 3.28 Metastable phase diagrams for samples fabricated by means of (A) an rf diode sputterring technique (6) and (B) a dc plasmatron sputtering technique (9).

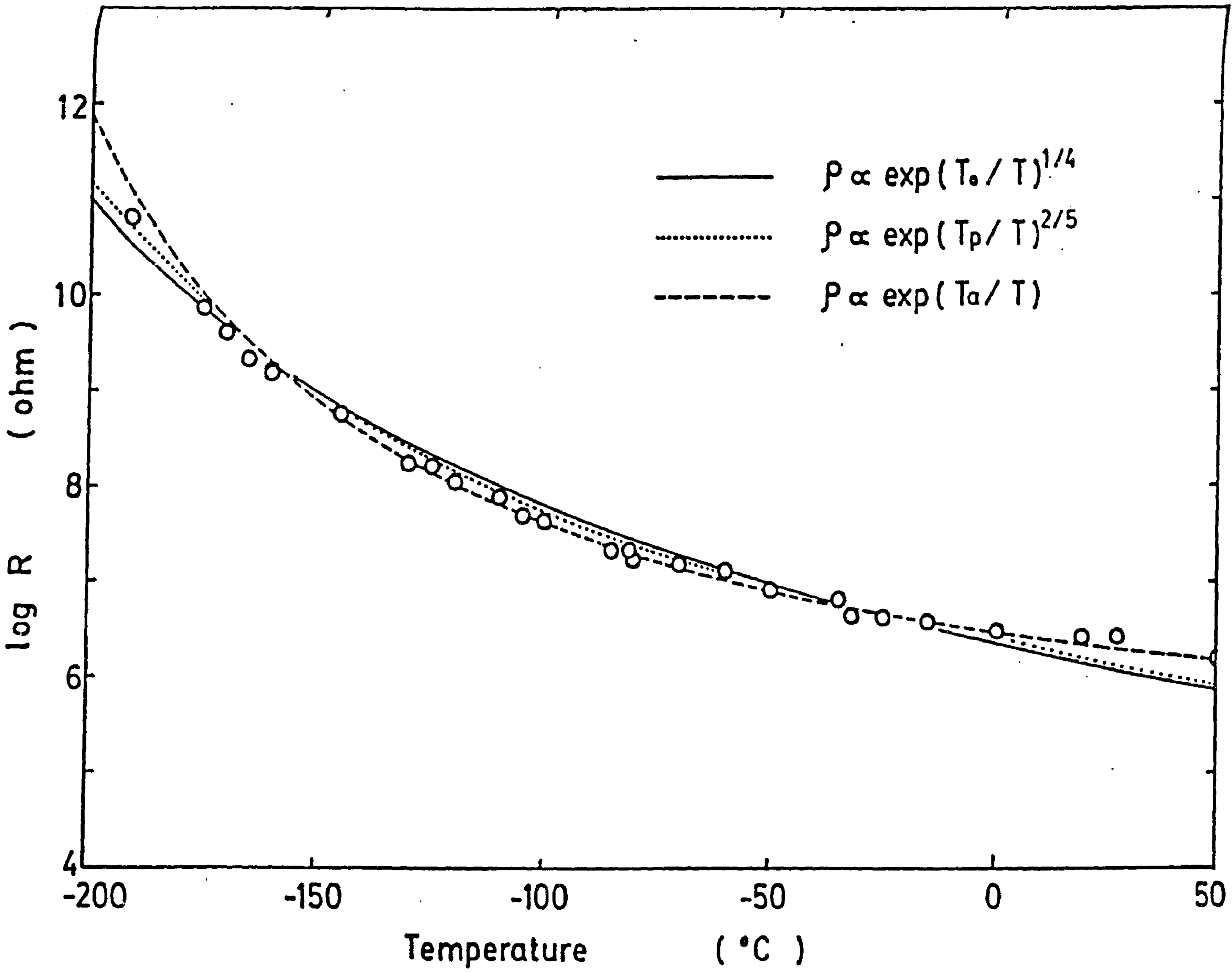

Figure 3.29 Resistivity of Sample (3) in terms of temperature. Curves are for three different electrical conduction mechanisms.

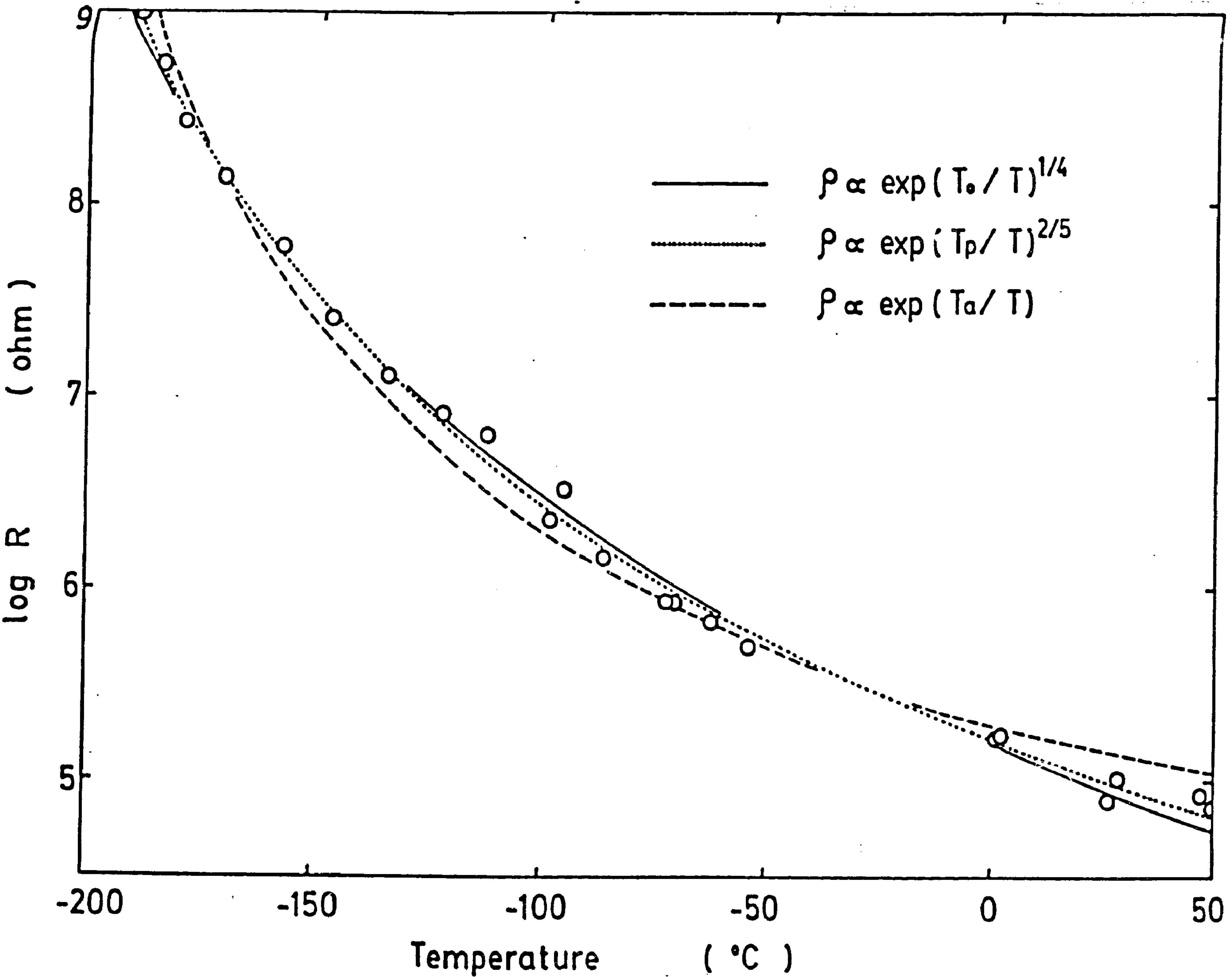

Figure 3.30 Resistivity of Sample (6) in terms of temperature. Curves are for three different electrical conduction mechanisms.

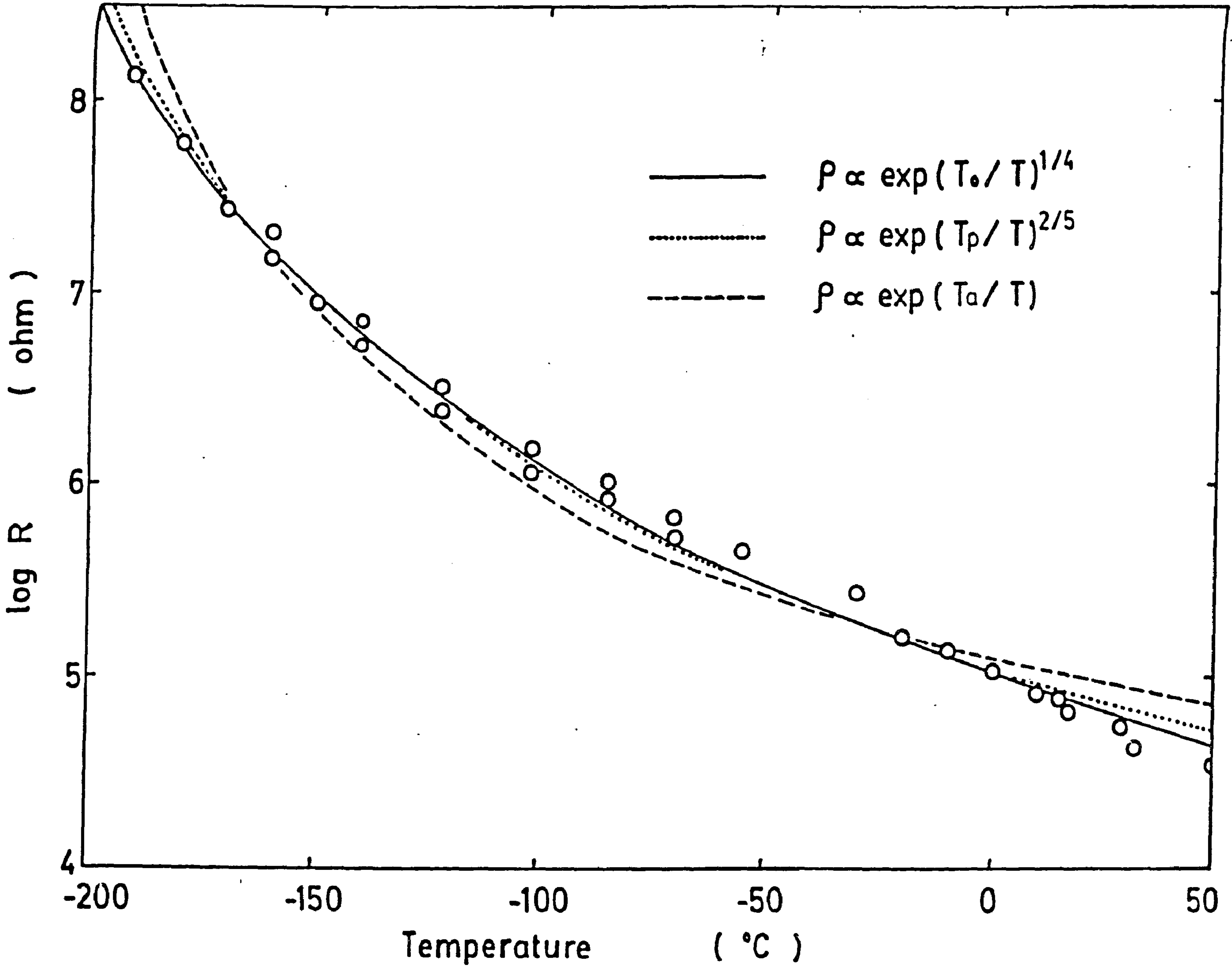

Figure 3.31 Resistivity of Sample (9) in terms of temperature. Curves are for three different electrical conduction mechanisms.

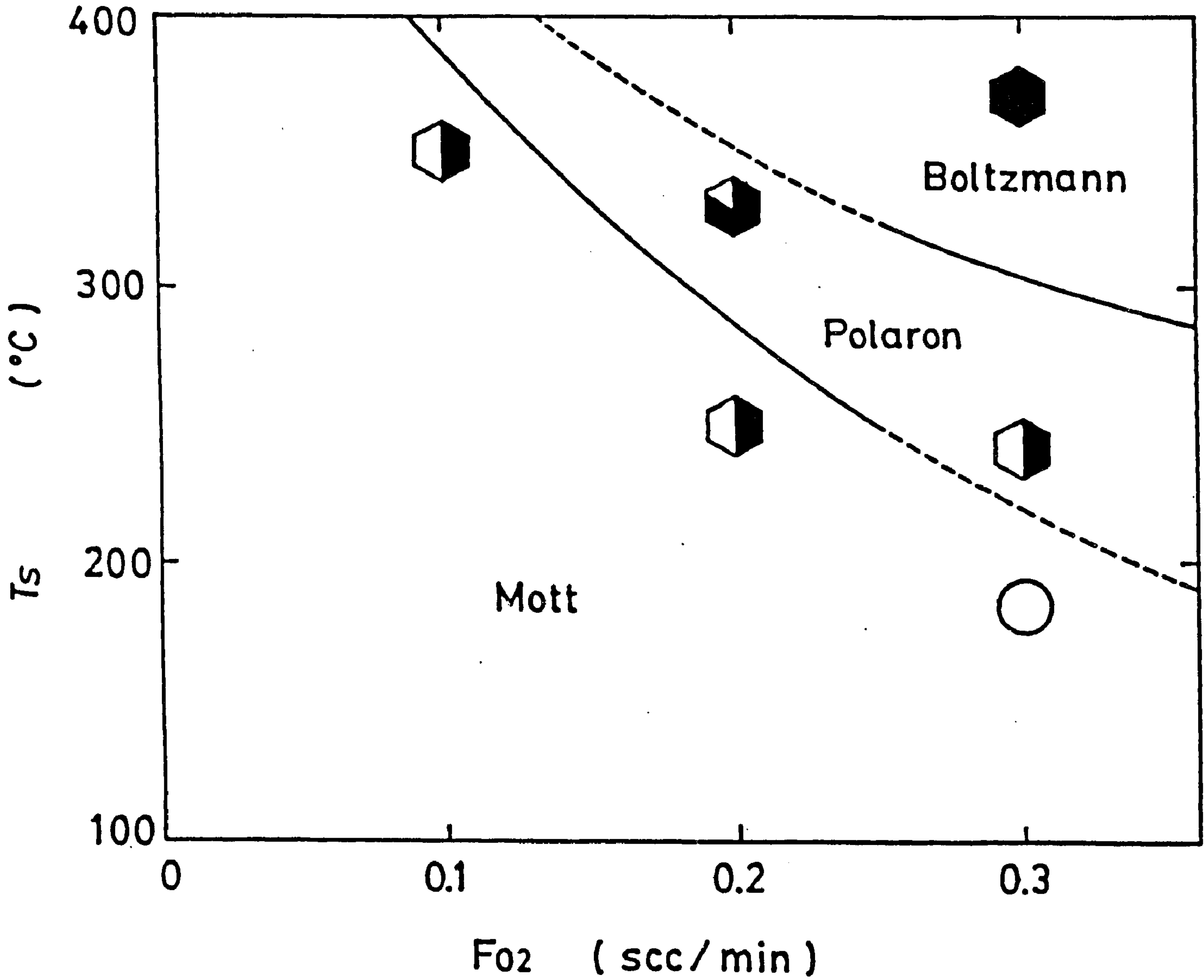

Figure 3.32 Electrical conduction mechanism diagram superimposed on the "metastable phase diagram".

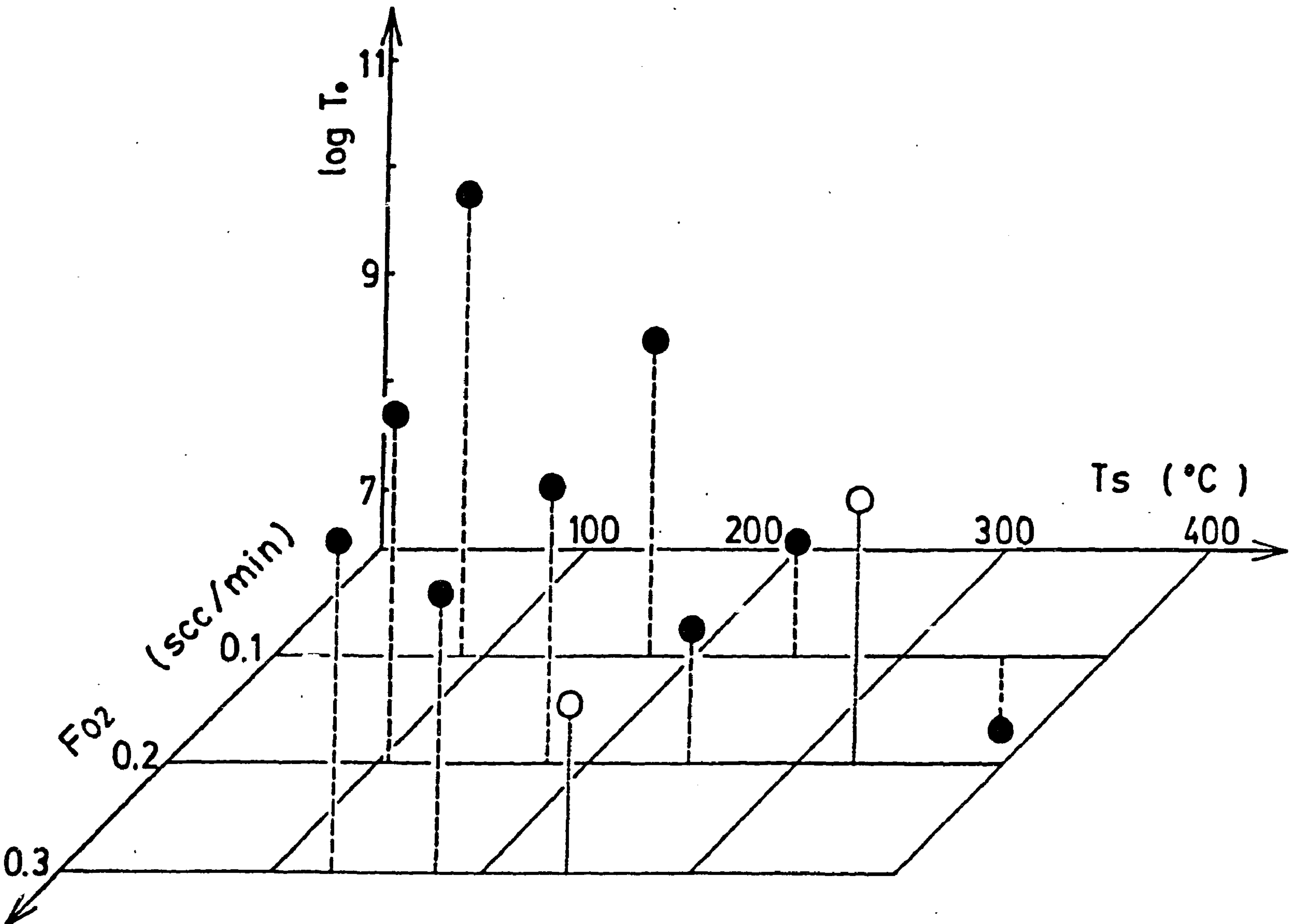

Figure 3.33 Parameter T_o used in eq (3.15) for the Mott mechanism in terms of substrate temperature (T_s) and oxygen gas flow rate (F_{O_2}).

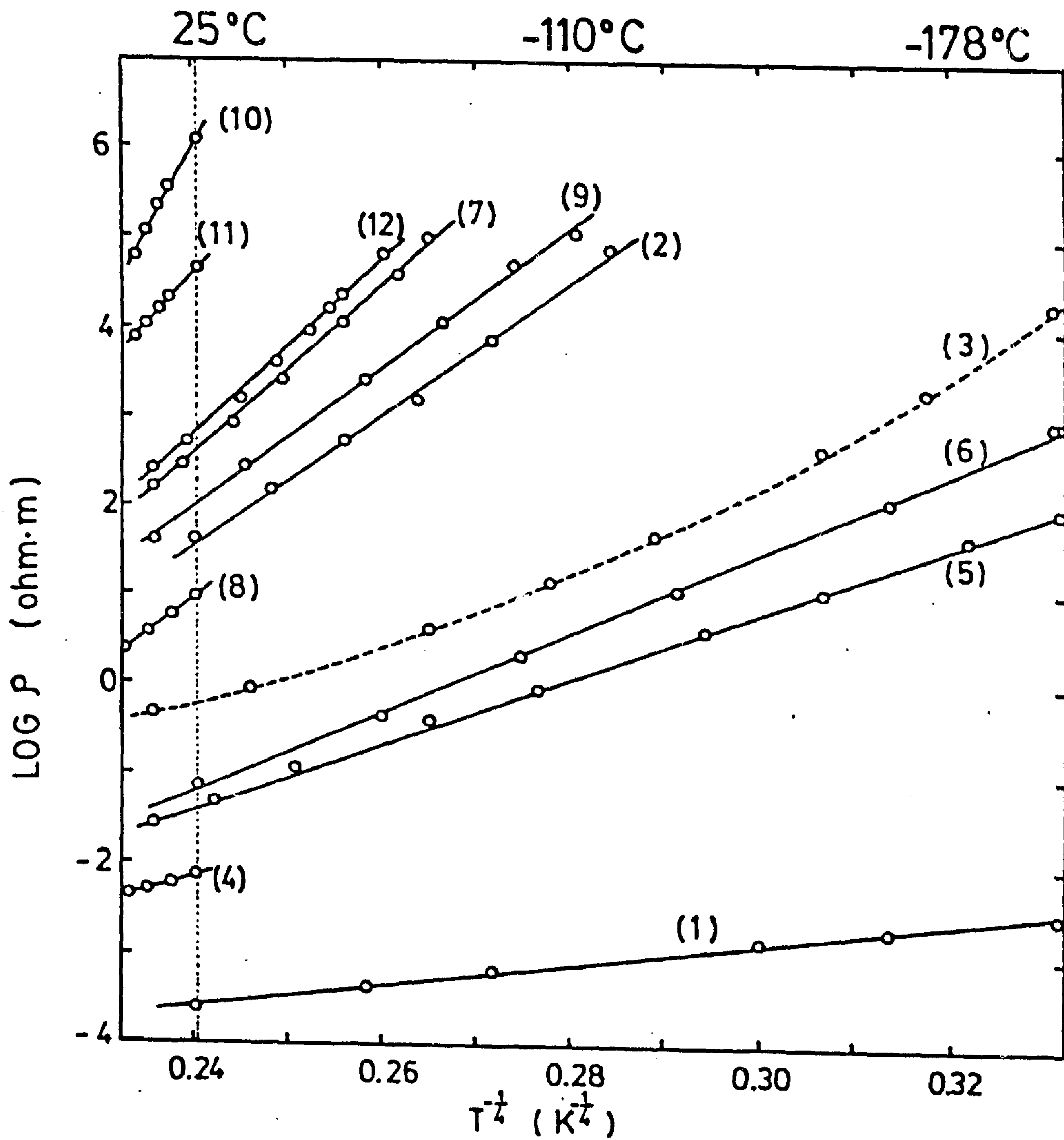

Figure 3.34 Resistivities of Samples (1) to (12) versus temperature.

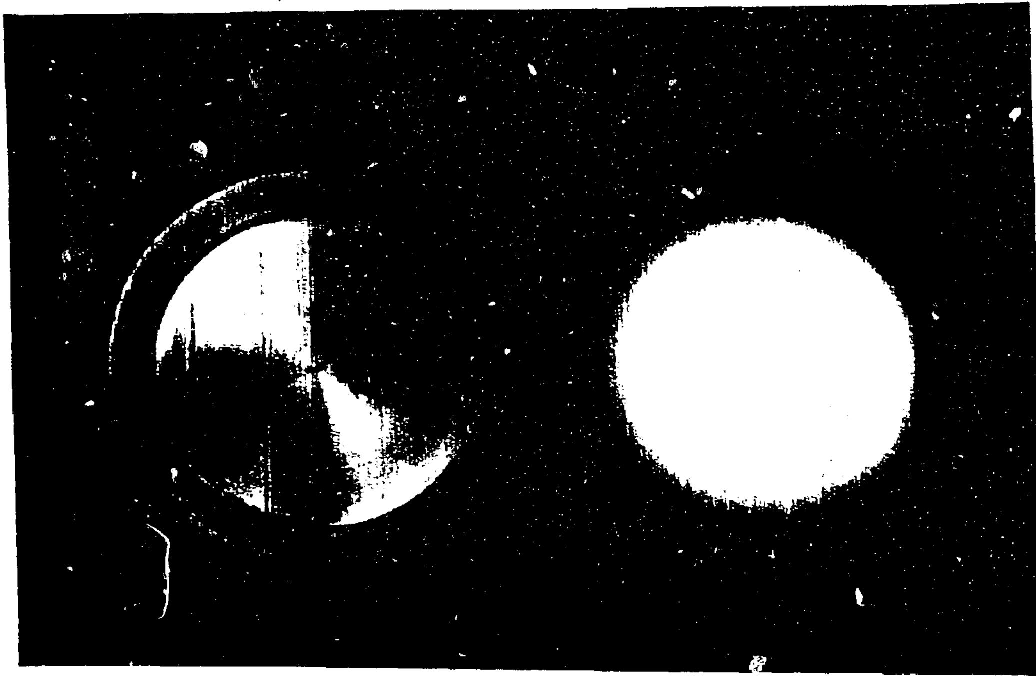

(A)

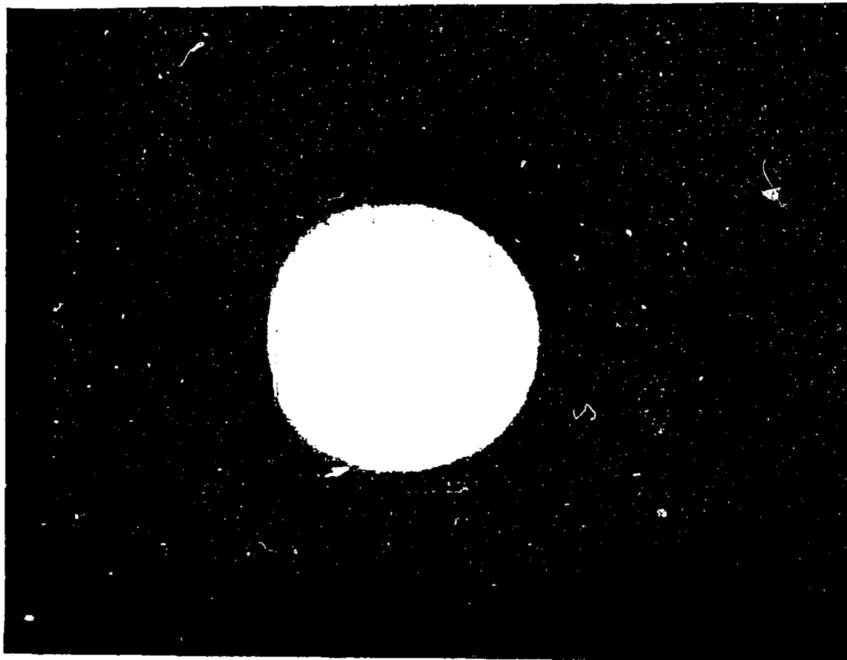

(B)

Figure 4.1 (A) Ti metal and $BaSiO_3$ discs. (B) Composite sputtering target of $BaSiO_3$ disc embedded at the centre of Ti disc.

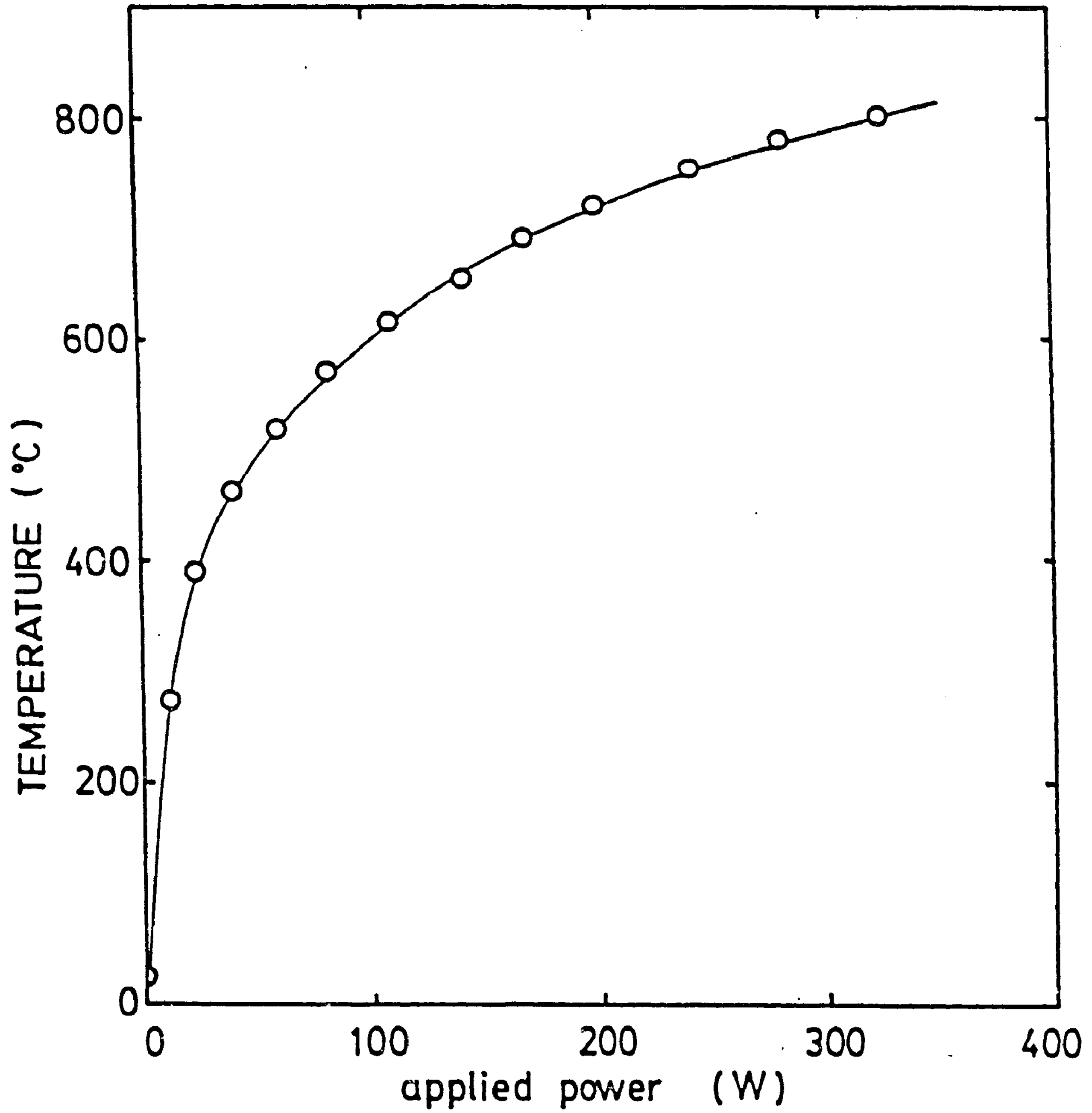

Figure 4.2 Temperature -vs- power relation of "new" heater. Tantalum wire was used as the heating element.

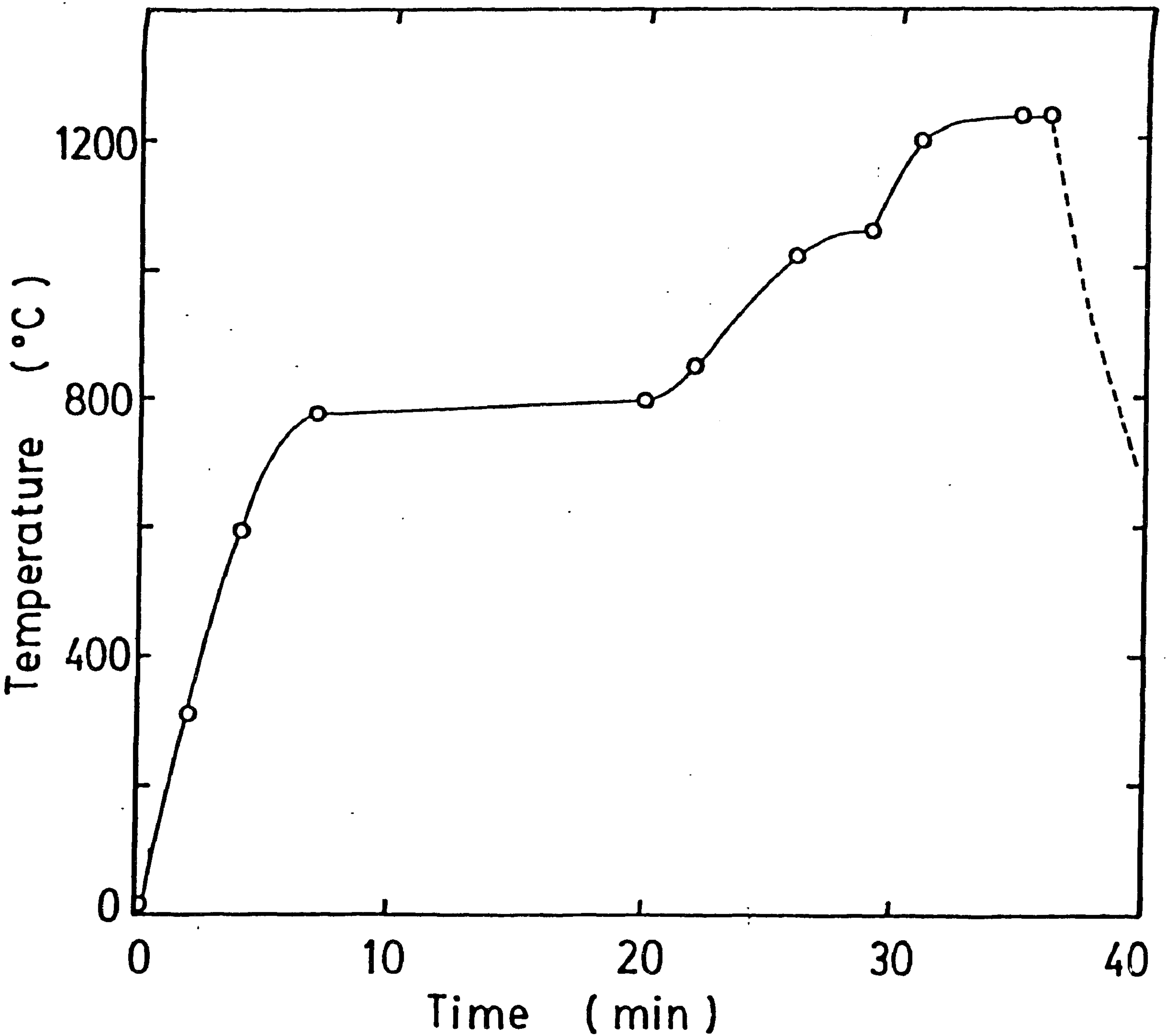

Figure 4.3 Heating program for sintering Target III.

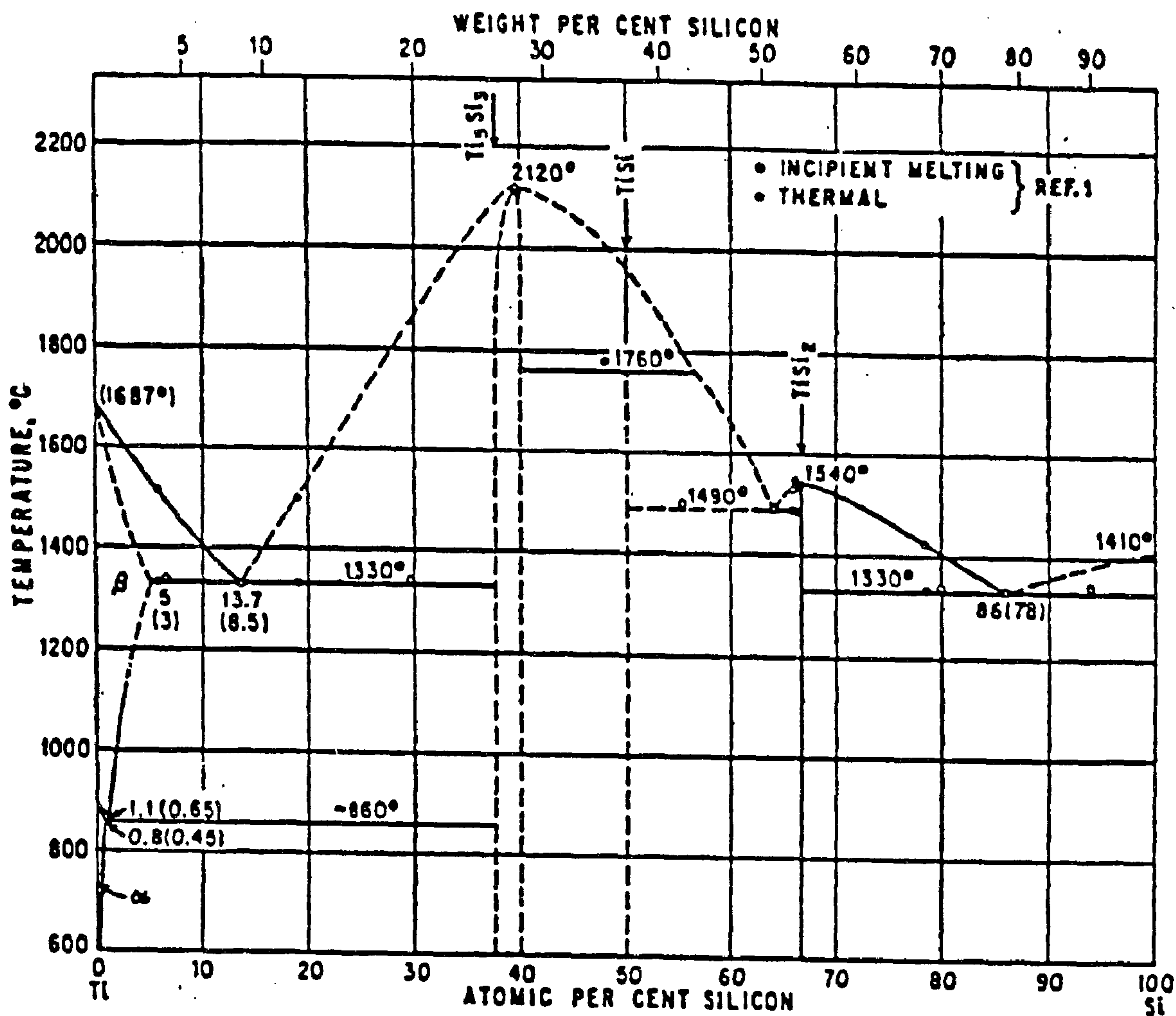

Figure 4.4   Titanium-silicon phase diagram (129).

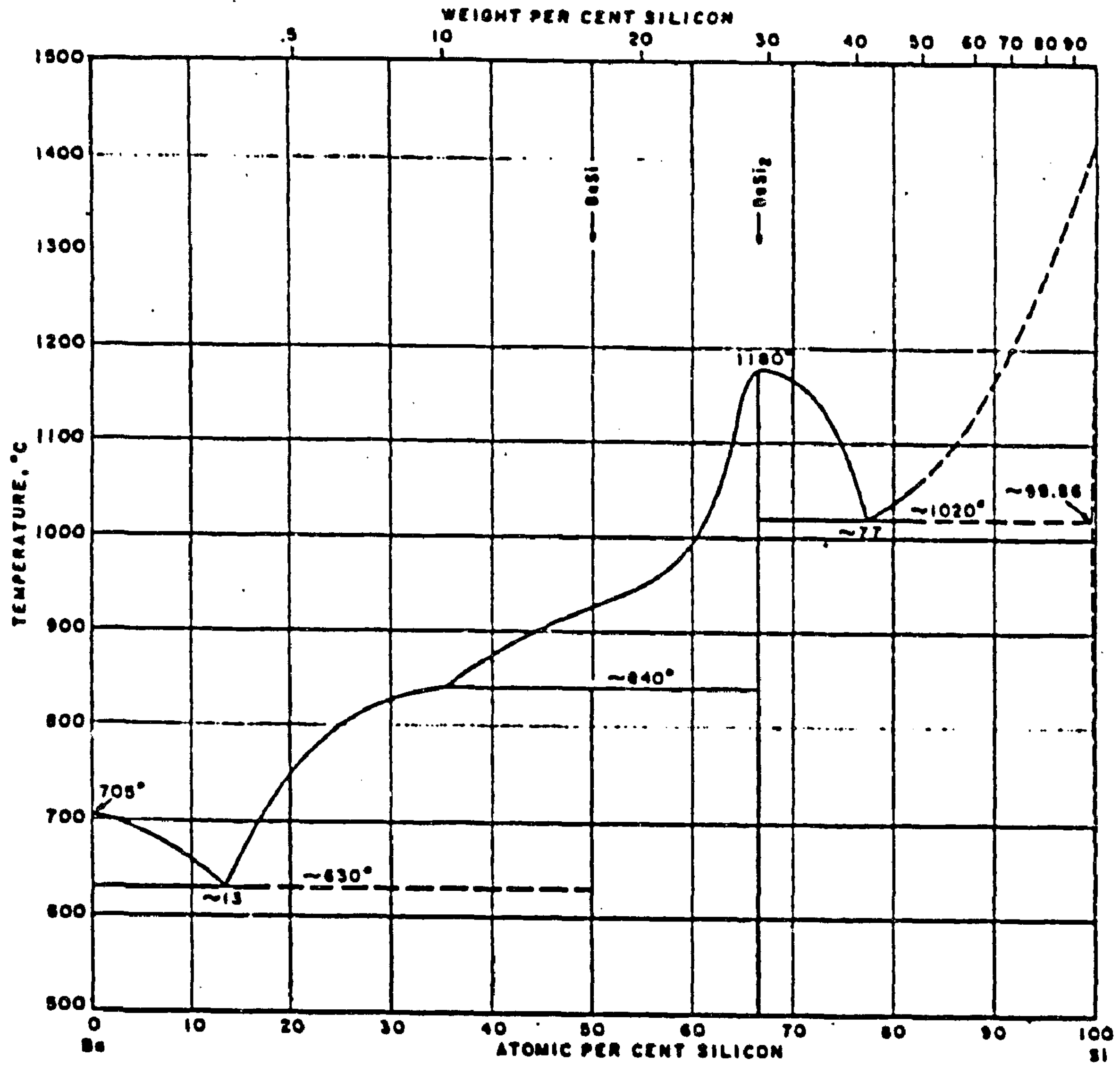

Figure 4.5 Silicon-barium phase diagram (129).

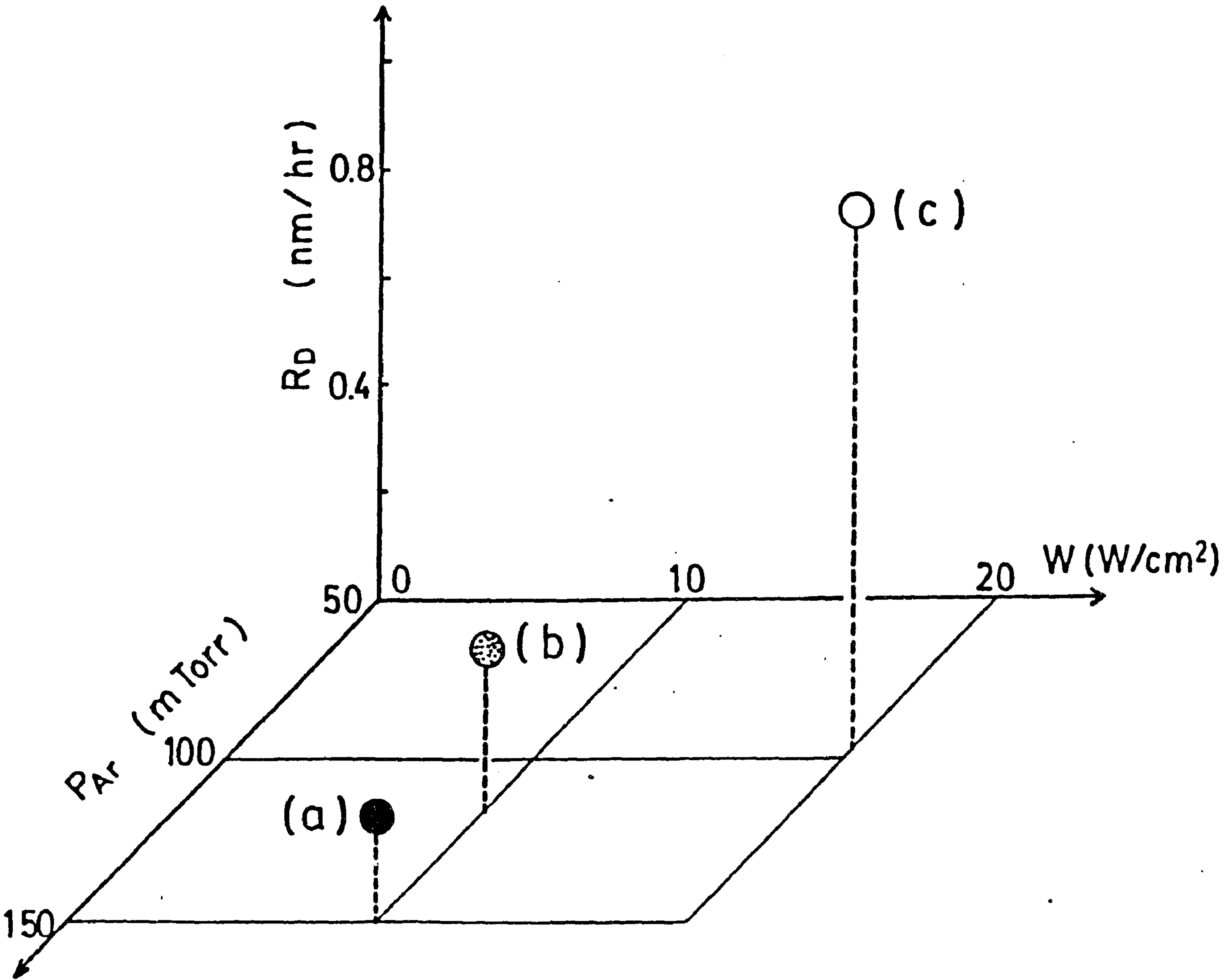

Figure 4.6 Deposition rate of Ba-Si-Ti oxide thin film Samples (a), (b) and (c) (defined in section 4.22) in terms of Ar partial pressure, P_{Ar}, and power density, W, applied to the target.

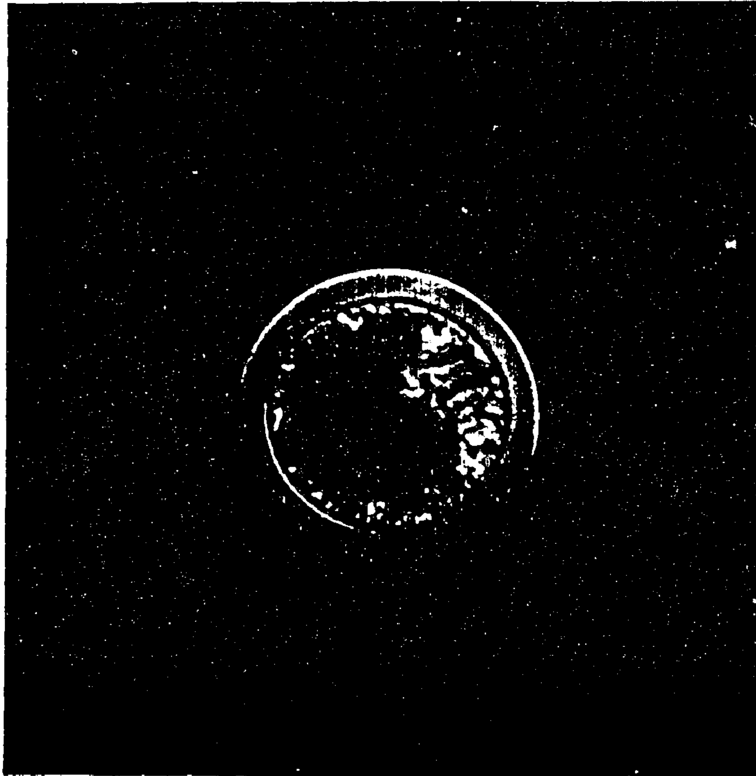

Figure 4.7 Target I (defined in section 4.21) after sputtering.

10μm

Figure 4.8 Scanning electron micrograph of thin film sputter deposited from Target I.

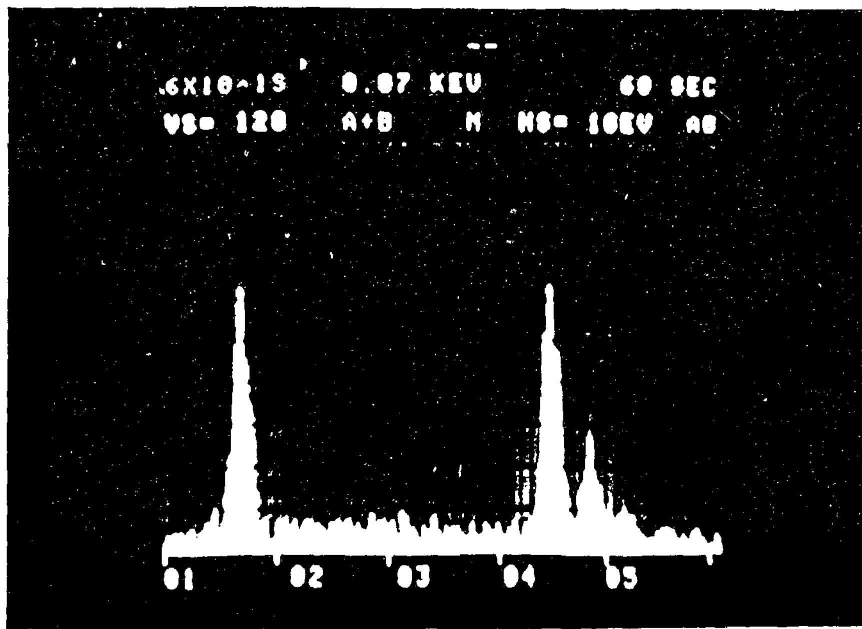

(A)

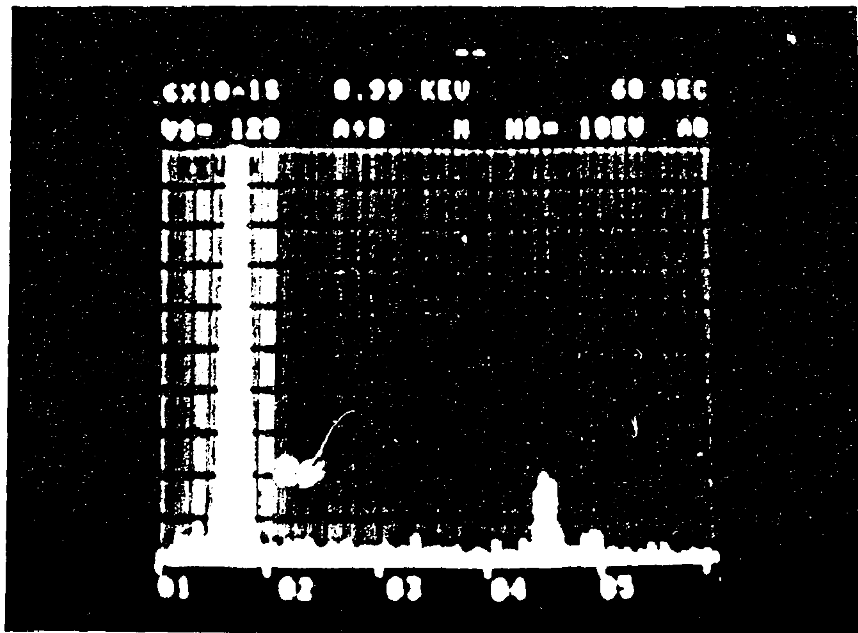

(B)

Figure 4.9 Energy dispersion spectra (using Kevex) for (A) grain and (B) background of the thin film shown in figure 4.8.

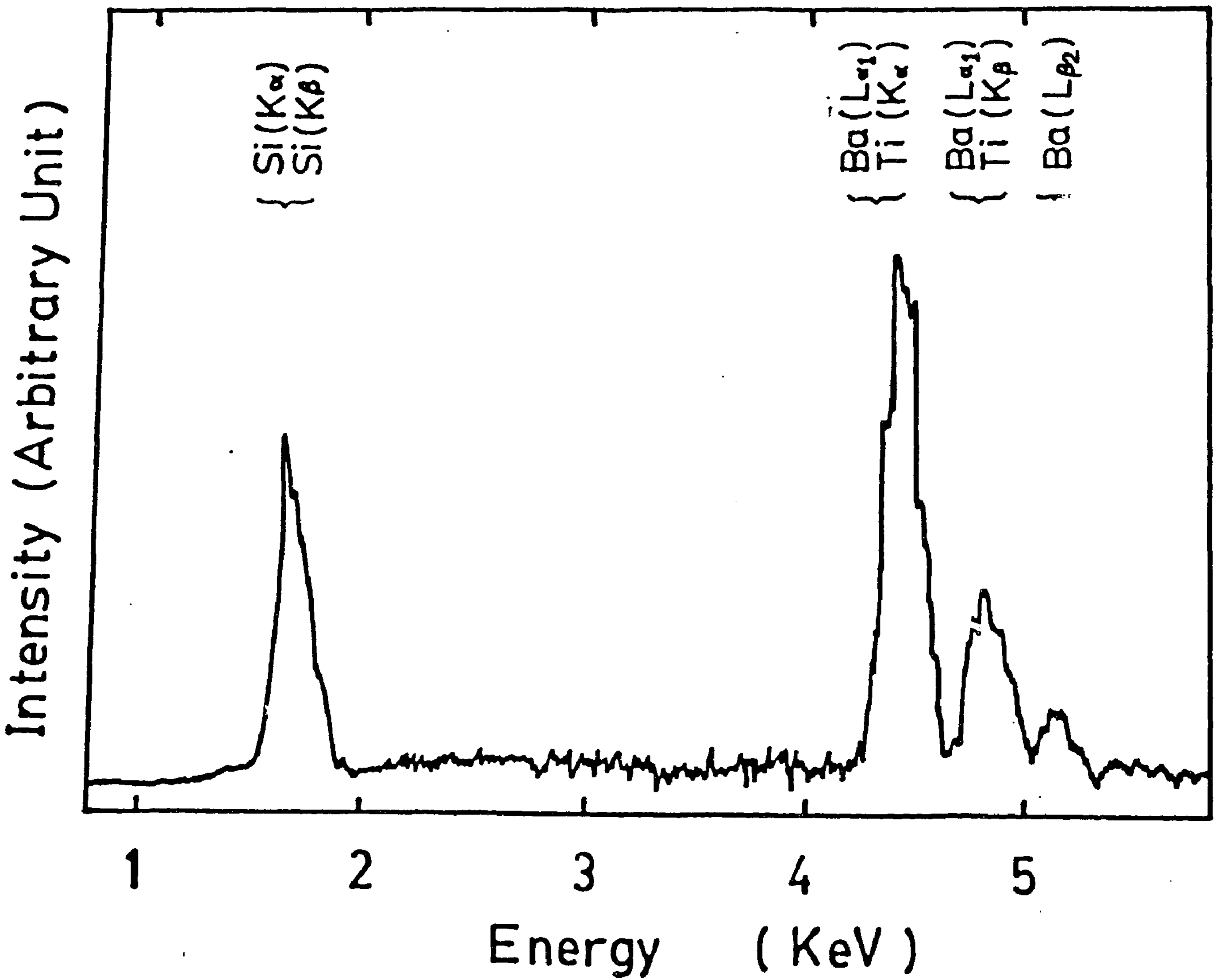

Figure 4.10 Spectrum of energy dispersion x-ray analysis (Kevex) of $Ba_2Si_2TiO_8$ ceramics (15).

(a)

20μm

Figure 4.11 Scanning electron micrographs of thin films sputter deposited from metallic Target III (defined in sectioh 4.21) at (a) P_{Ar}=150 m Torr and power density applied to the target, W= 10 W/cm^2, (b) P_{Ar}=115 m Torr and W=10 W/cm^{2}and (c) P_{Ar}=85 mTorr and W=20 W/cm^2. In all the cases, the oxygen gas flow rate is kept constant at 0.2 scc/min(see next page for (b) and (c)).

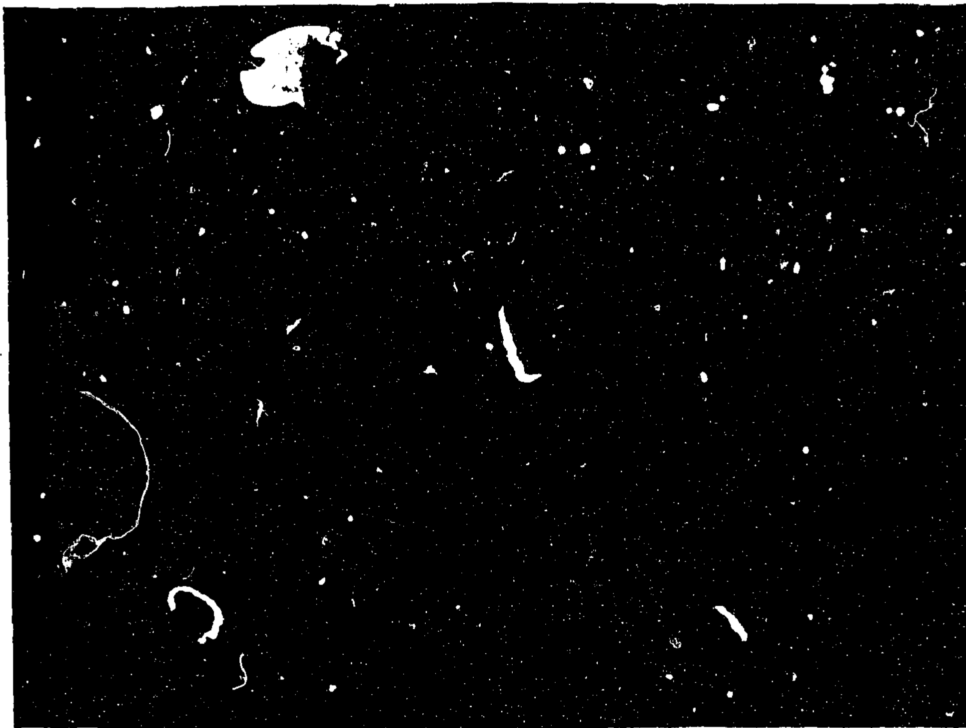

(b)

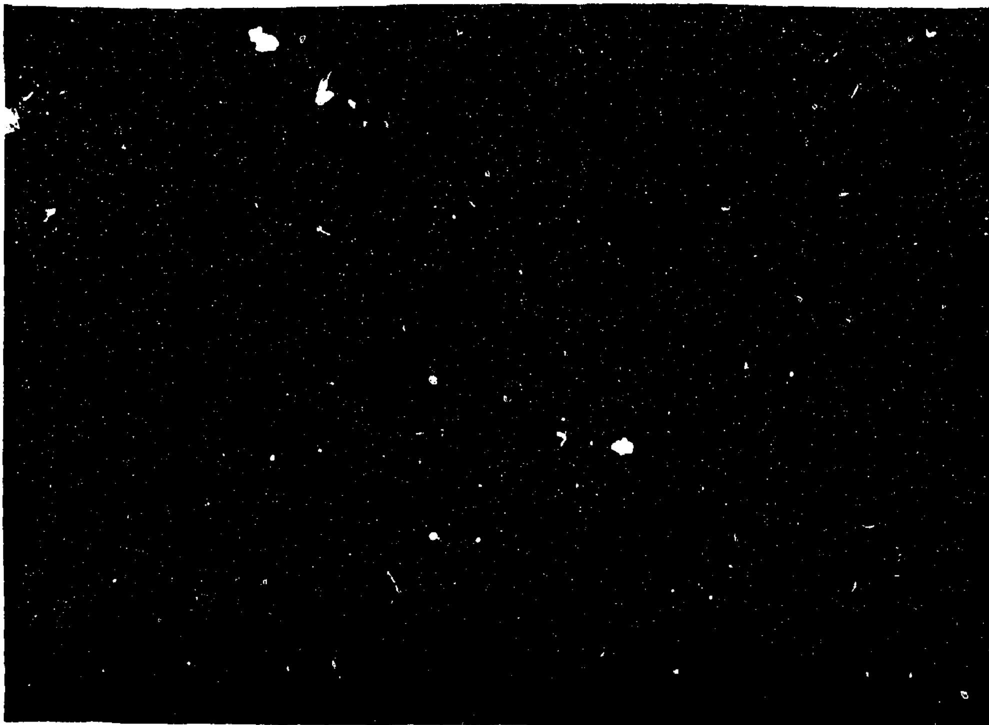

(c)

20 μm

Figure 4.11 (continued)

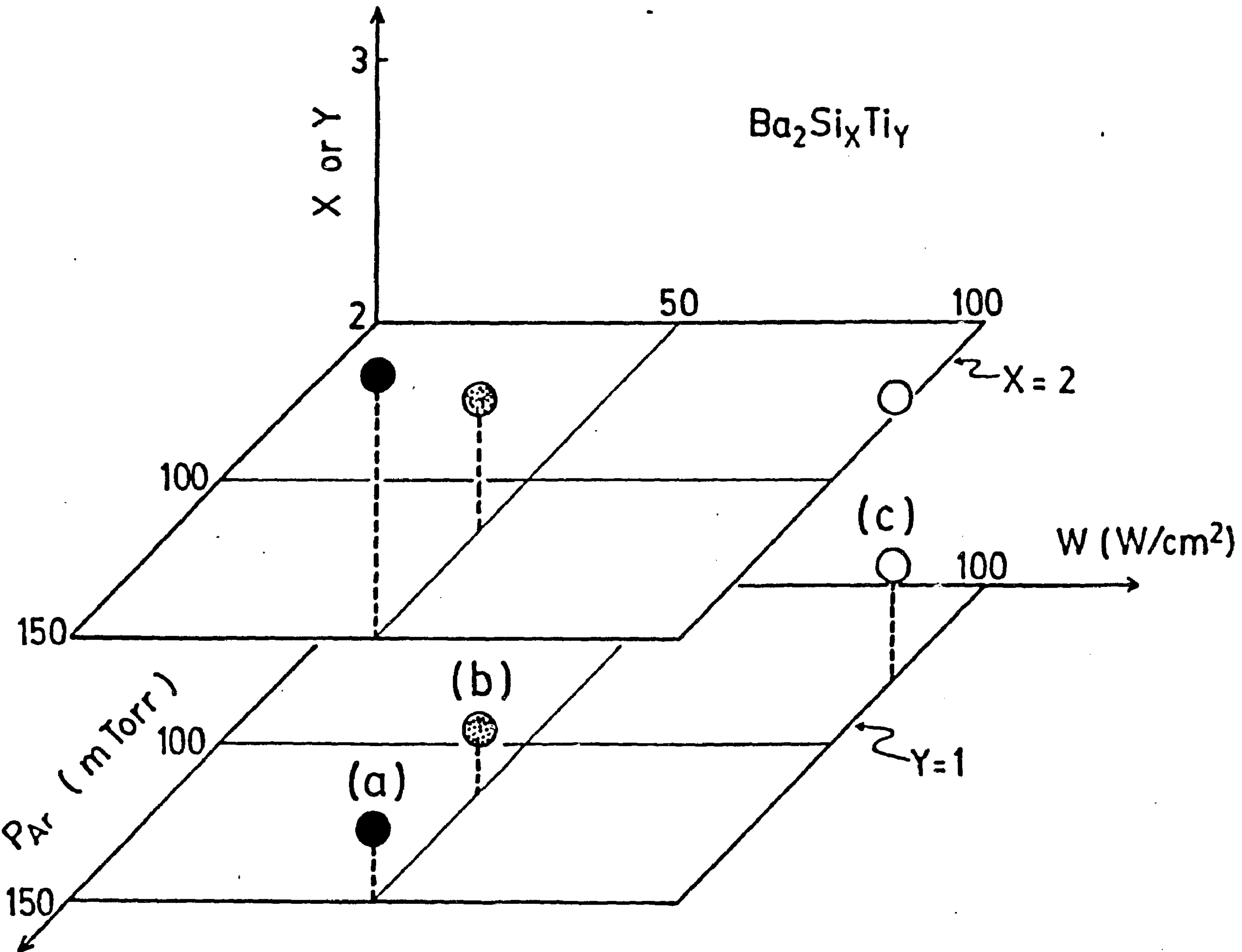

Figure 4.12 Compositions of Samples (a), (b) and (c) (defined in figure 4.11) versus argon gas partial pressure, P_{Ar}, and power density applied to the target, W.

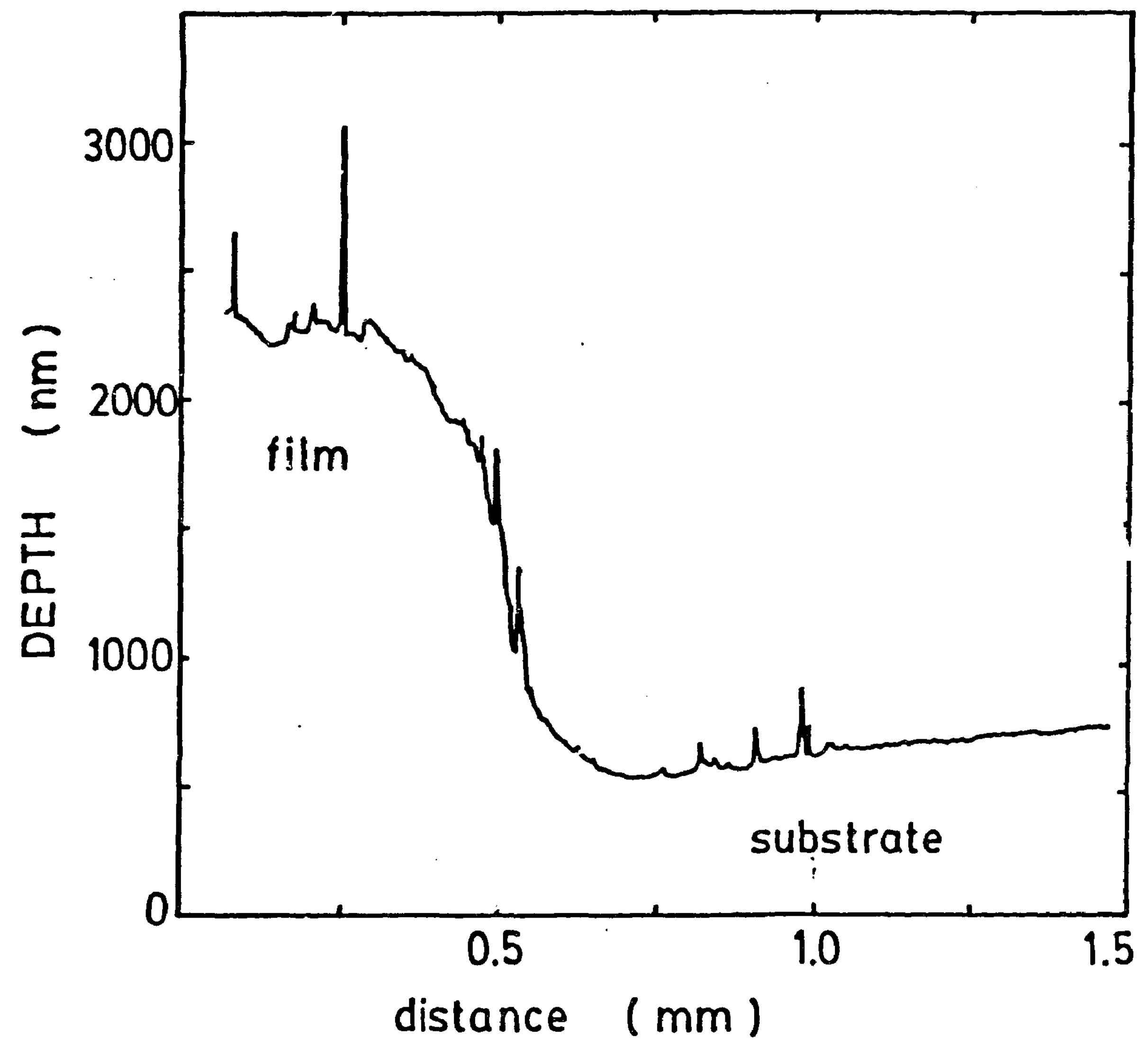

Figure A1 Titanium thin film thickness measured by a stylus method.

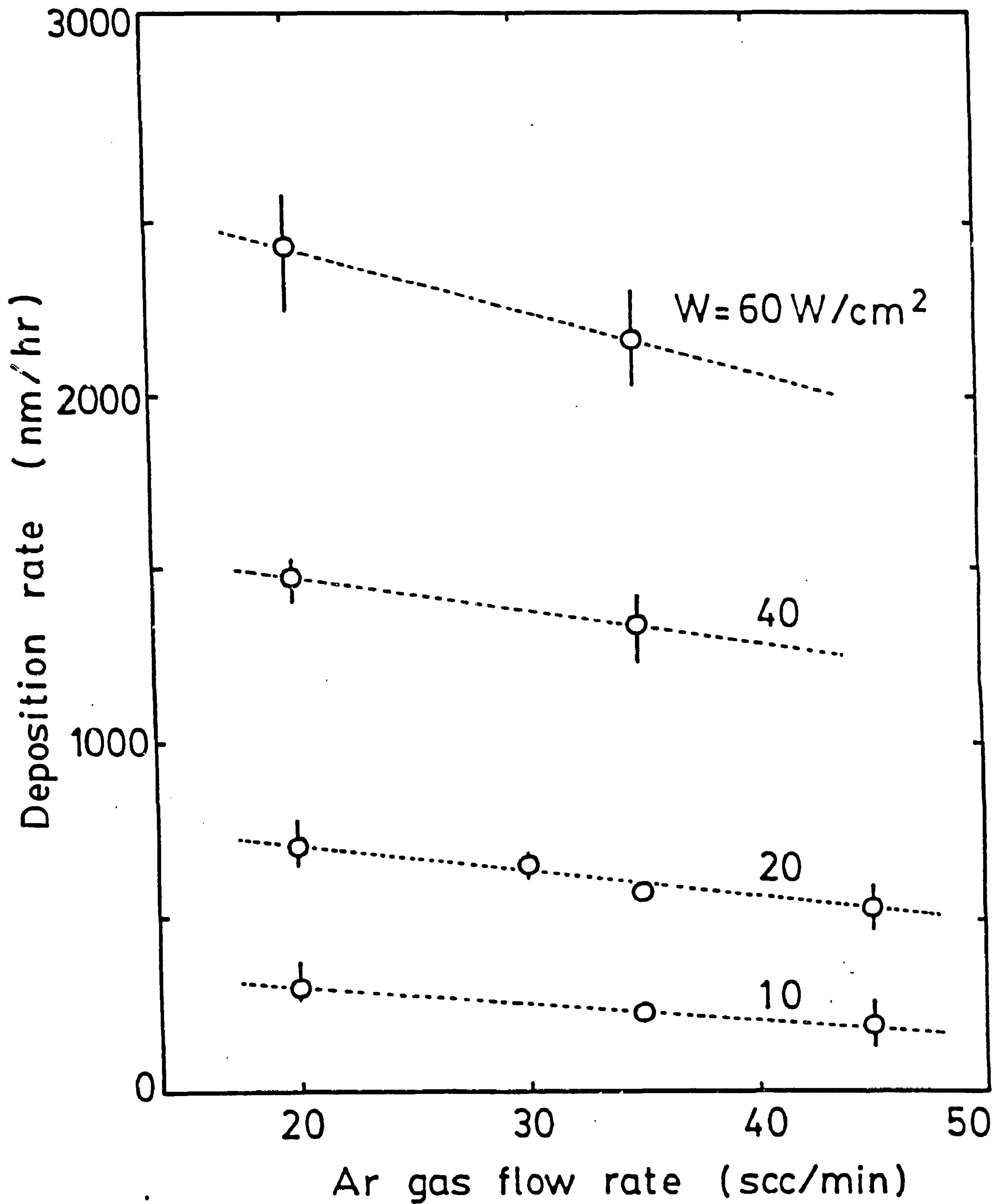

Figure B1 Deposition rate, R_D, of titanium thin films versus Ar partial pressure, P

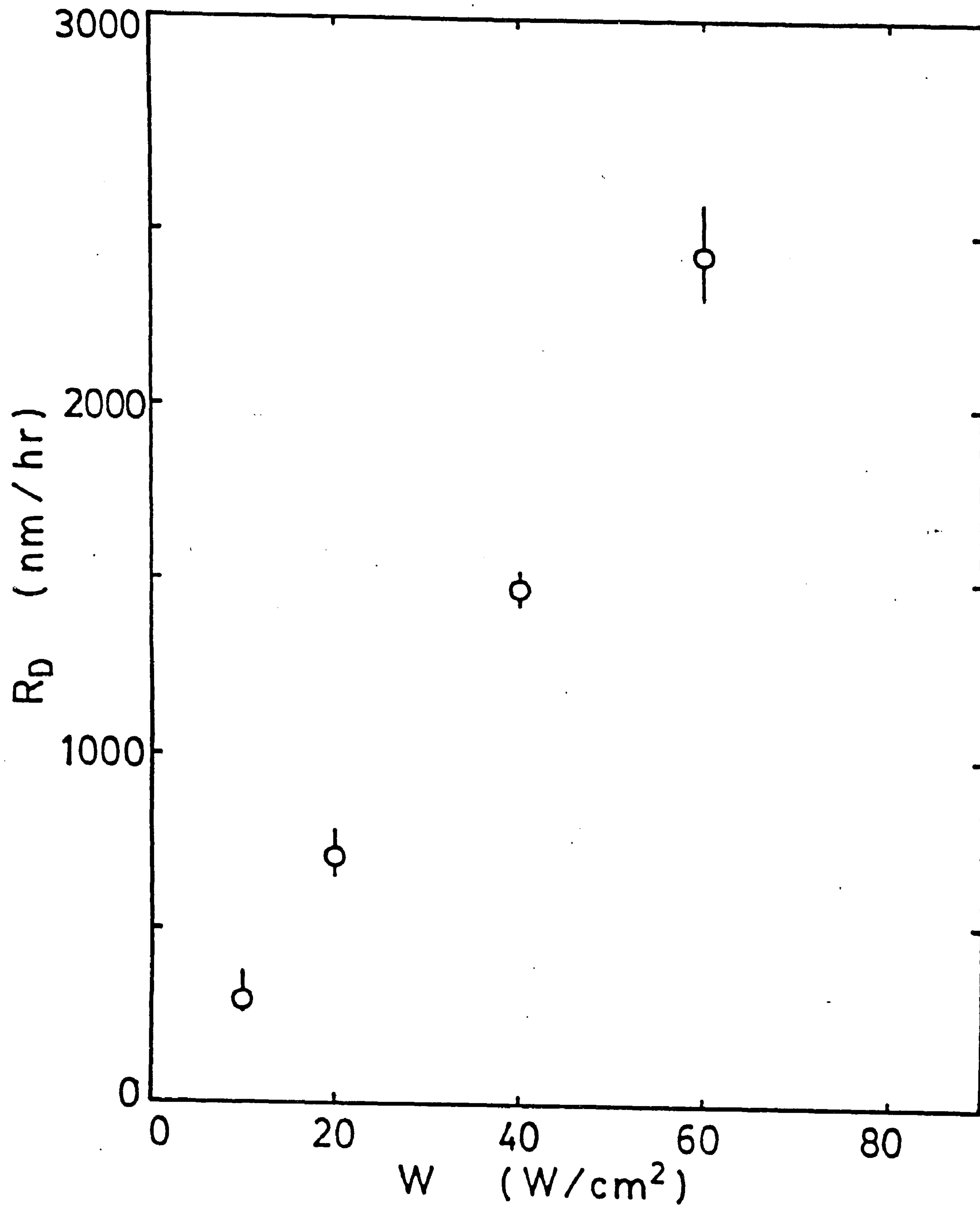

Figure B2 Deposition rate, R_D, of titanium thin films versus power density applied to the target, W

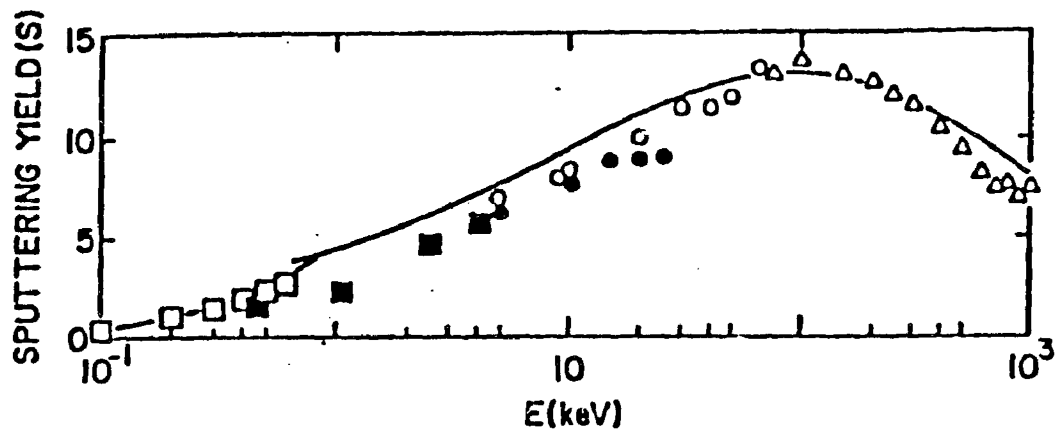

Figure B3 Sputtering yield of Cu as a function of Kr ion bombardment energy (142-147).

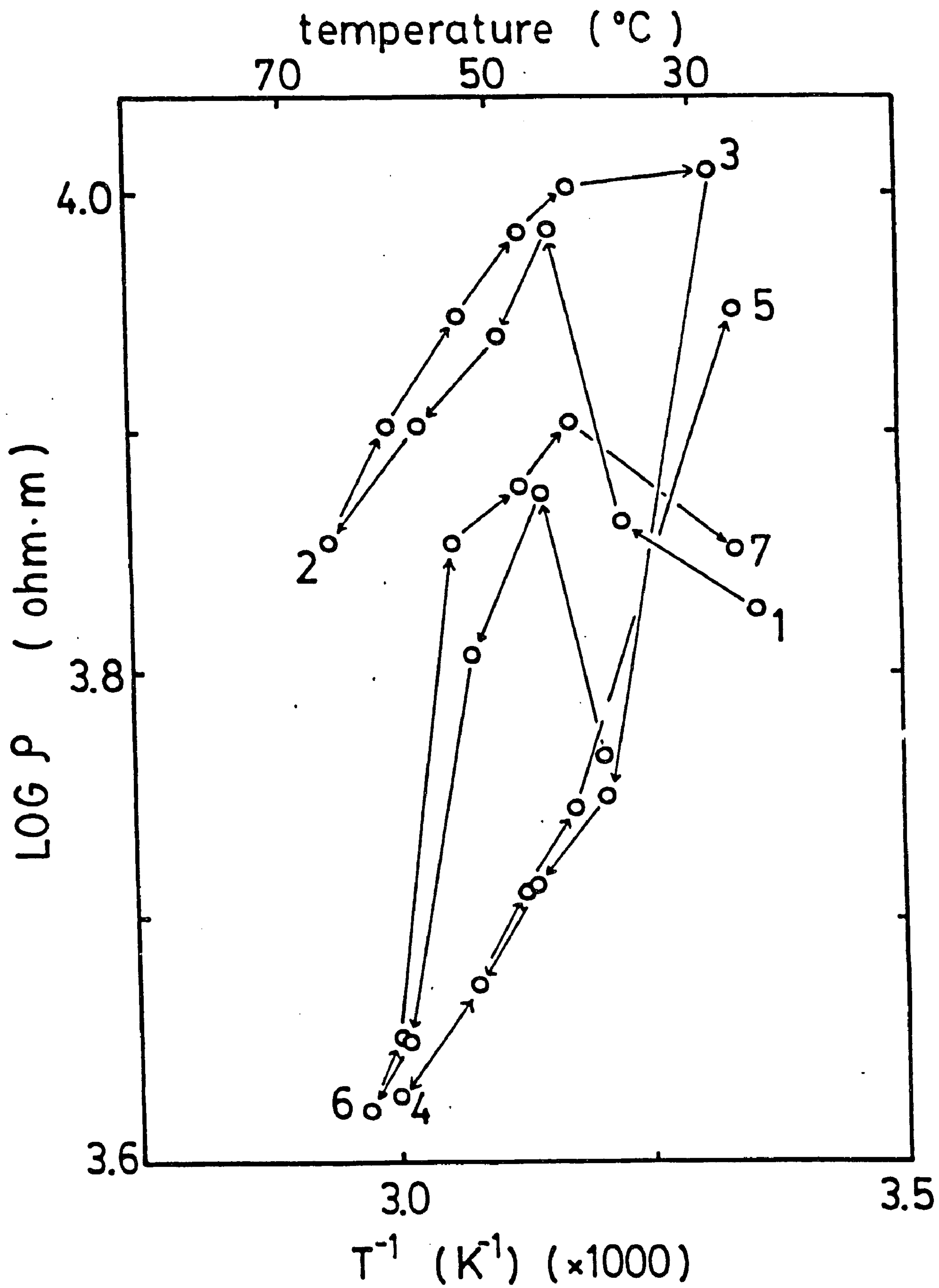

Figure C1 Resistivity of Sample (4) with Al electrodes in terms of temperature.

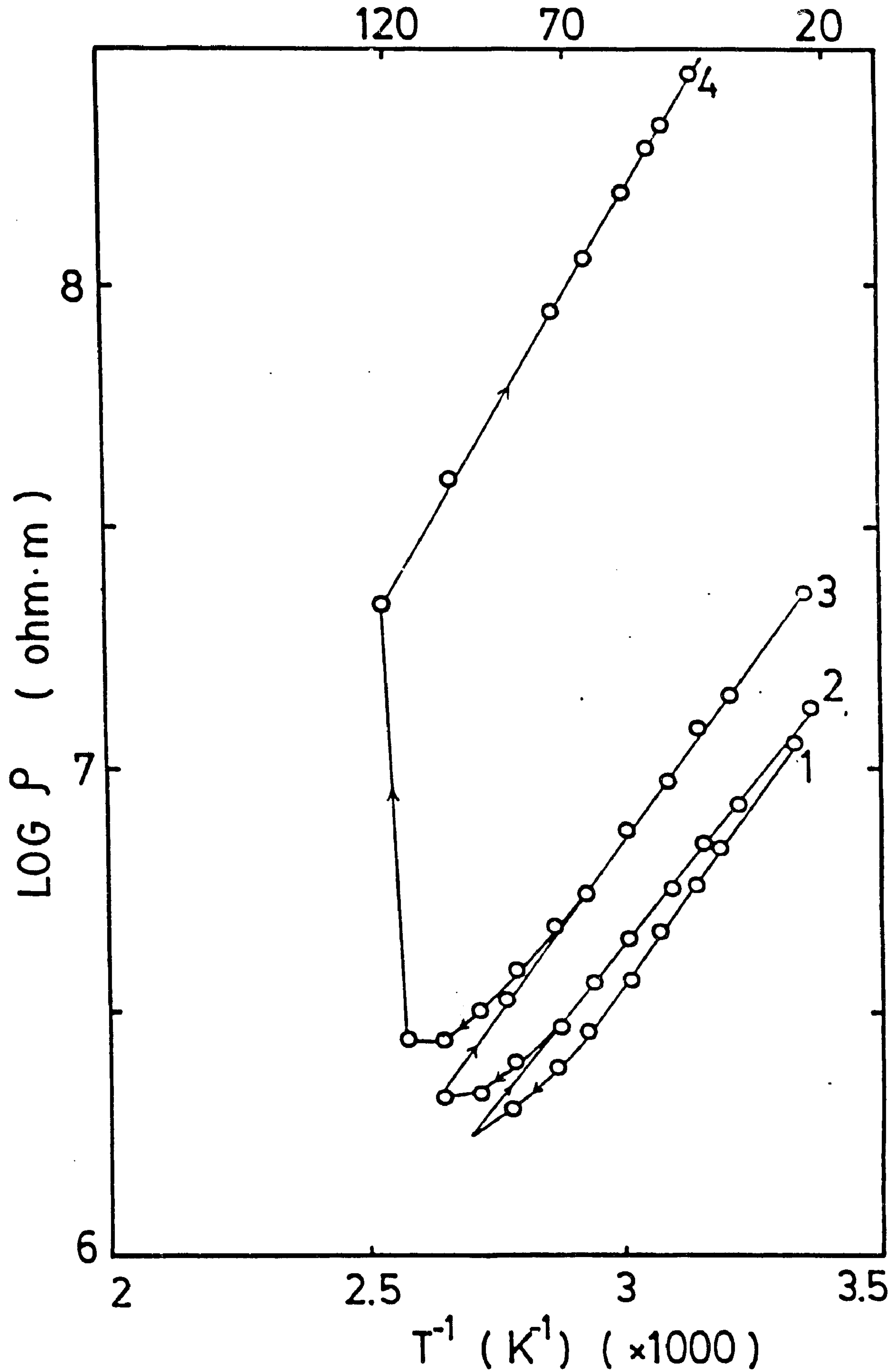

Figure C2 Resistivity of Sample (8) with Au electrodes in

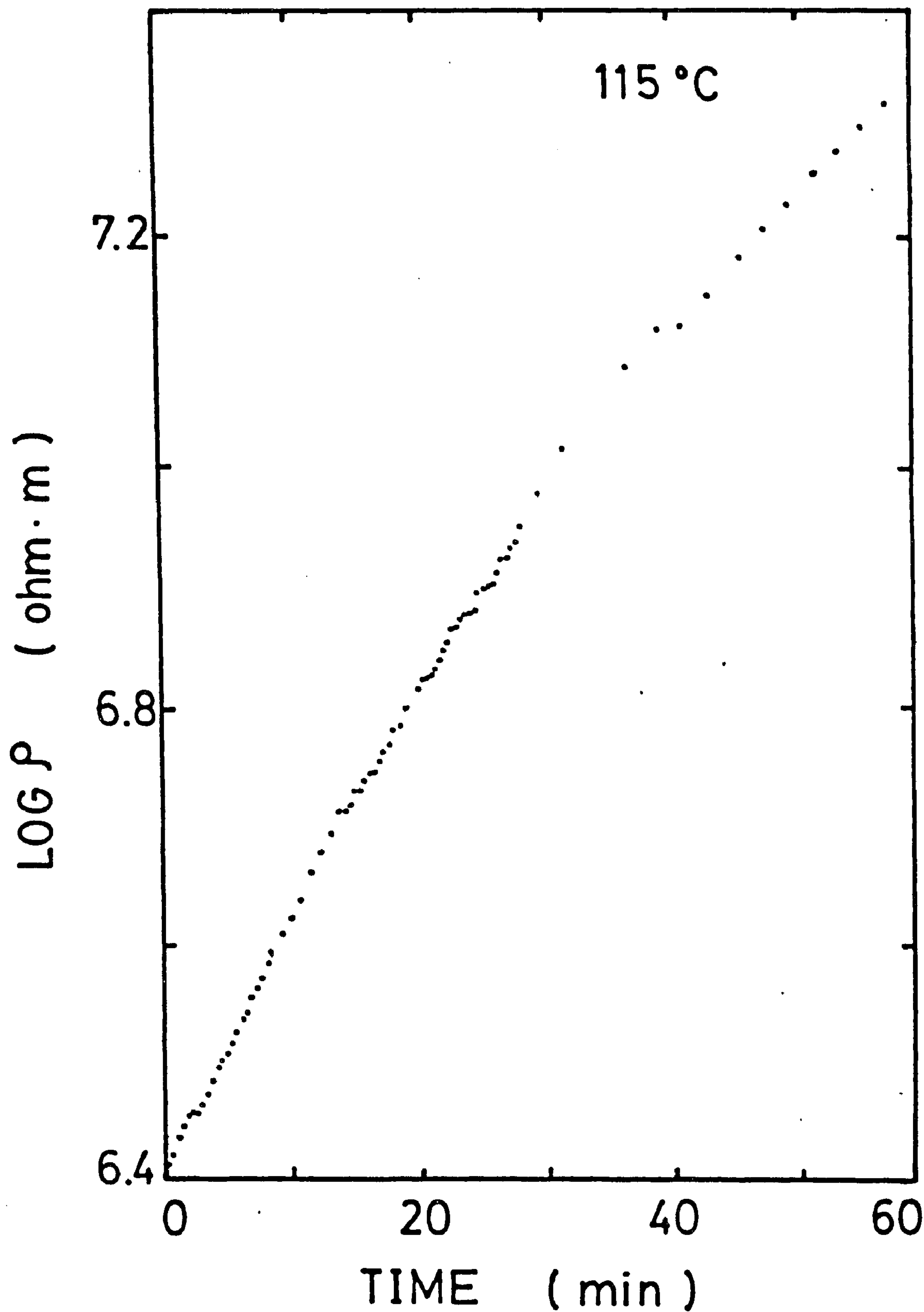

Figure C3 Resistivity of Sample (8) at 115°C as a function of time.

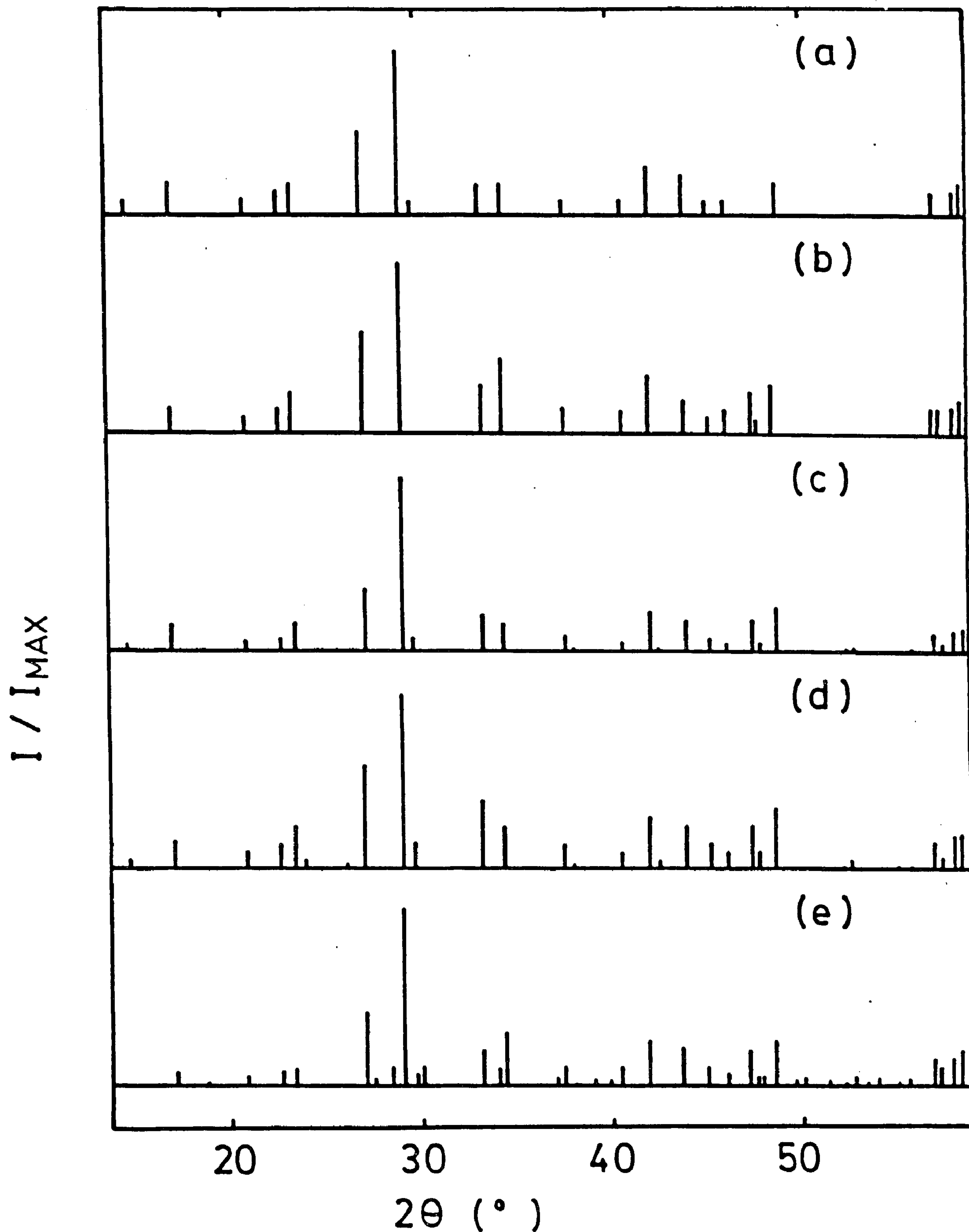

Figure D1 X-ray diffraction patterns of (a) $Ba_2Si_2TiO_8$ (BST)(in JCPD card) and (b) $BaSiTiO_5$ (in JCPD card). (c) Calculated BST pattern. Experimentally obtained x-ray diffraction pattern from the sample which had the Ba:Si:Ti ratios equal to